NMR studies of adsorption processes upon activated carbon

Jonathan Shaw

Shaw, Jonathan (1998) NMR studies of adsorption processes upon activated carbon. Doctoral thesis, Durham University.

NMR STUDIES OF ADSORPTION PROCESSES UPON ACTIVATED CARBON

by

Jonathan Shaw B.Sc. (Hons.)
Graduate Society
University of Durham

A thesis submitted in partial fulfilment of the requirements for the degree of Doctor of Philosophy

Department of Chemistry
University of Durham
1998

NMR STUDIES OF ADSORPTION PROCESSES UPON ACTIVATED CARBON

Jonathan Shaw B.Sc. (Hons.)
Submitted for the degree of Doctor of Philosophy
1998

ABSTRACT

This thesis is concerned with the adsorption behaviour of adsorbate molecules upon activated carbon. Limitations in bulk gravimetric measurements mean that the mechanism of adsorption for adsorbates upon carbonaceous materials is poorly characterised. The information obtained from NMR experiments performed upon the adsorbate molecules is applied to provide additional understanding of the adsorption process.

A systematic study of a phosphate/phosphonate – adsorbent system is performed, and a theoretical basis for the results observed is discussed in terms of molecular mobility and the penetration of molecules into pores of differing sizes. Calculated pore volumes obtained from NMR data are discussed. It is demonstrated that phosphate and phosphonate molecules adsorb initially within larger pores at the surface of the adsorbent and subsequently progress deeper within the porous volume. The effects of magic-angle spinning and proton decoupling upon the adsorbate spectra obtained are also addressed. Relaxation measurements are used to study the motional freedom of adsorbed molecules and the measurements provide further corroboration to the interpretation of spectra expounded. The study is then extended to analyse the adsorption of adsorbate molecules upon carbon adsorbents with other adsorbate molecules pre-adsorbed. Analysis of spectra provides information upon the movement of both the primarily adsorbed material and secondary adsorbate within the pore volume. Preferential adsorption of phosphate molecules over water molecules is demonstrated. Finally, dynamic NMR techniques are used to characterise the exchange of adsorbate within the porous volume with excess adsorbate upon the exterior of the carbon adsorbent.

MEMORANDUM

The research presented in this thesis has been carried out in the Department of Chemistry, University of Durham, between October 1995 and September 1998. Unless otherwise stated it is the original work of the author. None of this work has been submitted for any other degree.

ACKNOWLEDGEMENTS

Firstly, I would like to thank CBD, Porton Down and my two project supervisors, Mandy Ness and Paul Norman, for providing a research studentship allowing me to study in this area. Paul, in particular, has shared his knowledge and enthusiasm unstintingly whenever asked. I am also extremely grateful to Professor Robin Harris of Durham University for accepting me as a member of his research group. His supervision, encouragement, and grammatical precision have been much appreciated. On a more day to day basis I have benefited greatly from the expertise of several members of the RKH group, most especially Dr. Alison Nordon, Dr. Eric Hughes and Barry Say. Alison helped me greatly in the fundamentals of the NMR experiment and NMR theory and was to be relied upon whenever the spectrometer refused to behave. Eric brought to the group an understanding of all things Wigner and graciously guided me through many of the trickier passages within Haeberlen. Conversations with Barry, our relaxation expert, could always be relied upon to yield the odd pearl of wisdom.

I have also had the pleasure of working with many other people over the last three years. My thanks to Alan, Ian, Peter, Minoru, Ulrisch, Gustavo, Regis, Phillippe, Eric, Claudia, Marco, Raouf, Naser, Tim, Alison, Gary, Susan, Julian, Lindsey, Helen and Stefan. Perhaps you might remember the better times? Finally I would like to thank my "non-professional" friends, the various footballers, basketball players, housemates, and other like-minded souls who helped make my time in Durham so much more enjoyable.

To my Parents

CONTENTS

1. NMR THEORY

2. ACTIVATED CARBON

3. EXPERIMENTAL

4. A 1D NMR STUDY OF A SINGLE ADSORBATE-ADSORBENT SYSTEM

5. COMPETITION BETWEEN DIFFERENT ADSORBATE MOLECULES WITHIN THE PORE SYSTEM STUDIED BY MAS NMR

SYMBOLS

β	Orientation of principal component of interaction tensor to B_0
γ	1. Nuclear gyromagnetic ratio 2. Liquid surface tension
δ	Chemical Shift
$\Delta\delta$	Change in chemical shift
ζ	Anisotropy of shielding tensor
η	Tensor asymmetry factor
μ	Nuclear magnetic moment
ν	Larmor precession frequency of nucleus
ρ	Density matrix
σ	Shielding tensor
σ_{iso}	Isotropic component of shielding tensor
τ_c	Correlation time for molecular-level motion
$\Im$	Dyson time-ordering operator
χ	Bulk magnetic susceptibility
ω_0	Angular precession frequency of nucleus about B_0
ω_1	Angular precession frequency of nucleus about $\mathbf{B_1}$
A_j	Absorption mode peak at frequency ω_j
$\mathbf{B_0}$	Static magnetic field
$\mathbf{B_1}$	Radio frequency magnetic field associated with frequency ν_1
D_j	Dispersion mode peak at frequency ω_j
$\mathbf{D}^x$	Element of Wigner rotation matrix of order x
$\hat{H}$	Hamiltonian Operator
I	Nuclear spin quantum number (of dilute nuclei)
J	Indirect spin-spin coupling constant
M^0	Equilibrium macroscopic magnetisation for spin system in presence of B_0
M_I	Total magnetic component quantum number
M_x	Component of macroscopic magnetisation along the x-axis
$\mathbf{P}$	Angular momentum
P	Coherence level order
S	Nuclear spin quantum number (of abundant spin nuclei)
T_1	Spin-lattice relaxation time
$T_{1\rho}$	Spin-lattice relaxation time in the rotating frame
T_2	Spin-spin relaxation time
U(t)	Spin-evolution operator
V_M	Molar volume of liquid

ABBREVIATIONS

ADC	Analogue to Digital Converter
BET	Method of isotherm classification named after the authors Brunaeur, Emmett and Teller
CBDE	Chemical and Biological Defence Establishment
CW	Continuous Wave
CYCLOPS	Cyclically Ordered Phase Cycle
DMMP	Di-methyl methyl phosphonate
E_a	Activation Energy
EXSY	Exchange Spectroscopy
FID	Free Induction Decay
FT	Fourier Transform
FWHM	Width of resonances observed (Full Width at Half Maximum)
HPPD	High Power Proton Decoupling
IBMS	Isotropic Bulk Magnetic Susceptibility
PAS	Principal Axis System
PDMSO	Poly di-methyl siloxane
Peak I	The low-frequency peak observed upon addition of adsorbate to C
Peak II	The unshifted peak observed upon further addition of adsorbate to C
PICA	Classification of coconut shell used in this study
PSD	Pore Size Distribution
PVDC	Polyvinyl di-chloride
S/N	Signal to Noise ratio
SA	Shielding Anisotropy
SC2	Classification of coconut shell used in this study
SPI	Selective Polarisation Inversion
TMP	Tri-methyl phosphate
VFM	Volume Filling of Micropores
VT	Variable Temperature

NMR THEORY

In the fifty years since nuclear magnetic resonance was first observed in bulk materials[1], NMR has become the technique of choice for analysing chemical structure in a wide variety of applications. The fundamental theory of the subject is well documented and there are many textbooks that treat the subject at length and from a variety of perspectives (for example[2-9]). The most basic of summaries of the theory of NMR spectroscopy, using classical vectors to visualise the changes occurring during the NMR experiment, is outlined in section 1.1. A more rigorous introduction to the nuclear spin Hamiltonian, describing the evolution of the spin system, follows in section 1.2. Further theoretical discussions pertaining to specific experiments can be found in the appropriate sections of the thesis.

1.1. FUNDAMENTAL THEORY OF NMR

1.1.1. NUCLEAR SPIN AND ANGULAR MOMENTUM

NMR is the absorption of radiofrequency radiation caused by transitions between the spin states of nuclei. Quantum mechanics states that the angular momentum, **P**, of an isolated particle is limited to discrete values, which are determined by the nuclear spin quantum number, I. Angular momentum is a vector property and to be fully defined an orientation must also be specified. Quantum mechanically this is done via another quantum number, M_I, which fully describes the allowed nuclear spin states.

Equation 1.1

$$\vec{P} = \hbar\sqrt{I(I+1)}$$

Equation 1.2

$$M_I = -I, -I+1, \ldots, I-1, I$$

A moving charged body causes an associated magnetic field, and because the angular momentum of the isolated particle is quantized, the magnetic moment, μ, of the particle will be quantized also. The magnetic moment is proportional to the angular momentum, with a constant of proportionality, γ, that is nucleus specific. γ can be positive or negative depending on whether the spin magnetic moment is parallel or anti-parallel to the spin angular momentum.

$$\vec{\mu} = \gamma\vec{P} = \gamma\hbar\sqrt{I(I+1)}$$ *Equation 1.3*

In the absence of an external magnetic field, all quantized values of the nuclear magnetic moment are equivalent in energy (degenerate).

1.1.2. MAGNETISATION AND PRECESSION

The NMR experiment applies a strong magnetic field, $\mathbf{B}_0$, in a direction defined as z, to the nucleus so that the degeneracy in the nuclear magnetic moment is removed. Each spin state has energy, U, determined by M_I. Clearly there will be (2I+1) non-degenerate energy levels, each separated by $\gamma\hbar\mathbf{B}_0$.

$$U = -\mu_z\vec{B}_0 = -\gamma\hbar M_I\vec{B}_0$$ *Equation 1.4*

A useful method for discussing the effect of $\mathbf{B}_0$ and pulsed Fourier Transform (FT) NMR is to consider the classical motion of the nuclear magnetic moment under the condition of constant total energy. The application of $\mathbf{B}_0$ exerts a torque upon the magnetic moment. The angle that μ makes with $\mathbf{B}_0$ is a function of the nuclear spin-state, M_I, and is invariant at constant energy, which means that only the component of angular momentum perpendicular to both $\mathbf{B}_0$ and μ is affected. The net result is therefore a rotation of the direction of μ in a precession cone about $\mathbf{B}_0$. The angular frequency of the resultant "Larmor precession" is given by

$$\nu_L = -\frac{\gamma}{2\pi}B_0$$ *Equation 1.5*

Each orientation of μ relative to $\mathbf{B}_0$ arises from different spin states with different energies, and therefore the application of the magnetic field results in the nuclei being spread over a variety of discrete energy levels. For nuclei with a spin quantum number $I = {}^1/_2$ (including most commonly acquired nuclei such as ^1H, ^{13}C and ^{31}P) there are two precession cones and two energy levels. These are commonly termed the α and β states.

If a large number of spin-$^1/_2$ nuclei are considered, all with identical Larmor frequencies, the relative population of the two non-degenerate spin states will be described by a Boltzmann distribution. There will be a slightly greater number of nuclei in the lower energy α state.

$$\frac{N_\beta}{N_\alpha} = \exp\left(\frac{-\Delta E}{kT}\right) \qquad \textit{Equation 1.6}$$

The sample magnetisation, $\mathbf{M}$, is simply a summation of all the nuclear magnetic moments. The slight difference in the two populations produces a net magnetisation in the positive z direction, whilst the components of μ precessing in the xy plane have a random distribution resulting in a net transverse magnetisation of zero. Therefore there is a net magnetisation at equilibrium, $\mathbf{M}_0$, that is stationary and aligned along the z-axis.

1.1.3. RESONANCE AND THE ROTATING FRAME OF REFERENCE

To achieve resonance, electromagnetic radiation is applied to the sample. This radiation acts as a second magnetic field, $\mathbf{B}_1$, perpendicular to, and rotating about, $\mathbf{B}_0$ at the radiation frequency. If the radiation frequency is matched to the Larmor frequency of the nucleus, the nuclei feel a consistent torque away from $\mathbf{B}_0$ and the angle between $\mathbf{B}_0$ and μ changes. In other words, the spin-states of the nuclei are being altered and resonance is occurring. An alternative way of looking at the resonance condition is to state that the energy of the applied radiofrequency is equal to the energy difference between the two nuclear spin-states, providing the energy to allow transitions to occur.

The result of this is that the bulk magnetisation vector precesses about both $\mathbf{B}_0$ and $\mathbf{B}_1$ in an extremely complex manner at resonance. The motion may be visualised more simply by discussing the magnetisation in terms of a rotating frame of reference precessing about $\mathbf{B}_0$ at the rate of $\mathbf{B}_1$. The z′-axis is parallel to $\mathbf{B}_0$, and the x′ and y′-axes are in the static xy plane, rotating about z′ at the radio frequency ν_1. Each magnetic moment then appears to be static, and the precession of the bulk magnetisation may be considered as solely due to, and about, $\mathbf{B}_1$. In a typical NMR experiment, the magnetisation is detected in the rotating frame along the y′-axis and results are more conveniently considered within this frame. In general, all discussions within this thesis will implicitly be in terms of the rotating frame of reference, and the axes will be referred to simply as x, y and z.

1.1.4. THE SINGLE PULSE EXPERIMENT

If the radiofrequency $\mathbf{B}_1$ field is at resonance, a consistent torque will be exerted upon the net magnetisation, forcing it to precess about the $\mathbf{B}_1$ (x) axis. The precession rate is dependent upon the strength of the radio-frequency field applied. The detected magnetisation along the y-axis, M_y, is simply related to the angle through which the magnetisation has precessed.

$$M_y = M_0 \sin\left(\gamma \vec{B}_1 t\right) \qquad \textit{Equation 1.7}$$

The rate of precession about $\mathbf{B}_1$ is known, so altering the duration of the radio-frequency pulse, t, applied controls the pulse angle. As a consequence of the uncertainty principle, these short pulses have inexact frequencies, and will therefore excite all nuclei of the same element within a sample, including those possessing slightly different Larmor frequencies. After the $\mathbf{B}_1$ field has been applied detection of the magnetisation commences following a brief "dead time" to allow the spectrometer electronics to recover from the pulse.

The magnetisation is detected along the y-axis, so the optimum pulse duration in this experiment is one that precesses the sample magnetisation through 90°, known as a 90° or $^{\pi}/_{2}$ pulse. Typical $^{\pi}/_{2}$ pulse durations used experimentally are around 5 μs. The signal is detected as a free-induction decay (FID) and follows the decay of magnetisation as it relaxes back to its equilibrium value of zero in the xy plane. The measurement of M_y over time yields an interferogram built up from the return to magnetic equilibrium of all the excited nuclei within the sample. Each chemically different nucleus will possess a different Larmor frequency, as discussed below, and the resulting time-domain FID can be difficult to analyse directly. Therefore a Fourier transform (FT) is performed upon the data, yielding a frequency-domain spectrum, which can be analysed more conveniently.

1.1.5. SHIELDING AND COUPLING

The discussion has so far assumed that the effective $\mathbf{B}_0$ field experienced by the nuclei is constant across the sample and that the spin-states of all the nuclei of the same element are at identical energies. This assumption would result in a single resonance appearing in the spectra of each sample. However, a cursory glance at almost any NMR spectrum will show that this is not the case. Nuclei in different chemical positions within the sample precess at different frequencies because the local magnetic field experienced by a nucleus is affected by the local electronic charge distribution. This is because the external applied magnetic field induces electronic motion such that the magnetic field generated by the electrons opposes the original magnetic field. The result of this is that each chemically different nucleus within a sample will resonate at a slightly different frequency, and their signals may be distinguished from one another in the final NMR spectrum. The shielding experienced by a nucleus is a tensor property as it also depends upon the angular orientation of the molecule to $\mathbf{B}_0$, leading to “shielding anisotropy” or SA, whereby the chemical shift observed for a powdered solid is spread over a large frequency range. In situations with a high degree of molecular motion, such as in solution, the rapid motion of the molecule will average out the chemical shift interaction to a single value, δ.

The local magnetic field will also be perturbed by neighbouring nuclear spin states, again affecting the nuclei's Larmor frequency. This is termed "coupling" of spins. There are three mechanisms of coupling: dipolar, quadrupolar, and indirect coupling. The first two of these three interactions all cause broadening of each resonance line and along with SA are the reason that the spectra of solids acquired without the use of averaging techniques are generally broad and featureless. In molecules undergoing motional averaging the broadening is not observed, as the dipolar and quadrupolar couplings average to zero whilst the indirect coupling averages to a single value, "J". J is a small constant and is not generally observed unless the lines are extremely narrow.

To summarise, the simple NMR experiment involves forcing the nuclear magnetisation vectors into the transverse plane and observing their behaviour as they return to equilibrium. The evolution of the vectors, and thus the spectrum obtained after Fourier transformation, depends greatly upon the local electronic environment about each of the nuclei. Because of this the spectrum can provide a great deal of structural information to the NMR spectroscopist.

1.2. EVOLUTION OF THE SPIN SYSTEM

In the discussion above, the time-evolution of the spin system was addressed in terms of magnetisation vectors. This is a valuable method with which to visualise certain simple NMR experiments, but a more rigorous treatment is required to understand fully the evolution of the spin system. Spectral lines arise from transitions between nuclear spin states and therefore quantum mechanical methods should be used. The energy of the spin states is an observable property and the operator corresponding to this property is known as the Hamiltonian. The nuclear spin Hamiltonian contains terms that account for the physically different external and internal interactions acting upon the spins, and governs the time-evolution of the system.

1.2.1. THE DENSITY MATRIX

The evolution of the spin system is determined by the spin Hamiltonian. The theory used to follow the evolution is known as density matrix formalism. This treatment allows the evolution of a large, statistical ensemble of spins to be described[7, 8]. In a typical ensemble, the spins are in a variety of spin states, governed by thermal equilibrium. The density matrix, ρ, describes the probability that each spin within the ensemble is in a certain spin state at any given time, and thus describes the time evolution of the entire spin system

The equation of motion analogous to the time-dependent Schrodinger equation for isolated nuclear spins is given by the Liouville-von Neumann equation.

$$\frac{\hbar}{i}\frac{d\rho}{dt} = -\left[\hat{H}, \rho\right] \qquad \text{Equation 1.8}$$

For a time-invariant Hamiltonian, integration yields the density matrix describing the state of the spin ensemble at any given time.

$$\rho(t) = U^{-1}(t)\rho(0)U(t)$$ Equation 1.9

where U(t) is the spin evolution operator, or propagator, given by

$$U(t) = \exp(-i\hat{H}t)$$ Equation 1.10

If the Hamiltonian varies over the time interval of interest then the time interval may be split up into smaller periods over which the Hamiltonian becomes constant. In this case, the evolution operator is obtained by repeated integration over each smaller time period. Over a total period, t, the evolution operator is given by

$$U(t) = \Im\exp\left(-i\int_0^t \hat{H}(t)dt\right)$$ Equation 1.11

$\Im$ is the Dyson time ordering operator, placing the interaction Hamiltonians in the order in which they act upon the spin system. It is unity in cases where the Hamiltonian commutes with itself at all times, such as the shielding interaction. The expectation value of an observable operator is found by evaluating the trace of its product and the density operator of the system being observed. The evolution of the spin system is governed by the density operator and this, in turn, is determined by the nuclear spin Hamiltonian. Therefore the evolution of the spin system, and the spectrum obtained, can be altered with various techniques that control the effect of each of the terms comprising the total spin Hamiltonian.

1.2.2. THE NUCLEAR SPIN HAMILTONIAN

In diamagnetic non-conducting substances the nuclear spin Hamiltonian can be expressed as a sum of terms

$$\hbar \hat{\mathrm{H}}_{Nuclear} = \hbar \hat{H}_Z + \hbar \hat{H}_{RF} + \hbar \hat{H}_S + \hbar \hat{H}_Q + \hbar \hat{H}_{SR} + \hbar \hat{H}_D + \hbar \hat{H}_J \qquad \text{Equation 1.12}$$

The subscripts, Z and RF refer to the effect of the external static and radiofrequency magnetic fields, which are generally assumed to be constant over all nuclei. Because of this, the Zeeman term is normally ignored when considering the evolution of the spin system between pulses. All other terms, referring to chemical shielding, quadrupolar coupling, spin-rotational interaction, dipolar coupling and indirect coupling are classed as internal Hamiltonians and will influence the spectrum obtained directly, as was briefly outlined in the preceding section. The main Hamiltonians with which this thesis is concerned are the shielding Hamiltonian, H_S and the dipolar coupling Hamiltonian, H_D. The effect of these Hamiltonians upon the spectra is demonstrated first for the shielding Hamiltonian.

1.2.2.1. The Shielding Hamiltonian

In the presence of the static magnetic field, the motion of the electron cloud about a nuclear spin generates a localised, inherently anisotropic magnetic field that interacts with the nuclear spins. At the i^{th} nucleus a magnetic field, B, is induced by the surrounding electrons.

$$\vec{B}_{induced}(i) = -\hat{\sigma}(i) \bullet \vec{B}_0 \qquad \text{Equation 1.13}$$

The energy resulting from this induced field, $E_S(i)$ can be calculated, and replacing the classical magnetic moment vector with its quantum mechanical equivalent and summing over all spins in the system yields the Hamiltonian.

$$H_S = \sum_{i}^{spins} H_S(i) = \hbar \sum_{i}^{spins} \gamma_i \vec{I}(i) \bullet \hat{\sigma}(i) \bullet \vec{B}_0$$ *Equation 1.14*

For convenience, the two vector components, I and B_0, may be combined to form a dyadic product, T. If the summation over all spins is implicitly assumed, equation 1.14 then simply becomes a scalar product of two tensors.

Equation 1.15

$$H_S = \gamma_n \sum_{\alpha,\beta=1}^{3} \hat{\sigma}_{\alpha\beta} \hat{T}_{\beta\alpha}$$

The time-evolution of the spin system is being observed using laboratory equipment, and it is necessary to express both the dyadic product tensor and the shielding tensor in the laboratory frame of reference to evaluate the effect of the Hamiltonian upon the observed signal. The most convenient way to obtain σ and T in the laboratory frame is to express them in terms of irreducible spherical co-ordinates and, if necessary, rotate these into the laboratory frame of reference.

Any interaction tensor, R can be placed within a set of axes such that the tensor is described by a diagonalised matrix. This is known as the interactions' Principal Axis System (PAS). The diagonal matrix elements are called the principal components of the tensor, R_{XX}, R_{YY} and R_{ZZ}. The diagonalised tensor is then decomposed into its irreducible Cartesian co-ordinate components. Any rank two tensor, such as σ, may be decomposed into three irreducible Cartesian tensors of rank 0,1 and 2. The rank zero tensor is the isotropic constituent of the original tensor, the rank one tensor contains the traceless antisymmetric portion of the tensor, whilst the rank two tensor describes the traceless symmetric part[9, 10]. In principle, σ can contain all three components, but only the isotropic and traceless symmetric parts are readily measurable by NMR, so the rank one tensor is ignored and the shielding tensor is treated as symmetric. The irreducible Cartesian components of the shielding tensor are then converted into irreducible spherical co-ordinates to facilitate rotation between co-ordinate systems. The paper by Smith, Palke and Gerig[10] provides a detailed mathematical description of the procedure. The PAS shielding tensor can be expressed in terms of 4 irreducible spherical co-ordinate components because the rest cancel to zero due to the symmetry of the tensor[9].

The irreducible spherical co-ordinate components of the tensor in the PAS are usually written in the form

$$\rho_{00} = -\frac{1}{\sqrt{3}}\sigma_{iso} \qquad \zeta = \sigma_{zz} - \frac{1}{3}Tr\sigma$$
$$\rho_{20} = \sqrt{\frac{3}{2}}\zeta \qquad \eta = \frac{\sigma_{yy} - \sigma_{xx}}{\delta}$$
$$\rho_{2\pm2} = -\frac{1}{2}\eta\zeta \qquad \sigma_{iso} = Tr\overline{\sigma}$$

Equations 1.16

ζ provides a measure of the anisotropy of the interaction, whilst η is known as the asymmetry parameter of the shielding tensor and describes the symmetry of the interaction in the plane perpendicular to the largest component, σ_{ZZ}.

From these spherical co-ordinates it is relatively straightforward to express the shielding tensor in the laboratory frame using the Wigner rotation matrices. Each cylindrical tensor element is multiplied by a linear combination of Wigner rotation elements, $D^{l}_{m'm}$, as described by Haeberlen[9].

$$R_{lm} = \sum_{m'} D^{l}{}_{m'm}(\alpha,\beta,\gamma)\rho_{lm'}$$

Equation 1.17

The irreducible cylindrical components of the shielding tensor in the laboratory frame are usually left in this form, as the full expansion often proves to be rather involved despite the cancellation of many of the terms.

The dyadic product vector of the nuclear spin and the static magnetic field, T, can be treated in a similar way, only there is no need to rotate the co-ordinate system, as the PAS of T is already the laboratory frame. Symmetry arguments again mean that T consists of only four non-zero components, T_{00}, T_{20} and $T_{2\pm1}$. The spin-factor terms, T_{lm}, $m\neq0$ do not commute with the Zeeman Hamiltonian, and are ignored, as they do not contribute to NMR spectra acquired at high magnetic fields[7]. Thus the non-zero spin factors are

$$T_{00} = I_0 B_0$$
$$T_{20} = \sqrt{\frac{2}{3}} I_0 B_0$$

Equations 1.18

It is now possible to combine the two laboratory frame tensors, T and R, to evaluate the shielding Hamiltonian, using the equivalent of equation 1.15 in terms of irreducible spherical tensor operators.

$$H_S = \gamma_n \sum_l \sum_{m=-l}^{l} (-1)^m R_{l-m} T_{lm} \qquad \text{Equation 1.19}$$

The full expansion of this expression appears daunting at first sight, but the majority of terms are zero from symmetry considerations, or are set to zero using the high-field approximation. The truncated Hamiltonian becomes

$$H_S = \gamma_n \left(T_{00} R_{00} + T_{20} R_{20} \right)$$

$$H_S = \gamma_n T_{00} \rho_{00} + \gamma_n T_{20} \sum_{m'} D^2{}_{m',0}(\alpha,\beta,\gamma) \rho_{2m'} \qquad \text{Equations 1.20}$$

Expanding the Wigner matrix terms and utilising several simple trigonometric relations, the usual form of the laboratory-frame shielding Hamiltonian is obtained.

$$H_S = \gamma_n I_0 B_0 \left\{ \sigma_{iso} + \zeta \left(\frac{\left(3\cos^2\beta - 1\right) + \eta \sin^2\beta \cos(2\gamma)}{2} \right) \right\} \qquad \text{Equation 1.21}$$

In this form it is easy to see that there is an isotropic term, independent of orientation, and an anisotropic term. In a sample that does not undergo any form of Hamiltonian averaging the orientation of the principal component of the shielding tensor to the static magnetic field, β, will affect the energy of the nuclear spin transitions. This means that the Larmor frequency of the nucleus will vary with orientation and the spectrum will exhibit an isotropic chemical shift with associated shielding anisotropy broadening.

1.2.2.2. The Dipolar Hamiltonian

Dipolar coupling of the nucleus under study to protons within the sample is the most common obstacle to high-resolution NMR of dilute nuclei in solids. The dipolar term within the spin Hamiltonian arises from the magnetic fields generated by the nuclear magnetic moments associated with the spins of all neighbouring nuclei. The field contribution from a neighbouring nucleus depends upon the spin orientation of that nucleus, which is, in general, completely random. For an ensemble of spins within a macroscopic sample, there will be a variation in the magnetic field strength at the nuclei of interest. This manifests itself as a variation in the Larmor frequency of the given nucleus, leading to the dipolar line broadening. For nuclei attached directly to protons, the resulting line broadening may be as great as 50 kHz. The dipolar interaction tensor can be examined in an analogous way to that of the shielding tensor outlined above.

The energy of interaction of two nuclear dipoles can be conveniently derived from classical equations describing the interaction of two magnets[12]. The classical equation can be put into quantum mechanical terms by replacing the classical magnetic moment vectors by their quantum mechanical equivalents and summing over all pairs of spins.

$$E_D(ik) = \left[\frac{\mu_i \mu_k}{r_{ik}^{3}} - \frac{3(\mu_i \bullet r_{ik})(\mu_k \bullet r_{ik})}{r_{ik}^{5}} \right] \qquad \textit{Equation 1.22}$$

$$H_D = \hbar \sum_{i<k}^{spins} \left(\frac{-\gamma_i \gamma_k \hbar}{r_{ik}^{3}} \right) \left[\frac{3(\vec{I}_i \bullet \vec{r}_{ik})(\vec{I}_k \bullet \vec{r}_{ik})}{r_{ik}^{2}} - \vec{I}_i \bullet \vec{I}_k \right] \qquad \textit{Equation 1.23}$$

The equation is further simplified by combining the spin parts of the Hamiltonian into a single dyadic product tensor.

$$H_D = -2\gamma_i \gamma_k \hbar \sum_{\alpha,\beta=1}^{3} \hat{D}_{\alpha,\beta} \hat{T}_{\beta,\alpha} \qquad \textit{Equation 1.24}$$

As before, the tensor, D, is converted into irreducible spherical co-ordinate components. The fact that the dipolar tensor is traceless and symmetric (i.e. D_{iso} and η equal zero) means that all bar one of these components are zero. From equations 1.16,

$$\rho_{20} = \sqrt{\frac{3}{2}}\delta = \sqrt{\frac{3}{2}} \times r_{ik}^{-3}$$ *Equation 1.25*

Therefore the dipolar equivalent to equation 1.20, calculating the dipolar tensor components in the laboratory frame, becomes simply

$$R_{2m} = D^2{}_{0,m}(\alpha,\beta,\gamma)\rho_{20}$$ *Equation 1.26*

The only secular, non-zero component of the dyadic product of the two nuclear spin vectors, T, can be shown to be[6, 10]

$$T_{20} = \frac{1}{\sqrt{6}}\left[2I^i{}_z I^k{}_z\right]$$ *Equation 1.27*

The components are then introduced into the following expression to form the final, truncated, Hamiltonian.

$$H_D = \frac{-\sqrt{6}\gamma^i\gamma^k\hbar}{r_{ik}^3}\sum_{m'}(-1)^{m'} D^2{}_{0,-m'}(\alpha,\beta,\gamma)T_{2m'}$$ *Equation 1.28*

$$H_D = \frac{-\gamma^i\gamma^k\hbar}{r_{ik}^3}\left(\frac{3\cos^2\beta - 1}{2}\right)\left[2I^i{}_0 I^k{}_0\right]$$ *Equation 1.29*

Once again, the dependence of the Hamiltonian on the angle β introduces broadening into the NMR spectrum. The absence of an isotropic part in the expression for dipolar coupling implies that under averaging conditions dipolar coupling may be removed completely.

1.2.2.3. External Hamiltonians

The external Hamiltonians describe the effect of the applied magnetic fields upon the spins. The Zeeman Hamiltonian is concerned with the effect of the static **B**$_0$ field. The vector components of the field are defined to be $(0,0,B_Z)$, and the Zeeman Hamiltonian is generally written as one of the equivalent forms

$$\hat{H}_Z = -\sum_i \mu_z{}^i B_z = -B_z \sum_i \gamma^i I_z{}^i = -\sum_i \omega_0{}^i I_z{}^i \qquad \textit{Equation 1.30}$$

The radio-frequency Hamiltonian is concerned with the **B**$_1$ magnetic field(s) applied perpendicular to **B**$_0$. The linearly polarised field may be decomposed into two counter-rotating components, one of which may be neglected at high **B**$_0$. In the static frame the Hamiltonian may be written

$$\hat{H}_{rf} = -B_1(t)\cos[\omega t + \varphi(t)] \sum_i \gamma^i I_x{}^i \qquad \textit{Equation 1.31}$$

The Zeeman Hamiltonian is required whenever calculations are performed within the rotating frame, whilst the radio-frequency Hamiltonian is used to determine the effect of pulses upon the spin system.

1.3. REFERENCES

1. E. M. Purcell, H. C. Torrey, R. V. Pound, *Phys. Rev.*, **69**, 37 (1946)
2. R. K. Harris, *"Nuclear Magnetic resonance Spectroscopy –a physicochemical approach"*, Longman Scientific and Technical (1987)
3. E. O. Stejskal, J. D. Memory, *"High Resolution NMR in the Solid State"*, Oxford University Press (1994)
4. K. Schmidt-Rohr, H. W. Spiess, *"Multidimensional Solid State NMR and Polymers"*, Academic Press Ltd. (London) (1994)
5. G. D. Mateescu, A. Valeriu, *"2D NMR – Density Matrix and Product Operator treatment"*, Solomon Press (New Jersey) (1993)
6. H. Friebolin, *"Basic One and Two Dimensional NMR Spectroscopy"*, VCH New York (1993)
7. Abragam, *"The Principles of Nuclear Magnetism"*, Oxford University Press (1961)
8. R. R. Ernst, G. Bodenhausen, A. A. Wokaun *"Principles of NMR in 1 and 2 Dimensions"*, Clarendon Press Oxford (1987)
9. U. Haeberlen, *"High Resolution in Solids: Selective Averaging"*, Academic Press (London) (1976)
10. S. A. Smith, W. E. Palke and J. T. Gerig, *Concepts in Magnetic Resonance*, **4**, 107-144 (1992)
11. J. H. Van Vleck, *Phys. Rev.* **74**, 1168 (1948)
12. R. K. Harris, *Multinuclear Magnetic Resonance in Liquids and Solids – Chemical Applications*, (Editors: P. Granger and R. K. Harris), NATO ASI, Maratea, 1988

ACTIVATED CARBON

2.1. SYNTHESIS OF ACTIVATED CARBON

"Activated carbon" is the generic term used to describe an entire family of carbon-based materials that have been physically and chemically treated in order to create the activated end product. A wide range of raw materials with a high carbon content (for example[1, 2]) has been used for the process, and the nature and behaviour of the end product depends upon the source and the precise conditions used in the manufacture. The majority of the carbons provided by the CBDE for this study are derived from nutshells[3] (i.e. SC2 and PICA). They have been treated in such a way as to generate a full range of pore sizes with a large proportion of micro-pores. The conditions of the manufacture can be used to tailor nature of the carbon end product to a limited extent, and the manufacturers tend to keep the exact conditions used to themselves. In general, the production of these materials occurs in two stages: an initial carbonisation of the base material followed by activation of the carbonised product. Activated carbon is used in a wide range of applications, almost all utilising the carbon's enormous adsorption capacity. Common examples include air purification in a variety of situations, the recovery of longer chain alkanes from natural gas and the removal of colloidal impurities from sugar syrup during refining.

2.1.1. CARBONISATION OF THE RAW MATERIAL

Carbonisation consists of removing the non-carbon elements from the base material by thermal decomposition. This is achieved by heating the material in an inert atmosphere at temperatures above 600°C. The non-carbon material is expelled as gaseous by-products, and the carbon shrinks and hardens to form rudimentary pores. The residual carbon atoms form sheets comprising condensed aromatic ring systems. The arrangement of these sheets is highly irregular and the irregularity provides the initial basic pore structure. The mechanism of carbon formation from pure polyvinyl dichloride has been studied by Taylor[4]. His conclusions are summarised in Figure 2.1. This is clearly an idealised case, but demonstrates how the aromatic nature of the activated carbon arises.

$$\left[\ C_2H_2Cl_2\ \right]_n \rightarrow 2nC + 2nHCl$$

The first stage involves the loss of one HCl molecule per pair of carbon atoms.

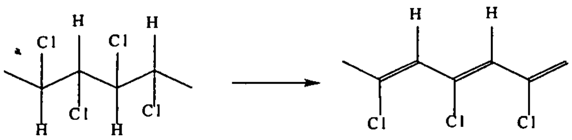

This process occurs as a two step process, initiated at a point of strain in the polymer. The rate of formation is increased in oxygen, suggesting a free radical mechanism. Further loss of HCl cannot occur from a single chain, as it is both chemically and sterically unlikely. Additionally the re-organizational energy of arranging the polymer into straight chains is very high, so a cross condensation is postulated, followed by further elimination

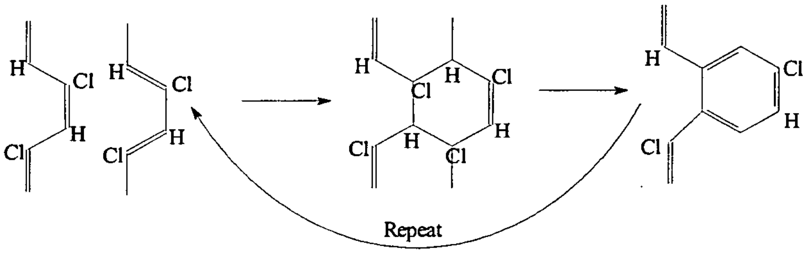

Figure 2.1. The mechanism of formation of activated carbon from PVDC.

Differences in the treatment of material at this stage will tend to affect the final physical form of the end material. Exposure to a higher temperature for a greater period of time will result in a harder, denser final product. The porosity and surface structure of samples produced using solely this process are found to depend greatly upon the temperature at which the carbonisation occurs[5]. However, the secondary activation process controls the final porosity of the material to a far greater extent.

2.1.2. ACTIVATION OF THE CARBONISED PRODUCT

There are two main methods of activating the carbonised material. The methods differ in the processes used to oxidise and burn off a proportion of the carbon material. Chemical activation uses an oxidising agent that is impregnated into the starting material. The oxidising agent degrades a fraction of the carbon, as the material is pyrolysed at about 500°C in an inert atmosphere. The unreacted agent is then washed off. Common activation agents used include phosphoric acid, zinc chloride, sulphuric acid, potassium hydroxide and sodium hydroxide[6]. The porous structure tends to be more uniform than that created using physical activation, and is heavily dependent upon the extent and type of oxidant impregnation[7]. Physical activation uses an oxidising gas such as steam, carbon dioxide or air and is carried out at approximately 1000°C. The activation agent burns away the more accessible portions of the carbon skeleton, giving off carbon monoxide and dioxide. The extent of activation is dependent upon the oxidising gas used, reaction temperature and the duration of the activation process.

A number of papers have been published upon the mechanism of carbon activation[8] and the methods of controlling the porosity formed. Disorganised, non-graphitic material is burned off initially, unblocking the pores formed during the earlier carbonisation process. After this, aromatic carbon is burnt off in progressively larger sheets, introducing oxygenated active sites and a greater number of pores into the carbon. As the burn-off continues, walls between pores are also burnt, increasing the proportion of large pores considerably. M^{c}Enancy and Dovaston[9] found that the nitrogen adsorption isotherms of a range of micro-porous carbons varied significantly with the activation temperature used in their production. Lower activation temperatures were found to create a greater proportion of meso- and macro-pores. Tomkow et al.[10] have found that the range of pore sizes obtained can be controlled by the choice of gas used as an oxidising agent.

2.2. CHARACTERISATION OF ACTIVATED CARBON

The remarkable adsorption properties of activated carbon have been well known for over 200 years[11], and since they were discovered there has been a great deal of interest in the behaviour of these materials. The structure of activated carbon has been studied using a variety of techniques over many years. The studies can be loosely grouped into three areas, those examining the nature of reactive carbon and oxygenated "active sites" within the carbon, those characterising the porous structure, and those which study the bulk adsorption properties. The latter two are intrinsically linked as the pore volume necessarily determines the adsorption capacity of the carbon -the major mechanism of adsorption in these systems occurs via pore-based capillary condensation.

2.2.1. ANALYSIS OF CARBON-OXYGEN SURFACE GROUPS

The oxidation of the carbon surface during the activation process also introduces oxygen in a variety of chemical functionalities. An estimation of the total amount of acidic oxide on the carbon surface can be obtained by measuring the amount of base removed from a given amount of solution by a known mass of carbon[12]. Typical values obtained are equivalent to 3 to 15 mmol of acidic oxygen per gram of carbon material. This is a significant amount, and suggests that the behaviour of carbon adsorbents will be affected considerably by the nature of the surface chemistry. Research in this area has accelerated recently[12, 13] as modification of the surface chemistry becomes an increasingly attractive route towards designing carbon materials with tailored adsorption behaviour[14].

Early thermal desorption studies[15, 16] of graphite gave evidence of two distinct types of surface chemical structure. At 300°C carbon dioxide was evolved as one structure decomposed, whilst at temperatures above 500°C significant carbon monoxide evolution occurred. The authors tentatively ascribed the initial carbon dioxide evolution to decomposition of carboxyl or lactonic functionalities, whilst the carbon monoxide was thought to evolve from phenol or quinone structures. Barton et al.[17] performed a similar study upon Spheron-6 carbon, and found two distinct temperature-dependent rates of evolution of carbon dioxide in addition to the higher temperature formation of carbon monoxide. This demonstrated the presence of three (or more) distinct surface functionalities.

Infrared (IR) spectroscopy has been used with some success to identify the groups present within the carbon black. Comparison of the samples before and after alkali treatment allows different groups to be distinguished by their acidity, and this approach has been used to distinguish several groups within overlapping peaks. Initially, the absorption of the bulk of the infrared radiation by the black surface caused sensitivity problems[18], though this difficulty has been largely circumvented by the introduction of Fourier Transform Infra Red (FTIR) spectroscopy[19]. Various authors[20-23] have identified and assigned bands corresponding to carboxylate ions, lactones, unsaturated δ-lactones, carboxylic acid anhydrides, quinones, phenols, and aromatic ring stretches. Polarography[18] has been used in order to try and provide further information upon the quinone structures suggested by IR measurements though no definitive conclusions could be reached. NMR experiments have also been performed upon a variety of activated carbons[24]. Static proton NMR provides evidence for at least three varieties of oxygenated adsorption centre, whilst ^{13}C MAS NMR spectra show a large, broad isotropic peak in the range 110 to 130 ppm. This is in the chemical shift region for aromatic and alkenic carbon (cf. graphite at 190 ppm) and led the author to tentatively suggest that the structure of the carbon was most likely to be a disordered, cross-linked, 3D lattice of small graphene planes.

Surface science techniques have been used to probe the upper layers of the carbon material but cannot provide data upon the internal structure of the adsorbent. Carbon[25] and oxygen[26] 1s X-ray photoelectron spectroscopy (XPS) and secondary-ion mass spectrometry[27] (SIMS) have been used to identify several distinct oxygenated surface sites but unequivocal assignment has not been achieved. Recent work by Thomas et al.[28] using oxygen K-edge X-ray absorption near-edge spectroscopy (XANES) has demonstrated the presence of several surface oxygen complexes, and has also been able to identify distinct anhydride and lactone functionalities. It is expected that as the technique develops it will yield more information upon the exact structure of the oxygen surface complexes on activated carbons.

2.2.2. THE ADSORPTION ISOTHERM

When a gas or vapour is brought into contact with a clean carbon surface some of it will become attached to the surface in the form of an adsorbed layer. Any solid is capable of adsorbing a certain amount of gas but the extent of adsorption, at a given temperature and pressure, is mainly determined by the surface area of the solid. This provides an explanation for the enormous adsorption capacity of activated charcoal. The relationship between the equilibrium amount of gas adsorbed and the pressure of the gas, at a certain temperature, is known as the adsorption isotherm. The shape of the adsorption isotherm depends upon the exact nature of the adsorbate – adsorbent interaction, and provides a way in which the interactions may be broadly classified.

Brunaeur, Emmett and Teller[29] classified the adsorption isotherm of a material on an adsorbent as one of 5 types. The various adsorption isotherms may be seen in Figure 2.2. Type 1 isotherms generally occur in materials that are almost completely microporous, and were first encountered in the study of charcoal adsorbents. The rapid initial rise in the isotherm results from filling of the narrow pores at low vapour pressures, followed by a long flat branch during which almost no adsorption occurs. At high partial pressures a further uptake is sometimes observed, and this region may exhibit hysteresis[30]. Type 2 and type 3 isotherms arise from non-porous materials, such as graphite. The differences between them arise from the strength of the interactions between the adsorbate and the adsorbent. These two isotherm classifications are discussed in more detail in section 2.3.1. Type 4 isotherms, which usually exhibit significant hysteresis, result from adsorbents with a large proportion of mesopores. They are often described as the porous equivalent to type 2 isotherms. Type 5 isotherms occur in porous solids with weak interactions between the adsorbate and adsorbent, and are considered to be the porous equivalent to type 3 isotherms.

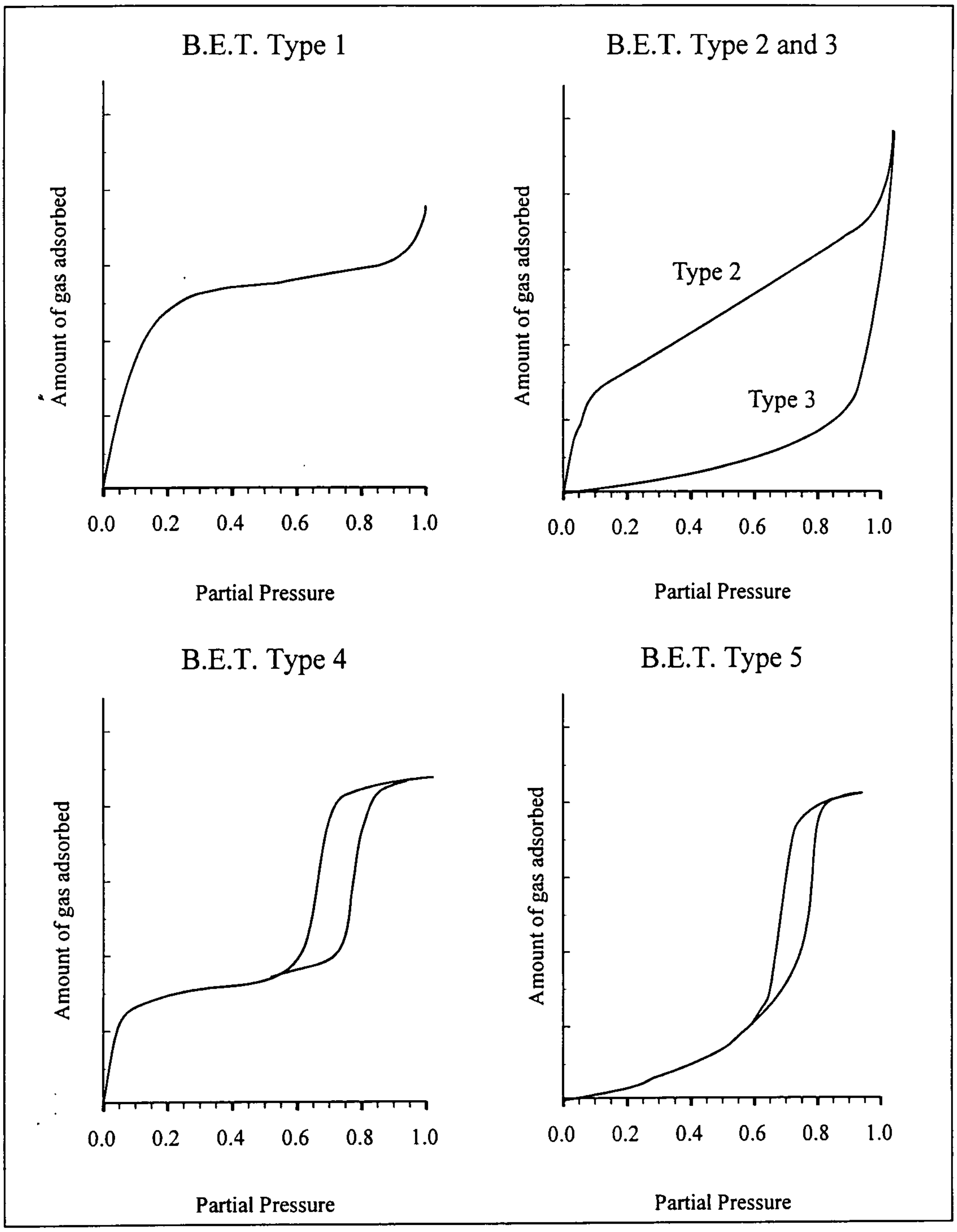

Figure 2.2. The B.E.T. classification of adsorption isotherms.

Adsorption isotherms of most materials upon activated carbon are usually labeled BET type 1 or 4. Water upon some carbons[31] has been classified as midway between types 4 and 5. The type 1 and type 4 isotherms are both explained in broadly the same way, though the exact features differ slightly according to the proportion of various sized pores within the adsorbent. As the vapour pressure above the solid is increased, the amount of material adsorbed rapidly increases, corresponding to material adsorbed on the surface and within small micro-pores. As the pressure increases further the rate of adsorption slows down until the vapour pressure reaches a point where it is sufficient to condense material in the mesopores, when another rapid uptake is observed. As the vapour pressure reaches saturation, the adsorption slows down again, limited by the volume of suitable size pores. Hysteresis is generally the result of capillary condensation within mesopores.

2.2.2.1. Theoretical Description of the Adsorption isotherm

An activated carbon is an extremely complicated adsorbent. It has an elaborate pore structure, made up of variously shaped and sized pores, physically connected to one another in a complex and poorly characterised manner. In addition, activated carbons also have a variety of chemical structures within them, comprising areas of graphene plane, plane dislocations and discontinuities, and various oxygenated heterogeneities. Clearly a full theory describing the adsorption of molecules to this type of material is likely to be extremely complex. Many theories exist, fitting parts of the adsorption isotherms observed for various molecules to physical characteristics within the carbon. A brief look at the enormous volume of scientific literature within this subject area quickly demonstrates the profusion of different, and often conflicting, conclusions reached. Research is usually divided between the study of non-polar molecules, such as alkanes, and polar molecules, usually water vapour. Two modes of adsorption are generally studied, vapour phase adsorption and the adsorption resulting from immersion of the carbon sample in binary mixtures[110, 111]. Adsorption of liquids upon the surface of carbons has not been explored. However, mechanistic results obtained from vapour-phase studies may be applied to results obtained from the current study.

The Dubinin[32] theory of volume filling of micropores has proved to be useful in the study of the adsorption of non-polar organic vapours to activated carbon. This theory is concerned almost exclusively with the porous nature of the carbon and assumes that the process of molecular adsorption is a combination of initial adsorption to the carbon surface throughout the pores followed by capillary condensation within progressively larger pores. Adsorption occurs on the surface through dispersion or dipolar forces between the molecules and the adsorbent. The first monolayer of molecules will be strongly held by these forces (typically in the range 5 – 50 kJ mol^{-1} for molecules adsorbed on carbon), subsequent multilayers less and less so. This process also accounts for the rapid initial filling of the small micropores, where there is an overlap of adsorption potentials from opposite walls[33]. As the vapour pressure increases, progressively larger pores are filled by the adsorbate through a process termed capillary condensation. The final flat portion of the isotherm occurring at partial pressures approaching 1 is simply bulk liquid condensing in the larger pores. Zsigmondy[34] was the first to suggest that condensation would occur in pores at pressures considerably lower than that of normal saturation vapour pressure. He came to this conclusion by thinking of each pore as an extremely fine capillary, in which adsorbed liquids would undergo a large capillary rise. Capillary rise occurs because the vapour pressure above a concave liquid surface is less than that above a flat liquid interface. This was discussed in thermodynamic terms by Kelvin, who derived an expression for the vapour pressure above a curved surface

$$\ln\left(\frac{p_r}{p_0}\right) = -\frac{2\gamma V_m}{rRT}\cos\phi \qquad \textit{Equation 2.1}$$

In the Kelvin equation, p_0 is the saturation vapour pressure, p_r is the vapour pressure required for condensation above the curved liquid surface, γ the liquid surface tension, V_m the molar volume of the liquid, and r the radius of the capillary. The angle ϕ is the contact angle between the liquid and the walls of the capillary. The adsorbate is generally assumed to wet the walls of the pore, so the contact angle is taken to be zero. The Kelvin equation may be extended to calculate capillary condensation effects in variously shaped pores, but in all cases the overlying theory is the same. Using this equation it is possible to work out the partial pressure required for capillary condensation to occur in a certain pore size. For example[33], benzene at 20°C will condense in pores of 5 nm radius and below at a relative vapour pressure of $p_r/p_0 = 0.66$ whereas in pores of 50 nm radius condensation would require $p_r/p_0 = 0.96$. Therefore the driving force for capillary condensation is greatest in the smallest pores, and, for a certain adsorbate loading, all the pores of a certain size and below will be filled with adsorbed molecules whilst the rest will be empty. This is the central tenet of Dubinin's VFM theory.

Capillary condensation also provides a complete explanation for adsorption hysteresis. This term refers to characteristics where the adsorption curve, as vapour pressure is increased, does not coincide with the desorption curve as the vapour pressure is decreased. Firstly, there is the phenomenon of contact angle hysteresis, which states that the contact angle on adsorption is greater than that during desorption. From a consideration of the Kelvin equation, this effectively means that the pressure below which liquid vaporizes from a particular pore will be lower than that required for condensation to occur within it. A further explanation for this may arise from the shape of the pores[35], or the way in which they interconnect. Wider pores in the interior of the carbon, only accessible through narrower pores, would provide another explanation for the hysteresis. Network theory[36] is concerned with these more complex descriptions of pore structure.

The adsorption of polar molecules on activated carbon, and in particular the role of the oxygenated sites in the adsorption mechanism, has proved an even more contentious area. Dubinin[37, 38] has suggested that oxygenated sites act as primary adsorption centres for water molecules at low vapour pressures. As the pressure increases these sites can then act as secondary adsorption sites[58, 59] until islands of water upon the carbon surface, centred at each oxygenated heterogeneity, are formed. This suggestion was lent further weight by Puri[39] and co-workers, who concluded that oxygenated sites played a key role in determining the shape of the adsorption isotherm of carbon with water. They found that sites which yielded carbon dioxide in thermal desorption studies controlled the extent of hysteresis, and furthermore that one mole of active sites adsorbed one mole of water. Barton et al.[40], in a similar piece of research, reported a value of 1.6 moles of water per mole of active sites. Once these sites had been removed Puri et al. observed almost no hysteresis in the adsorption isotherm. This led them to conclude that capillary condensation did not play a significant role in adsorption of water upon carbon. Conversely, early work by Wiig and Juhola[41] suggested that condensation of water in capillaries is the major process occurring during adsorption onto charcoal.

Kiselev[42] wisely chose the middle ground, finding that adsorption of water on a variety of carbons depended upon both the degree of oxidation and the micropore volume within the adsorbent. Bansal et al.[43], in their study of the adsorption of water vapour onto a variety of polymer-based carbons, came to an identical conclusion. They found that the degree of carbon oxidation controlled the shape of the adsorption isotherm at low pressures whilst the pore structure determined the isotherm shape at higher partial pressures as pore filling started to occur. Studies performed upon the adsorption of a variety of polar molecules, such as small alcohols and amines[44], led the authors to conclude that initial adsorption occurs at active sites, followed by bulk filling of pores at slightly greater partial pressures.

2.2.2.2. Experimental Characterisation of the Adsorption Isotherm

Adsorption isotherms may be obtained in a variety of ways, though the two most commonly found in the literature are the gravimetric and volumetric methods. The volumetric method basically consists of enclosing the adsorbent in a container of known volume and adding successive charges of the measurement gas, often nitrogen, from a volumetric container. After the addition of each dose of nitrogen, pressure readings in the adsorbent container are taken until there is no detectable change. When equilibrium has been reached the pressure of gas in the adsorbent container is measured and the quantity of gas left is calculated from the gas laws. Simple subtraction yields the amount of gas adsorbed by the adsorbent. A similar process is applied in order to obtain desorption isotherms, though in this case the pressure inside the adsorbent container is gradually lowered by sequentially opening the container to an evacuated volumetric vessel.

The gravimetric method relies upon intermittent weighing of the adsorbent to calculate the amount of gas adsorbed at a variety of pressures. Modern methods[45] suspend the solid from a balance so that the increase in weight may be measured directly. The major problem in this method is in the construction of balances of sufficient sensitivity, though this becomes less important for activated carbons, with their large internal surface areas (typically of the order of 1200 cm^2 g^{-1}). 1 μg of benzene at 25°C corresponds to 30 cm^2, so a microbalance with sensitivity in the microgram range can give a precision of around 1% for a typical sample of 3 g of carbon. The construction of a number of microbalances possessing the requisite sensitivity has been described in the literature[46].

2.2.3. CHARACTERISATION OF POROUS STRUCTURE

A convenient classification of pores was suggested by Dubinin[47], and subsequently taken up by IUPAC[48]. The system classifies pores as one of three types: macro-, meso-, and micro-pores. The classification is technically dependent upon the width of the pore entrances, but in practice the classification of pore size also relies upon the behaviour of the adsorbate molecules within them. Micropores adsorb material extremely strongly due to the overlapping interactions from opposite walls, whilst mesopores are characterised by capillary condensation and hysteresis. Adsorption behaviour within macropores is considered similar to that on an external surface. Classically, a micropore has an entrance < 2 nm across, mesopores have entrances ranging between 2 and 50 nm, whilst macropores have entrances in excess of 50 nm.

2.2.3.1. Pore Size Distributions obtained from the Adsorption Isotherm.

As the previous section has demonstrated, the number and size of the various pores (the pore size distribution, or PSD) plays the most significant role in determining the shape of activated carbon adsorption isotherms. The Kelvin equation (equation 2.1) relates the adsorption isotherm to the maximum filled pore radius, and thus may be used to obtain a pore-size distribution plot. This procedure makes the approximation that adsorption is entirely governed by capillary condensation in the pores, and does not make allowance for the layers adsorbed initially on the surfaces and pore walls. Using the theory of pore filling, the amount of material adsorbed at any point, x_1, on the isotherm corresponds to the volume, v_1 of all the pores which have radii up to and including radius, r_1. Plotting a graph of v against r and taking the first derivative, ($^{dv}/_{dr}$), yields the final pore-size distribution curve[49].

As noted above, the main problem with this approach is that the effect of the surface adsorbed material is completely neglected, and various procedures[50, 51] have been suggested to allow for these molecules and to provide a more accurate description of the PSD. There are several other approximations implicit within the Kelvin equation itself that also lead to errors in the PSD obtained by this procedure. These include the assumptions that the surface tension of the liquid is unchanged within pores, that the pores are cylindrical and that the contact angle of the adsorbate on the pore walls is zero. Gregg and Sing[33] note "despite all these uncertainties, calculations of PSDs by the Kelvin method are far from valueless. Provided that the limitations of the method are recognized, it can be very valuable [in many applications]".

2.2.3.2. Mercury Porosimetry

If the angle of contact between a liquid and a solid, φ, is greater than 90°, the pressure will be greater on the convex rather than the concave side of the meniscus. Using similar reasoning to that of Kelvin, it is clear that an excess pressure, ΔP, will be required to force liquid into a capillary. Via an adaptation of the Young-Laplace equation, an expression for the excess pressure required to force the liquid into cylindrical pores of radius, r, can be given

$$\Delta P = \frac{2\gamma}{r}\cos\varphi$$ *Equation 2.2*

Once again, γ denotes the surface tension of the liquid.

This equation forms the basis of the mercury porosimetry method for measuring PSDs. Taking a typical value of φ of 140° and an excess pressure of 1 atmosphere, one obtains a value of r = 7 μm for mercury at 20°C. In order to explore the full range of mesopores, down to r = 2 nm, pressures of ~3500 atmospheres are required. The mercury porosimeter is a machine capable of delivering suitably high pressures and measuring the volume of mercury taken up by the pores.

Zwietering[52] compares the modified Kelvin and mercury porosimetry methods for a chromium oxide / iron oxide catalyst with a narrow PSD in the region of 15 nm. Reasonable agreement is found between the two techniques, though there were noticeable differences between the two plots. Dubinin's group has also studied several activated carbons with isotherms of BET type 1 using this technique. They too found reasonable agreement between the two methods.

2.3. NMR STUDIES OF ACTIVATED CARBON

There are several problems inherent in the study of adsorbates upon graphite and activated carbons by NMR, and these have contributed to the relative scarcity of papers in this field. The most obvious problem is that of the signal-to-noise ratio obtained from the experiment. The signal obtained from a species adsorbed onto another substance is much reduced compared to that obtained from a bulk sample simply because the amount of material, and hence the number of nuclei, is so much less. Prior to the advent of FT techniques, this proved an insurmountable problem and effectively limited the study of these systems to proton NMR. The small chemical shift range of protons, coupled with the incomplete motional narrowing in the adsorbed species meant that the spectra obtained generally possessed little fine structure that could be interpreted. Yet another problem that several authors have commented upon is that the graphene sheets are conductive and therefore absorb the applied radiofrequency, leading to several experimental difficulties.

An early paper providing evidence of interactions occurring between adsorbate molecules and carbon via NMR was published[53] in 1973. In this study, the low temperature spectra of benzene were recorded in the bulk phase and after the addition of charcoal. Solid benzene has a distinctive "powder pattern" due to the symmetry within the molecule. In the case of benzene adsorbed on charcoal there was an overlap of a motionally averaged line with the powder pattern, demonstrating that a proportion of the molecules was still mobile. The proportion depended upon the thermal treatment of the sample –flash cooling of the system gave a large isotropic line, whilst slow cooling led to there being no isotropic peak. Cross-polarisation between proton and carbon was also used to discriminate between the molecules in different situations – a long contact time could be used to eliminate the isotropic signal due to a shorter relaxation parameter, $T_{1\rho}$. The authors concluded that the presence of the adsorbent leads to a range of motional correlation times that allow the adsorbate to show several stages of motional averaging simultaneously.

The ability to discriminate between the regions via relaxation times also showed that they were physically distinct, as spin diffusion did not occur between them.

2.3.1. THE CHEMICAL SHIFT OF ADSORBED MATERIALS

An experimental result common to all the papers concerned with the adsorption of molecules onto graphite or carbonised adsorbent is the low-frequency chemical shift observed upon adsorption. In all cases, the authors suggest the shift is the result of proximity to graphene planes within the adsorbent. A review article by Tabony[54] collates the results obtained from several earlier studies upon graphite and discusses the chemical shift observed for a variety of adsorbate molecules in terms of their known adsorption behaviour. Adsorption of simple molecules onto non-porous graphite tends to be either Type 2 or Type 3, depending upon the nature of the adsorbate used.

A Type 2 isotherm is defined as that occurring when the enthalpy of adsorption of the adsorbate onto the graphite surface is greater than the enthalpy of condensation of the bulk material at the experimental temperature. The adsorbate "wets" the surface, forming uniform monolayers and multilayers, and a progressive increase in the amount of material adsorbed is observed as the vapour partial pressure increases. The formation of successive layers has been observed[55] as pronounced steps in the adsorption isotherm of methane on graphite at 77 K. A similar process has been studied via proton NMR of neo-pentane ($C(CH_3)_4$) upon graphite[54]. At low neo-pentane concentrations, proton chemical shifts of –30 ppm, with respect to those observed in solution, are observed and as the amount of adsorbate on the surface increases, the chemical shift decreases to ~-20 ppm. As the coverage increases beyond one monolayer, the chemical shift is observed to decrease further. Calculations performed by the authors on the adsorbate chemical shift suggest that initially the molecules are held in a fixed "tripod down" orientation with respect to the surface, before steric requirements require the molecules to orient in a mixture of "tripod up" and "tripod down" orientations. As the layers build up, the chemical shift, averaged over all molecules, clearly decreases as the average distance of the molecule from the graphite plane increases. Support for these conclusions was provided by several calculations performed by Kiselev et al.[56] which predicted identical behaviour to that concluded from the NMR data. The most important conclusion within the paper, regarding the evaluation of chemical shift measurements, is that adsorbed molecules within multilayers can exchange position rapidly between layers, yielding an averaged chemical shift. This interpretation of the "averaged" chemical shift has also been formally outlined elsewhere[57].

Type 3 isotherms occur when the adsorption enthalpy of the adsorbate onto the graphite surface is less than the enthalpy of adsorbate condensation. In this case, adsorption only occurs because of a thermodynamically favourable entropy term, and the tendency is for the adsorbate to form island of multilayers, or nucleated crystallites centred at surface heterogeneities. Ammonia on graphite[58] has a typical Type 3 isotherm, and the mechanism of adsorbate addition is corroborated by NMR chemical shift data[59]. As the amount of adsorbate added increases, the low-frequency chemical shift increases from ~-20 ppm, again with respect to that observed in solution, to ~-35 ppm at one monolayer coverage before decreasing again as more material is added. This behaviour is ascribed to the fact that ammonia adsorbs initially at surface heterogeneities upon the graphite surface, such as projecting ketone groups or other oxygenated species, and that these sites then promote secondary adsorption. The oxygenated sites possess much smaller local magnetic susceptibility anisotropies than areas of pure graphite plane, and consequently the low-frequency chemical shift demonstrated by the adsorbate molecules is smaller at these sites. As secondary condensation occurs, and the ammonia spreads over the graphite plane, the magnitude of the average low-frequency chemical shift increases. The decrease in chemical shift beyond monolayer coverage simply occurs because of multilayer or droplet formation. Water upon graphite[58] is another example of a Type 3 isotherm, but NMR spectra recorded upon these systems show strikingly different adsorbate behaviour to that of ammonia upon graphite. Two lines are observed in the spectrum of calculated monolayer adsorption, one at ~-15 ppm and another, more intense line which is unshifted with respect to bulk water. Both lines are taken to arise from aggregations of water droplets either held at oxygenated sites upon the surface (for the water with a chemical shift of −15 ppm), or at a much greater distance from the surface. The appearance of the second line is not completely unexpected, as isotherm studies have shown[60] that the maximum amount of water adsorbed by graphite is much less than that equivalent to one monolayer.

Several years later, a series of papers appeared, studying the adsorption of various materials onto activated carbon. The motivation for these experiments came from industry, which was looking for ways to exploit the adsorption performance of activated charcoal to control the evaporation of gasoline. Therefore the first of the papers published was a static proton NMR study of gasoline adsorbed on a variety of activated carbons[61]. On adsorption, the spectra of gasoline suffered substantial broadening such that the complex solution-state spectrum was reduced to a single broad peak. This broad peak was shifted to low frequency (with respect to the averaged solution-state spectra) by between 2 and 10 ppm depending upon the carbon. The authors stated that the chemical shift of the gasoline peak within the carbon was the averaged value of molecules condensed within pores between 2 and 3 nm in diameter and those adsorbed directly on the surface. They then went on to suggest that the molecules condensed within pores would not see a significant chemical shift, and therefore the greater the volume of pores of the correct diameter, the smaller the shift to lower frequency. They also noted a strong relationship between ease of gasoline desorption and chemical shift, with the carbons showing greater low-frequency shifts demonstrating a greater affinity for the adsorbed gasoline. The study was extended further to include a variety of pure hydrocarbons[62] and alcohols[63]. These two papers reach similar conclusions on the size of the low-frequency chemical shift –that the chemical shift provided a means of estimating the ratio between material adsorbed onto the carbon surface and that condensed within pores of less than 3 nm in diameter.

Drago et al.[64] believed that molecules within different sized pores possess different chemical shifts as a result of the different ratios of rapidly exchanging molecules close to graphene planes comprising the pore walls. His experimental technique involved the addition of solutions, comprising various concentrations of adsorbates in CCl_4, to carbon. The adsorbate molecules he chose (CH_3CN, C_6H_6, and CH_2Cl_2) had only one resonance in their solution-state proton spectra. The samples were then examined by static proton NMR and the broad peak envelopes obtained for the molecules after addition to the carbon adsorbent were deconvolved into five smaller peaks. The peaks were ascribed to molecules still in solution and molecules within macropores, mesopores, large micropores and small micropores. A justification for such an approach was that the shifts to low frequency, with respect to the pure liquid, for each of these peaks were extremely similar for the different adsorbate molecules. It was observed that at low molecular concentrations in CCl_4 the low-frequency peaks (ascribed to the smaller pores) were more pronounced and, as the concentration of the probe molecules increased, the higher frequency peaks gradually become more prominent. This is in accordance with the theory of pore filling, which suggests that the driving force behind capillary condensation is greatest in smaller pores[34, 65]. Drago considers the fitting of the inhomogenous broad envelope to only 5 peaks to be a demonstration that only certain sized pores exist, and, whilst this is rather contentious, his explanations of the changes observed in the NMR spectra with concentration are both reasonable and plausible.

Deuterium MAS NMR experiments performed in Durham[66] have shown the importance of pore structure in the adsorption of water on carbon. Known amounts of D_2O were added to a series of nutshell-derived carbons, activated to varying degrees. The MAS spectra of these samples consisted of two peaks, a broad peak at approximately –6 ppm with a narrow peak at a position essentially unshifted from that of liquid D_2O. The narrow peak only became evident at high loadings and was ascribed to excess water, condensed upon the outer surfaces of the carbon. The broad peak intensity depended upon the degree of activation, and was related closely to the total pore volume of the carbon. The broad peak clearly arose from water molecules adsorbed (or condensed) within the pores of the carbon.

2.3.2. LINEWIDTH MEASUREMENTS UPON ADSORBED MATERIALS

Another easily measured NMR parameter that changes significantly after adsorption onto carbon is the width of the NMR lines. The width of the low-frequency peak, which is inherently related to the relaxation parameter, T_2, provides an important indicator regarding the mobility of the material upon the surface. Several of the broadening interactions that are averaged by molecular mobility in solution-state NMR are no longer completely averaged due to the presence of the adsorbent, and these can also be used to provide information upon the molecules' environment. In the main, authors have attached less importance to the phenomenon of line broadening than that of chemical shift, but as linewidths of > 1000 Hz are routinely observed for static NMR spectra of liquid adsorbates in these systems line-broadening can provide important information.

Tabony and co-workers[59] measured the static proton linewidth of the low-frequency ammonia peak at a variety of ammonia loadings on graphite. This BET type 3 system showed a variation in linewidth from 1500 Hz at 0.5-monolayer addition to around 1000 Hz after the addition of 5 monolayer equivalents. The results were not discussed in any great detail, but were taken to provide evidence that the adsorbate molecules became progressively more mobile as the amount of material added increased.

Yuoru[61], in his study on gasoline adsorption by various charcoals, found that the width of the low-frequency peak was related to the adsorption capacity of the carbon. He interpreted this to show that as the amount of material within the pores increased, the material became more mobile. At a simplistic level, it would be expected that as the pore size increases the average mobility of the molecules within the pore will also increase due to the lower ratio of adsorbed molecules. Youru was also the first to comment on the greater linewidths observed within carbons derived from coal. He explained that the coal-based material had a large amount of paramagnetic impurity, and the spectra of the adsorbed molecules would show correspondingly large amounts of additional dipolar broadening. The group's later papers[62, 63] on the adsorption of hydrocarbons and alcohols onto activated carbon provided broadly similar conclusions.

Drago's paper on "pore-resolved porosimetry"[64] discussed the linewidth for each of his deconvolved peaks. He found that as the pore sizes became larger, the linewidth obtained for the molecules within that pore decreased, gradually approaching the value obtained for the pure liquid. The conclusion to the paper states that the different linewidths obtained for each of the pore sizes result from rapid exchange of weakly bound surface molecules with those in the liquid-like multilayers.

A recent paper from Durham[67], again on deuterium MAS NMR, has studied the variation in observed linewidth at low adsorbate loadings. Initial adsorption was thought to occur at sites on the carbon surface where the adsorbate molecule is restricted in its motion to the greatest degree. This seems reasonable as it is well known[33] that adsorption in B.E.T. type 3 and 5 systems is driven by the decrease in entropy as the motion of adsorbates is decreased upon the adsorbent. The linewidth of the signal is taken as a direct measure of the adsorbate motion, and therefore as a measure of the extent of adsorption. Good agreement is reached between gravimetric and linewidth measurements on the extent of D_2O adsorption in the carbon, and several isotherms are derived from the NMR data. The authors conclude that the results demonstrate conclusively the physical significance of NMR measurements in adsorption studies on activated carbon.

2.4. THE LOW FREQUENCY CHEMICAL SHIFT

2.4.1. BULK MAGNETIC SUSCEPTIBILITY AND CHEMICAL SHIFT

If $\mathbf{B}_0$ is the magnetic field applied to a solid sample of bulk magnetic susceptibility χ_m, it is possible to describe the effective field at the nucleus of study as the sum of the applied field and a series of small corrections[68, 69]

$$B_{eff} = B_0 + \chi_v B_0 \times \left(\left(\frac{4\pi}{3} \right) - \alpha + k \right) + h_4 \qquad \textit{Equation 2.3}$$

The first correction is due to the field caused by the spherical Lorentz surface of the sample. The following term describes the "de-magnetising" field, where the parameter α depends upon the sample shape and on the orientation of the sample with respect to B_0. The third correction depends upon the distribution of magnetic fields within the Lorentz sphere, which is described by an empirical constant, k. The last term, h_4, arises from the shielding effect of the electrons surrounding the nucleus, and is usually characterised in homogenous samples by the "chemical shift".

The subdivision of the above equation into magnetic susceptibility terms and a chemical shielding term is somewhat arbitrary[70], especially as both effects arise from circular magnetic currents induced in the sample by the application of $\mathbf{B}_0$. In general, the magnetic susceptibility term is used when describing remote electron currents that contribute to a uniform bulk magnetic property for the sample (i.e. χ_m is taken to be uniform over all nuclei within the sample), whilst the shielding term designates specific currents at the nucleus of interest. In liquid samples, this term separation can be justified because the rapid molecular diffusion averages intermolecular effects to a reasonably uniform magnetisation vector. In situations where there is not such extensive intermolecular motion, as occurs in the samples analysed within this project, the absence of rapid motional averaging makes the division of the local magnetic field variation into a shielding and bulk magnetic susceptibility part rather more difficult. Usually the magnetic susceptibility terms are ignored, as they are by definition largely the same over the entire sample and therefore do not affect the appearance of the spectrum. However, when comparing two samples with vastly different magnetic susceptibilities (such as between liquid adsorbates and carbon-adsorbate systems) it is necessary to consider these terms too. In heterogeneous samples, such as adsorbate molecules upon a carbonaceous surface, it is not possible to simply ascribe the chemical shift observed solely to the local intra-molecular electronic environment term. Proximate inter-molecular currents between the graphitised adsorbent and the nuclei of study do not average to a uniform value, but depend upon the orientation and position of the adsorbate molecule with respect to the surface. Grant[70] suggests that "when designation of sizeable intermolecular currents from neighbouring molecules to χ_m fails to meet the criterion that the susceptibility should be a homogenous bulk property, these proximate intermolecular shielding currents should appropriately be included as part of the chemical shift".

Graphite, activated carbons and other graphitised carbonaceous adsorbents possess a large and highly anisotropic local magnetic susceptibility, and this introduces a low-frequency resonance shift and spectral broadening into the NMR signal obtained from species adsorbed upon these materials. The characteristic resonance shifts observed upon these adsorbents do not occur in samples containing adsorbents with small magnetic susceptibilities. For example, neo-pentane on titanium dioxide, water on silver iodide, and water on a non-graphitised carbon black all demonstrate negligible chemical shifts with respect to the pure adsorbate liquids[54]. Using the criterion suggested by Grant, the effect of the adsorbent magnetic susceptibility upon the spectrum can be divided into an isotropic bulk magnetic susceptibility (IBMS) effect and an anisotropic magnetic susceptibility "chemical shift".

2.4.1.1. The Effect of IBMS Upon Adsorbate Spectra

The IBMS of the carbon particles may introduce a small resonance frequency shift through the first three terms of the above expansion (Equation 2.3). The presence of material with a differing magnetic susceptibility may also introduce dipolar broadening into the static spectrum. In an analogous experiment[71], the addition of spherical glass beads to a sample of liquid water has been shown to leave the chemical shift of the water the same, but increase the static proton linewidth of liquid water from ~5 Hz to over 120 Hz. This is because glass beads possess a different magnetic susceptibility to water and appear as magnetic dipoles in the liquid. The static spectra of adsorbates upon carbon recorded in this study and discussed in Chapter 4 have shown that the IBMS makes almost no difference to the chemical shift of the adsorbate. Dipolar interactions may be averaged out completely by spinning the sample at the magic-angle at speeds greater than the interaction linewidth. It has been demonstrated that under MAS conditions the resulting dipolar field, and hence the broadening of the water signal, is completely removed[72-74]. This means that MAS experiments performed upon the systems within this study are not affected by the adsorbent IBMS and we may effectively ignore any contribution when discussing MAS spectra.

The anisotropic part of the carbon magnetic susceptibility interaction alters the chemical environment about the adsorbed species dependent upon its position and orientation within the sample. This results in a "proper" shielding tensor contribution, which is averaged to a single value, σ, by MAS. The low frequency chemical shifts observed in the spectra of material adsorbed on graphite in the literature can be described using models developed to explain the abnormally large high-frequency chemical shifts[75] observed in the proton spectra of aromatic molecules. These models estimate the magnetic field generated by the aromatic molecules and then calculate the effect of the field upon nuclei at various positions about the ring.

2.4.2. METHODS OF CALCULATING AROMATIC CHEMICAL SHIFTS

The usual approach to evaluating the expected chemical shift of protons attached to an aromatic ring system involves calculating the "ring currents" induced by B_0. From the derived ring-currents, it is possible to calculate the magnetic shielding introduced by the current. Pauling[76] first noted that the probability distribution function for the π-electron orbital wavefunctions in benzene was significant only in two ring-shaped regions above and below the molecular plane. Pauling noted that the electrons in these orbitals should be able to "pass almost imperceptibly from the field of one carbon atom to the next". Twenty years later, Pople[77] applied Pauling's ideas to predict NMR chemical shifts in aromatic molecules arising from these "ring-currents". Since then, the literature upon this subject has grown astronomically[78], and ring-currents are cited frequently in explaining the source of chemical shifts.

2.4.2.1. Classical Calculation of Ring Current Effects

In general, calculations commence by assuming that the benzene ring possesses six π-electrons circulating in a superconducting ring about the molecule[77, 79]. Classical physical relations are then used to evaluate the perturbing effect these circulating electrons have upon the local magnetic field. An electronic circulation is induced in the π electrons by the application of B_0 along the benzene molecule z-axis. The electron movement may be expressed as a current, I, causing a magnetic moment, μ

$$\mu_{equiv} = \mu_0 AI = -\frac{3e^2 B_0 r^2}{2m} \cdot \frac{\mu_0}{4\pi} \qquad \textit{Equation 2.4}$$

Pople[77] substituted the circular magnetic shell arising from this current with that arising from an equivalent point dipole at the centre of the benzene hexagon in order to simplify the calculation of the induced magnetic field. Using this model, there is no induced free electron current if B_0 lies in the plane of the ring. This means that the two perpendicular contributions to the shielding tensor are zero. If the nucleus we are interested in lies at an angle, ϕ and distance, R from the benzene z-axis then the calculated principal tensor values become:

$$\Delta\sigma_{yy} = \Delta\sigma_{xx} = 0$$

$$\Delta\sigma_{zz} = \chi_{zz}\frac{(1-3\cos^2\phi)}{R^3} = \frac{\mu_{equiv}}{B_0}\frac{(1-3\cos^2\phi)}{R^3}$$

Equations 2.5

In order to obtain the net contribution to the isotropic shielding the sum of these values is simply divided by three. Thus the change in the isotropic chemical shift, $\Delta\sigma$, introduced by the ring-current can be written as

$$\Delta\sigma_{iso} = \frac{\mu_0}{4\pi}\cdot\frac{e^2}{2m}\cdot\frac{r^2}{R^3}\cdot\left(1-3\cos^2\phi\right)$$

Equation 2.6

This simple model has been used quantitatively by several authors to predict proton chemical shifts[80, 81]. Later papers, rather than calculating an equivalent dipole, calculate the magnetic field arising directly from the circulating electronic ring current[82, 83]. Taking the centre of the benzene molecule as the origin, the shielding, $\Delta\sigma$ at a point with cylindrical co-ordinates (ρ, z), both expressed in units of r, can be calculated by[84]

$$\Delta\sigma = \frac{\mu_0}{4\pi}\cdot\frac{-e^2}{\pi m}\cdot\frac{1}{\pi r^2}\cdot\frac{1}{\left[(1+\rho)^2+z^2\right]^{1/2}}\cdot\left[K(k)+\frac{1-\rho^2-z^2}{(1-\rho)^2+z^2}\cdot E(k)\right]$$

In the equation above, K(k) and E(k) are complete elliptic integrals. The modulus of these integrals is given by the expression

$$k^2 = \frac{4\rho}{(1+\rho)^2+z^2}$$

Equation 2.7

Numerical values of K and E can be obtained for any pair of values, ρ and z, by evaluating k and looking up the corresponding values in a standard integral table (e.g.[85]). Simplifying the procedure still further, a table of shielding values as a function of nuclear position has been published by Johnson and Bovey[86] and used extensively. The equivalent dipole concept was tentatively extended to polycyclic molecules[80] using the assumption that the current in each further aromatic ring is equal to and independent from that of the benzene ring. Whilst this is obviously not the case if the Pauling model is applied rigorously, the observed proton chemical shift of small polycyclic systems is calculated reasonably accurately[87] by a summation of the magnetic fields generated by each ring. When the calculation is performed upon larger aromatic molecules the equation gives rather less accurate results. The equivalent dipole model has been used with some success in the study of porphyrins with the single central point dipole being replaced by a pair of dipoles above and below the molecular plane[88]. This refinement is introduced to allow for the fact that the "current loops" are actually situated above and below the plane of the molecule.

2.4.2.2. Quantum mechanical methods

London[89] introduced the application of quantum mechanical ideas to π-electron ring currents, as an extension of the Bloch molecular-orbital (M.O.) theory of metals and the M.O. theory of Huckel. A full treatment of the Huckel-London method with the various extensions and improvements introduced by later authors is given in the review article by Haigh and Mallion[78]. The basic calculation involves the modification of the secular equations arising from a Linear Combination of Atomic Orbitals (L.C.A.O.) scheme so that they describe the molecule in the presence of an externally applied magnetic field. Pure London theory is directed to finding the eigenvalues and eigenvectors of the effective Hamiltonian of an electron in the magnetic field. As in most quantum mechanical problems, assumptions are made in order to reduce the calculated matrix elements in number and complexity. The "London approximations" have often been cited as weaknesses in the London theory[90, 91]. The assumptions made are based upon the premise that the electrons are mobile and form interatomic currents. Two significant examples of this are that "local" terms describing essentially pure atomic orbitals (A.O's) are assumed not to contribute to the Hamiltonian, and that the electrons in the π M.O's are most likely to be found equidistant between adjoining carbon atoms in the molecular plane.

Calculation of the secular determinant of the Hamiltonian demonstrates that if the molecule does not comprise a closed loop then the external field has no effect upon the molecule. This has often been cited as the quantum-mechanical justification for the use of "ring-currents" to describe the effect of the $\mathbf{B}_0$ field. Further to this, the interaction is shown to be proportional to the magnetic flux through the polygon enclosed by the carbon atoms, which in a homogenous magnetic field is proportional to the area of the ring system. Magnetic susceptibilities, χ^{π}, and "ring currents", J^{π}, can be calculated from the roots of the secular determinant. From these values, the predicted chemical shift can be obtained. The Haigh-Mallion tables, describing chemical shift as a function of position in a manner similar to those calculated using the Johnson-Bovey model have been published[92], and used by authors in the calculation of chemical shifts and magnetic susceptibilities of simple aromatic molecules.

2.4.2.3. Comparison of the models used

Isolated values for proton chemical shifts determined from the calculations above appear to be fairly inaccurate when compared to experimental values. However the calculations assume that magnetic susceptibility and anisotropy arise solely from the π orbital "ring current" effects, with no account being taken of the effects of the σ electron framework. It has been shown[93] that the π electrons in an aromatic system only account for 70 per cent of the measured magnetic susceptibility and anisotropy, and therefore any calculations performed using solely that consideration will suffer large errors. Actual separation of the magnetic susceptibility into the various orbital contributions is an extremely difficult process[94], so results have generally been presented and discussed in terms of a correction for aromatic protons when compared to protons attached to localised double bonds in closely related molecules[95].

When the σ framework is accounted for, the classical calculations give reasonable results. Studies performed upon benzene molecules with (1,4) alkyl bridges, such as [10]-para-cyclophane[82] have demonstrated that over distances of several bond lengths, the equivalent dipole model gives extremely accurate results for the predicted chemical shift. Over smaller distances, the equivalent dipole approximation introduces significant errors, and it is necessary to perform the full magnetic field calculation. Collation of experimental data and comparison with calculated values leads to a correlation co-efficient of 0.85 for the classical equivalent dipole model and 0.96 for the full classical ring-current magnetic field calculation. Values approaching 1 are now obtained when various calculated and empirical corrections[96] have been introduced into the calculation. This lends considerable credibility to the classical ring current model as a means of estimating chemical shifts and, in addition to its conceptual simplicity, offers another explanation as to why it is cited so frequently. Several authors have expressed their disquiet about such frequent use of purely classical models. Farnum and Wilcox[96] wrote that "classical models have the limitation of being only a partial representation of a complete quantum-mechanical solution" and Dailey[97] has stated that "classical and semi-classical theories seem incapable of giving a satisfactory and simultaneously coherent account of both magnetic susceptibilities and chemical shift data".

As the fundamentals of quantum-mechanical theory become better understood and computing power continues to increase, the models used to calculate magnetic susceptibility tensors and aryl proton chemical shifts give progressively better results. Newer models[90, 98] that explicitly account for the effect of the σ framework approach the experimental values for magnetic susceptibility of benzene extremely closely.

2.4.2.4. Criticisms of the ring current model

The arguments and calculations outlined above assume that "ring-currents" are at the heart of the experimental phenomena observed in measurements upon aromatic systems. However, the current is not something that may be observed directly and there has been extensive debate as to whether the experimental properties measured for aromatic molecules demonstrate conclusively the existence of these so-called ring-currents. Given that London's paper demonstrated a quantum-mechanical justification for the use of ring-currents in the calculation of magnetic susceptibilities, disagreement has long centred upon the quantum mechanics used as a basis for that paper. In particular, Musher[93, 99] disputed the legitimacy of making a

σ-π separation and then treating the π electrons as a special case because of the additional mobility arising from their "delocalisation". Musher believed that local diamagnetic anisotropy effects could account for the magnetic susceptibility and proton chemical shifts observed in benzene molecules and suggested a "localised increment" model to calculate the magnetic susceptibility of benzenoid molecules. He claimed that this method could reproduce experimental anisotropy measurements more closely than was possible via any theoretical approach based upon the concept of ring currents. The "localised increment" model suggested has hardly been used in the literature, so the veracity of this claim is questionable. Gaidis and West[100] have made the point that Musher's "localised increment" model cannot account for the extremely large proton chemical shifts observed in porphyrin molecules. Kumanova and Rebane[101] considered the experimental values obtained for the magnetic susceptibilities, χ, of four series of cyclic hydrocarbons. They drew plots of the dependence of the diamagnetic susceptibility on the number of double bonds in the ring, and found that in general the addition of another double bond produced a linear change in χ. However, a sharp jump in the susceptibility is observed when the number of double bonds increases to its maximum value (2 in five-membered rings, 3 in six- and seven-membered rings, 4 in eight-membered rings). The authors concluded that the sole reason for the jump in susceptibility was the "introduction of a ring current due to the π electrons".

Several authors have noted the problems inherent in proving or disproving theoretical considerations by experimental measurement. The agreement that Musher obtained without ring-currents is not sufficient reason to deny their existence, and conversely neither is the fact that "ring-current" theories compare well with experiment sufficient evidence to prove that they do. Ring-current considerations continue to be cited frequently in the explanation of NMR spectra, and it appears that the bulk of authors have taken the view that it would be unwise to discard the ring current model, which "has worked so well in so many instances"[100].

2.4.2.5. Ring Current calculations performed for adsorbates on graphite

Adsorbate molecules such as benzene[101], neopentane[59] and ammonia[102] adsorbed in a monolayer upon graphite generally show a low-frequency proton chemical shift of approximately 25-30 ppm. Monolayer coverage upon graphite is effectively an ideal environment to model, as it means that all molecules are adsorbed directly to the uniform graphite surface at a consistent distance. Any calculations performed for adsorption upon graphene sheets generally use this value as a theoretical target. Neutron diffraction studies performed on a monolayer of benzene adsorbed upon graphite[54] give a graphite – benzene distance (R) of 0.32 nm. As the adsorbate molecule is adsorbed above the graphene planes, one may assume that the angle between the nuclei of study and the benzene hexad axis in the calculations described above is 0°. Using these two values, the expected adsorbate molecule chemical shift caused by the diamagnetic susceptibility of the adsorbent can be calculated from each of the various models discussed above. If either of the two classical ring current models is used, a value for the chemical shift of approximately -1.7 ppm is obtained. The predicted chemical shift using London's quantum-mechanical treatment via the Haigh-Mallion tables is about –1.6 ppm.

Whilst these calculations predict a chemical shift of the correct sign and an associated large anisotropy, the results are clearly nowhere near large enough to explain fully the interaction between the graphite surface and the adsorbate molecule. The main reason for the failure of the various ring current calculations to account for the size of the low-frequency shift is that the isolated benzene molecule used as a model adsorbent does not describe the extensively de-localised nature of the carbon graphene surface adequately. It has been noted experimentally that the size of an aromatic molecule's magnetic susceptibility and anisotropy increase as the aromatic ring system becomes more extensive[103], and exceptionally large chemical shifts in hydrogen atoms attached to these ring systems[104, 105] have been observed. Pople[80] assumed that the ring currents increased proportionally with the number of rings and achieved surprisingly accurate results when calculating ring proton chemical shifts in small polycyclic molecules. Similarly, London's quantum mechanical treatment of "ring current" effects predicts that the magnetic susceptibility anisotropy arising from aromatic π orbitals would be proportional to the square of the area of the ring system.

A typical example of the increased magnetic susceptibility of larger molecules is [7]-helicene or coronene (a molecule consisting of seven benzene rings arranged as a large hexagonal plane), which has a total magnetic anisotropy almost 8 times that of benzene[106]. The magnetic susceptibility anisotropy of the helicenes is not as large as that predicted by London because of the mechanism of successive addition of benzene rings. The steric interactions present whilst further rings are added cause distortion to a non-planar geometry[107], and consequently the measured anisotropy is less than that predicted. However, the magnetic susceptibility still increases significantly, and we would expect the adsorbate chemical shift observed to reflect this increase.

2.4.2.6. Measured equivalent dipole correction

An approach to predicting the chemical shifts of adsorbates upon graphite, which allows for the increasing magnetic susceptibility of progressively larger aromatic molecules, is to use bulk magnetic susceptibility values obtained from crystal measurements. It is then assumed that these values arise solely from single point dipoles at the centre of the molecules. The model is extremely simple, but when taken in conjunction with the ring current calculations above can provide a means to extend the "ring-current" model in a semi-quantitative manner. The principal values of the axially symmetric susceptibility tensor of graphite used in this calculation are obtained from crystal measurements. The accepted values for the principal tensor components are[54]:

$$\chi_{zz} = \chi_{//} = -94.6\times10^{-6}\cdot cm^3 mol^{-1}$$

$$\chi_{xx} = \chi_{yy} = \chi_{\perp} = -34.9\times10^{-6}\cdot cm^3 mol^{-1}$$

If the nucleus lies at an angle, θ and distance, R to the graphite z-axis then these values may be used to calculate the isotropic average shielding and the anisotropy of the interaction using the relations[108]

$$\Delta\sigma_{iso} = \frac{\chi_{//} - \chi_{\perp}}{3R^3}\left(1 - 3\cos^2\theta\right)$$

$$\Delta(\Delta\sigma) = \frac{\chi_{//} + \frac{1}{2}\chi_{\perp}}{R^3}\left(1 - 3\cos^2\theta\right)$$

Equations 2.9 and 2.10

In this example the molecules are clearly sitting directly above the graphene plane and therefore the angular orientation term, θ, is assumed to be 0. The results from these calculations predict a low frequency chemical shift of -27 ppm, which is very close to the value of ~-30 ppm observed in the proton spectra of benzene upon graphite. As a gauge of the model's accuracy, the additional high frequency chemical shift predicted for aromatic ring protons using crystal susceptibility measurements obtained from benzene[109] was calculated to be 2.1 ppm. This compares to the experimental value of approximately 1.8 ppm. The results of the ring-current model taken in conjunction with this measured correction show that the diamagnetic susceptibility may be related to the aromatic nature of the graphene planes, and the size of the chemical shift explained satisfactorily in terms of the magnitude of the graphite diamagnetic susceptibility.

As the number of aromatic rings is increased, the delocalised electronic motion about the atoms becomes more complex, and the path can no longer be approximated to a circle. This means that the approximations forming the basis of the ring-current model become significantly more difficult to justify. Additionally, the approximation of the magnetic field arising from a complex circulating current to a single point dipole is grossly inadequate at distances comparable to the dimensions of the electronic distribution. As the area of the electronic distribution increases, the model becomes more and more approximate. These considerations mean that the results from this calculation cannot be cited with any accuracy, but they certainly show that the observed adsorbate low-frequency chemical shift of ~30 ppm upon graphite is broadly in agreement with that predicted via a consideration of the ring currents present in the adsorbent.

2.5. REFERENCES

1. A. A. Merchant, M. A. Petrich, *Chem. Eng. Comm.*, **118**, 251 (1992)
2. F. Rodriguez-Reinoso, J de D. Lopez-Gonzalez, C. Berenguer, *Carbon*, **20**, 513 (1982)
3. F. Rodriguez-Reinoso, J de D. Lopez-Gonzalez, C. Berenguer, *Carbon*, **22**, 13 (1984)
4. D. J. Taylor, Ph.D Thesis, Bristol (1966)
5. D. M. Mackay, P. V. Roberts, *Carbon*, **20**, 95 (1982)
6. A. N. Weinerberg, T. M. O'Grady, *U.S. Patent* 4,082,694, Apr. 4, 1978
7. F. Kraehenbuehl, H. F. Stoekli, P. Ehrburger, A. Addoun, *Carbon,* **24**,112 (1996)
8. H. Marsh, B. Rand, *Carbon*, **9**, 47 (1971)
9. B. M^{c}Enancy, N. Dovaston, **13**, 515 (1975)
10. K. Tomkow, T. Siemieniewska, F. Czechowski, A. Ganowska, *Fuel,* **56**, 121 (1977)
11. C. W. Scheele, *"Chemical Observations on Air and Fire"*, 182 (1780)
12. S. S. Barton, M. J. B. Evans, E. Halliop, J. A. F. MacDonald, *Langmuir*, **13**, 1332 (1997)
13. J. A. Menendez, B. Xia, J. Phillips, L. R. Radovic, *Langmuir*, **13**, 3414 (1997)
14. E. D. Dimotakis, M. P. Cal, J. Economy, M. J. Rood, S. M. Larson, *Environ. Sci. Technol.*, **29**, 1876 (1995)
15. G. Trembley, F. J. Vastola, P. L. Walker, *Carbon*, **16**, 35 (1978)
16. S. Matsumoto, N. Seteka, *Carbon*, **17**, 303 (1979)
17. S. S. Barton, D. J. Gillespie, B. H. Harrison, *Carbon*, **11**, 649 (1973)
18. J. V. Hallam, H. V. Drushell, *J. Phys. Chem.*, **62**, 110 (1958)

19. M. Starsinic, R. L. Taylor, P. L. Walker, *Carbon*, **21**, 69 (1983)

20. V. A. Garten, D. E. Weiss, *Rev. Pure Appl. Chem.*, 7,69 (1957)

21. G. Ishizaki, I .Marti, *Carbon*, **19**, 409 (1981)

22. J. M. O'Reilly, R. A. Mosher, *Carbon*, **23**, 47 (1983)

23. C. Morterra, M. J. D. Low, A. G. Sererdice, *Carbon*, **22**, 5 (1984)

24. A. W. Greisch, *M.Sc. Thesis*, University of Iowa (1990)

25. S. R. Keleman, P. J. Kwiatek, *Energy and Fuels*, **9**, 841 (1995)

26. M. Barber, E. L. Evans, J. M. Thomas, *Chem. Phys. Lett.*, **18**, 423 (1973)

27. R. R. Martin, N. S. M^c^Intyre, J. A. MacPhee, K. T. Aye, *Energy and Fuels*, **2**, 118 (1988)

28. J. A. Turner, K. M. Thomas, A. E. Russell, *Carbon*, **35**, 983 (1997)

29. S. Brunaeur, P. H. Emmett, E. Teller, *J. Am. Chem. Soc.*, **60**, 309 (1938)

30. R. M. Culver, N. S. Heath, *Trans. Faraday Soc.*, **51**, 1569 (1955)

31. J. J. Kipling, R. B. Wilson, *Trans. Faraday Soc.*", **56**, 562 (1960)

32. M. M. Dubinin, E. D. Zaverina, V. V. Serpinski, *J. Phys. Chem. Soc.*, 1760 (1955)

33. S. J. Gregg, K. S. W. Sing, *"Adsorption, Surface Area and Porosity"*, Chapter 3, Academic Press (London) Ltd. (1967)

34. A. Zsigmondy, *Z. Anorg. Chem.*, **71**, 356 (1911)

35. J. W. M^{c}Bain, *J. Amer. Chem. Soc.*, **57**, 699 (1935)

36. F. R. Metz, *Micromeritics Micro Report*, 4th Quarter 1992

37. M. M. Dubinin, *Carbon*, **18**, 355 (1980)

38. M. M. Dubinin, *Carbon*, **19**, 402 (1981)

39. B. R. Puri, K. Murari, D. D. Singh, *J. Phys. Chem.*, **37**, 65 (1961)

40. S. S. Barton, M. J. B. Evans, J. Holland, J. E. Koresh, *Carbon*, **22**, 265 (1984)

41. E. O. Wiig, A. J. Juhola, *J. Am. Chem. Soc.*, **71**, 2069 (1949)

42. A. V. Kiselev, *"The Structure and Properties of Porous Solids"*, Butterworth, London (1958)

43. R. C. Bansal, T. L. Dhami, S. Parkash, *Carbon*, **16**, 389

44. M. Rozwadowski, R. Wojsz, *Chem. Papers*, **29**, 660 (1975)

45. L. B. Adams, C. R. Hall, R. J. Holmes, R. A. Newton, *Carbon*, **26**, 451 (1988)

46. M. J. Katz, *"Vacuum Microbalance Techniques, Volume 1"*, Plenum Press (1961)

47. M. M. Dubinin, *Chem Rev.*, **60**, 235 (1960)

48. I.U.P.A.C, Manual of symbols and technology: Appendix 2, *Pure and Applied Chem,* **31**, 578 (1972)

49. C. G. Schull, *J. Amer. Chem. Soc.*, **70**, 1410 (1948)

50. E. P. Barrett, L. G. Joyner, P. H. Halenda, *J. Amer. Chem. Soc*, **73**, 373 (1951)

51. R. W. Cranston, F. A. Inkley, *"Advances in Catalysis Vol 9"*, Academic Press (1957)

52. P. Zwietering, *"The Structure and Properties of Porous Solids"*, Butterworth, London (1957)

53. S. Kaplan, H. A. Resing, J. S. Waugh, *J. Chem. Phys.*, **59**, 5681 (1973)

54. J. Tabony, *Progress in NMR Spec.*, **14**, 1 (1980)

55. A. Thomy, X. Duval, *J. Chim. Phys.*, **67**, 1101 (1970)

56. A. V. Kiselev, N. N. Avgul, *"Chemistry and Physics of Carbon Vol. 6"*, Marcel Dekker, New York (1970)

57. M. D. Sefcik, J. Schaefer, E. O. Stejskal, "*Magnetic Resonance In Colloid and Interface Science*", A. C. S. Symposium Series 34, 109 (1976)

58. G. Bomchil, N. Harris, M. Leslie, J. Tabony, J. W. White, P. Gamlen, R. K. Thomas, T. D. Trewern, *J. Chem. Soc. Faraday Trans. I* **75**, 1535 (1979)

59. J. Tabony, G. Bomchil, N. Harris, M. Leslie, J. W. White, P. Gamlen, R. K. Thomas, T. D. Trewern, *J. Chem. Soc. Faraday Trans. I* **75**, 1570 (1979)

60. A. C. Zettlemayer, E. M^{c}Cafferty, *Croat. Chim. Acta.*, **45**, 173 (1973)

61. D. Youru, *Chinese Journal of Microwave and Radiofrequency Spectroscopy*, **3**, 159 (1986)

62. D. Youru, S. Lianfong, K. Yuhua, H. Aiguo, *Acta Physico-Chimica Sinica*, **4**, 250 (1988)

63. Y. Du, H-Z Yuan, D-H Wu, Y-H Kong, *Magn. Reson. Chem.*, **27**, 987 (1989)

64. R. S. Drago, D. C. Ferris, D. S. Burns, *J. Am. Chem. Soc.*, **117**, 6914 (1995)

65. D. J. Shaw, *"Introduction to Colloid and Surface Chemistry"*, Butterworth and Co. (1980)

66. R. K. Harris, T. V. Thompson, P. Forshaw, N. Foley, K. M. Thomas, P. R. Norman, C. Pottage, *Carbon*, **34**, 1275 (1996)

67. R. K. Harris, T. V. Thompson, P. R. Norman, C. Pottage, A. N. Trethewey, *J. Chem. Soc. Faraday Trans.*, **91**, 1795 (1995)

68. W. C. Dickinson, *Phys. Rev.*, **81**, 717 (1951)

69. J. L. Bonardet, J. P. Fraissard, *J. Mag. Reson.*, **22**, 543 (1976)

70. D. M. Grant, "Chemical Shift Tensors", *Encyclopaedia of NMR*, (Editors D. M. Grant, R. K. Harris), Wiley, London (1996)

71. D. Doskovilova, D. D. Tao, B. Schneider, *Czech. J. Phys. B.*, **25**, 202 (1975)

72. R. J. Abraham, J. Fisher, P. Loftus, *"Introduction to NMR Spectroscopy"*, John Wiley and Sons (1988), p19

73. M. E. Stoll, T. J. Majors, *Phys. Rev. B.*, **24**, 2859 (1981)

74. A. N. Garroway, *J. Magn. Reson.*, , 168 (1982)

75. L. H. Meyer, A. Saika, H. S. Gutowsky, *J. Am. Chem. Soc.*, **75**, 4567 (1953)

76. L. Pauling, *J. Chem. Phys.*, **4**, 673 (1936)

77. J. A. Pople, *J. Chem. Phys.*, **24**, 1111 (1956)

78. C. W. Haigh, R. B. Mallion, *Prog. NMR Spectrosc.*, **13**, 303 (1980)

79. C. E. Johnson Jr., F. A. Bovey, *J. Chem. Phys.*, **29**, 1012 (1958)

80. H. J. Bernstein, W. G. Schneider, J. A. Pople, *Proc. Roy. Soc. London*, **A236**, 515 (1956)

81. I. J. Maddox, R. M^{c}Weeney, *J. Chem. Phys.*, **36**, 2353 (1962)

82. J. S. Waugh, R. W. Fessenden, *J. Am. Chem. Soc.*, **79**, 846 (1957)

83. J. S. Waugh, R. W. Fessenden, *J. Am. Chem. Soc.*, **80**, 6697 (1958)

84. W. R. Smythe, *"Static and Dynamic Electricity"*, M^{c}Graw-Hill (1939), p267

85. Peirce Integral Tables, p121

86. J. W. Elmsley, J. Feeney, L. H. Sutcliffe, *"High Resolution Nuclear Magnetic Resonance Spectroscopy"*, Pergamon Press, Oxford (1965) Vol. 1, Appendix B

87. J. D. Memory, *J. Chem. Phys.*, **38**, 1341 (1963)

88. R. J. Abraham, *Mol. Phys.*, **4**, 145 (1961)

89. F. London, *J. Chem. Phys.*, **5**, 837 (1937)

90. C. A. Coulson, J. A. N. F. Gomes, R. B. Mallion, *Mol. Phys.*, **30**, 713 (1975)

91. A. T. Amos, H. G. F. Roberts, *Mol. Phys.*, **20**, 1081 (1971)

92. C. W. Haigh, R. B. Mallion, *Org. Magn. Reson.*, **4**, 203 (1972)

93. J. I. Musher, *J. Chem. Phys.*, **43**, 4081 (1965)

94. C. A. Coulson, R. B. Mallion, *J. Am. Chem. Soc.*, **98**, 592 (1976)

95. R. J. Abraham, J. Fisher, P. Loftus, *"Introduction to NMR Spectroscopy"*, John Wiley and Sons (1988), 19

96. D. G. Farnum, C. F. Wilcox, *J. Am. Chem. Soc.*, **89**, 5379 (1967)

97. B. P. Dailey, *J. Chem. Phys.*, **41**, 2304 (1964)

98. D. W. Davies, *Nature*, **190**, 1102 (1961)

99. J. I. Musher, *Adv. Mag. Res.*, **2**, 177 (1966)

100. J. M. Gaidis, R. West, *J. Chem. Phys.*, **46**, 1218 (1967)

101. J. Tabony, J. W. White, M. Coulon, J. C. Delachaume, *Surface Science*, **95**, 282 (1980)

102. J. Tabony, J. W. White, *Mol.Phys.*, **40**, 1209 (1980)

103. R. J. Myers, *"Molecular Magnetism and Magnetic Resonance spectroscopy"*, Prentice Hall (1973), p120

104. H. A. Staab, F. Binnig, *Tetrahedron Letters*, 319 (1964)

105. E. Vogel, W. Pretzer, W. A. Boll, *Tetrahedron Letters*, 3613 (1965)

106. M. T. Rogers, *J. Am. Chem. Soc.*, **69**, 1506 (1947)

107. W. H. Laarhoven, R. J. F. Nivard, *Tetrahedron*, **28**, 1803 (1972)

108. R. K. Harris, *Multinuclear Magnetic Resonance in Liquids and Solids – Chemical Applications"* (Editors: P. Granger and R. K. Harris), NATO ASI, Maratea, 1988

109. A. A. Bothner-By, J. A. Pople, *"Annual Review of Physical Chemistry"*, **16**, 43 (1965)

110. B. Alduri, *Reviews in Chemical Engineering*, **11**, 101 (1995)

111. A. M. Goncalves da Silva, V. A. M. Soaves, J. C. Calado, M. B. de Carvalho, "*J. Chem. Soc. Faraday Trans.*", **87**, 3799 (1991)

EXPERIMENTAL

3.1. SAMPLE PREPARATION AND CHARACTERISATION

All samples of carbon studied were prepared and supplied by DERA at Porton Down. The characterisation data upon these carbon samples were also obtained from Porton Down. Both phosphorus-based adsorbates (tri-methyl phosphate –TMP and di-methyl methyl phosphonate –DMMP) and ^2H_2O were supplied by Aldrich. The bulk liquid density of each of the adsorbates at RTP was used to calculate the volume of material in various positions within the pores. The values used were 1.21 g cm^{-3} for TMP, 1.15 g cm^{-3} for DMMP, 1.00 g cm^{-3} for H_2O and 1.10 g cm^{-3} for D_2O.

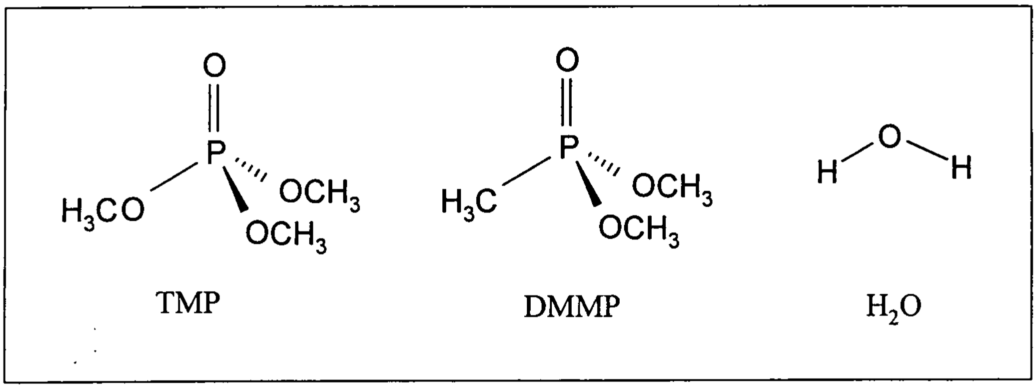

Figure 3.1. Structure of the adsorbate materials used within this study

3.1.1. CARBON CHARACTERISATION DATA

The bulk of the work in this study has been performed upon SC2 nutshell carbon. A nutshell carbon was used because it has been demonstrated that carbons derived from organic materials tend to possess a relatively low proportion (< 2% w/w) of ash within the pore structure[1]. Such ash remains after incomplete carbonisation of the raw material and comprises inorganic material left over after the activation treatment. The ash contains paramagnetic impurities, such as iron, which can cause large dipolar fields and broaden spectra by up one hundred kHz[2]. In addition, the nutshell carbon has a broad range of pore sizes, providing a varied environment for study using NMR. Nitrogen adsorption measurements upon a typical sample of SC2 yield a B.E.T. Specific Surface Area of 1114 m^2 g^{-1}. Alpha-s analysis gave values for the total pore volume of 0.540 mL g^{-1} and a micropore volume of 0.425 mL g^{-1}. Mercury porosimetry measurements showed that the majority of the porous volume is associated with pores of less than 100 nm in diameter, with approximately 47% of the volume residing in the mesoporous 2-50 nm range. About 40% of the pore volume is found in pores of less than 2 nm diameter. The data obtained from mercury porosimetry are shown in Figure 3.2.

3.1.2. EXPERIMENTAL SAMPLE PREPARATION

It was necessary to ensure that the carbon surface was initially free of moisture, so that the pore structure was empty and would allow the adsorbate to adsorb freely. Carbon samples were stored in airtight jars between experiments, and were then dried prior to use. This was achieved by heating the carbon sample under vacuum for approximately 8 hours. Typical conditions used for this were 90°C and 5 x 10^{-4} atmospheres. The carbons would then be allowed to cool under vacuum prior to the addition of the adsorbate.

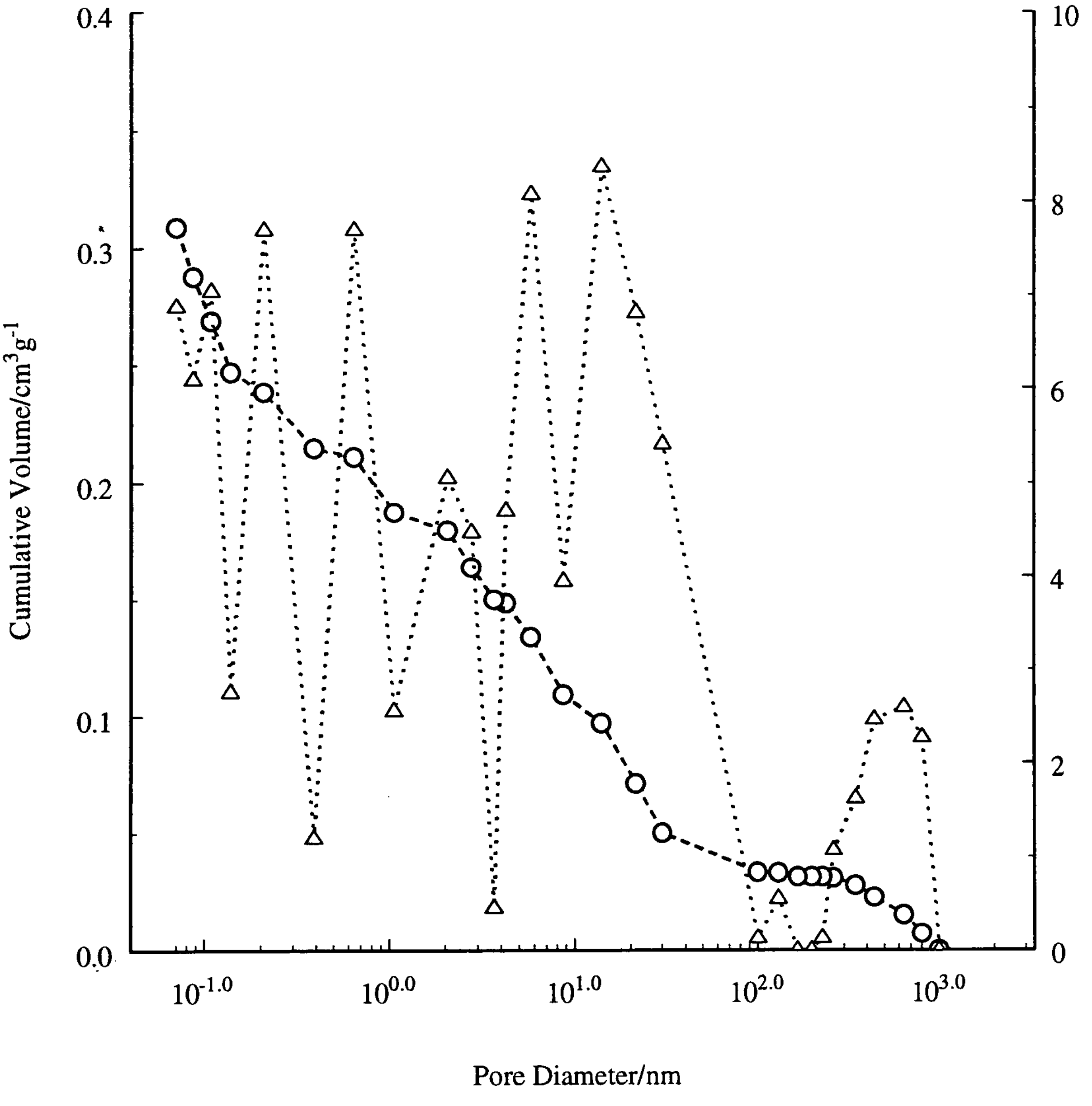

Figure 3.2. Pore size distribution of SC2 carbon obtained by mercury porosimetry. Circles represent the cumulative volume of the pores (left hand axis) whilst triangles show the percentage of the total volume of each pore diameter (right hand axis).

3.1.3. ADSORBATE ADDITION

The amount of adsorbate added to the carbon surface had an important influence upon the spectra obtained and it was necessary to measure this value as accurately as possible. The quantity added could be controlled roughly by adding the adsorbate via a micro-syringe. Once this had been done, an accurate measure of the amount added could be calculated by mass difference. Masses added are usually quoted as a percentage of the mass of the carbon and are accurate to within ± 0.5%.

Wherever possible, the carbon sample was transferred under vacuum to a dry-box where the adsorbates could be added in an inert nitrogen atmosphere. This was time consuming to perform and in many cases, where the experiment required rapid adsorbate addition and transfer to the spectrometer, impossible. Alternatively, the addition could be performed in the laboratory atmosphere, though obviously this introduced the possibility of contamination of the samples from atmospheric moisture. With practice it became possible to remove the vacuum from the carbon sample, add a measured amount of the adsorbate and seal the sample in less than ten seconds. The two different adsorbate addition techniques were compared by acquiring spectra of samples prepared by each technique. No discernible difference was observed between the spectra obtained from samples prepared by the two methods for a variety of adsorbates, including $^{2}H_2O$, TMP and DMMP. From the results, it appears that adding adsorbate material in air does not affect the experimental results significantly. That said, wherever possible adsorbate material was added within the glove-box.

3.1.4. SAMPLE SEALING.

It was important to ensure that the samples were sealed during the course of experiments for several reasons. Because the system undergoing study comprises a liquid portion, it was possible that a proportion might vaporise and escape away from the carbon surface. Some experiments involved heating the sample to over 140°C, so this presented a serious possibility. If the vapour loss occurred, it would render many of the quantitative results obtained from the experiment invalid and might introduce spurious background signals into subsequent spectra. It also had to be ensured that atmospheric water vapour could not adsorb onto the carbon surface whilst an experiment was being performed.

Samples were sealed in one of two manners, again dependent upon the time available for the procedure to be carried out. In situations where it needed to be done as quickly as possible, the adsorbate and carbon were placed within a hollow Kel-F rotor insert and an airtight end-cap put on. The Kel-F inserts were made to order by the departmental workshops and were found to perform very well. The caps could be forced on extremely tightly via the application of pressure, and frequently needed cutting off in order to re-obtain the sample at the end of the experiment. Over the course of a 24 hour experiment, the mass of the sample would typically remain constant to within ± 0.1%. Problems were encountered when re-using older inserts, especially in experiments performed using water as an adsorbate. The volatility of water, coupled with the weak interaction of the water with the carbon surface, meant that occasionally there was significant mass loss during a long experiment. Additionally it was found that the interior surface of inserts became scratched through use making them difficult to clean properly. Spurious peaks were observed in several experiments, which did not reappear when the experiment was repeated in new inserts, and were attributed to ground-in carbon dust.

In situations where it was possible to take more time over the sample sealing, glassblowing techniques were used. The full procedure is detailed elsewhere[3, 4, 5], but is outlined briefly below. The adsorbate was added to the dehydrated carbon in a specially constructed glass tube. This tube has a small bulb at the bottom, which will fit neatly inside a 7.5 mm MAS rotor where the sample is placed and two constrictions approximately 12 and 150 mm above the bottom. The tube is then re-attached to the vacuum line and the vacuum fleetingly re-applied. A hand blowtorch is then used to melt the upper constriction and the portion of the vessel containing the carbon pulled slowly downwards. As the system is under reduced pressure, the molten glass will close over, and a sealed tube containing the sample will result. A similar process is performed at the second, lower constriction, but the sample is cooled with liquid nitrogen and placed within brass holders, acting as heat sinks, in order to prevent the sample being heated, and possibly affected, by the sealing process. The final product is a small sealed ampoule, which will fit securely within a MAS rotor. Care must be taken to make sure that the ampoule is as axially symmetric as possible so that it will spin without trouble when placed within the rotor. Clearly there is no danger that material can escape from the ampoule, so this was the technique of choice when preparing samples upon which long experiments were to be performed.

3.1.5. MAS ROTOR PACKING.

The MAS rotors will not spin freely if there is an uneven distribution of mass within the rotor, or if the insert is free to move in any way. The inserts are placed within the rotor between two layers of a fine packing powder that fills any gaps between the insert and the rotor wall. Pressure is applied to pack in the powder as tightly as possible. Ideally the packing powder should be as fine as possible and show no NMR signal for the nuclei to be studied. Flowers of sulphur were generally used, but for high temperature operation sodium chloride crystals, finely ground, were chosen.

3.2. THE NMR EXPERIMENT

All experiments detailed within this thesis were performed upon a Chemagnetics CMX200 spectrometer. The spectrometer uses an Oxford instruments wide-bore (89.5 mm) superconducting magnet generating a magnetic field strength of 4.7 T. This gives resonance frequencies of 81.02, 30.72 and 27.01 MHz for ^{31}P, ^{2}H and ^{17}O nuclei respectively. The system is controlled from a Sun workstation interface using the Chemagnetics Spinsight software package.

3.2.1. MAGIC-ANGLE SPINNING (MAS)

The Chemagnetics probes used over the course of this study use pencil-spinning modules with independent bearing and drive gas inlets. The supply gas is dry air, which is passed at 70 psi into an automated PID spinning rate controller. This is capable of maintaining the MAS rate to within ± 1 Hz for a well-packed sample. Typically spinning rates of 0.8 to 1.5 kHz were used, although higher spinning rates up to 7 kHz may be achieved. The probes used 7.5 mm Zirconia pencil rotors with PTFE end-caps and spacers, and Kel-F drive-tips.

3.2.2. VARIABLE TEMPERATURE (VT) OPERATION

The Chemagnetics system uses a distinct variable-temperature gas inlet, which is independent of the bearing and drive gas lines. The VT gas used is nitrogen, supplied at 50 psi. The temperature of the VT gas is controlled by a heater within the spectrometer, which is connected to a thermocouple in the probe, allowing the desired temperature to be maintained to within ± 0.1°C. For low-temperature operation, the VT gas is passed through a heat exchanger in liquid nitrogen and then heated to the desired temperature. Experimental temperatures ranging from –140°C to 200°C were attainable.

Because the thermocouple is placed in the VT gas flow before the gas passes over the sample it is necessary to calibrate the actual temperature at the sample. Accurate VT calibration is complicated by the frictional heating effect caused by MAS[6, 7] and the existence of MAS-induced temperature gradients within the rotor[8]. This means that the temperature within the sample will vary with MAS rate, necessitating temperature calibration at several spinning speeds. There are several possible techniques[9-12] for temperature calibration, each of which has certain advantages and disadvantages. The method chosen in this study involves looking at the frequency difference between the two ^{1}H lines of methanol adsorbed onto tetrakis(trimethylsilyl)silane[13]. Because this method involves acquiring proton signals, it is extremely quick to carry out, and may be used upon all probes.

Each time the experimental temperature was changed, the sample was left at the new temperature for a quarter of an hour in order to ensure the whole of the sample had reached the new temperature.

3.2.3. SPECTROMETER OPTIMISATION

In order to obtain the best resolution and S/N possible, one must make sure that the spectrometer is set up optimally. Some procedures only need to be performed periodically as they are sample-invariant, whilst others must be carried out each time the experimental sample is changed. The two main procedures that should be performed each time the spectrometer is used are setting the shims[14] and the magic angle. The shims are a number of small electrical coils within the magnet body, the current in which may be varied to minimise magnetic field inhomogeneity over the entirety of the sample. They are generally optimised by minimising the line-width of the ^{1}H signal for PDMSO. The rotor angle was set to the magic angle by maximising the first-order quadrupolar rotational echoes in the ^{79}Br FID of solid KBr.

Each time the sample is changed, either bodily or with a change of temperature, it is necessary to re-tune the probe. This involves altering several variable capacitors within the probe in order to make sure that the impedances between the transmitter and probe and between the probe and pre-amplifier are matched[15]. This makes the power transfer to and from the probe as efficient as possible, maximising the signal obtained from the sample. The conductivity of the carbon sample made the RF circuits very difficult to tune exactly, thus decreasing the signal obtained from the experiment. One must also calibrate the transmitter powers to give a known angular nutation of the sample's magnetisation in a defined time. This was achieved by obtaining the signal null point corresponding to a nutation of 180^0 degrees. This procedure is more difficult for carbonaceous samples than in standard non-conducting powder samples.

3.2.4. PULSE SEQUENCES

The applicability of the huge variety of solid-state NMR pulse sequences to room temperature studies of these carbon-adsorbate systems is limited by the existence of substantial movement of the adsorbate molecules. This means that there is very little effective dipolar coupling between nuclei, and therefore cross-polarisation and complex solid-state techniques cannot be applied, and high power proton decoupling is not required. Thus the bulk of the spectra were acquired using only a single channel to excite the sample with no decoupling, in conjunction with slow (~ 0.8 kHz) MAS. Quadrature detection was employed. Experiments with more complex pulse sequences are described within the thesis at the appropriate point.

3.2.5. ACCURACY OF RESULTS

Chemical shifts within this study are generally referenced to the resonance of the pure liquid adsorbate, as the primary interest is in the changes occurring in the spectra upon adsorption onto the carbon adsorbent. All quoted relative chemical shifts between experiments are accurate within ± 0.1 ppm, whilst spectral measurements recorded during the same experiment may be considered to be accurate to within half that value. The measured peak areas during the course of an experiment (in both 1 and 2D experiments) are given in arbitrary units, accurate to within ± 1%. Wherever comparison is needed between different samples, the total intensity of each material is normalised. The measured linewidths are accurate to within ± 10 Hz. Errors in the other NMR parameters reported in the thesis are discussed within the appropriate sections of the thesis.

3.3. FURTHER SAMPLE COMPLICATIONS

3.3.1. THE EFFECT OF SAMPLE CONDUCTIVITY UPON EFFECTIVE RF PULSE STRENGTH

The conductive nature of the carbonaceous adsorbents used in this study creates several problems in examining the systems by NMR. It has already been noted that it is often difficult to tune the RF circuits within the probe when studying these samples. The problem is not too great in practice, as the tuning profile for the carbons is extremely broad and therefore the extent of the mistune is rarely very large. However, mistuning means that the transmitter power needed for an effective 90° pulse upon the sample is increased whilst the signal obtained is decreased. This is because the impedances of the transmitter and probe are not matched, so power transfer between the two is inefficient.

A more significant problem is the effect of conducting graphitic carbon areas in absorbing RF power input by the transmitter. The transmitter powers required to obtain defined pulse angles upon these samples may be up to 30% greater than those required for liquid adsorbates alone. This is independent of any tuning difficulties experienced with the sample. In experiments where accurate pulse calibration is critical, pulse power and duration cannot be set upon standard references but have to be set upon the actual sample. This can prove time consuming because of the poor S/N ratio obtained from the NMR experiments upon adsorbed systems and the relatively long ^{31}P T_1 relaxation time. The situation is complicated even further because the molecules are in a variety of positions upon the carbon adsorbent. Molecules will be affected less by the radio-frequency pulses if they are in close proximity to RF-absorbing graphitic carbon. The chemical shift also depends upon the distance between the adsorbate and the carbon surface, so it is found that, as the chemical shift decreases, the effective power of a radio-frequency pulse decreases also. For example, adsorbate molecules at 0 ppm are affected to a significantly greater extent by RF pulses than adsorbate molecules at the low-frequency end of the broad peak. This has been observed when trying to set a 180° pulse, as it was impossible to obtain a null signal at both ends of the spectrum simultaneously. As a consequence of this variation in RF pulse efficiency there will be a slight discrepancy in the total spectral intensity dependent upon the position of the adsorbate molecules upon the carbon surface. This means that in experiments that observe movement of adsorbate from one site to another, slight errors may be introduced into the measurement of the number of nuclei at each site. The variation in effective pulse power also makes it difficult to set pulse power and duration accurately, which can be critical in complex experiments.

The effect was studied by observing the effect of changing the pulse duration by 0.05 μs increments around a nominal 10 μs 180^0 pulse (Figure 3.3). The transmitter frequency was set in the centre of the spectrum at –5 ppm. As the effective pulse duration increases, the magnetisation of the adsorbate nuclei should nutate through an increasing angle. As this angle passes from one side of 180^0 to the other, the NMR signal should pass through a null point (as the magnetisation passes through the –z-axis) and then become negative. Nuclei experiencing larger effective RF pulse powers (towards the high-frequency end of the spectrum) would be expected to pass through the spectral null point at shorter pulse durations than nuclei in more heavily "shielded" environments. Figure 3.3 demonstrates that this is observed. After a pulse duration of 9.75 μs it is seen that all isochromats have precessed less than 180°, as the entire spectrum is still positive. As the pulse duration is increased to 9.85 μs, the peak at 0 ppm is no longer observed, as the isochromats forming this peak have precessed exactly 180°. As the pulse duration progressively increases, the broad peak intensity gradually becomes more negative, commencing at the higher frequency end. After 10.10 μs, the whole spectrum has become negative, as all isochromats have precessed well beyond 180°. When considered in conjunction with the conclusions reached in chapter 4, the experiment lends further credibility to the interpretation of the way in which the molecules' average proximity to the carbon surface is reflected in the spectrum of the adsorbate material.

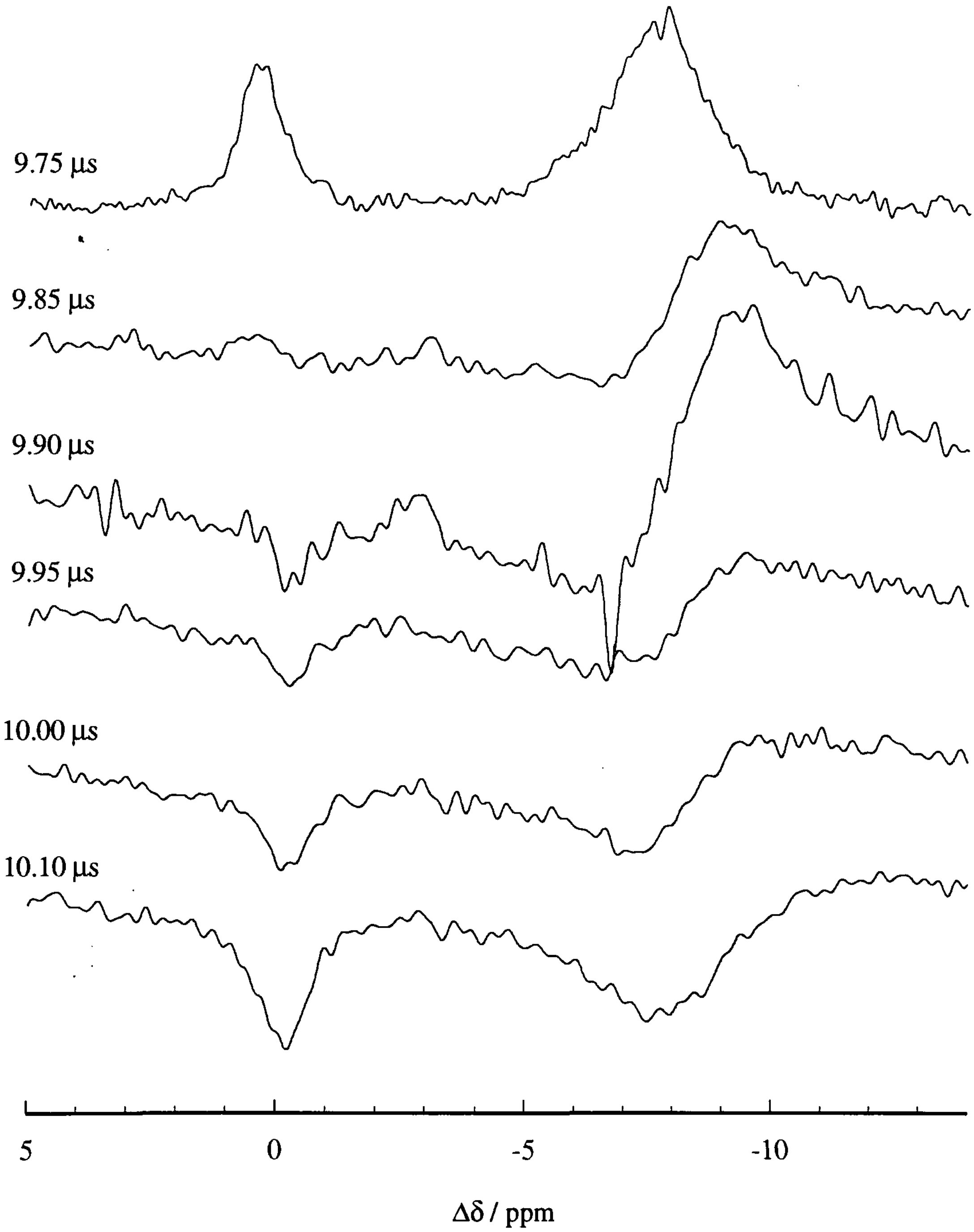

Figure 3.3. Variation in the spectrum obtained from a single-pulse experiment with pulse duration applied. The B_1 power used was approximately equivalent to a 5 μs $^{\pi}/_{2}$pulse. The sample was 75% w/w TMP upon SC2 carbon

3.3.2. THE EFFECT OF MAS UPON ADSORBATE DISTRIBUTION

Magic-angle spinning (MAS) is an essential technique in solid-state NMR experiments. The application of MAS at sufficient rates completely removes the broadening caused by shielding anisotropy. MAS may also remove the effect of weak heteronuclear dipolar coupling to protons, though this is often eliminated by using high-power decoupling at the proton frequency. The combination of techniques allows high-resolution dilute-spin spectra of solid samples to be obtained. The benefits of the application of MAS to the systems studied within this thesis can be seen clearly in Chapter 4. MAS is routinely performed at speeds of 7 kHz or greater and at these speeds there are enormous physical forces acting upon the sample. This is not a problem in solid materials, in which the nuclei are not free to move. However, the large extent of mobility present in the adsorbate / adsorbent systems means that the effect of the forces introduced by MAS upon the molecules must be considered. A series of single-pulse experiments, comparing the spectra recorded at a variety of spinning speeds, was performed on various samples. Spectra recorded for ^2H_2O upon SC2 carbon at a variety of spinning speeds are shown in Figure 3.4, whilst the variation in peak area with MAS rate for ^2H_2O upon SC2 carbon is shown in Table 3.1. No significant variation was noted in peak area distribution with TMP upon SC2 carbon as the MAS rate was altered.

The effect of spinning speed on each system depends upon the strength of the interaction between the carbon and the adsorbate molecule. Water, which generally yields a B.E.T. Type 3 isotherm upon graphite (occurring when the enthalpy of condensation is greater than the enthalpy of adsorption onto the carbon surface), is affected to a far greater extent than the phosphorus-containing materials. The organo-phosphorus materials bind more strongly to the carbon surface and yield Type 2 isotherms on graphite. The additional strength of interaction reduces the freedom of movement for these materials. This experiment demonstrates the importance of keeping MAS rates to the minimum necessary when studying these systems. Consequently, MAS rates over 1.5 kHz were rarely employed.

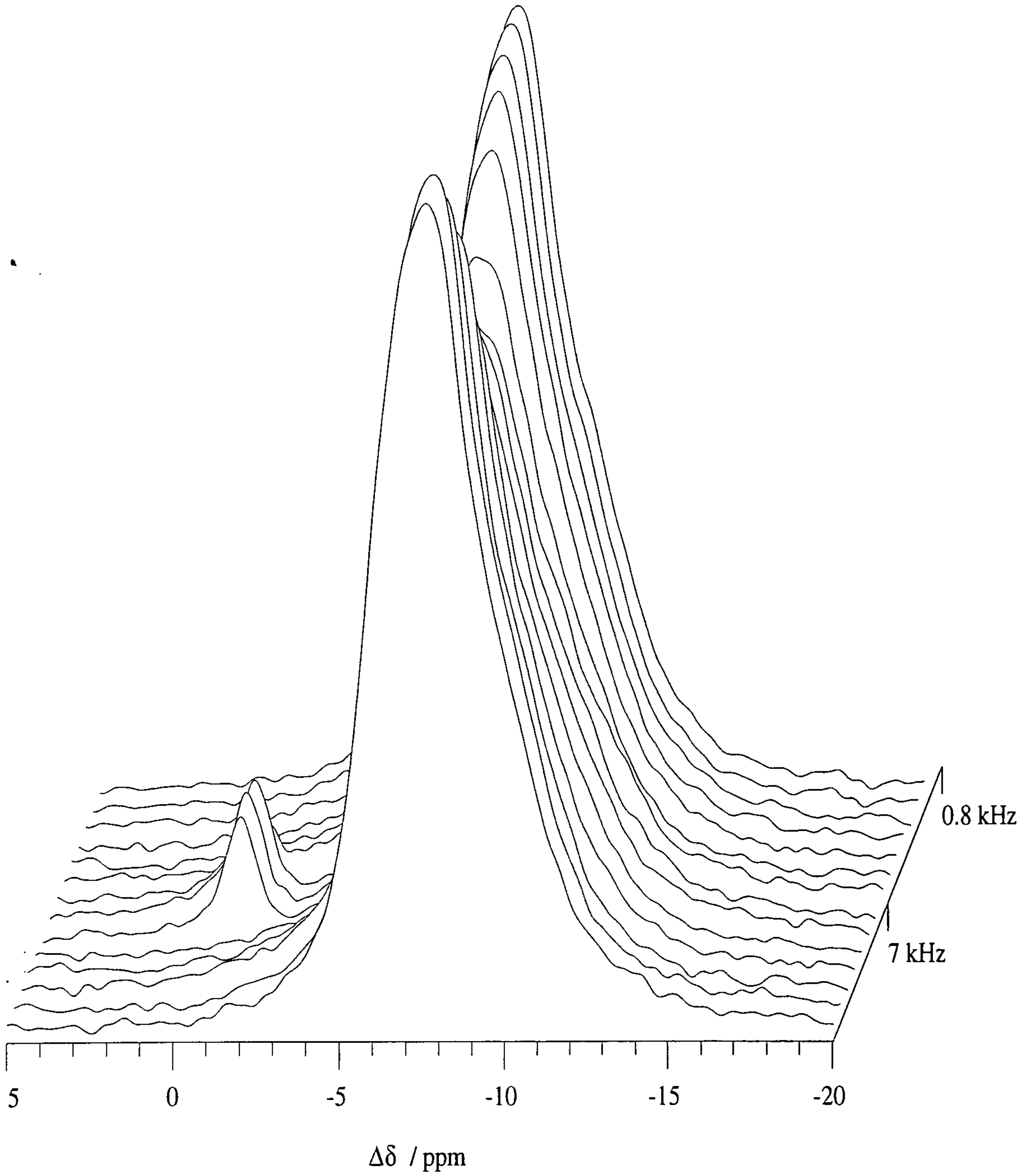

Figure 3.4. Variation in ^2H MAS spectra of 40% w/w deuterated water upon SC2 carbon. The y-axis shows spectra acquired at approximately 1 kHz intervals, increasing from 0.8 kHz to 7 kHz and then back to 0.8 kHz. Note the effect of MAS is competely reversible.

Spinning Speed / kHz	Low Frequency Peak Area	Unshifted Peak Area
0	20.2	0
1	20.1	0
2	19.9	0.4
3	19.7	0.5
4	19.7	0.6
5	19.0	1.2
6	18.6	1.6
5	19.1	1.2
4	19.6	0.5
3	19.8	0.3
2	20.2	0
1	20.3	0

Table 3.1. Variation in peak areas with MAS rate for ^2H spectra of 35% w/w D_2O upon SC2 activated carbon. The samples were left to equilibrate for 30 minutes at each spinning speed prior to acquisition. Note that the effect of MAS upon the spectrum is completely reversible.

3.4. REFERENCES

1. S. E. Meech, L. Pears, P. R. Norman, "*Carbon Surface Modification*", Poster presentation at British Carbon Group Conference on Current UK Research in Carbon, Universityof Loughborough, 16th September 1997
2. A. R. Brough, C. P. Grey, C. M. Dobson, *J. Am. Chem. Soc.*, **115**, 7318 (1993)
3. T. V. Thompson. Ph.D. Thesis, University of Durham (1995).
4. L. W. Beck, J. L. White, J. F. Haw, *J. Magn. Reson. A*, **99**, 182 (1992)
5. P. J. Giammatteo, W. W. Hellmuth, F. G. Ticehurst, P. W. Cope, *J. Magn. Reson.*, **71**, 14 (1987)
6. T. Bjorholm, H. J. Jakobsen, *J. Magn. Reson.*, **84**, 204 (1989).
7. A. Biliecki, D. P. Burum, *J. Magn. Reson. A*, **116**, 215 (1995).
8. T. Mildner, H. Ernst, D. Freude, *Solid State NMR*, **5**, 269 (1995).
9. L. C. M. van Gorkom, J. M. Hook, M. B. Logan, J. V. Hanna, R. E. Wasylishen, *Magn. Reson. Chem.*, **33**, 791 (1995).
10. G.-J. M. P. van Moorsel, R. Ernst, H. van Eck, C. P. Grey, *J. Magn. Reson. A*, **113**, 159 (1995)
11. B. Wehrle, F. Aguilar-Parilla, H.-H. Limbach, *J. Magn. Reson. A*, **87**, 584 (1990)
12. J. F. Haw, G. C. Campbell, R. C. Crosby, *Anal. Chem.*, **58**, 3172 (1986)
13. A. E. Aliev, K. D. M. Harris, *Magn. Reson. Chem.*, **32**, 366 (1994)
14. G. N. Chmurny, D. I. Hoult, *Con. Mag. Res.*, **2**, 131 (1990)
15. D. D. Traficante, *Con. Mag. Res.*, **1**, 73 (1989)

A 1D NMR STUDY OF A SINGLE ADSORBATE-ADSORBENT SYSTEM

Phosphorus-31 is regarded as a good nucleus on which to perform NMR experiments. It is a spin-$^1/_2$ nucleus, with 100% natural abundance and high receptivity, all of which enhance the S/N ratio obtainable from the NMR experiment. Given the inherent benefits of ^{31}P NMR, tri-methyl phosphate (TMP) was chosen as the adsorbate molecule for this study for several further reasons. The main reason was that tri-methyl phosphate is similar in structure to several of the phosphorus-based toxin molecules that the carbon filters may be exposed to when used in the field. This meant that the conclusions reached within this portion of the thesis would have a degree of practical applicability. Secondly, in order to simplify the interpretation of spectra acquired upon addition to carbon, a molecule that showed a single reasonably narrow line in the phosphorus spectrum of the material in its pure state was required. Finally, the TMP molecule is also reasonably small and will be able to explore the bulk of the porous volume of the carbon.

In order to discuss the adsorption of TMP within the pores of the activated carbon it is necessary to consider the relation between the PSD of the carbon and the size of the TMP molecule. The PSD results obtained for SC2 carbon via mercury porosimetry measurements were outlined in chapter 3. A variety of low energy conformations of TMP was studied using the Gaussian[11] and Cache[12] molecular modelling packages. The molecular volume and molecular diameters along a variety of axes were calculated for each of these conformers using an electron density envelope of 0.001 e bohr^{-3}. The calculations showed that each molecule of TMP has a volume of approximately 700 Å^3, whilst the various diameters of the molecule depend more critically upon the conformation. The lowest energy conformation found for the molecule is shown in Figure 4.1. In this case the molecule may be roughly approximated to a thick disc, 6 Å in diameter by 4 Å in depth. Whilst this is a crude model, it is certainly adequate when the assumptions made in determining a carbon PSD from mercury porosimetry data are considered. Comparison of these values with the mercury porosimetry data suggests that the TMP molecules can explore approximately 70% of the pore volume of SC2 carbon.

4.1. SPECTRA OF LIQUID TMP

Tri-methyl phosphate is a mobile liquid and the NMR spectrum obtained for the pure sample is unaffected by SA, dipolar coupling or quadrupolar coupling. This is because the interactions are averaged away by the rapid molecular re-orientation occurring within the liquid sample. In this case the only interactions that need to be considered are those of scalar coupling and the isotropic chemical shift. TMP has a single phosphorus nucleus per molecule and a single chemical shift is observed in the phosphorus spectrum, occurring at +2.4 ppm with respect to a standard reference of 85% H_3PO_4 at zero. The scalar coupling mechanism relies upon transmission of spin information between spin-active nuclei through the bonding electrons. In liquid TMP, there is $^3J_{P\text{-}C\text{-}O\text{-}H}$ spin-spin coupling of the phosphorus to nine equivalent protons, which should result in a decet in the ^{31}P spectrum. Indeed, this is what is observed on a well-shimmed solution-state machine[1]. However, upon the Chemagnetics CMX200 solid-state spectrometer, the resolution was insufficient to observe all the lines, and a single, broadened resonance was observed (Figure 4.2). The resonance was narrowed (from 60 to 32 Hz) with the application of proton decoupling. The proton spectrum of TMP acquired upon the Chemagnetics system proves more informative, as a doublet from each of the equivalent protons is observed, with the splitting caused by $^3J_{H\text{-}C\text{-}O\text{-}P}$ spin-spin coupling to phosphorus. The value of the spin-spin coupling constant, J, is 10.2 Hz. The splitting can be removed by continuously irradiating the sample at the phosphorus frequency during acquisition. In order to simplify discussion of the results obtained, the chemical shift of the phosphorus nucleus within pure liquid TMP has been taken to be zero throughout the current chapter. The results are more easily discussed in terms of a change in chemical shift, $\Delta\delta$, observed upon addition to the carbon adsorbent, rather than absolute chemical shifts.

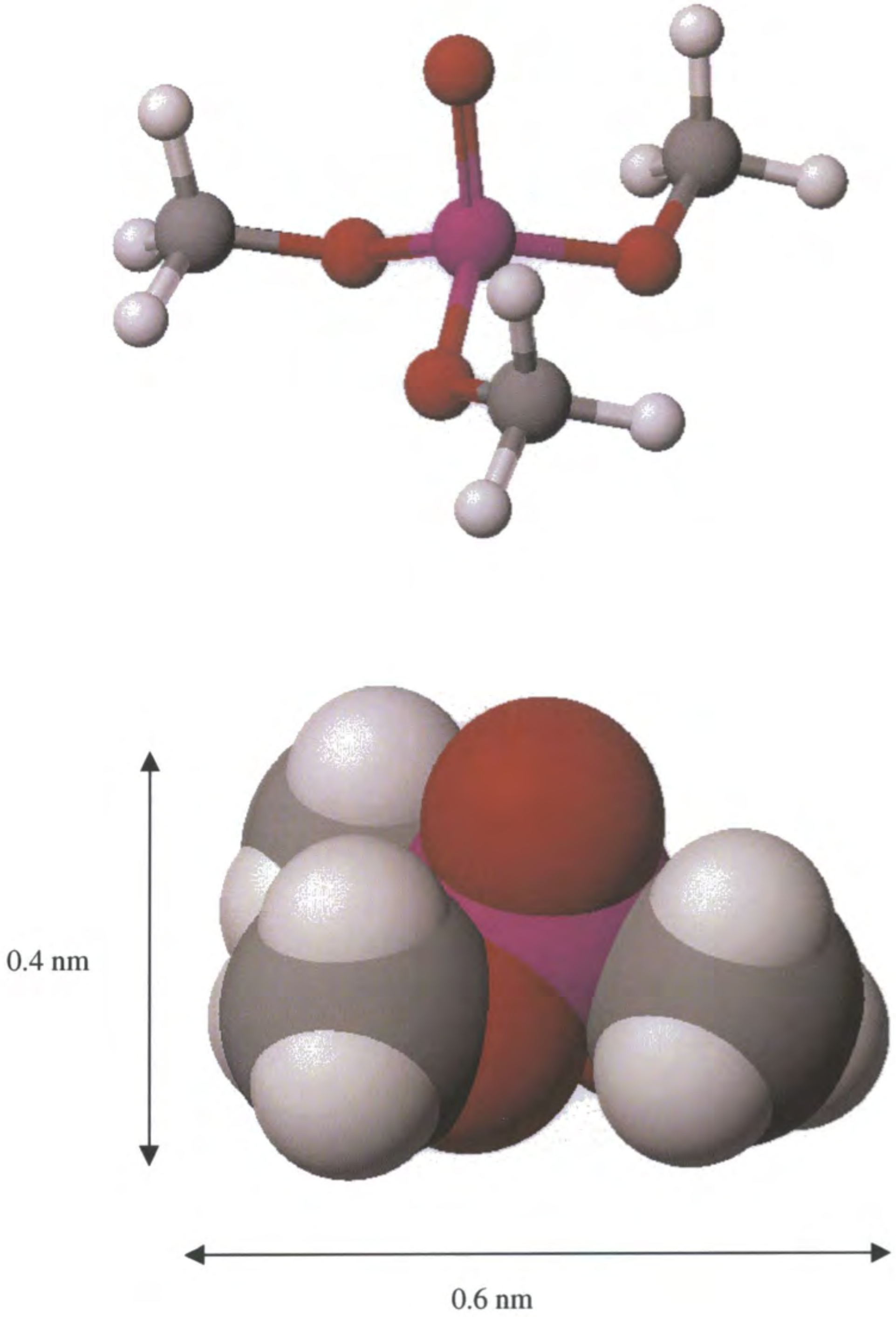

Figure 4.1. Calculated lowest energy conformation of a single tri-methyl phosphate molecule.

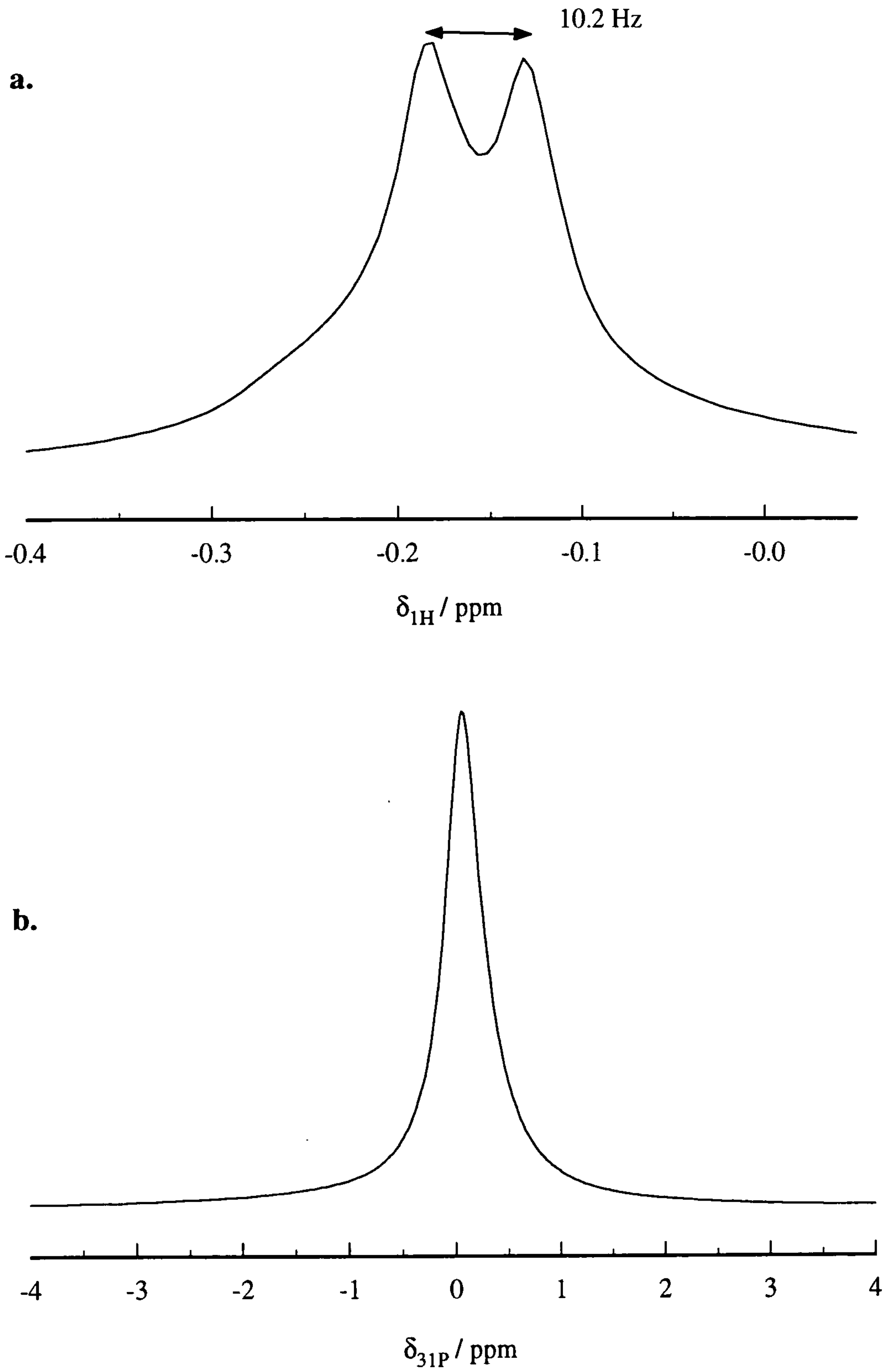

Figure 4.2. Spectra acquired for a sample of liquid TMP. a) ^{1}H spectrum b) ^{31}P spectrum

4.1.1. INTERACTION AVERAGING BY ISOTROPIC MOLECULAR MOTION

The rapid motion of the molecules within solutions means that over the acquisition period of the NMR experiment, the molecule explores a wide variety of random orientations with respect to the static magnetic field. Therefore the irreducible spherical tensor operators, $R_{l,m}$, within the internal Hamiltonians are evaluated over all orientations, which has an averaging affect on the interactions. This can be illustrated using the expression for the shielding Hamiltonian developed in Chapter 1.

$$\hat{H}_S = \gamma_n \sum_{l} \sum_{m=-l}^{l} (-1)^m R_{l,-m} T_{l,m} \qquad \textit{Equation 4.1}$$

It has been shown that all irreducible spherical tensor operators, $R_{l,m}$, $l > 0$, vanish when averaged over all orientations[2]. In chapter 1 the expression for the shielding Hamiltonian was expanded to give

$$\hat{H}_S = \gamma_n I_0 B_0 \left\{ \sigma_{iso} + \zeta \left(\frac{\left(3\cos^2\beta - 1\right) + \eta \sin^2\beta \cos(2\gamma)}{2} \right) \right\} \qquad \textit{Equation 4.2}$$

Integration between limits of 0 and 2π for both expressions within the brackets yields zero and therefore the entire anisotropic portion of the Hamiltonian disappears, leaving simply

$$\hat{H}_S = \gamma_n I_0 B_0 \sigma_{iso} \qquad \textit{Equation 4.3}$$

The dipolar Hamiltonian has a similar form to that of the shielding Hamiltonian and again the various $R_{l,m}$ trigonometric expressions within the expansion all cancel to zero. In addition to this, the dipolar tensor is traceless in the PAS and therefore the R_{00} term is also equal to zero. This means that the entire Hamiltonian becomes zero and no dipolar coupling (either inter- or intra-molecular) is observed at all in spectra of mobile liquids and solutions.

4.2. SPECTRA OF ADSORBED TMP UPON SC2 CARBON

4.2.1. THE SINGLE PULSE EXPERIMENT

4.2.1.1. Experimental Procedure

The experimental method for these experiments was extremely simple. In each case, the samples were left to equilibrate for 2 hours prior to acquisition. A 5 μs 90° pulse was applied with a recycle delay of 8 seconds. 256 transients were recorded and no proton decoupling was applied. The FIDs were processed in an identical manner for each sample, and analysed using the deconvolution algorithms provided within the Spinsight software.

Because the total peak envelope observed consists of more than one peak, deconvolution is required in order to evaluate the areas, chemical shifts and linewidths of each constituent peak. Reasonable agreement was attained (an R^2 value of < 0.01 for the experimental data and the sum of the calculated peaks) by modelling the underlying peak shapes as being 50% Gaussian and 50% Lorentzian in nature. There is no explicit theoretical reason for modelling the peaks in this manner and the ratio of the two functions used for the fitted model was optimised manually. The static spectrum envelope was assumed to be made up of two peaks, and this was corroborated by the results of later MAS experiments. A typical example of a deconvolved spectrum, showing the two peaks calculated to comprise the overall lineshape and a residual error function, is shown in Figure 4.3. For these samples the deconvolution procedure is an approximation because (as will be shown later) the deconvolved low-frequency peak is itself a superposition of a large number of component peaks and cannot be properly described by a single mathematical function. The plot of residual errors in Figure 4.3 shows that the greatest inaccuracies in the deconvolved spectra occur in the fitting of the composite broad peak. The spectral parameters obtained for the low-frequency peak are considered a "weighted mean" of the parameters of each of the peaks comprising the overall broad peak.

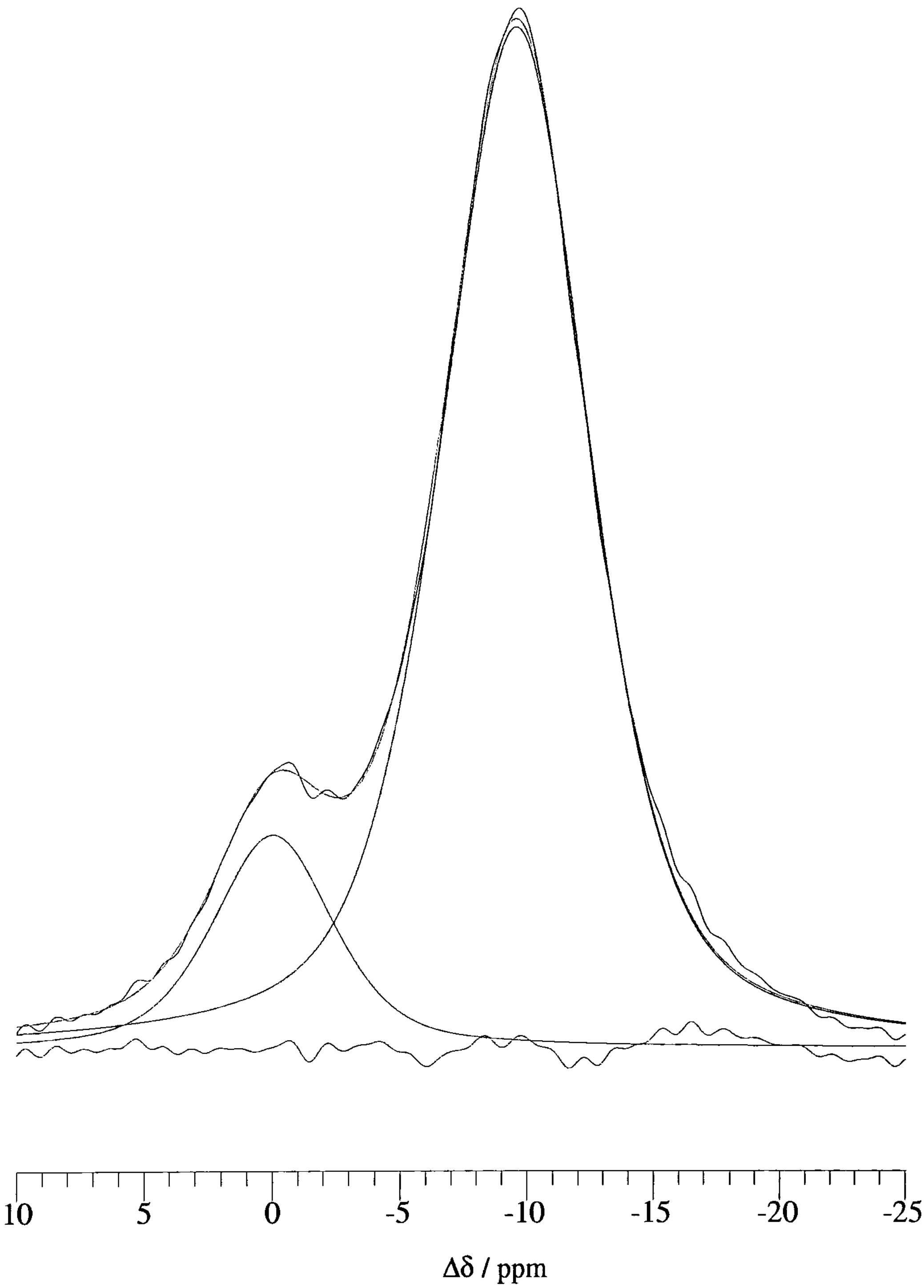

Figure 4.3. Static single pulse spectrum of 40% w/w TMP upon SC2 carbon (black). The two peaks comprising the fitted envelope (red) are shown in blue. The residual error function of the fitting procedure is shown in green

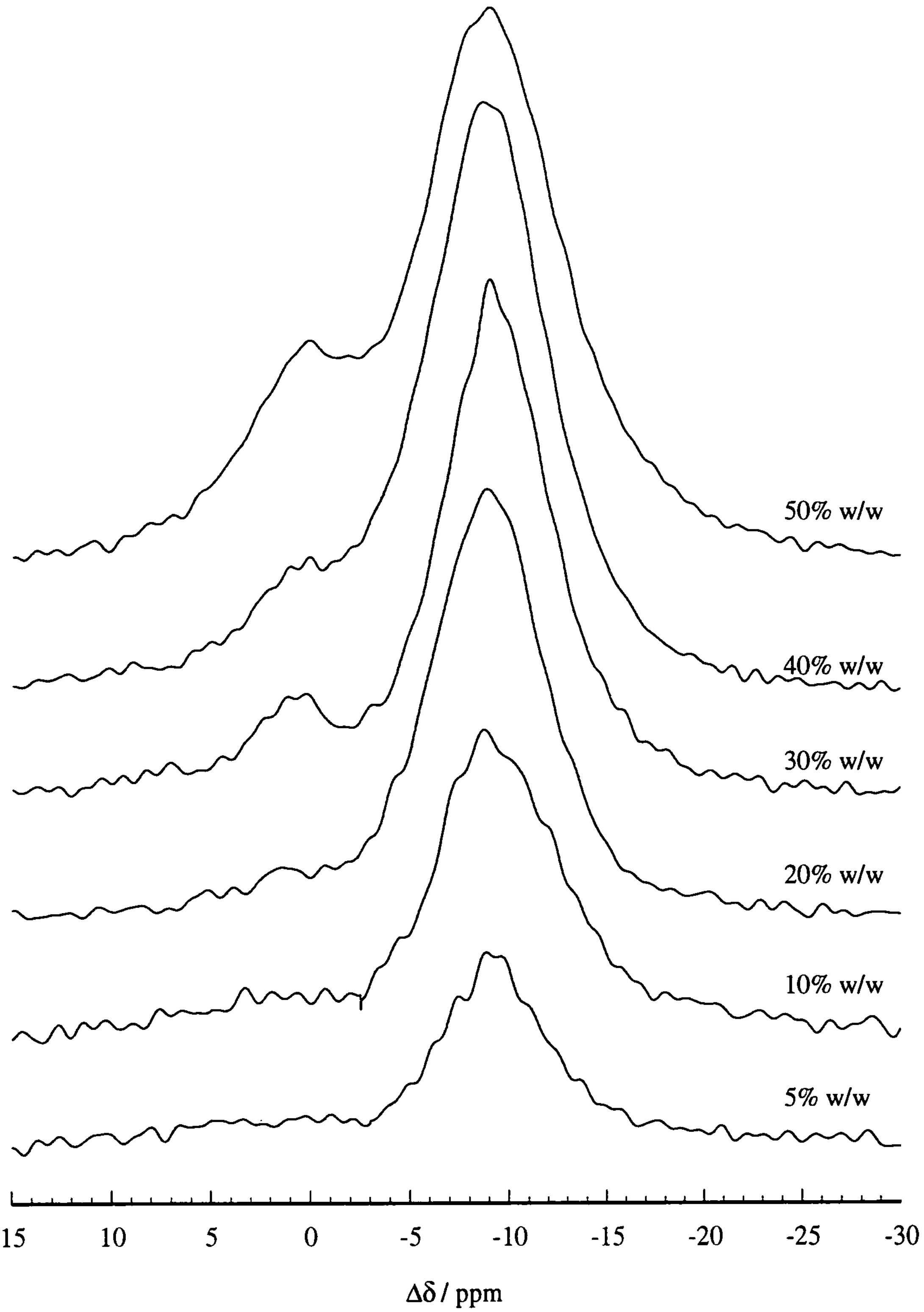

Figure 4.4. Static single-pulse spectra acquired for a variety of TMP loadings upon SC2 carbon.

4.2.1.2 Experimental Results

Clearly the addition of TMP to activated carbon alters the TMP phosphorus spectrum enormously (Figure 4.4). The single narrow line seen for the liquid sample is broadened extensively (from ~40 Hz for the liquid adsorbate to ~500 Hz for the adsorbed material) and experiences a large low frequency shift ($\Delta\delta \approx$-9.5 ppm). The area of the overall peak increases with the amount of adsorbate material added to the system, though there is not an exact correspondence between the two values. This is because of intensity complications introduced by the presence of the adsorbent graphene sheets. The relation between the peak integrals and the amount of adsorbate added to the system is shown in Table 4.1.

Exact Load	**Peak I Area**	**Peak II Area**	**Total Peak Area**
5.1 %	27.1	-	27.1
9.9 %	54.7	-	54.7
20.1 %	108	1.5	110
30.1 %	155	9.9	165
40.0 %	195	24.6	220
49.8 %	210	68.7	279

Table 4.1. Variation in deconvolved peak areas (in arbitrary units) obtained from static spectra with the amount of TMP added to SC2 carbon.

The chemical shift of peak I varies with adsorbate loading, the shift to low frequency becoming less pronounced as the amount of adsorbate in the system increases. At higher loadings (>25% w/w) a further peak, peak II appears in the spectrum. This occurs at a position essentially the same as that of pure TMP, and it too is broadened with respect to the liquid signal. As the amount of adsorbate material added increases further, both peak areas increase and the two peaks start to overlap one another. Thompson[10] has shown that as the amount of adsorbate added continues to increase beyond 60 to 70% w/w, a much greater proportion of the material enters peak II, whilst peak I appears to have a finite maximum size.

The width of the lines within the spectrum also vary with loading, and the chemical shift and line width of each line as a function of the amount of adsorbate added to the carbon are presented in table 4.2.

Load	**Peak II**		**Peak I**	
	$\Delta\nu_{half}$ / Hz	**$\Delta\delta$ / ppm**	**$\Delta\nu_{half}$ / Hz**	**$\Delta\delta$ / ppm**
5 %	-	-	420	-10.1
10 %	-	-	480	-9.6
20 %	500	0	490	-9.3
30 %	460	0.2	530	-9.0
40 %	340	0.1	530	-9.0
50 %	360	0.0	510	-8.8

Table 4.2. Variation in deconvolved peak chemical shift and width obtained from static spectra with the amount of TMP added to SC2 carbon

4.2.1 SINGLE PULSE EXPERIMENT WITH PROTON DECOUPLING

4.2.2.1. Averaging in spin-space

The averaging effect of time dependence upon interaction Hamiltonians has already been shown in the narrow lines attainable by solution-state NMR. In that case, time dependence is introduced into the internal Hamiltonians through the $R_{l,m}$ spin parameters. This is known as averaging in co-ordinate space and occurs through physical motion of the molecules and nuclei being studied. Magic-angle spinning provides another example of co-ordinate space averaging. An alternative way to average interaction Hamiltonians is to make the $T_{l,m}$ spin operators time dependent. This is done by applying pulse sequences that affect the spin system and cause the direction of magnetisation to change. All decoupling pulse sequences are examples of this "spin-space" averaging. The effect of irradiating abundant (S) spin nuclei during acquisition of dilute (I) spin spectra is discussed below. Within the solid state, high-power proton decoupling (HPPD) at a single frequency is usually sufficient to remove the coupling between the nuclei of study and all protons within the sample. This is because flip-flop fluctuations within the proton spin bath cause the irradiation to be spread over all the protons irrespective of their resonance frequency. This is not the case in solutions where homonuclear dipolar coupling between the protons is averaged by the molecular motion. More complex decoupling techniques are generally required to fully remove the heteronuclear coupling between each of the protons and the target nuclei. Proton decoupling is explored within this section of the thesis as a means of obtaining narrower lines for adsorbates upon activated carbon. The motion of the adsorbates upon the carbon surface meant that homonuclear proton dipolar coupling was possibly not sufficient to ensure all protons within the sample were excited by HPPD. Thus the narrowing introduced by more complex "solution-state" techniques upon the samples was also explored.

4.2.2.2. Decoupling Pulse Sequences

Heteronuclear decoupling aims to ensure that the spin system evolves under the influence of an effective internal Hamiltonian that no longer includes the heteronuclear dipolar coupling Hamiltonian as part of it. It has long been known that the coupling may be removed by irradiating the sample with a second linearly polarised r.f. field during acquisition. The effective Hamiltonian in this situation is

$$\hat{H}_{eff} = \hat{H}^{I}{}_{Z} + \hat{H}^{S}{}_{Z} + \hat{H}_{D(IS)} + H^{S}{}_{rf} \qquad \textit{Equation 4.4}$$

In order to consider the effect of "off-resonance" decoupling, the S-spin Zeeman Hamiltonian is partitioned into an on-resonance and a correction term. Using the definitions from chapter 1

$$\hat{H}_{eff} = -\omega_{0(I)} I_Z - S_z\left(\omega_{0(S)} + \Delta\omega\right) - \gamma_S B_2 \cos\omega_2 t + \hbar\gamma_I\gamma_S \sum_{i,k} D^{ik}{}_{zz} I_z^{\,i} S_z^{\,k} \qquad \textit{Equation 4.5}$$

The Hamiltonians can be calculated and treated more conveniently in a frame of reference rotating with the spins. This representation, denoted by the subscript R, is introduced by pre- and post-multiplying the total spin Hamiltonian by the evolution operators of the Zeeman and the B_2 Radio-frequency Hamiltonian.

The B_2 field is applied along the x-axis.

$$\hat{H}_{eff,R}(t) = U^{S}{}_{rf}{}^{-1}(t) U_Z{}^{-1}(t) \hat{H}_{\mathrm{int}} U_Z(t) U^{S}{}_{rf}(t)$$

where

$$U^{S}{}_{rf} = \exp(i\omega_2 S_x t)$$

$$U_Z = \exp\left(i(H_Z{}^{I} - \omega_{0(S)} S_z)t\right) \qquad \textit{Equations 4.6}$$

In this (rotating-I, doubly rotating-S) frame, the Zeeman terms and the on-resonance decoupling terms disappear leaving an effective, time dependent, Hamiltonian.

$$\hat{H}_{eff,R}(t) = \hbar\gamma_I\gamma_S \sum_{i,k} D^{ik}{}_{zz} I_z{}^{i}\left(S_z{}^{k}\cos\omega_2 t - S_y{}^{k}\sin\omega_2 t\right) - \left[\Delta\omega\left(S_z\cos\omega_2 t - S_y\sin\omega_2 t\right)\right]$$

Equation 4.7

This effective Hamiltonian has a periodicity of $2\pi/\omega_2$ (i.e. the various rotations return the S-spin operators to their original position at each multiple of this time) and can be conveniently described using Average Hamiltonian Theory[2, 16]. The central result of the average Hamiltonian theory states that a spin-system subject to cyclic, external forces behaves as if it were developing according to a constant Hamiltonian, F. The constant Hamiltonian may be approximated via the time average of $H_{\mathrm{eff,\,R}}(t)$, often termed $\overline{H}^{(0)}$, and an infinite series of progressively smaller corrections, $\overline{H}^{(n)}$. Usually the corrections rapidly converge to zero, meaning that the series needs only to be considered to the second or third term.

It is sufficient to calculate the behaviour of the system over the complete cycle in order to define it for all times. In this case the time average of the effective Hamiltonian disappears completely over long decoupling periods, independent of frequency offset or the B_2 field intensity. However, evaluation of the first correction term shows that the efficiency of heteronuclear dipolar coupling is dependent upon these parameters. For the current situation, with just one I nucleus per molecule, the first correction term for I spin spectra is equal to

$$\overline{H}^{(1)} = -\frac{\Delta\omega}{\omega_2}\sum_{i,k}\hbar\gamma^{I(i)}\gamma^{S(k)} D^{ik}{}_{zz}\cdot I^{i}{}_{z} S^{k}{}_{x} \qquad \textit{Equation 4.8}$$

The second correction term shows that if the B_2 field is precisely on resonance, there is still a (much smaller) residual broadening effect, which is reduced as the B_2 field strength is increased. In samples with strong S-spin homonuclear dipolar coupling the problem of frequency offset is not as great as would be predicted because of flip-flop fluctuations between the S spins, which effectively "smears" the decoupling frequency over the entirety of the abundant spin frequency range. Off-resonance effects are reduced and more efficient decoupling than that predicted occurs. However, in the majority of situations encountered, the variation in chemical shift of the abundant spin resonances means that the $\overline{H}^{(1)}$ term is by far the most important in evaluating the effect of decoupling upon the I spin spectra. One strategy for minimising this term is merely to increase B_2, but experimental limitations on the power that may be applied to the sample mean that this approach is limited in scope.

An alternative approach is to use complex decoupling sequences that are more "robust" to decoupling frequency offset. These more complex "broadband" pulse sequences are based upon composite pulses[18, 19]. The pulses are a train of contiguous or near-contiguous radiofrequency pulses with different phases. The pulse train emulates the effect of a single, simple pulse, but has a compensatory mechanism that renders it less sensitive to experimental imperfection (including resonance-offset effects). It was quickly realised that the composite pulse could be applied to the problem of developing a broad band decoupling scheme[20]. The authors found that the average Hamiltonian, $\overline{H}^{(0)}$ could be made equal to zero by replacing the continuous irradiation by four successive pulse sequences, R R R′ R′ provided that R accurately inverts longitudinal magnetisation over the frequency range of interest, as for example with R = $90_x180_y90_x$. R′ is similar except that it employs pulses shifted in phase by π radians with respect to R. In other words

$$RI_ZR^{-1} = -I_Z \qquad R' = R_{-Z}(\pi)RR_Z(\pi) \qquad R_Z(\pi) = \exp(i\pi I_Z)$$

The pulse sequence, R R R′ R′, was termed the M-LEV4 cycle after the principal author of the paper, Malcolm Levitt. The authors developed an expression for the average Hamiltonian for an isolated spin pair during the application of each composite R pulse.

If the duration of each of the four elements of the cycle is denoted t, the average Hamiltonian for the first time element can be written as

$$h^{(0)} = \hbar\gamma_I\gamma_S D_{ZZ} I_Z \frac{1}{t}\int_0^t \left(S_Z{}^k \cos\omega_2 t - S_y{}^k \sin\omega_2 t\right) - \Delta\omega\frac{1}{t}\int_0^t \left(S_Z{}^k \cos\omega_2 t - S_y{}^k \sin\omega_2 t\right)$$

Equation 4.9

Over the full cycle time of 4t the average Hamiltonian becomes

$$\overline{H}^{(0)} = \frac{1}{4}\left\{h^{(0)} + R^{-1}h^{(0)}R + R^{-1}(R')^{-1}h^{(0)}R'R + R^{-1}(R')^{-1}(R')^{-1}h^{(0)}R'R'R\right\}$$

Equation 4.10

Using the relation between R and R′ above, and the property that $R^2 = 1$, the authors showed that $\overline{H}^{(0)}$ is equal to zero, as in the application of continuous wave decoupling. In addition the decoupling is far more effective over a greater range of frequencies due to the properties of the composite pulses comprising the decoupling sequence.

However, even composite pulse sequences cannot invert longitudinal magnetisation perfectly across the entire proton frequency range, and incompletely averaged magnetisation is left over, which prevents the sequence being truly cyclic. This limits the efficiency of the decouping[22]. The basic MLEV-4 sequence can be improved by successively employing 180° phase shifts to cancel out any residual transverse components that arise by reversing the spin operator rotations to take the transverse components back to their initial positions. In addition the sequences are also permuted cyclically to average the z-components of the residual magnetisation. This leads to the build up of progressively superior decoupling sequences[24] such as MLEV-16 (RRR′R′ R′RRR′ R′R′RR RR′R′R) and MLEV-64. As the iterative build-up continues, the decoupling becomes more effective, but the period of the cycle increases until the periodic time constraint can no longer be met.

Waugh[22] demonstrated that a permutation of the pulse sequence does not have to involve moving the order of entire composite pulses, but may involve the permutation of single pulses. A typical 90° pulse removes most of the z-component magnetisation extremely effectively over a reasonably broad range of frequencies, and this means that only the residual z-components after the 90° pulse is applied then need to be averaged for decoupling to occur. This was the method adopted to develop the WALTZ series of pulse sequences[23]. Of these sequences, WALTZ-16 is most commonly used. It possesses excellent decoupling characteristics over a bandwidth of $\pm(\gamma B_2/2\pi)$, and is much less reliant upon accurate pulse-phase setting than the equivalent MLEV sequence[21].

4.2.2.3. Experimental Procedure

Spectra for various samples were recorded sequentially in three different ways. Firstly, the spectra were recorded without decoupling, as in section 4.2. After that the spectra were recorded with 50 kHz continuous-wave proton decoupling (equivalent to a 5 μs ^{1}H 90° pulse duration), whilst the other experimental parameters were kept the same. Lastly, spectra were recorded with WALTZ-16 multiple pulse decoupling. Experimental limitations meant that the WALTZ decoupling power was limited to 10 μs ^{1}H 90° pulse durations. In both cases the proton frequency was set at the resonance of the signals arising from the adsorbate in the proton spectrum. The spectra were again analysed using the deconvolution package within Spinsight.

4.2.2.4. Experimental Results

Figure 4.5 shows two example static spectra (of 50% w/w TMP upon SC2) acquired under different decoupling regimes. The lower spectrum was acquired with continuous-wave proton decoupling whilst the top spectrum was recorded with WALTZ-16 decoupling. Comparison of the bottom spectrum with that acquired in the absence of proton decoupling (Figure 4.4) shows that the continuous wave decoupling has a negligible effect. Though the effect is still not pronounced, the upper spectrum has been narrowed slightly with respect to the other two, and the resolution of the two peaks is increased slightly. The FWHM linewidths obtained via deconvolution for each spectrum are given in table 4.3.

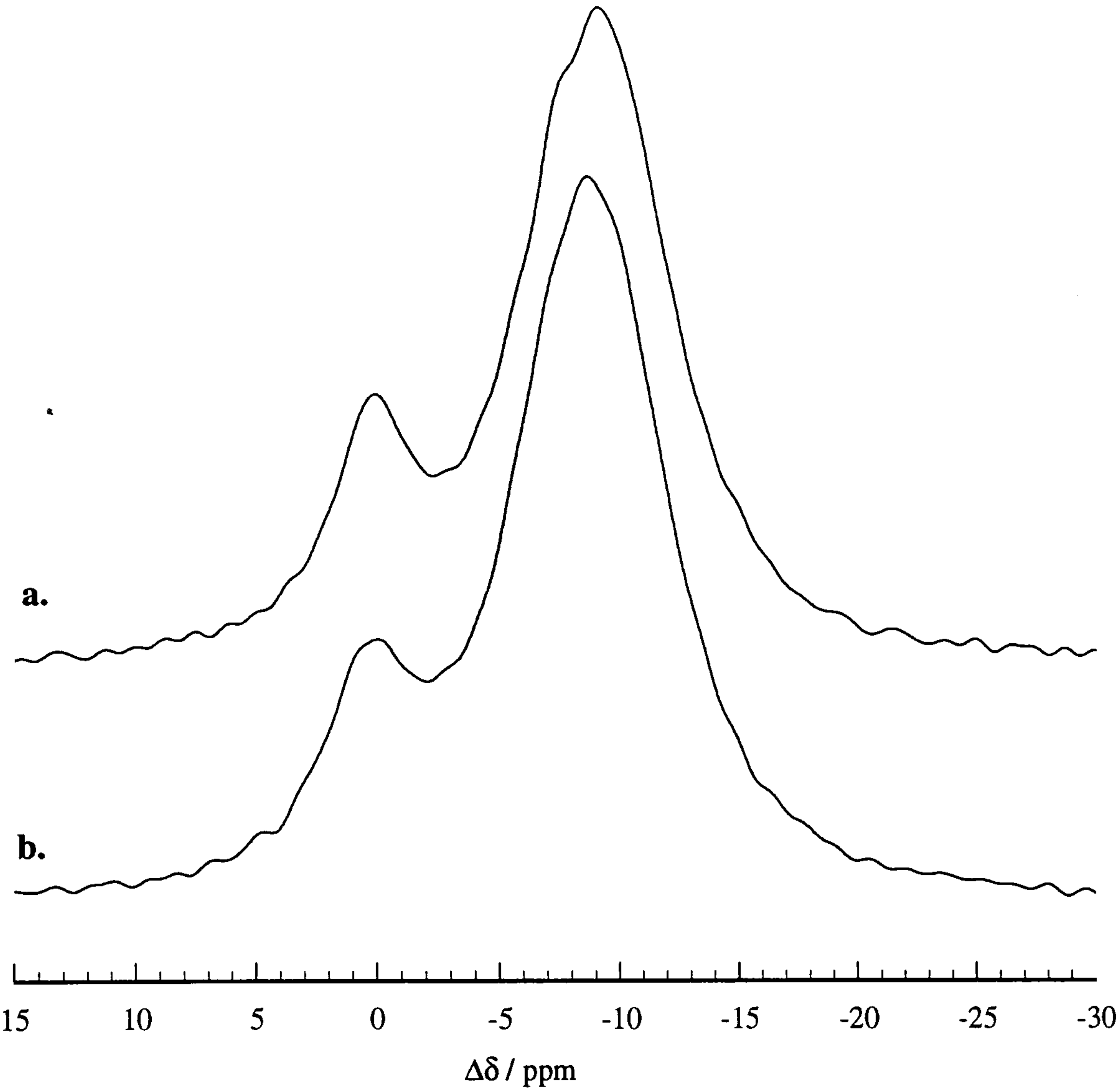

Figure 4.5. Static ^{31}P spectra of 40% w/w TMP upon SC2 carbon. a) with WALTZ-16 proton decoupling b) with 50 kHz continuous wave proton decoupling.

Decoupling Technique	**Peak I width / Hz**	**Peak II width / Hz**
No decoupling	590	360
CW decoupling	600	340
WALTZ-16 decoupling	560	320

Table 4.3. Comparison of static peak widths for a variety of decoupling pulse sequences applied to 50% w/w TMP upon SC2 carbon.

4.2.3. MAGIC-ANGLE SPINNING SINGLE PULSE EXPERIMENT

4.2.3.1. Interaction Averaging by MAS

Solution-state spectra exhibit narrow lines because rapid molecular motion averages the spin operators of the anisotropic chemical shift and dipolar interactions. In solid samples a similar spatial averaging may be achieved by mechanically rotating the sample about an axis inclined at the magic angle (β = 54.7°) relative to the static magnetic field. The technique was first demonstrated by Andrew et al.[3] and Lowe[4] who realised that the second-rank spin interactions (such as heteronuclear dipolar coupling and SA) could be eliminated by macroscopic sample rotation. The effect of MAS can be demonstrated using the standard expression for the sample-frame shielding Hamiltonian.

$$H_{SA} = \gamma_n T_{00}\rho_{00} + \gamma_n T_{20}\sum_{m'} D^2{}_{m',0}(\alpha,\beta,\gamma)\rho_{2m'} \qquad \textit{Equation 4.11}$$

For a sample undergoing macroscopic rotation the sample frame and laboratory frame no longer coincide. Calculating the shielding Hamiltonian for a sample undergoing MAS requires another, time-dependent, Wigner rotation in order to convert the rotating sample frame to that of the laboratory axis system.

$$H_{SA} = \gamma_n T_{00}\rho_{00} + \gamma_n T_{20}\sum_{m'} D^2{}_{m',0}(0,\beta'',\omega_r t)\sum_{m''} D^2{}_{m'',m'}(\alpha,\beta,\gamma)\rho_{2m''} \qquad \textit{Equation 4.12}$$

In the second rotation, the first Wigner angle is zero because the Hamiltonian is unaffected by a rotation about $\mathbf{B}_0$. β'' is the angle between the rotor axis and $\mathbf{B}_0$, and $\omega_r t$ describes the azimuth of the rotor fixed axis with respect to $\mathbf{B}_0$. The second Wigner rotation matrix elements all have a dependence upon $\exp(im'\omega_r t)$ and this term may be factored out of the equation.

$$H_{SA} = \gamma_n T_{00}\rho_{00} + \gamma_n T_{20}\sum_{m',m''} e^{-im'\omega_r t} D^2{}_{m',0}(0,\beta,0) \times D^2{}_{m'',m'}(\alpha,\beta,\gamma,t)\rho_{2m''} \qquad \textit{Equation 4.13}$$

If the assumption that the spinning rate is infinite is made, the terms (m'≠0) all disappear and the Hamiltonian simplifies to

$$H_{SA} = \gamma_n T_{00}\rho_{00} + \gamma_n T_{20}\sum_{m'} D^2{}_{0,0}(0,\beta,0) \times D^2{}_{m',0}(\alpha,\beta,\gamma)\rho_{2m'}$$

$$\hat{H}_{SA} = \gamma_n\left(T_{00}R_{00} + \frac{1}{2}\left(3\cos^2\beta' - 1\right)T_{20}\sum_{m'} D^2{}_{m',0}(\alpha,\beta,\gamma)\rho_{2m'}\right)$$ *Equation 4.14*

In practice, the spinning speed applied only needs to be greater than the static broadening caused by the interaction. If the angle between the rotor and the static magnetic field, β', is chosen to be the magic angle, so that $3\cos^2\beta' = 1$, the anisotropic part of the shielding tensor is eliminated and we are left with an identical expression to that obtained for the solution-state shielding Hamiltonian.

$$\hat{H}_{SA} = \gamma_n I_0 B_0 \sigma_{iso}$$ *Equation 4.15*

A similar consideration for the heteronuclear dipolar interaction between an isolated spin pair demonstrates that the dipolar Hamiltonian is averaged by MAS in an identical way, though because the dipolar tensor is traceless, the R_{00} term is zero and the dipolar Hamiltonian disappears completely.

4.2.3.2. Spinning sidebands

In practice, the spinning speed is often not as great as the interaction static linewidth and it becomes necessary to consider the additional exponential terms within the shielding Hamiltonian and their effect upon the spectrum. It is found that there is a contribution from the m' terms, which appear as echoes within the FID at intervals of time equal to the rotor period. Fourier transformation yields a MAS spectrum composed of a sharp peak at the isotropic chemical shift, flanked by a set of "spinning sidebands" spaced at integral multiples of ω_r. A more quantitative analysis of spinning sideband patterns has been performed by Maricq and Waugh[5]. The sidebands occur because shielding is an inhomogenous interaction, meaning that the Hamiltonian commutes with itself at all times and can therefore be averaged to some degree even if the rotation frequency is less than the magnitude of the interaction. During each rotor period crystallites in the sample traverse a range of frequencies with an average frequency equal to that of the isotropic chemical shift. At the completion of each rotor period, the magnetisation evolution due to the interactions is totally recovered and a train of "rotational echoes" is observed in the time domain FID.

4.2.3.3. MAS in the presence of slow molecular motion

In samples with an intermediate amount of molecular motion, the movement of the nuclei is not described solely by a rotation about the magic angle. The averaging is complicated by interference between the frequency of nuclear motion and the MAS rate, which results in incomplete spatial averaging of the interaction Hamiltonians. Abragam[6] has developed a description of the density matrix describing the evolution of a spin system subject to a perturbation that is a random function of time. This has been applied to the effect of MAS upon the SA broadening exhibited by molecules undergoing slow molecular motion by Waugh et al.[7].

The calculation commences from the standard sample spinning shielding Hamiltonian. The motion of the molecules means that the angles α, β and γ all become time dependent. Using Abragam's description for the density matrix of a perturbed ensemble of spins, an equation of motion analogous to the Bloch equations, describing the signal decay in the transverse plane, was developed. From this the residual linewidth as a function of MAS rate and molecular correlation time was expressed.

Abragam's equation of motion for the spin density matrix is written as

$$\frac{d\rho}{dt} = -\int_0^\infty \left\langle \hat{H}(t), \hat{H}(t-\tau), \rho \right\rangle_{av} d\tau \qquad \text{Equation 4.16}$$

The authors substituted the expressions for the two Hamiltonians, with H(t) being indexed by (m′, m″) and H(t-τ) by (n′, n″), separated the spin and spatial portions of each Hamiltonian and put the equation into a form analogous to that of the Bloch equations by taking the trace of both sides with the observable I_+.

$$\left\langle \frac{dI_+}{dt} \right\rangle = -\left[T_{20},\left[T_{20},I_+\right]\right] \times \int_0^\infty \left\langle f(t)_{m',m'} \cdot f(t-\tau)_{n',n'} \right\rangle_{av} d\tau \qquad \textit{Equation 4.18}$$

The spin and spatial parts of this expression were then expanded and evaluated. Waugh et al. defined the motion as an isotropic diffusive Gaussian-Markoff process, and a calculated value of T_2 in terms of the MAS rate and the correlation time for the motion was finally obtained.

$$\frac{1}{T_2} = \frac{1}{15}\omega_0^2\zeta^2\left(1+\frac{\eta^2}{3}\right)\left(\frac{\tau_c}{1+4\omega_r^2\tau_c^2}+\frac{2\tau_c}{1+\omega_r^2\tau_c^2}\right) \qquad \textit{Equation 4.17}$$

The authors assumed that the molecular motion of the molecules would result in a Lorentzian lineshape, and plotted linewidth against MAS rate for a variety of molecular motional rates. Figure 4.6 plots the calculated linewidth against molecular motion correlation time for a variety of MAS rates. The important conclusion to be drawn from this calculation is that there are two regimes of line narrowing. One is the so-called strong collision limit ($\omega_r\tau >> 1$) where there is coherent spatial averaging caused by MAS. The other regime is the weak collision area ($\omega_r\tau << 1$) where there is incoherent averaging caused by the random molecular motion within the sample. In areas of intermediate motion between these two limits, the two effects interfere destructively resulting in incomplete averaging of the interactions, and a larger residual line-width.

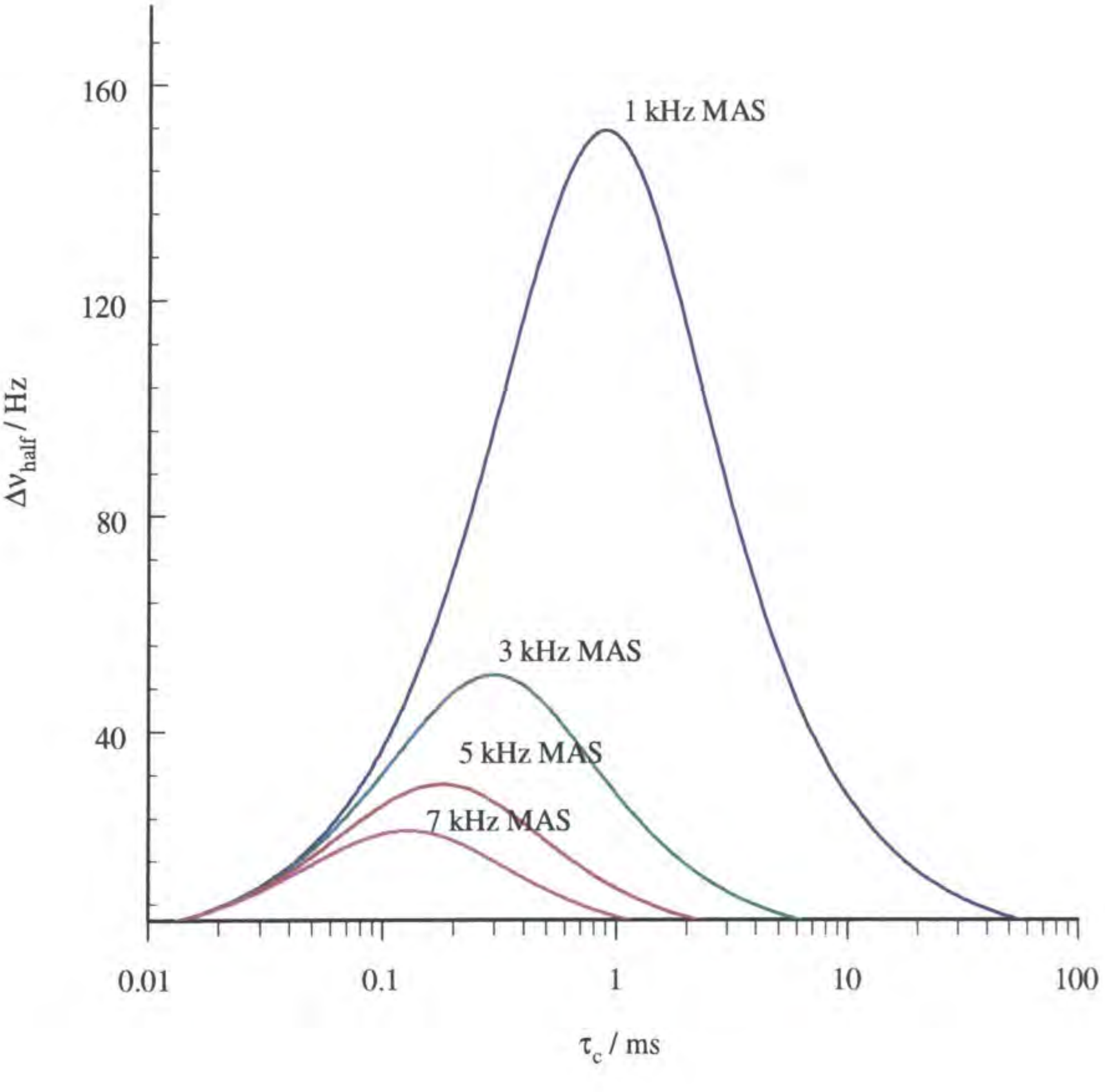

Figure 4.6. Graph plotting the calculated NMR linewidth due to shielding anisotropy against the correlation time of isotropic molecular motion for a variety of applied MAS rates. The motion has been assumed to be a diffusive Gaussian-Markoff process. Note that it is not possible to completely narrow the signals arising from molecules with an intermediate amount of motion (10^{-2} ms > t_c > 1 ms) with MAS.

4.2.3.4. Experimental Procedure

The samples were left to equilibrate in sealed containers for 2 hours prior to spectral acquisition. Spectra were recorded using an identical pulse program to that in section 4.2, but this time MAS was applied. The static linewidth of these samples is approximately 1 kHz, so spinning at ~1.2 kHz is adequate to average the SA and heteronuclear dipolar coupling without obtaining spinning sidebands. In fact, the width of the overlapping lines comprising the spectra is considerably less than this and the minimum stable probe spinning speed of 0.7 kHz was used in most experiments without spinning sidebands being visible. No additional narrowing was observed as the MAS rate was increased. As noted in Chapter 3, the possible physical effects of macroscopic sample rotation on adsorbate distribution within the pores means that it is advantageous to keep MAS rates as low as possible. In this series of experiments, the peak areas obtained for static and MAS experiments were identical, and it was concluded that 0.7 kHz MAS did not affect samples unduly. Deconvolution was not needed to separate the two peaks, but the inhomogenous nature of peak I meant that performing deconvolution once again allowed "weighted mean" spectral values for the molecules giving rise to peak I to be obtained. In this case the best agreement was obtained by modelling peak II as a Lorentzian lineshape, whilst the broad peak I envelope was once again modelled as being composed of an equal mixture of Gaussian and Lorentzian character.

4.2.3.5. Experimental Results

The motion of the molecules upon the surface places the sample in the "intermediate motion" category discussed above, and therefore neither the heteronuclear dipolar coupling nor the shielding interaction is averaged completely by MAS. However, MAS does narrow the lines considerably with respect to the static spectra acquired, leaving two clearly distinguishable lines. Spectra recorded with different amounts of TMP upon SC2 carbon are shown in Figure 4.7.

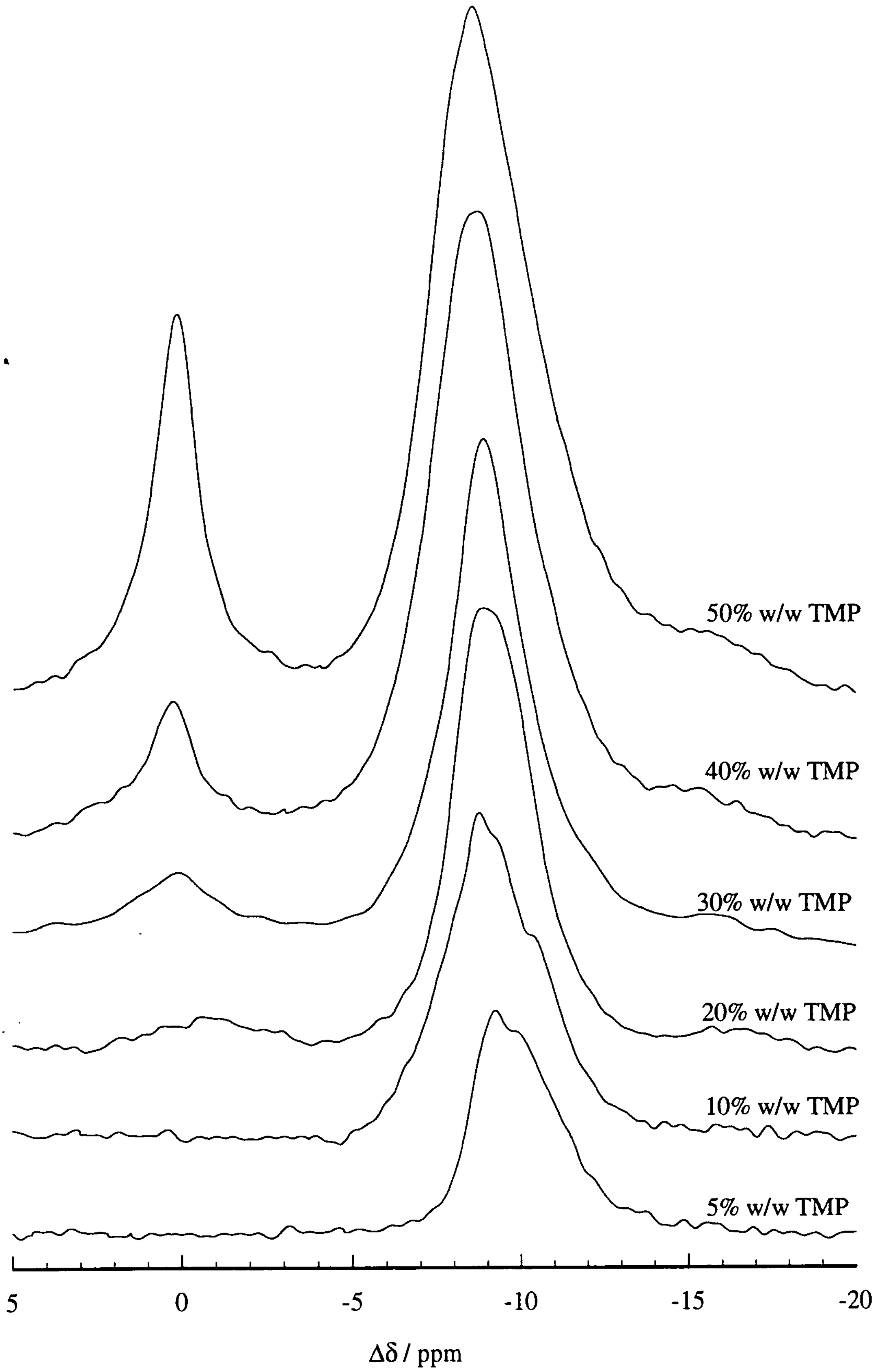

Figure 4.7. Single-pulse spectra acquired with MAS at 0.7 kHz for a variety of TMP loadings upon SC2 carbon.

The major features of each spectrum, such as peak chemical shift, intensity and linewidth are summarised in table 4.4. The results obtained are analogous to those for the static case, but the MAS narrowing affords greater resolution and increased S/N.

Load	**Peak II**		**Peak I**	
	$\Delta\nu_{half}$ / Hz	**$\Delta\delta$ / ppm**	**$\Delta\nu_{half}$ / Hz**	**$\Delta\delta$ / ppm**
5 %	-	-	230	-9.2
10 %	-	-	260	-9.1
20 %	600	-1.0	230	-8.8
30 %	310	0.1	290	-8.7
40 %	190	0.0	320	-8.5
50 %	100	-0.2	280	-8.3

Table 4.4. Variation in peak width and chemical shift obtained from MAS spectra with the amount of TMP added to SC2 carbon

At low loadings, a single broad line is observed, shifted to low frequency by approximately –9 ppm. As the amount of adsorbate added to the carbon increases, the line becomes slightly broader and shifts back towards higher frequency. After approximately 30% w/w TMP has been added to the carbon, another peak, centred at approximately 0 ppm appears. As more adsorbate is added, both peaks increase in size, though as the amount of adsorbate increases further the growth of peak I becomes slower than that of the peak II. Peak I continues to move slowly towards higher frequency with increasing adsorbate loading. The chemical shift of the new peak does not change significantly as it increases in intensity but it does become much narrower, approaching that of the pure liquid at very high loadings.

4.2.4. DISCUSSION

In order to discuss the results from this chapter properly, it is necessary to jump ahead and summarise the results of T_2 relaxation experiments performed in chapter 7. The MAS T_2 experiments performed within that chapter demonstrate conclusively that the low frequency peak is made up of a number of overlapping peaks of variable width. This means that the deconvolved broad peak must be considered a collection of overlapping peaks, each with a slightly different chemical shift, intensity, area and linewidth. As mentioned previously this means that the numerical values obtained from the deconvolution process form a weighted mean of the values belonging to each of the constituent peaks making up peak I.

4.2.4.1. The interaction between TMP and carbon

The precise internal structure of activated carbon is not known, and indeed this is one of the reasons the current study is being conducted. The carbon internal surface is generally perceived to be a mixture of non-graphitised and graphitised carbon areas, with a number of "oxygenated sites" left over as an artefact of the activation process. The NMR spectra of small amounts of adsorbed TMP upon carbon show a large low-frequency chemical shift, and therefore the graphene areas play a major role in the initial adsorption of TMP. This is very much as would be expected from a consideration of the charge distribution of the TMP molecule.

Graphite has a perfectly homogenous surface, characterised by a region of π electron density above the plane of the surface. It will therefore interact strongly with electron-deficient groups. Semi-empirical molecular orbital calculations[11, 12] show that the TMP molecule possesses a large dipole, with a large partial positive charge on the phosphorus atom and a smaller partial positive charge on each of the three methyl groups. The central phosphorus nucleus is surrounded by electronegative oxygen atoms, and cannot bind directly to the carbon surface. Therefore it is thought that TMP binds to the activated carbon surface via a dipolar mechanism with the methyl groups in a "tripod down" orientation. More complex calculations on the energy of various orientations of TMP to graphite performed using classical optimisation methods show that the "tripod down" orientation is by far the lowest energy conformation. The oxygenated sites on the carbon may also play a role in TMP adsorption, interacting with the methyl groups of the TMP molecule through weak (O-C-H—O_{carbon}) hydrogen bonds[13, 14].

4.2.4.2. The Source of the Chemical Shift of Peak I

The most noticeable difference between the phosphorus spectra of liquid and adsorbed TMP is the large low-frequency chemical shift introduced upon adsorption to the carbon surface. This effect can be explained through the influence of proximate graphene planes to the adsorbed TMP molecules. However, the situation is complicated by the amount of molecular motion present in the adsorbate molecules within the carbon porous volume. Previous authors in the field, such as those discussed in chapter 2, have generally rationalised their results by suggesting that the motion of molecules adsorbed upon the carbon surface is limited compared to that of molecules in the bulk phase, but that molecules within a single pore may exchange position relatively freely. Several of the results achieved in this chapter agree with this suggestion. For example, the absence of a narrow, solution-state line superimposed over the broad spectrum observed shows that all of the molecules added to the carbon adsorbent experience a similar effect, and this implies that there is a degree of molecular exchange occurring within the system. The limited number of molecules about the entrance to each pore means that the exchange of molecules will effectively be restricted to a single pore during the course of a single NMR experiment.

Chapter 2 demonstrated that the size of any low frequency chemical shift observed in molecules adsorbed on graphitised carbon was dependent solely upon the distance between the nucleus and the aromatic graphene layer. In a system where molecules are rapidly exchanging position with one another, such as within a single pore, the average of these distances determines the chemical shift observed for all the molecules within that system. It is this that provides an explanation for the inhomogenous nature of peak I. Each pore has a slightly different surface-area to volume ratio, from the smallest of micropores which has only material adsorbed directly to the surface within it, to large mesopores with a rapidly exchanging collection of directly adsorbed and non-adsorbed molecules. As each pore differs, so too will the averaged chemical shift of the molecules within that pore, depending upon the (time-averaged) ratio between molecules adsorbed upon the pore walls and molecules free to move about the centre of the pore. For example, molecules within the small micropores will possess an averaged low-frequency chemical shift approximately equal to that of a single adsorbed molecule, whilst molecules within larger pores will exhibit a considerably smaller shift. Dubinin's theory of the volume filling of micropores (VFM) states that adsorbate material will fill progressively larger and larger pores. Thus it would be expected that the low-frequency chemical shift of peak I obtained from the spectra at various loadings becomes progressively smaller as the amount of adsorbate added to the carbon increases. This is observed, with the average low-frequency chemical shift obtained from the static spectra decreasing from -10.1 ppm to –8.8 ppm as the amount of TMP added to the pore system increases from 5% w/w/ to 40% w/w. A similar effect was observed in the MAS series of experiments, with the chemical shift decreasing from –9.2 ppm to –8.3 ppm. The difference between the chemical shift values for the low-frequency peak obtained from static and MAS experiments arises from the inhomogenous nature of the peak. The averaging of the spin Hamiltonian caused by MAS narrows different portions of peak I to a differing extent and thus the chemical shift observed changes after the application of MAS.

Molecules adsorbed at one of the oxygenated sites within the carbon would exhibit a smaller chemical shift due to the greater distance between the molecule and the graphene planes. However, in the context of a pore filled with rapidly exchanging molecules, the effect of the oxygenated sites should not be particularly marked. Their presence should simply reduce the pore-averaged chemical shift by a small amount compared with an identically sized pore without oxygenated sites. The effect of oxygenated heterogeneities is greater in the adsorption behaviour of water to activated carbon as the heterogeneities act as primary adsorption sites for the hydrophilic adsorbate molecules. This is discussed at greater length in chapter 5.

4.2.4.3. The Magnitude of the Broad Peak Chemical Shift

In Chapter 2 the predicted proton chemical shift of a monolayer of benzene molecules adsorbed on graphite was calculated to be approximately –26 ppm. The static phosphorus spectra obtained for TMP upon SC2 show peak intensity extending down to approximately -17 ppm whilst MAS spectra at high loadings show a small amount of intensity extending to approximately the same value. In order to evaluate whether this is a reasonable maximum value the distance between the phosphorus nucleus in TMP and the carbonaceous surface must be obtained. Once again, the MOPAC package was used to model the situation using a classical mechanics optimisation. The lowest energy conformation of TMP upon graphite calculated by this process yielded a graphite-phosphorus distance of approximately 0.37 nm. Taking this value and inserting it into the crystal susceptibility component calculation from chapter 2 yields a predicted maximum chemical shift of –16.5 ppm. This value is very close to the experimental value obtained from this series of experiments, and provides further evidence that the explanation for the source of the chemical shift is correct. The calculated chemical shift is a maximum value occurring only if the pores were composed entirely of graphene carbon, without any oxygenated sites or non-aromatic carbon. The correspondence between the observed and calculated maximum chemical shift suggests that most of the smallest pores in SC2 carbon are composed mainly of graphene carbon.

4.2.4.4. Peak II

At higher loadings another peak is observed in the spectrum. This peak does not experience the large low-frequency chemical shift characteristic of adsorption to the graphene carbon. Thompson[10] ascribed the peak to “excess” adsorbate on the carbon exterior surface, presumably between grains of material, or within large macro-pores, though no explanation for the absence of chemical shift was given. The chemical shift of Peak I is dependent upon the distance of the adsorbate molecule from the graphene planes. It follows that the appearance of an unshifted peak at high adsorbate loadings shows that some molecules must be situated in positions that are distant from the graphene planes within the adsorbent. Another question that relates to the presence of the narrow peak at higher loadings is why no intensity is observed between -1 ppm and -5 ppm in these MAS experiments.

Dubinin's VFM theory may provide an explanation for the absence of intensity above a certain chemical shift. Capillary condensation occurs because of the increased thermodynamic driving force of condensation in smaller pores, formally demonstrated in the Kelvin equation. The propensity for the material to condense is caused by interaction with the adsorbent surface and the interaction causes the material to behave in a different manner to the bulk liquid. For example it is found that the surface-liquid interaction causes the material to have a different density to that of the free liquid. The thermodynamics for the pore filling become progressively less favourable as the pore size increases until a pore size is reached above which the process of pore filling is no longer significantly lower in energy than condensation upon a flat surface. Thus any material within these pores will be solely adsorbed as multilayers upon the walls. This provides a possible explanation for the absence of intensity above -5 ppm in the spectra. If capillary condensation occurred within pores up to any size then intensity would be observed at every frequency from 0 ppm to the maximum chemical shift of –17 ppm. This is not observed and it is suggested that the material that gives rise to the high frequency end of peak I is within the maximum pore size in which pore filling by capillary condensation can occur.

There are several possibilities as to how the peak at 0 ppm may arise. One suggestion is that it may arise from molecules that are adsorbed in extremely large surface pores, such as those formed between carbon grains, in which the ratio of surface adsorbed to non-adsorbed material is so small as to produce a negligible chemical shift. Another suggestion is that the material is not in contact with the carbon at all, either existing as droplets of liquid within the sample volume or adsorbed upon the surface of the container used within the NMR experiment. When the resonance first appears, at loadings around 30 to 40%, it is reasonably broad, and the inference is that the peak arises from material adsorbed upon the container wall. Because the container is non-graphitic no low-frequency chemical shift is observed. As the size of the peak increases with loading the resonance exhibits more "liquid-like" behaviour, and this suggests that the excess adsorbate is in one of the alternative states, adsorbed within the very largest surface pores or existing as non-adsorbed liquid droplets somewhere within the sample.

4.2.4.5. The Source of the Increased Peak Linewidth

The interaction between TMP molecules and the carbon surface causes the translation and rotation of the adsorbed molecules to become significantly slower and anisotropic. This means that the Hamiltonian $R_{l,\,m}$ spin operators are no longer averaged to their isotropic values, and therefore broadening effects arising from a combination of several internal Hamiltonians –in this instance shielding anisotropy and heteronuclear dipolar coupling- can occur. The extensive narrowing observed in the spectra acquired with MAS compared to spectra acquired without demonstrates that this is the case. However, there is clearly still a great deal of motional averaging occurring as the peaks observed in the static NMR experiment are a lot less broad than typical values ($\Delta\nu_{half} \approx 20$ kHz) obtained from static solid-state dilute-spin experiments. In addition the broadening effect of peak overlap must also be considered when discussing the breadth of the low-frequency peak.

The decoupling experiments showed that proton-phosphorus dipolar coupling is responsible for very little of the broadening observed upon adsorption on to carbon. It is thought that this is because residual molecular motion has already averaged the bulk of the dipolar coupling between the phosphorus nucleus and neighbouring protons away. A rough calculation of the predicted coupling between a single methoxy proton and the phosphorus nucleus demonstrates that the width of the peaks observed is a lot less than that expected. Using the internuclear distance obtained from the calculated lowest energy conformation of TMP, ($r_{P\text{-}H} = 3.02\text{x}10^{-10}$ m), a phosphorus powder pattern with a dipolar coupling constant of almost 1.8 kHz is predicted. The effect of the 8 other methoxy protons, all at comparable distances, would be to broaden the pattern still further. It has already been shown that the total width of the static low-frequency peak envelope is only approximately 600 Hz in total, and therefore there must be a large residual amount of motion to scale the width of the peak to such an extent. WALTZ-16 did introduce a small amount of narrowing (clearly visible in the increased separation of the two peaks in figure 4.5) so there is a degree of residual heteronuclear dipolar coupling, but the bulk of the observed broadening must arise from shielding anisotropy and peak overlap.

Several of the previous NMR studies outlined in Chapter 2 discussed the significance of the additional width present in the low-frequency peaks of adsorbed molecules. It was also noted in the two loading experiments that the width of the low-frequency peak varied in a regular manner. Peak I was relatively narrow at low loadings, increased slightly for intermediate loadings and then became narrower again as the loadings continued to increase. This is a result of the way in which the chemical shift varies with the area of peak I. For small quantities of adsorbate, a modest increase in the amount of adsorbate causes a large change in chemical shift, whilst the inverse is true for higher loadings. Thus, even though the motion of the molecules is increased as more adsorbate enters progressively larger pores the peak envelope still becomes wider initially as more adsorbate is added. This is because the greater range of pore sizes explored by the molecules causes the inhomogenous broad peak to cover a broader range of chemical shifts. As the loading continues to increase the peak narrows once again because the large amount of motion present in the adsorbate molecules being added is no longer offset by a similar increase in the variation of the chemical shift.

4.2.4.6. Peak Areas

The peak areas obtained closely follow the amount of adsorbate material added, as occurs normally in a NMR experiment. Usually, if the number of nuclei within the sample is doubled, the NMR signal obtained from the sample is doubled also. The correspondence between peak area and amount of material is not exact in this case due to two main reasons. Firstly there is the analytical problem of modelling the inhomogenous broad peak as a single mathematical function, which introduces a form of "rounding error" into the peak-area calculation. Secondly, proximate conducting graphene planes affect the radiofrequency pulse strength at the nuclei of study. As was noted in Chapter 3, the 90° pulse duration required to excite TMP molecules adsorbed upon carbon is approximately 30% longer than that set upon the pure phosphate sample, and the exact position of the molecule within the porous volume further alters the radiofrequency power required. Material adsorbs initially in the smaller micropores and the average distance of the primarily adsorbed material from the carbon graphene planes will be less than the material in larger pores or in positions a greater distance from the graphene planes. The material at lesser distances from the graphene planes will yield a smaller signal because the effective B_1 power at that position is smaller. Thus it is found that the signal intensity for 5.2 % w/w TMP upon SC2 is rather less than a quarter that observed for 20.1 % w/w.

Peak areas can also be used to calculate the mass of material adsorbed within the porous volume of the carbon. From this it is possible to calculate a rough value for the volume of the pores, though the approximations used within the calculations mean that the results obtained are extremely rough. It is assumed that the presence of the peak at 0 ppm arises only after the pore volume is completely full, though the absence of intensity above –5 ppm shows that this is not true. The continued rise in low-frequency peak area as more adsorbate is added also shows that this is not the case, and therefore the pore volumes calculated by this method will be an underestimate. It is also assumed that the density of the adsorbed material is equal to the value obtained from density measurements of the bulk liquid, though it is well known that this is not the case (e.g.[31]). Peak II appears in the spectrum at approximately 25% w/w, and using the density measurement of TMP ($\rho = 1.21$ g cm^{-3}) this equals ~0.21 cm^{-3} of TMP adsorbed per gram of carbon. PSD measurements obtained from mercury porosimetry show that approximately 70% of the pore volume is accessible to TMP molecules and so the pore volume of the carbon is calculated to be approximately 0.30 cm^{-3} g^{-1}. This compares to a value of 0.54 cm^{-3} g^{-1} obtained from alpha-s analysis of the nitrogen adsorption isotherm. If the peak I area measurement from the 50% w/w experiment is used then the volume of the pores is calculated to be approximately 0.46 cm^{-3} g^{-1}, closer to the "accepted" value but still not at all accurate. Apart from the assumptions within the calculation outlined above, the major reason that the carbon pore volumes calculated are so low is because two hours is not sufficient time for equilibrium to be attained in the adsorption of TMP to carbon. The study of the adsorption process of TMP upon SC2 carbon over time forms the focus of the following section.

4.3. VARIATION IN MAS SPECTRA WITH TIME AFTER ADSORPTION

4.3.1 EXPERIMENTAL PROCEDURE

This series of experiments was conducted for a single sample, acquiring spectra at intervals after 50% w/w TMP had been added to the SC2 carbon surface. For the first 4 hours spectra were recorded every 5 minutes. For the next 18 hours, spectra were recorded at 30-minute intervals. The spectra were acquired using 8 transients employing 3 μs pulses, (corresponding to a nutation angle of 56°, set upon a carbonaceous sample) with a recycle delay of 3 seconds. For comparison a single spectrum was also acquired 1 week later. MAS at 0.8 kHz was employed for each experiment. The spectra were analysed using the deconvolution algorithms within Spinsight. The total signal intensity was normalised to 1 for each slice.

It will be shown that the period during which the bulk of the changes in peak area occur is in the first few moments after adsorption. Unfortunately, it is not possible to observe this time using the experimental procedure outlined above. This is because the adsorbate has to be added to the carbon outside the spectrometer and the sample must then be placed inside the magnet and spun up to the requisite MAS rate prior to acquisition commencing. This process generally takes around $1^1/_2$ to 2 minutes. In addition to this, at least 4 acquisitions are required in order to obtain spectra with the requisite S/N ratio to interpret reasonably. This limits the rate at which experiments may be performed. It was found that the conditions used in this experiment (each experiment taking approximately 25 seconds) were approaching the practical minimum time for the experiment. The signal that is obtained from each experiment is an average of the molecules' position during the entire 25 second period, and therefore this technique is not suitable for the observation of processes that take place within the experimental time.

4.3.2 RESULTS

The spectrum acquired 2 minutes after the addition of TMP to SC2 is compared to that acquired 18 hours later in Figure 4.8. There is a marked difference between the two spectra. The peak at 0 ppm has been reduced in size and there has been a commensurate increase in the size of the low-frequency peak. The increased intensity occurs in the low-frequency portion of peak I, whilst the higher frequency part of the peak remains almost the same. The variation in the measured peak parameters with time after adsorption is outlined graphically in Figures 4.9 and 4.10. The ratio of peak I to peak II reaches approximately 80:20 within the first 5 minutes and over the course of the next 18 hours settles at approximately 92:8. A single spectrum recorded one week later showed a peak area ratio of 94:6. The average chemical shift of the low-frequency peak shows a significant shift to low frequency over the period of study. Two minutes after addition of the adsorbate the chemical shift is –8.4 ppm and this decreases by 0.5 ppm over the following 24 hours. After 1 week the chemical shift of the peak was found to be -9.0 ppm. Peak I increased in width from approximately 220 Hz to 260 Hz over the course of the experiment whilst the width of peak II increased from 87 Hz in the first spectrum to 110 Hz in the spectrum recorded after a week. It is felt that the increase in peak II linewidth is not particularly significant, particularly as the peak intensity ultimately becomes so small, introducing the possibility of large errors in the deconvolution process.

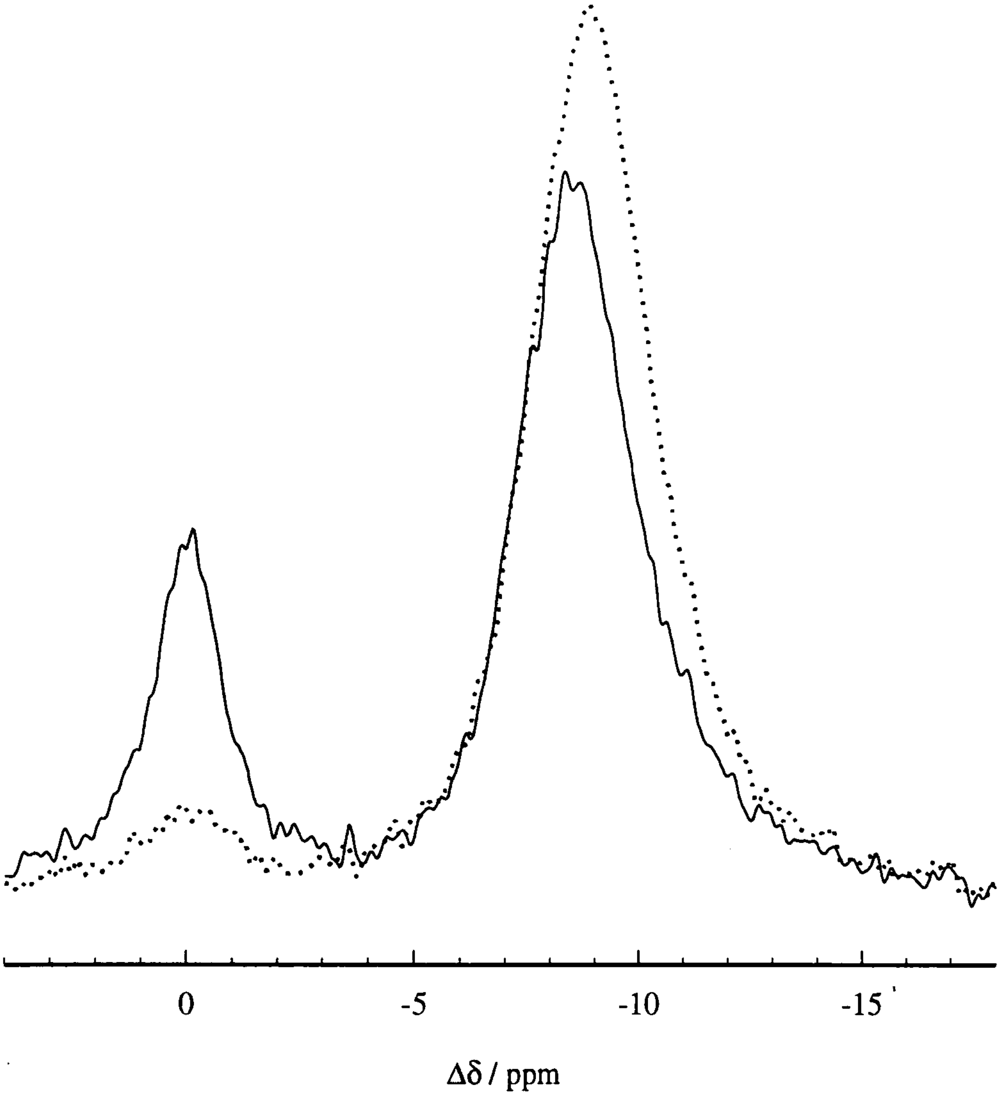

Figure 4.8. Spectra recorded 2 minutes (solid line) and 20 hours (dotted line) after the adsorption of 50% w/w to SC2 activated carbon. There has clearly been a significant shift of intensity from the peak at 0 ppm to the low-frequency portion of peak I over the course of the experiment.

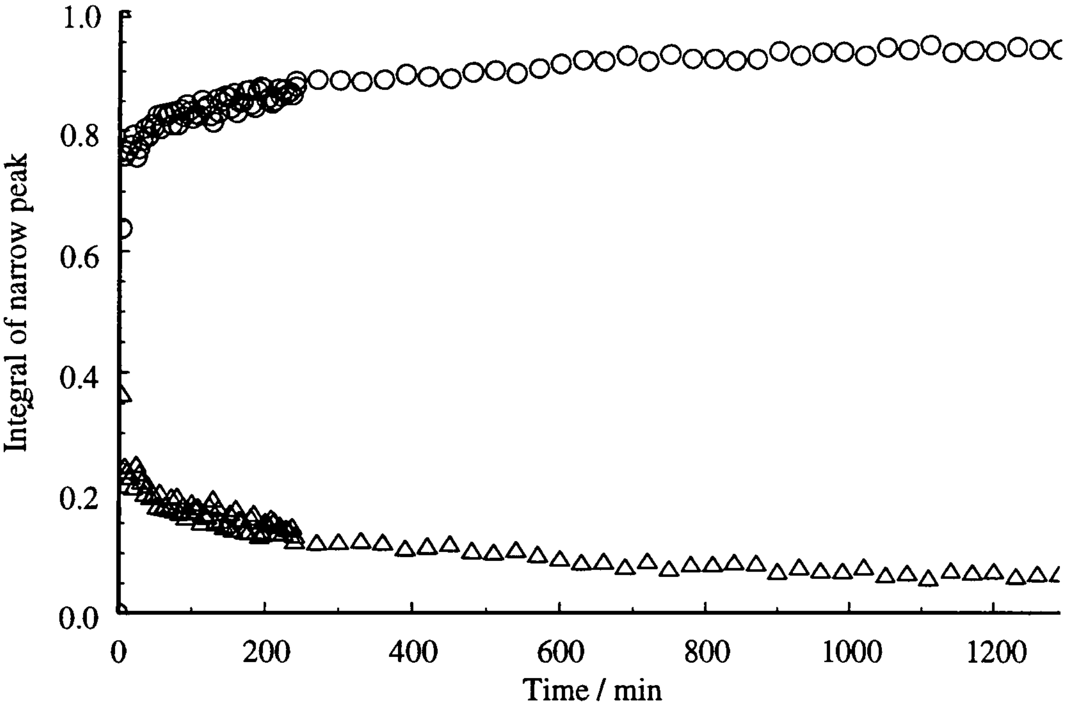

Figure 4.9. Variation in the areas of Peak I and Peak II (total intensity normalised to 1) plotted against time elapsed after addition of 50% w/w TMP to SC2 carbon.

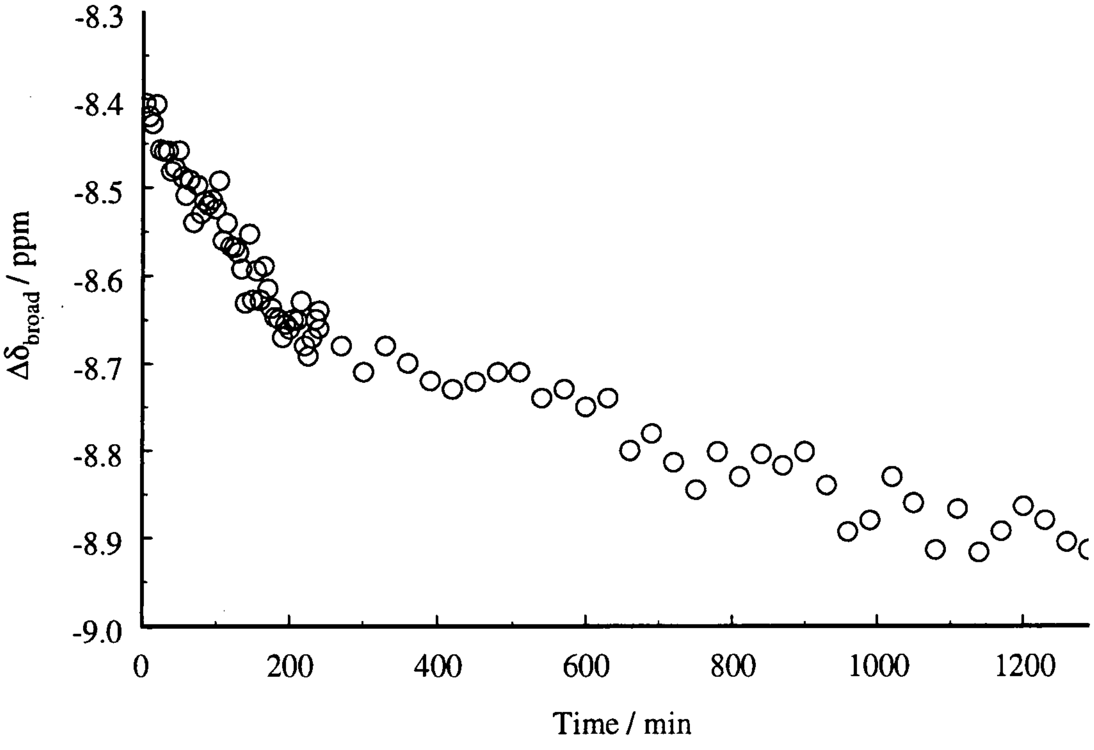

Figure 4.10. Variation in the calculated chemical shift of the low frequency peak against time elapsed after the addition of 50% w/w TMP to SC2 carbon.

4.3.3 CONCLUSIONS

The peak area information suggests that there is an extremely rapid adsorption process occurring within the first few minutes. Between the addition of the adsorbate and the first data point the low-frequency peak grows from 0 to account for ~70% of the total intensity. Unfortunately, the experimental procedure outlined above is unable to study this period. MAS probes have been designed to allow material to be added to samples whilst spinning[26], but there is still the problem of acquiring multiple transients and the long ^{31}P T_1 relaxation time, discussed in chapter 7, to contend with. At the moment it looks as though the problem is insurmountable. After the rapid initial adsorption there is a secondary adsorption process, evidence for which is shown by the slow increase in the area of peak I. This process is dramatically slower than the initial one and accounts for the adsorption of a further 25% of the total amount of adsorbate. The increase in low-frequency peak area is matched by an identical decrease in the area of peak II, showing that the adsorbate material is moving from one environment to another. Therefore the slow adsorption process involves the movement of molecules from external surfaces to situations within filled pores. Peak area measurements alone cannot provide any information on why the apparent capacity of the pores is increasing over time. One suggestion is simply that the material is slowly reaching and entering smaller, less accessible pores. Another suggestion is that the pores themselves are stretching to accommodate the large amount of adsorbate. "Pore swelling" is well documented[27, 28, 29], and it has been demonstrated that successive adsorption/ desorption cycles of TMP upon carbon increases the average pore size considerably[30].

Further information as to what is occurring is provided by the marked increase in the size of the low-frequency chemical shift, from an initial value of approximately -8.4 ppm down to a final value of –9 ppm. This shows that the average pore size in which the adsorbate molecules are adsorbed is becoming progressively, and significantly, smaller. This is clearly the opposite to what would be predicted if pore-swelling was the major mechanism accounting for the increased amount of

TMP adsorbed within the pore volume. It is thought that the increased low frequency shift of peak I shows that molecules are slowly entering smaller pores that were not immediately accessible upon initial addition. The results are corroborated by the increase in intensity of the low-frequency end of peak I. It is also interesting to note the lack of variation at the higher frequency end of the peak. The comparison of the two spectra suggests that the apparent increase in pore capacity arises from the adsorption of molecules into previously unexplored pores rather than an increase in the number of molecules within each pore.

The increase in the width of the low-frequency resonance arises because of the greater range of pore sizes, and hence chemical shifts, explored by the adsorbate molecules. It is possible that pore swelling may be occurring also, but on a much smaller scale than the continued entry of adsorbate into smaller pores. The increase in chemical shift continues for over 24 hours and the slow rate could be because many of the pores are partially blocked or are right in the heart of the porous volume, accessible only through a network of interconnecting branches. The result is particularly interesting given that gravimetric data usually suggest that equilibrium inside the pores is reached within a few hours. This highlights the inadequacy of gravimetric measurements, which cannot distinguish adsorption at different types of site within the pore volume.

The slow adsorption process also provides an explanation for the underestimation in the calculated carbon pore volume using peak area measurements obtained two hours after adsorption. The calculation performed earlier used peak area measurements obtained after two hours. The area ratio of peak I to peak II for 50% w/w TMP upon SC2 carbon was found to be approximately 82:18 after two hours, but after one week it had risen to 94:6. If the value obtained after one week is used in the pore volume calculation then a carbon pore volume of 0.55 cm^{-3} g^{-1} is obtained. This compares extremely well with the value obtained from the nitrogen adsorption isotherm of 0.54 cm^{-3} g^{-1}.

4.4. REFERENCES

1. M. M. Crutchfield, C. H. Dungan, J. H. Lecher, V. Mark, J. R. Van Wazer, *"Phosphorus-31 NMR"*, John Wiley and Sons (1967)
2. U. Haeberlen, *"High Resolution NMR in Solids: Selective Averaging"*, Academic Press, New York (1976), Chapter 4
3. E. R. Andrew, A. Bradbury, R. G. Eades, *Arch. Sci.*,**11**, 223 (1958)
4. I. J. Lowe, *Phys. Rev. Lett.*, **2**, 285 (1958)
5. M. M. Maricq, J. S. Waugh, *J. Chem. Phys.*, **70**, 3300 (1979)
6. A. Abragam, *"The Principles of Nuclear Magnetism"*, Oxford University Press (1961), Chapter 8
7. D. Suwelack, W. P. Rothwell, J. S. Waugh, *J. Chem. Phys.*, **73**, 2560 (1980)
8. J. Tabony, *Progress in NMR Spectrosc.*, **14**, 1 (1980)
9. R. K. Harris, T. V. Thompson, P. Forshaw, N. Foley, K. M. Thomas, P. R. Norman, C. Pottage, *Carbon*, **34**, 1275 (1996)
10. T. V. Thompson, Ph.D. Thesis, University of Durham (1995)
11. Gaussian 94, Revision E.2, M. J. Frisch, G. W. Trucks, H. B. Schlegel, P. M. W. Gill, B. G. Johnson, M. A. Robb, J. R. Cheeseman, T. Keith, G. A. Petersson, J. A. Montgomery, K. Raghavachari, M. A. Al-Laham, V. G. Zakrzewski, J. V. Ortiz, J. B. Foresman, J. Cioslowski, B. B. Stefanov, A. Nanayakkara, M. Challacombe, C. Y. Peng, P. Y. Ayala, W. Chen, M. W. Wong, J. L. Andres, E. S. Replogle, R. Gomperts, R. L. Martin, D. J. Fox, J. S. Binkley, D. J. Defrees, J. Baker, J. P. Stewart, M. Head-Gordon, C. Gonzalez, and J. A. Pople, Gaussian, Inc., Pittsburgh PA (1995)
12. CAChe version 3.0, Oxford Molecular Group Inc.
13. T. Steiner, *Chem. Commun.*, 727, 1997
14. T. Steiner, G. R. Desiraju, *Chem. Commun.*, 891, 1998

15. R. K. Harris, T. V. Thompson, P. R. Norman, C. Pottage, *J. Chem. Soc. Faraday Trans.* **92**, 2615 (1996)

16. R. R. Ernst, G. Bodenhausen, A. A. Wokaun "*Principles of NMR in 1 and 2 Dimensions*", Clarendon Press Oxford (1987)

17. M. Mehring, G. Sinning, *Phys. Rev. B,* **15**, 2519 (1977)

18. M. H. Levitt, R. Freeman, *J. Magn. Reson.*, **43**, 65 (1981)

19. M. H. Levitt, "Composite Pulses", *Encylopedia of NMR*, (Editors D. M. Grant, R. K. Harris), Wiley, London (1996)

20. M. H. Levitt, R. Freeman, *J. Magn. Reson.*, **43**, 502 (1981)

21. A. J. Shaka, J. Keeler, T. Frenkiel, R. Freeman, *J. Magn. Reson.*, **52**, 335 (1983)

22. J. S. Waugh, *J. Magn. Reson.*, **50**, 30 (1982)

23. A. J. Shaka, J. Keeler, R. Freeman, *J. Magn. Reson.*, **53**, 313 (1983)

24. M. H. Levitt, R. Freeman, T. Frenkiel, *J. Magn. Reson*, **50**, 157 (1982)

25. S. J. Gregg, K. S. W. Sing, "*Adsorption, Surface Area and Porosity*", Chapter 3, Academic Press (London) Ltd. (1967)

26. M. Hunger, T. Horvath, *J. Chem. Soc. Chem. Commun.*, **14**, 1423 (1995)

27. D. H. Bangham, *Proc. Roy. Soc. A.,* **130**, 81 (1930)

28. D. H. Bangham, *Proc. Roy. Soc. A.,* **166**, 572 (1932)

29. H. Yoshida, *Carbon,* **35**, 631 (1997)

30. H. F. Stoekli, A. Perret, P. Mena, *Carbon,* **18**, 443 (1980)

31. P. N. Aukett, N. Quirke, S. Riddiford, S. R. Tennison, *Carbon,* **30**, 913 (1992)

COMPETITION BETWEEN DIFFERENT ADSORBATE MOLECULES WITHIN THE PORE SYSTEM STUDIED BY MAS NMR.

5.1. THE COMPETITIVE ADSORPTION OF TMP AND DMMP

In order to generate a clear understanding of the changes induced in the behaviour of each adsorbate by the presence of another phosphorus-containing species, several time-dependent experiments were conducted. The two main experiments within this section studied the spectra of 50% w/w TMP added to SC2 carbon with 50% w/w DMMP pre-adsorbed and the inverse experiment (50% w/w DMMP added to SC2 with 50% w/w TMP pre-adsorbed). The spectra of 50% w/w DMMP and 50% w/w and 100% w/w of a 50:50 mixture of DMMP and TMP upon SC2 carbon over time were recorded as a series of control experiments. The results obtained from the study of 50% w/w TMP upon SC2 in the previous chapter were also used. Finally, as a further control experiment, the addition of 50% w/w TMP to SC2 carbon with 50% w/w TMP pre-adsorbed was also studied.

5.1.1. EXPERIMENTAL PROCEDURE

In all cases where two adsorbates were added sequentially, the adsorbate added initially was left to equilibrate for exactly two hours before the second adsorbate was added. Spectra were also recorded prior to the addition of the second adsorbate to enable a direct evaluation of the effect on the spectra of the second adsorbate. A pulse angle of 56° was applied, corresponding to a 5 μs π pulse, set upon a carbon adsorbate sample. A recycle delay of 3 seconds was used, and 16 acquisitions were taken, giving a total acquisition time of 48 seconds. The measurements were repeated either every 2 or 4 minutes for the first 2 hours of each experiment and then every half hour for the remainder of the experimental period. All chemical shifts are quoted relative to liquid

TMP at zero (+2.4 ppm with respect to 85% H_3PO_4). The peaks within the spectra were analysed using the deconvolution software within the Spinsight package, as described in Chapter 4.

5.1.2. EXPERIMENTAL RESULTS

5.1.2.1. Control Experiments

As would be expected from the discussion of the spectra arising from TMP upon activated carbon in chapter 4, each phosphorus-containing compound gave two distinct resonances upon addition to the carbon adsorbent. The resonances of each adsorbate were far enough apart for there to be no overlap between peaks, making the spectra simpler to analyse. The adsorbed TMP spectra comprised peak II at 0.00 ppm (relative to liquid TMP) and peak I at approximately -8.6 ppm. The spectra of adsorbed DMMP also yielded two peaks, but in this instance peak II occurred at 32.6 ppm with the associated peak I at approximately 22.0 ppm, again with respect to liquid TMP. An example spectrum for the two adsorbates upon SC2 carbon is shown in Figure 5.1.

The two control experiments performed for the addition of 50% w/w of each of DMMP and TMP yielded almost identical results. Figure 5.2 shows the variation in the peak areas obtained for both TMP and DMMP with time elapsed after addition to the carbon adsorbent. Figure 5.3 shows the variation in peak I chemical shift over time for each species. The similarity between each of the plots within each figure is marked and demonstrates the relation in behaviour of the two adsorbates. The results from the time-dependent study of TMP are discussed in chapter 4. The results of the identical experiment performed using DMMP were completely analogous to the results obtained for TMP, with a peak I to peak II area ratio of 92:8 obtained after 18 hours. There was an increase in the magnitude of the low-frequency chemical shift of peak I of approximately 0.7 ppm (from 22.4 to 21.7 ppm) over the course of the experiment, compared with the 0.6 ppm variation observed in the study of TMP. The width of the DMMP low-frequency peak increased from ~215 Hz after 2 minutes to ~250 Hz after 18 hours.

The control experiments in which equal amounts of each adsorbate were added simultaneously further demonstrated the similar adsorption behaviour of the two probe molecules. In peak area analyses for the two adsorbates, the plots due to the DMMP and TMP overlapped one another for the entirety of the experiment. The peak area and chemical shift results of the 50% w/w experiment using a mixture of the two adsorbates were almost identical to those obtained in each of the control experiments above. However, different results were obtained in the experiment using 100% w/w of the adsorbate mixture. The peak I to peak II area ratio in this instance increased from 45:55 after 2 minutes towards a value of roughly 55:45 after 2 hours. After 18 hours the peak area ratio obtained was approximately 58:42. Chemical shift measurements for both molecules again showed an increase in the magnitude of the low-frequency chemical shift over time but the final value obtained for each adsorbate was found to be at a slightly higher frequency than that obtained in the 50% w/w experiments. The chemical shift of DMMP peak I settled at approximately 21.90 ppm after 18 hours whilst the TMP peak I chemical shift was found to be –8.80 ppm. Linewidth measurements for each of the two low-frequency peaks again showed a gradual increase with time after adsorption, though they were noticeably less than the linewidths obtained in the two earlier experiments. A final linewidth of ~230 Hz for TMP and ~225 Hz for DMMP was observed in the 50% w/w mixed-adsorbate experiment compared to values of 260 and 250 Hz obtained in each of the respective single adsorbate experiments.

5.1.2.2. Sequential Adsorption Experiments

The peak area and chemical shift results from each of the two sequential adsorption experiments are shown in Figures 5.4 and 5.5. The results of the experiment studying the adsorption of DMMP onto carbon with TMP pre-adsorbed will be summarised first, followed by those for the inverse experiment. The ratio of peak I to peak II for DMMP was found to be approximately 20:80 after 2 minutes and reached 50:50 after approximately $1^1/_2$ hours. The peak area ratio then continued to increase throughout the experiment, reaching 60:40 after 18 hours. This compares to a final peak area ratio of 92:8 obtained for the adsorption of 50% w/w DMMP on to a clean carbon surface. Over the first few minutes of the experiment the TMP peak area ratio decreases in size from 85:15 to 55:45 but after 20 minutes starts to gradually increase in size once more. The ratio of peak I to peak II for TMP after 18 hours is approximately 72:28. There are also interesting variations in the chemical shift of peak I for each adsorbate with the time elapsed after the addition of the DMMP. The DMMP low-frequency peak shifts further to low frequency (from 22.20 ppm to 21.90 ppm) over the first hour or so before gradually returning to higher frequency. After 18 hours the chemical shift of peak I is approximately 22.05 ppm. The magnitude of the low-frequency chemical shift of the pre-adsorbed TMP shows a rapid initial decrease from –8.95 ppm to –8.75 ppm in the first hour, continuing up to -8.70 ppm after 18 hours.

The results obtained from the experiment studying the adsorption of TMP to carbon with DMMP pre-adsorbed show broadly analogous trends to those of the previous experiment. The ratio of peak I to peak II for TMP was ~30:70 after 2 minutes and rapidly increased to reach 50:50 after approximately 10 minutes. It continued to increase slowly throughout the experiment, eventually settling at approximately 65:35. This result compares to the final peak area ratio of 93:7 for 50% w/w TMP adsorbed upon a clean surface. The pre-adsorbed DMMP peak area ratio decreased rapidly from 85:15 at time zero to 60:40 after 10 minutes before gradually increasing once more to reach a value of ~75:25 after 18 hours. Chemical shift data also show a similar pattern to the previous experiment. The chemical shift of TMP peak I shows an initial shift to low frequency of –8.70 ppm, which increases to -8.85 ppm after 1 hour, followed by a slow shift back to higher frequency, reaching -8.60 ppm after 18 hours. The pre-adsorbed DMMP peak I shifts from an initial value of 21.65 ppm to ~21.95 ppm after 18 hours. In both of the sequential adsorption experiments linewidths did not exhibit any significant variation over the course of the experiment.

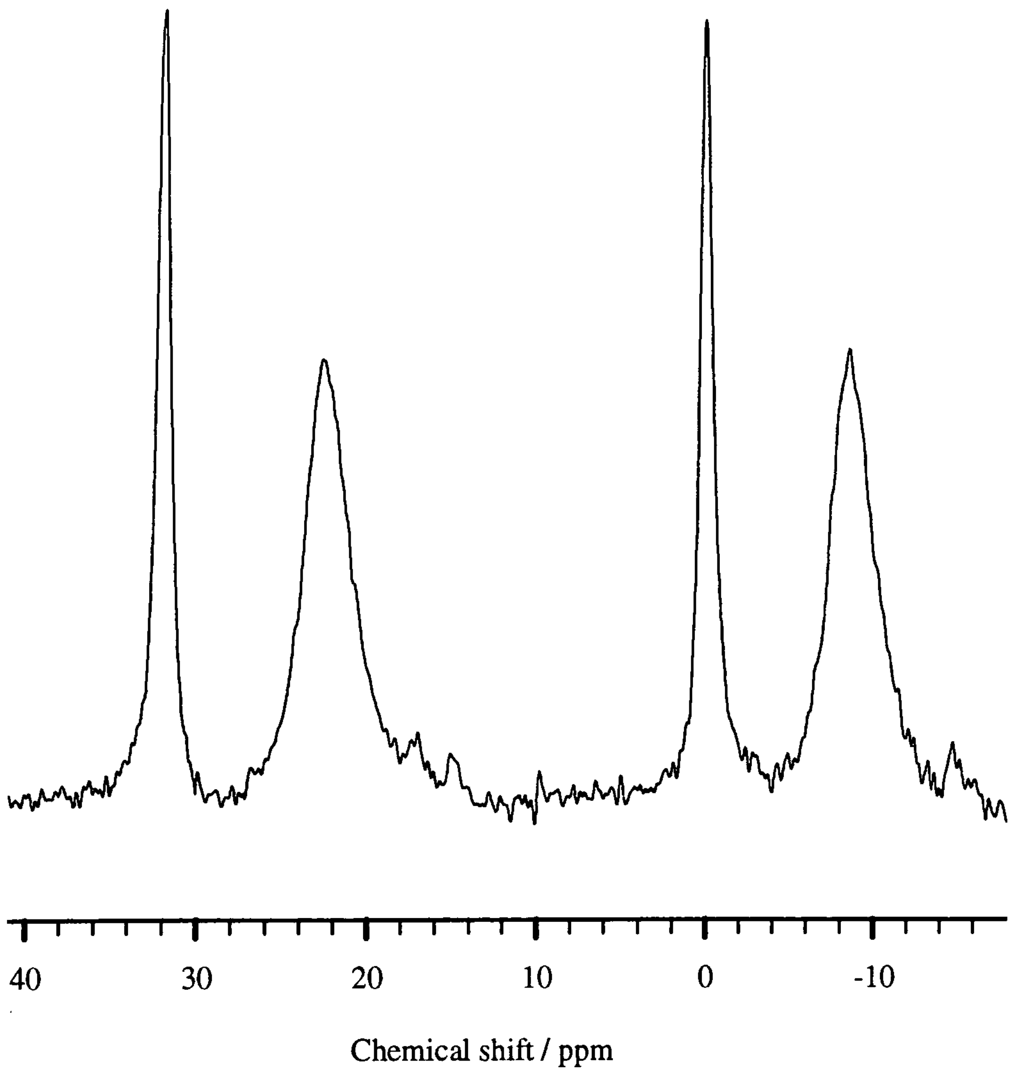

Figure 5.1. Spectrum obtained 16 hours after the addition of 50% w/w TMP to SC2 carbon with 50% w/w DMMP pre-adsorbed. The acquisition parameters are as in the text.

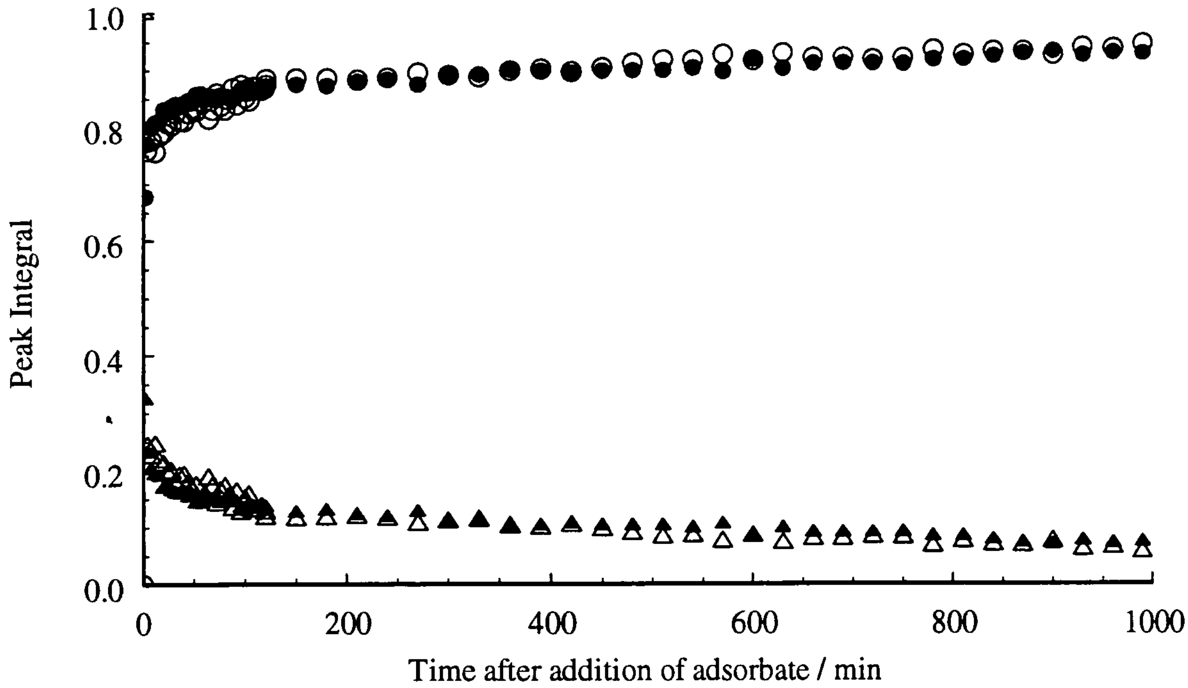

Figure 5.2. Measurements of peak area (total intensity normalised to 1) against time after adsorption for 50% w/w of each individual adsorbate on SC2 carbon. TMP results are shown by open symbols, DMMP filled. Circles denote peak I areas, triangles the areas of Peak II.

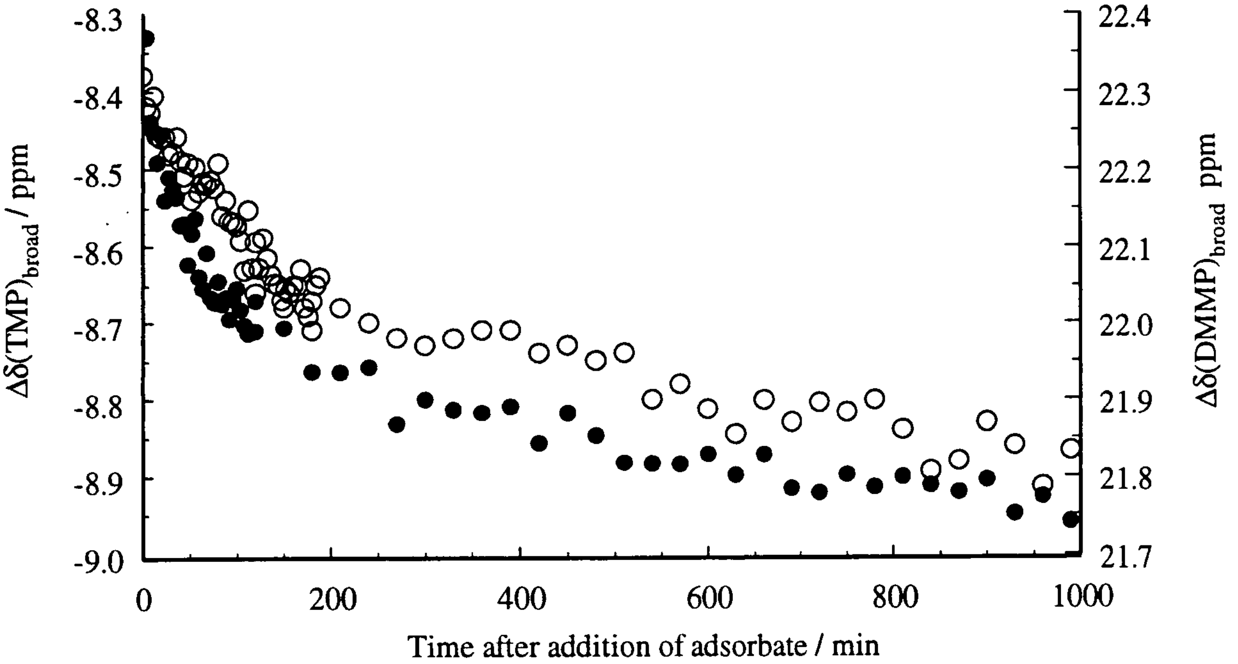

Figure 5.3. The variation in peak I chemical shift with time after adsorption for 50% w/w of each adsorbate. The open symbols refer to TMP, the closed symbols DMMP.

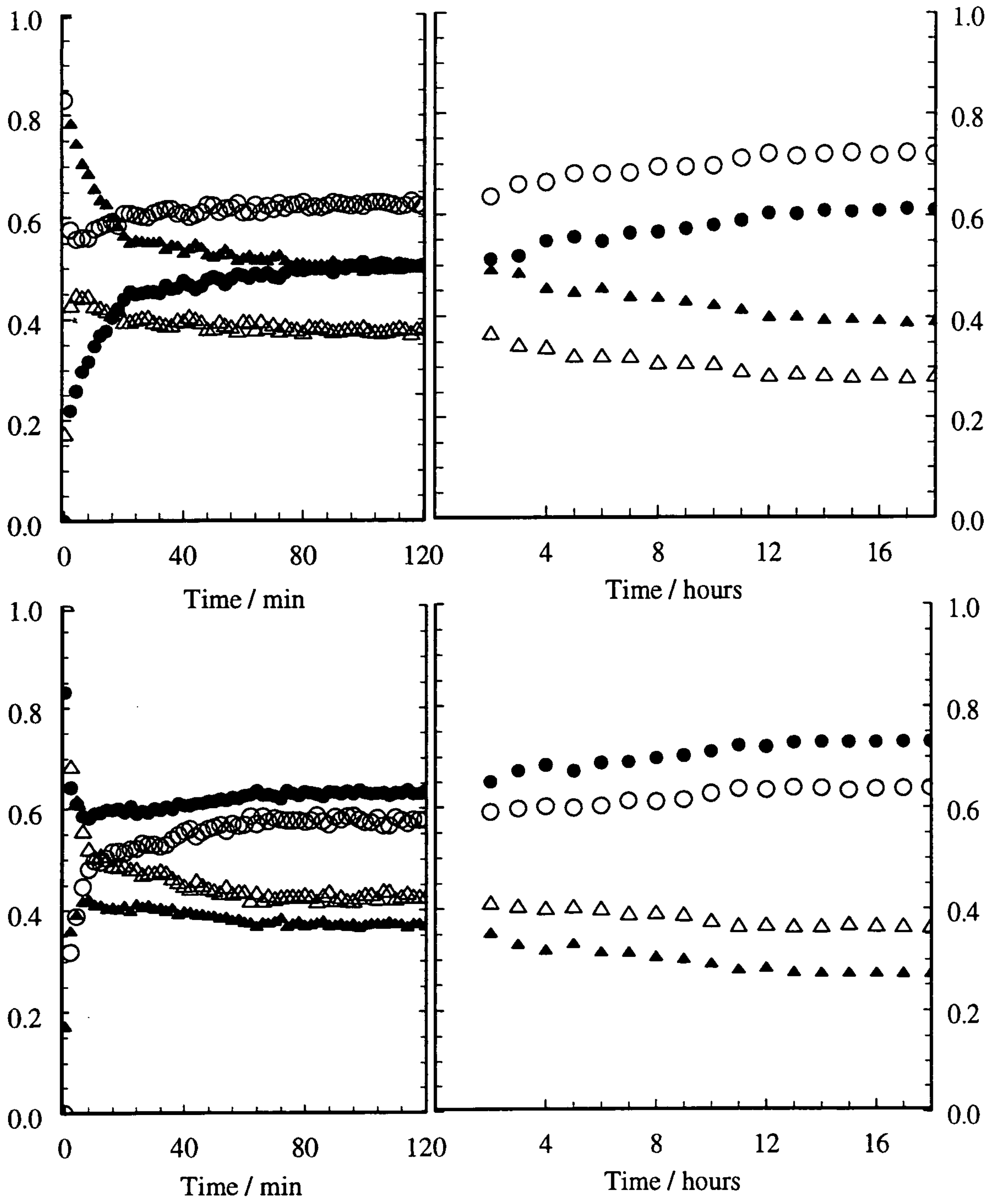

Figure 5.4. Plot of peak areas (total intensity of each adsorbate normalised to 1) against time elapsed after the addition of the second adsorbate. The upper plot shows the results obtained after the addition of DMMP to SC2 with TMP pre-adsorbed. The lower plot shows the peak areas obtained for the inverse experiment. Circles represent peak I areas, triangles peak II. Open symbols denote TMP, closed symbols DMMP.

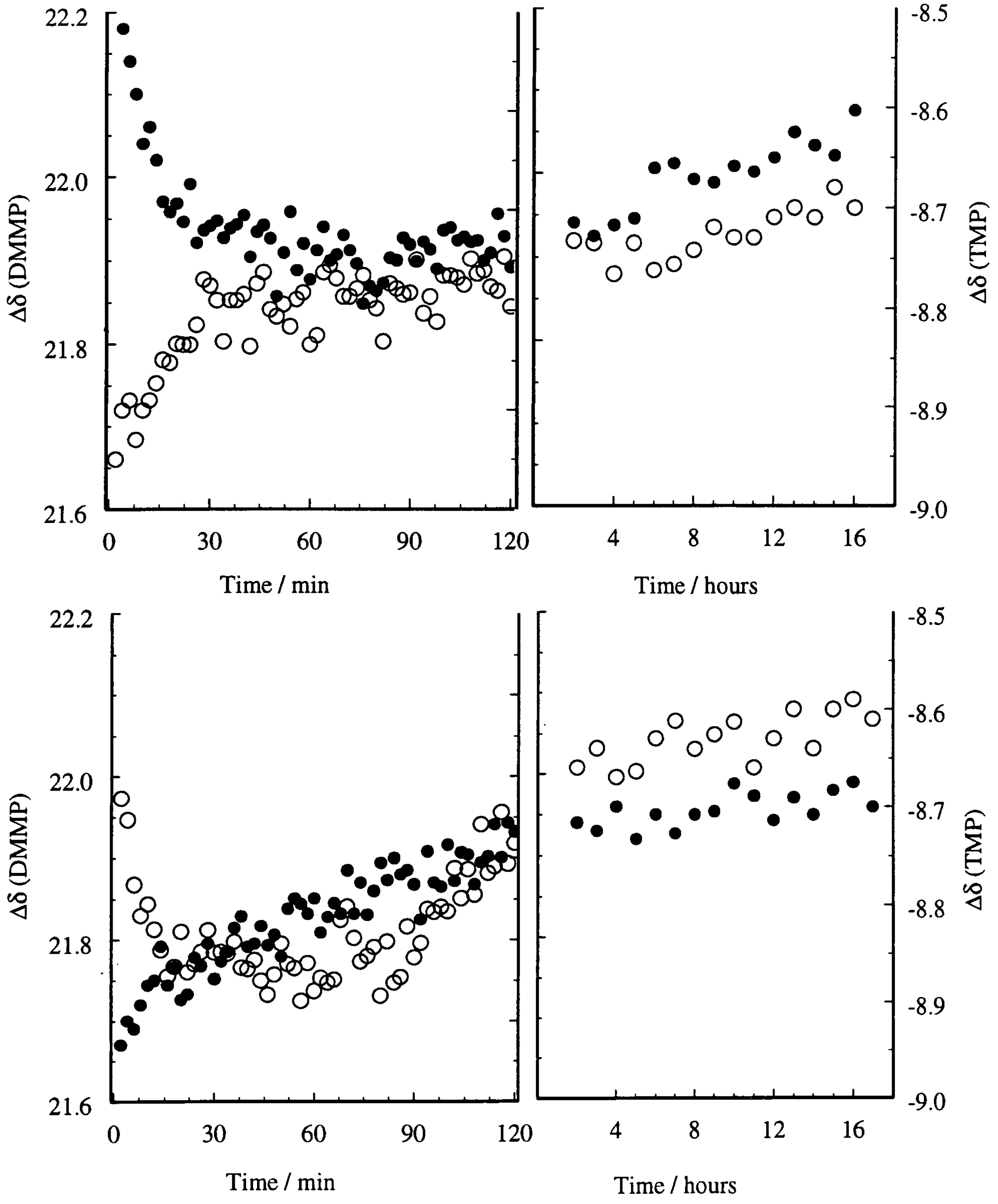

Figure 5.5. Variation in peak I chemical shift with time elapsed after the addition of the second adsorbate. The top plots result from the addition of DMMP to SC2 with TMP pre-adsorbed, whilst the lower plots result from the inverse experiment. Filled symbols represent DMMP, empty symbols denote TMP.

5.1.3. DISCUSSION

At the outset it should be noted that the difference in the chemical shifts of peak I relative to those of peak II between TMP (~-8.7 ppm) and DMMP (~-9.8 ppm) is not particularly significant within the context of this experiment. The chemical shift is simply a measure of the average distance and orientation of the phosphorus nucleus within the molecule with respect to the graphene basal planes of the carbon adsorbent. The TMP molecule has three methoxy groups holding the highly electropositive phosphorus nucleus away from the graphene basal planes present within the carbon, whereas DMMP has only two methoxy groups and a smaller methyl group. Consequently the phosphorus nucleus within a molecule of DMMP can approach the carbon surface more closely than the nucleus within a molecule of TMP, and a larger chemical shift is observed. The two molecules are similar in size to one another, and therefore the calculations relating adsorbate molecular size and the carbon porous volume that were discussed in chapter 4 apply equally to both phosphorus containing molecules discussed within this section.

The peak area and chemical shift results obtained in the three preliminary control experiments showed that the two phosphorus-containing molecules adsorbed in an almost identical manner. The similarity in the ratio of peak areas for each material after 24 hours and the similarity between the two plots in Figures 5.2 and 5.3 are particularly striking. As discussed in chapter 4, the increase in the area of peak I coupled to the increased low-frequency chemical shift shows that the slower adsorption process, occurring upon a timescale of hours, involves progressive adsorption into less accessible, smaller pores. The results did not differ whether the adsorbates were added in a mixture together or singly. It was also noted that the linewidths of peak I for both adsorbates were approximately 30 Hz narrower in the experiments adding 50% w/w of a mixture of the two adsorbates to the carbon than in the experiments studying the adsorption of 50 % w/w of a single adsorbate. It has been suggested that the narrowing could possibly arise because the two materials interfere with one another within the pore, preventing each material packing and ordering in as regular a pattern as when they are adsorbed separately.

The calculated capacity of the pore system was found to differ depending upon the amount of adsorbate added to the system. From the bulk liquid density of each adsorbate and the peak area ratio, adsorption values of ~0.39 $cm^3\ g^{-1}$ were obtained for both of the 50% w/w experiments. Using the rationale outlined in Chapter 4, this corresponds to a total pore volume of ~0.56 $cm^3\ g^{-1}$. However, using the peak area ratios from the 100% w/w experiment it is calculated that almost 0.55 cm^3 of adsorbate material is adsorbed within the pore volume per gram of carbon. The difference in pore capacity depending upon the amount of adsorbate added is related to the reduced low-frequency chemical shifts observed for both molecules in the 100% w/w experiment compared to the 50% w/w experiments. The magnitude of the chemical shift indicates that the average pore size explored by the molecules has increased in the experiment with a greater amount of added adsorbate. The only simple way this may be accounted for is through the size of the individual pores increasing. It is believed that this is a result of the well-documented phenomenon of pore swelling[1], whereby the adsorption of additional material within a pore forces the graphene planes apart, increasing the size of that pore. Pore swelling thus explains the increased adsorption capacity and the decrease in the size of the chemical shift for situations in which larger amounts of adsorbate are added to the system. In the light of these results, the assumption that only 70% of the pore volume is accessible to the adsorbate molecules may need to be re-evaluated when larger amounts of adsorbate are added to the carbon. For example, a total carbon pore volume of 0.80 $cm^{-3}\ g^{-1}$ is calculated from the peak area ratios observed 18 hours after the addition of 50% w/w DMMP to carbon with 50% w/w TMP pre-adsorbed.

The presence of another phosphorus-containing compound already on the carbon slowed down the initial adsorption of the second adsorbate considerably with respect to adsorption upon clean carbon. One benefit of this is that it allows the adsorption process to be observed more conveniently using the NMR technique. In both experiments (Figure 5.4) a decrease in the peak I to peak II area ratio is observed for the pre-adsorbed material during the initial adsorption of the second adsorbate. This results from molecules being displaced from within the pores as the other adsorbate enters, and would account for the slowed initial entry of the secondary adsorbate. Within ten minutes some of the displaced material re-enters the pore system in conjunction with the newly added material, with the pore volume increasing as this occurs. The slow entry of both adsorbates into the pores continues for over 18 hours as the pores slowly stretch to accommodate the increased quantity of phosphorus-containing adsorbate. The total volume of organophosphate adsorbed within the pores increases from ~0.36 cm^{-3} g^{-1} prior to the addition of the second adsorbate to ~0.58 cm^{-3} g^{-1} 18 hours after the second adsorbate was added. This is an increase in the adsorption capacity of the carbon of almost 60%. It is suggested that the two molecules might adsorb in different positions or in a different manner, though this is thought unlikely given the similarity in the two molecules' adsorption behaviour. In order to discount this possibility another control experiment (adding a further 50% w/w TMP to SC2 with 50% w/w TMP pre-adsorbed) was performed over 24 hours, and a similar increase in the volume of material adsorbed was observed, in this case up to 0.56 cm^{-3} g^{-1}.

Further information on the adsorption of the two adsorbates is provided by the chemical shifts of peak I recorded for each material. Almost identical trends are observed in both sequential addition experiments, leading to a conclusion that the effects are primarily due to the order of adsorption. In each case, peak I for the pre-adsorbed material shifts to higher frequency by ~0.3 ppm over the course of the experiment. As discussed previously, an increase in chemical shift implies that the average pore size in which the molecules reside has increased in size. Peak I arising from the adsorbate added second moves to lower frequency by a similar amount during the first hour or so as a result of the molecules' entrance into progressively smaller pores. After this period, the adsorbate low-frequency chemical shift gradually becomes smaller once more, and this trend continues until the end of the experiment. In both cases it was observed that the final chemical shift for each material is greater (i.e. at higher frequency) than that observed for the adsorbate in the experiments performed on the adsorption of 50% w/w of each material separately. This shows that the average pore size explored by the adsorbate molecules has increased in size relative to the pore size explored prior to the addition of the second adsorbate. This is once again in agreement with the suggestion that pores expand to accommodate the increase in adsorbate material. If there were no pore expansion it would be expected that the low-frequency chemical shift of the pre-adsorbed material would continue to increase slowly whilst the chemical shift of the second adsorbate would shift to low frequency as both adsorbate molecules moved deeper into the pore volume.

Another observation obtained from the two sequential adsorption experiments is that the pre-adsorbed material maintains a significantly greater proportion of adsorbate within the pores than that added later. In addition, the material added first has a slightly greater chemical shift than in the corresponding experiment in which it has been added second. This result, coupled with the earlier conclusion that the adsorption process onto clean carbon requires longer than 24 hours to reach equilibrium suggests that the initially adsorbed material maintains a "head-start" in the adsorption process occurring within the less accessible, smaller pores. Thus the initially adsorbed material also demonstrates a larger low-frequency chemical shift. The fact that such a large difference in the amounts of adsorbed material is maintained, even after 24 hours, could also demonstrate "pore-blocking" or related behaviour whereby the initially adsorbed material cannot be displaced from certain positions in which the molecules are particularly strongly bound, such as narrow pores. This process is obviously caused by a property of the carbon adsorption sites rather than by a property of either of the pre-adsorbed materials as a similar effect is observed independent of the order of adsorbate addition. This behaviour has been noted before in studies using long-chain alkanes[2, 3] but not, to our knowledge, for these simple phosphorus-containing compounds.

5.2. THE COMPETITIVE ADSORPTION OF D_2O AND H_2O

The adsorption isotherm of water upon graphite is classified as B.E.T. type 3, which is significantly different to the isotherms obtained for organic and organo-phosphorus materials upon graphite, which are classified as B.E.T. type 2. This means that the interaction of adsorption between a graphene surface and the water molecules is rather weak, whilst the interaction between the organo-phosphorus adsorbates and the graphene surface is much stronger[4]. The adsorption of water by activated carbon is believed to occur via two processes. Initially, adsorption occurs at active surface sites, such as ash or oxygenated heterogeneities, which act as primary nucleation sites[5]. Further adsorption occurs through hydrogen bonding between water molecules, with the activated sites acting as centres for water clusters[4]. The secondary adsorption mechanism occurring in the adsorption of water to activated carbon is via capillary condensation within the micro and meso-pores. The adsorption isotherms of water on activated carbon[6] are classified as B.E.T. type 5 and generally exhibit significant hysteresis, indicative of pore filling by capillary condensation. Various carbon scientists have concluded that the adsorption capacity of activated carbons with respect to water depends upon both the number of activated sites and the microporous volume of the carbon[7, 8, 9]. Considerations of the size of a water molecule and the P.S.D. of SC2 carbon suggest that ~85% of the pore volume is accessible by the water molecules.

5.2.1. EXPERIMENTAL PROCEDURE

An analogous series of experiments to those described above for two organophosphorus compounds was used to study the way in which the adsorption of water was affected by the presence of water already on the carbon. Isotopic labelling with deuterium enabled discrimination between the two "types" of water. In theory it should be possible to study the change in the NMR signal of either the deuterated or non-deuterated water over time. However, the spectra obtained by proton NMR on these samples is complicated by the presence of large, broad peaks arising from protons within the carbonaceous adsorbent. This means that it can be difficult to analyse the peaks ascribed to adsorbed water, especially at low loadings. Studying the deuterated adsorbate circumvents this problem.

Two sequential loading experiments were performed, studying the variation in spectra obtained with time elapsed after the addition of 50% w/w D_2O to SC2 carbon with 50% w/w H_2O pre-adsorbed and vice versa. Once again the adsorbate added initially was left to equilibrate for 2 hours prior to the addition of the second load. A control experiment was also performed studying the adsorption of 50% w/w D_2O on clean carbon. A 5 μs-90° pulse was applied, set using a sample of adsorbed D_2O upon carbon. A recycle delay of 3 seconds was used and 4 acquisitions taken for each spectrum. This gives a total acquisition time of 12 seconds. Spectra were acquired every minute for the first two hours and every thirty minutes thereafter. All chemical shifts are quoted relative to a sample of liquid D_2O, and the spectra analysed using the Spinsight software.

5.2.2. RESULTS

5.2.2.1. Control Experiment

The variations in the spectra and the measured parameters with the time elapsed after the addition of 50% w/w D_2O to SC2 carbon are shown in Figures 5.6, 5.7, 5.8 and 5.9. The peak area measurements show a similar pattern to those obtained for TMP and DMMP. The initial increase in the area of peak I is not as rapid as that observed for the phosphorus-containing molecules, but once again there is evidence of a subsequent slow increase in peak I area over the following 20 hours. The ratio in the area of peak I to peak II increases from 80:20 after 2 minutes to 92:8 after 18 hours. Once again there is an exactly equivalent decrease in peak II area. The two sets of adsorption experiments differ in the results obtained from analysis of the variation in the low-frequency peak chemical shift and linewidth. Whereas the experiments performed on the phosphate and phosphonate showed a gradual increase in magnitude of both chemical shift and the width of the resonance with time elapsed after addition, the current experiment showed a rather different trend in both of these parameters (Figures 5.8 and 5.9). The chemical shift of peak I is displaced to low frequency by approximately 0.2 ppm during the initial 90 minutes and reaches a maximum shift at this time. After flattening off at approximately –9.70 ppm there is a gradual shift to higher frequency continuing until the conclusion of the experiment. After 20 hours the chemical shift was roughly the same as it had been after 2 minutes, though peak area measurements demonstrate that the two spectra are rather different. Measurements of the resonance linewidth show an initial rapid decrease in linewidth from ~115 Hz to ~100 Hz during the first 30 minutes, followed by a slow return to ~110 Hz over the following 20 hours.

5.2.2.2. Sequential Adsorption Experiments

The variation in the measured spectral parameters with time elapsed after the addition of the second portion of water is shown in Figures 5.10, 5.11 and 5.12. In each figure the results obtained from the experiment in which deuterated water was pre-adsorbed are denoted by solid symbols whereas open symbols indicate the experiment with 50% w/w D_2O added to material containing 50% w/w H_2O pre-adsorbed. Prior to the addition of the second aliquot of water, 90% of the spectral intensity was associated with the low-frequency peak envelope. The broad peak envelope was centred at -9.65 ppm and was approximately 120 Hz in width. Within two minutes of the further addition of water to the system, the peak I to peak II area ratio for the pre-adsorbed water had decreased to 60:40. Over the following 18 hours the peak area ratio gradually increased again to reach a final value of 72:28. The water added second entered the pore system relatively slowly, with the peak area ratio increasing from 35:65 after two minutes to 50:50 after ~20 minutes and to 72:28 by the end of the experiment.

The low-frequency chemical shift of peak I arising from water that was initially adsorbed decreases slightly from –9.65 to –9.30 ppm upon addition of the second aliquot of water and the trend continues as the time elapsed increases. The shift of the initially adsorbed water is –9.00 ppm after 2 hours and has reached -8.30 ppm by the end of the experiment. In comparison, the chemical shift of the secondary adsorbate shows very little variation. Two minutes after adsorption the chemical shift of peak I arising from this material is -9.30 ppm and the shift remains reasonably constant throughout the experiment, settling at approximately –9.20 ppm. The width of the peak I arising from the initially adsorbed water increases from 125 Hz after 2 minutes to 140 Hz after 2 hours before decreasing slightly to ~135 Hz by the end of the experiment. The width of peak I resulting from the water added second showed a steady increase throughout the experiment, from ~110 Hz after 2 minutes to ~130 Hz after 18 hours.

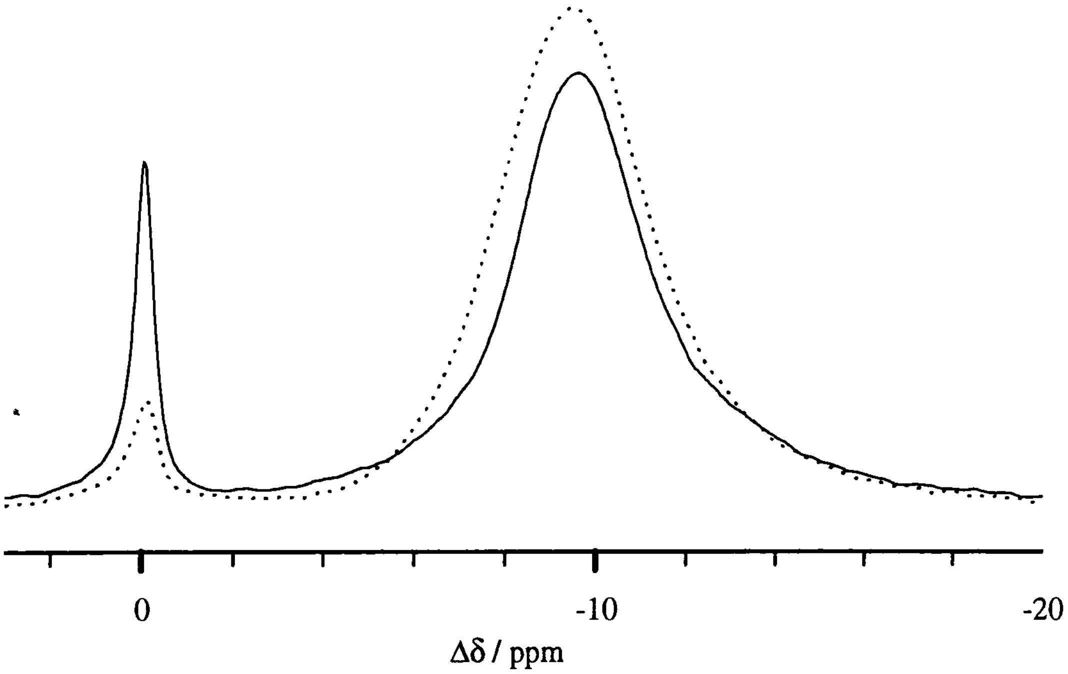

Figure 5.6. Comparison of spectra recorded at different times after addition of 50% w/w D_2O to SC2 carbon. The dotted line represents the spectrum obtained after 20 hours, the solid line was recorded after 2 minutes. The total intensity of each spectrum is equal.

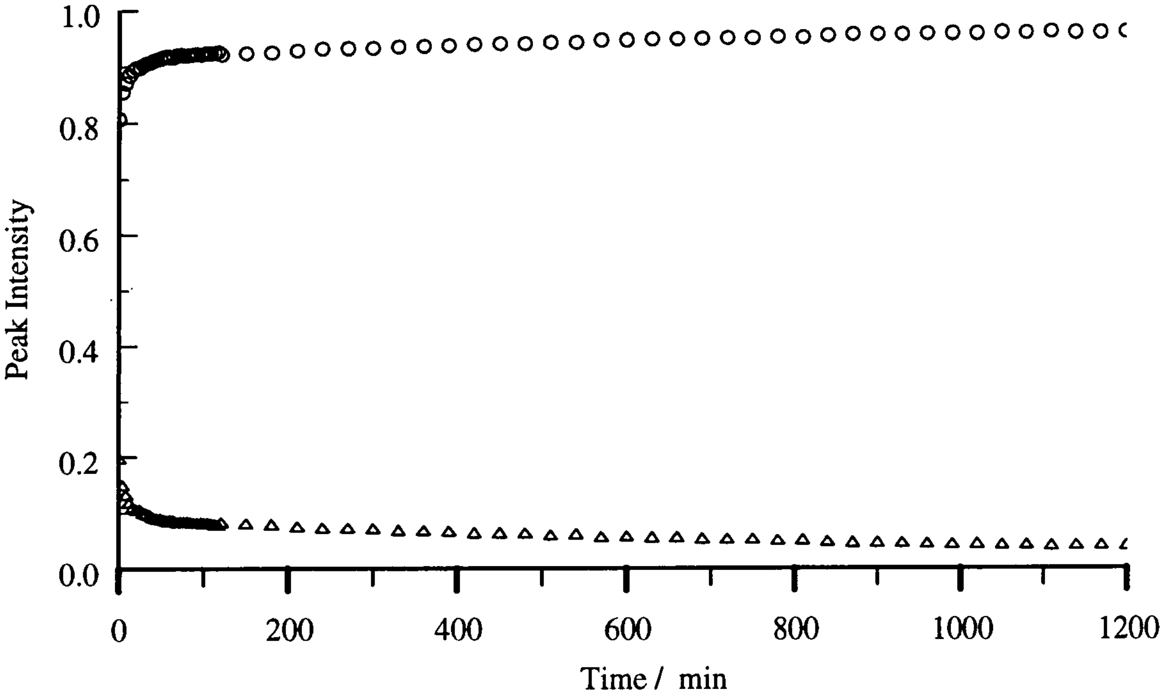

Figure 5.7. Variation in peak area (in arbitrary units) with time after adsorption of 50% w/w D_2O on SC2 carbon. Circles represent low-frequency peak area whilst triangles indicate the area of peak II.

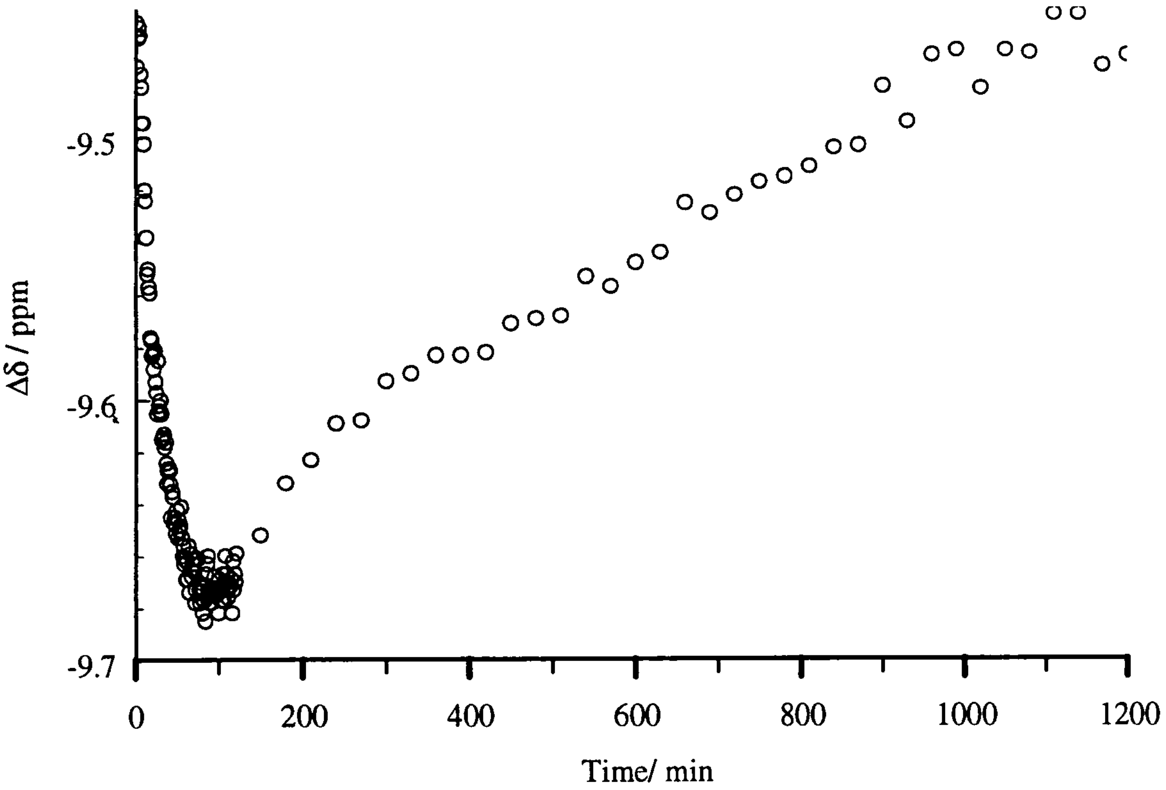

Figure 5.8. Variation in the chemical shift of the low-frequency peak with time elapsed after the addition of 50% w/w D_2O to SC2 carbon

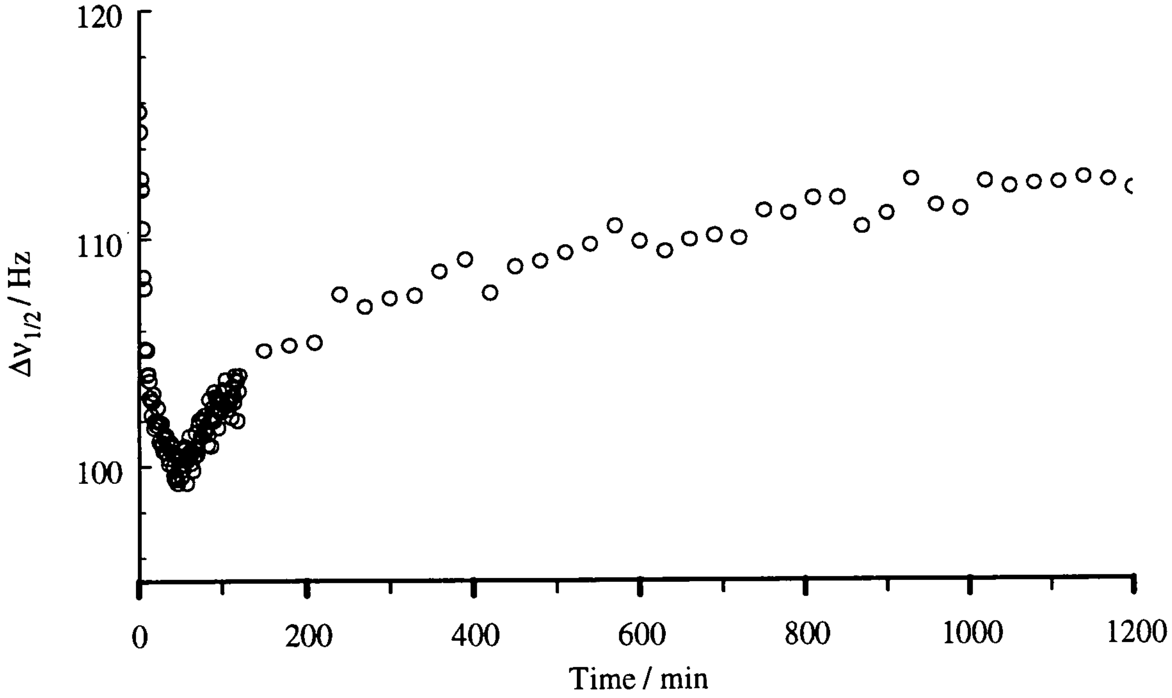

Figure 5.9. Variation in the width of the low-frequency peak with time after the addition of 50% w/w D_2O to SC2 carbon.

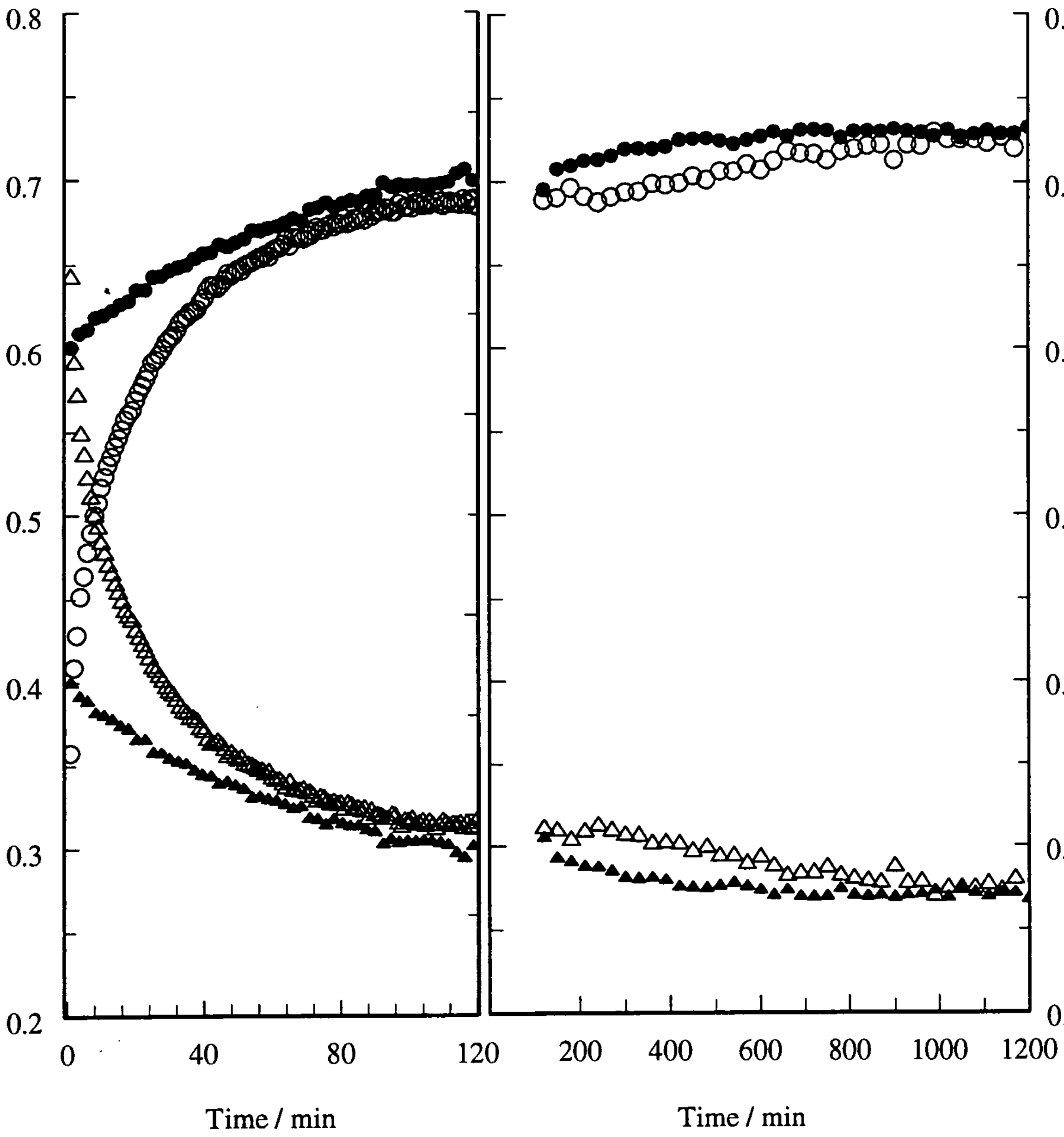

Figure 5.10. Variation in peak areas (total intensity of each adsorbate normalised to 1) with the time elapsed after the addition of the second aliquot of water. Solid symbols represent the peak areas of the initially adsorbed water whilst hollow symbols denote the material adsorbed second. Once again circles represent peak I areas, triangles peak II.

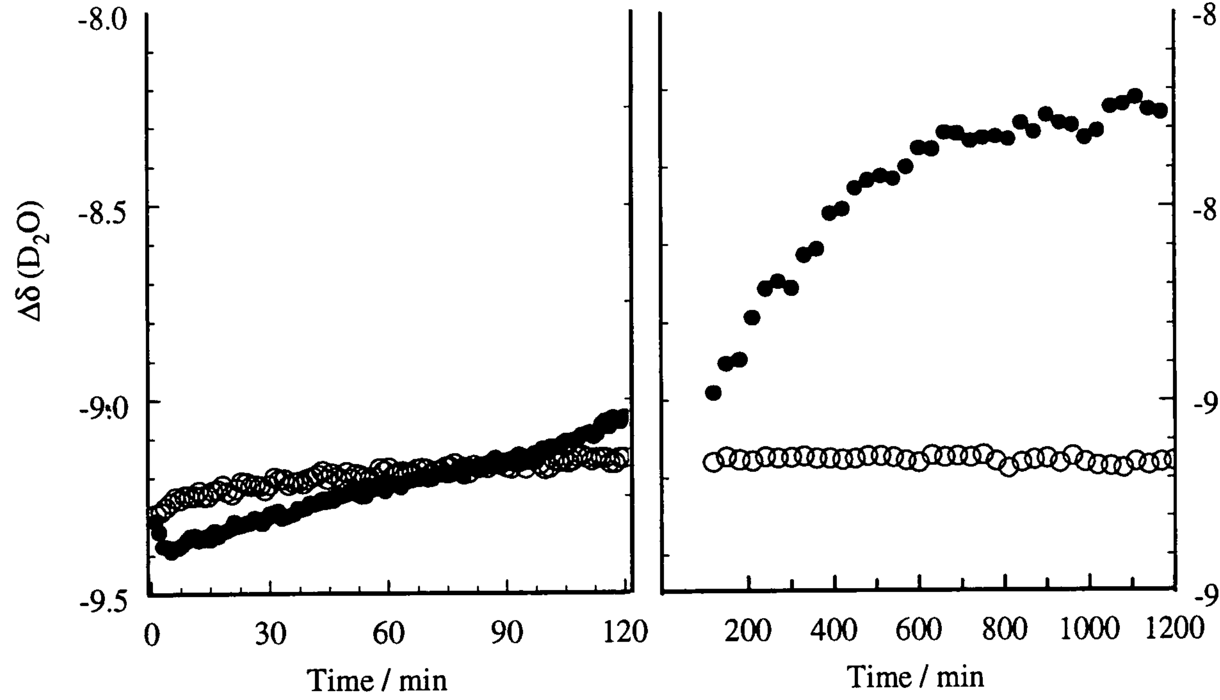

Figure 5.11. Variation in peak I chemical shift with time elapsed after the addition of the second aliquot of water. Solid symbols represent the initially adsorbed water, hollow symbols the water added second.

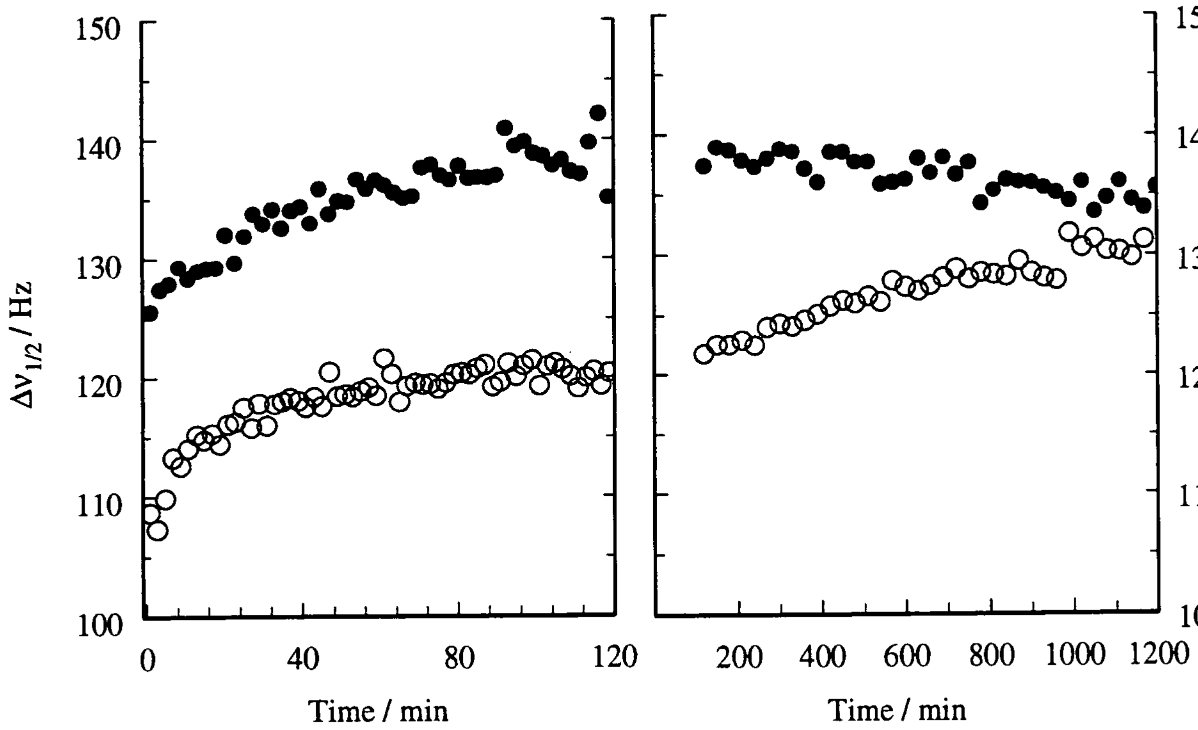

Figure 5.12. Variation in measured linewidth with time elapsed after the addition of the second adsorbate. Solid symbols represent pre-adsorbed water, hollow symbols that added second.

5.2.3. DISCUSSION

5.2.3.1. The Adsorption of water upon SC2 carbon

The information within Figures 5.7, 5.8, 5.9 and 5.10 shows that the adsorption process of water upon activated carbon is similar, but not completely analogous, to that of the phosphorus-containing molecules studied previously. Peak-area measurements demonstrate that water rapidly enters the pore system after being added to the sample surface. The measurements also show that a slow adsorption process continues throughout the experiment. Using the peak areas obtained after 20 hours and the density value of bulk deuterated water, it can be calculated that the carbon adsorbs roughly 0.42 cm^{-3} g^{-1} of deuterated water within its pores. Mercury porosimetry data suggests that ~85% of the carbon pore volume should be accessible to the deuterium oxide molecules, leading to a calculated pore volume of ~0.49 cm^{-3} g^{-1}.

The difference in the adsorption of water to that of organophosphorus compounds is shown by the variation in the chemical shift and linewidth of peak I over time. Given the large differences in the adsorption isotherms of the two materials, it is not surprising that a difference in adsorption mechanism is observed via NMR. Activated sites play a vital role in the adsorption of hydrophilic materials upon activated carbon, and it is thought that the activity of the sites in the adsorption of water provides an explanation for the trends observed. It is generally believed that adsorption of hydrophilic molecules occurs preferentially about oxygenated sites followed by capillary condensation within smaller pores. The anisotropy in the magnetic susceptibility experienced by a molecule adsorbed at an oxygenated heterogeneity, such as a projecting ketone group, will be less than that of molecules adsorbed upon the surrounding aromatic basal plane, both because of the increased distance of the adsorbed molecule from the plane and because of the disruption in the aromaticity of the plane introduced by the presence of the heterogeneity. Therefore molecules adsorbed at such sites will exhibit a reduced low-frequency chemical shift compared to those adsorbed directly upon a graphene plane.

Chemical shift and linewidth measurements imply that adsorption occurs in two, reasonably distinct, stages. During the initial hour after the addition of water to activated carbon the magnitude of the low-frequency chemical shift increases with a simultaneous decrease in the width of the resonance observed. The chemical shift results suggest that the average distance between the adsorbed molecules and the graphene surface is decreasing. This is thought to result from a gradual decrease in the pore sizes explored by the water molecules as adsorption progresses, in an analogous way to that of TMP adsorption. The variation in chemical shift is less pronounced than that of TMP because of a concurrent re-ordering of molecules about the oxygenated sites within the pores. This process becomes the more important effect after approximately 90 minutes and is discussed in more detail below. The linewidth of the low-frequency resonance is relatively small during this period because the adsorption of the water molecules upon the hydrophobic surface does not cause a significant decrease in the molecular mobility. Why a continuing decrease in linewidth is observed for the first 45 minutes is not certain.

Analysis of the spectra during the second period (from approximately $1^1/_2$ hours after adsorption onwards) shows that the shift of the peak I towards higher frequency is caused by an increase in the intensity of the higher frequency portion of the peak. It is also noted that a greater range of chemical shifts is being explored at that end of the peak. The movement of the average chemical shift towards higher frequency indicates that the mean distance of the adsorbed molecules from the graphene planes is becoming greater as the adsorption process continues. If a similar interpretation is used to that in chapter 4, the implication of the shift towards high frequency is that the average pore size explored by the water molecules is becoming progressively larger as the experiment continues. The possible effect of pore swelling cannot account for the increase in average pore size as there is only a very slight increase in pore capacity during this period. An increase in the size of pore explored also does not seem particularly likely, as it implies that there were a number of large pores that were not filled during the initial adsorption and it does not account for the simultaneous increase in low-frequency peak linewidth.

A more plausible explanation, and one that also accounts for the observed behaviour of the water molecules in subsequent competition experiments, is that the high frequency chemical shift is the result of an increase in the ratio of molecules adsorbed at activated sites compared to the molecules adsorbed as capillary condensate. This would be caused by a slow redistribution of water molecules about the oxygenated sites within filled pores, or possibly from the continued progression of adsorbate into pores with a larger proportion of surface oxides. The larger number of molecules strongly adsorbed at oxygenated sites also accounts for the increase in resonance linewidth, as the average mobility of the water molecules decreases.

It has also been suggested that these results arise from exchange of OH protons on the carbon with deuterium nuclei from the adsorbate. However, as discussed in chapter 2, alcohol groups do not form a significant proportion of the active sites within activated carbon. Preliminary control experiments have also demonstrated that very little exchange of this type occurs. 50% w/w D_2O was added to a sample of SC2 carbon and was left to equilibrate for over 24 hours. The sample was then heated under vacuum to remove the adsorbed water. The procedure was repeated 10 times over the course of two weeks. After the final vacuum treatment a single pulse experiment at the deuterium frequency was performed upon the carbon. No deuterium signal was obtained after acquiring for twelve hours. Thus it was shown that there was no significant exchange of nuclei between the carbon adsorbent and the adsorbate in this instance.

5.2.3.2. Sequential Adsorption Experiments

The interpretation of the results from this pair of experiments is complicated by the possibility of chemical exchange of nuclei between the two adsorbates. In aqueous solutions there is rapid exchange of protons and deuterons between molecules, and it is likely that inter-molecular atomic exchange will also occur within the pores. The process will not be as rapid as in solution because the two types of water are kept separate to some extent by the pores and the molecules are not in such intimate contact.

However, the changes in the deuterium spectra observed over time may arise from either movement of entire molecules within the pore system or simply from rapid inter-molecular exchange of atoms. It is clear that atomic exchange is not occurring as rapidly as in solution simply from the variation in the spectra observed over time. If HOD was rapidly formed from the mixture of H_2O and D_2O within the pores then no difference would be observed in the chemical shift and linewidths of each of the two species adsorbed first and second after several minutes. However, Figures 5.11 and 5.12 show that there are marked differences between the two, continuing (and in some cases increasing) until the end of the experiment. Clearly the atoms within the two species are not undergoing the same exchange process as is found in solution.

The results below are interpreted assuming that the main mechanism of exchange occurring is chemical exchange of molecules. However, this is not necessarily the case, and the possibility of inter-molecular atomic exchange should be borne in mind when drawing conclusions from the experiment. That said, the results from this section of the chapter tie in remarkably well with the results from the next series of experiments performed upon a system with no possibility of atomic exchange. Unambiguous results would be obtained from the competitive water adsorption experiments if each of the experiments was repeated using ^{17}O-labelled water in competition with normal water.

The results show that adding an increased amount of adsorbate to the system will force the porous volume to expand and adsorb more material. Prior to the addition of the second adsorbate the volume of water adsorbed within the pores of the carbon was 0.41 cm^{-3} g^{-1}. After two minutes the total volume adsorbed increased to approximately 0.48 cm^{-3} g^{-1} and continued to increase, reaching 0.6 cm^{-3} g^{-1} after 40 minutes and 0.7 cm^{-3} g^{-1} by the end of the experiment. This corresponds to an increase in the carbon pore capacity of almost 70%. Once again it is suggested that the slow increase in porous capacity occurs through pore expansion. In this instance the suggestion is slightly more tentative than for the experiments on organophosphorus compounds as the limited change in the low-frequency chemical shift of the material added second does not necessarily corroborate this rationale. As in the control experiment, a shift to higher frequency is mainly ascribed to preferential adsorption at activated sites rather than entry into progressively larger pores. The addition of the second aliquot of water causes the chemical shift of the initially adsorbed water to move to higher frequency by almost 1 ppm whilst the chemical shift of the water added second remains almost constant throughout the experiment. Clearly there is discrimination in the positions of adsorption between the two types of water, preventing exchange between the two environments. The results show that a greater proportion of the primarily adsorbed water molecules are displaced from non-activated sites, whilst water molecules initially adsorbed at activated sites are not displaced to such an extent. Therefore after 24 hours the majority of water molecules adsorbed at activated sites belong to the pre-adsorbed water whilst the molecules adsorbed as capillary condensate are made up of a mixture of both adsorbate materials. The greater percentage of initially adsorbed water at activated sites is also shown by the difference in the linewidth of the two adsorbates.

The preferential adsorption also provides an explanation as to why the secondary shift to high frequency observed in the experiment studying the adsorption of 50% w/w water on clean carbon is not observed in the chemical shift of the aliquot added second. The oxygenated sites at which reordering is thought to occur in the control experiment are already occupied in the competition experiment and therefore do not affect the spectrum of the secondary water aliquot. It is also interesting to note the similar trends in the chemical shift of pre-adsorbed water observed in the next section, studying the competition between TMP and D_2O.

5.3. THE COMPETITIVE ADSORPTION OF TMP AND D_2O

5.3.1. EXPERIMENTAL PROCEDURE

Two experiments were performed, studying the adsorption of 50% w/w D_2O to SC2 carbon with 50% w/w TMP pre-adsorbed and the converse experiment studying the adsorption of 50% w/w TMP to SC2 with 50% D_2O w/w pre-adsorbed. In each case the sample was allowed to equilibrate for two hours between the adsorption of the two aliquots. Each experimental run was performed twice, looking at the deuterium frequency in one of the two experiments and the phosphorus frequency in the other. The acquisition parameters used were the same as in section 5.1.1 when acquiring at the phosphorus frequency and the same as in section 5.2.1 when acquiring at the deuterium resonance. The results from the experiments studying the adsorption of each adsorbate to clean carbon, obtained previously, are referred to in the discussion section.

5.3.2. RESULTS

The results from the pair of experiments are shown in Figures 5.13, 5.14 and 5.15. In each figure the results from the experiment in which 50% w/w D_2O was added to SC2 carbon with 50% w/w TMP pre-adsorbed are shown in the higher of the two plots, whilst the results of the inverse experiment are shown at the bottom. The results obtained from TMP are shown as empty symbols whilst the results obtained from D_2O are denoted by solid symbols. The results obtained for the addition of water to SC2 with TMP pre-adsorbed are summarised first.

The spectrum recorded for SC2 with TMP adsorbed, recorded just prior to the addition of D_2O, gave a peak I to peak II area ratio of approximately 83:17. Two minutes after the addition of D_2O the TMP peak area ratio had decreased slightly to 79:21. In the same period the D_2O peak area ratio increased from 0:100 to 30:70. During the following 15 minutes the peak area ratio of both adsorbates increased, TMP from 79:21 to 83:17 and D_2O from 30:70 to 34:66. The TMP low-frequency peak area continued to increase slowly throughout the experiment and a final peak area ratio of approximately

90:10 is observed. At the same time the D_2O peak I to peak II area ratio decreases slightly to a value of 30:70. The ongoing adsorption of TMP after the adsorption of D_2O is also demonstrated by the continued increase in low-frequency chemical shift from –8.55 ppm observed at the start of the experiment to –8.80 ppm 20 hours later. The chemical shift of the low-frequency peak prior to the addition of D_2O was -8.60 ppm. The opposite trend to TMP is shown by D_2O as the chemical shift of the low-frequency chemical shift decreases from -9.20 ppm to –7.80 ppm over the course of the experiment. The linewidth of TMP undergoes a very slight increase from 250 Hz at the start of the experiment to ~270 Hz at the end, whilst the D_2O low-frequency resonance is broadened to a greater extent, from 150 Hz after 2 minutes to ~210 Hz after 20 hours.

The peak area results obtained for the experiment in which TMP was added to SC2 with D_2O pre-adsorbed are reasonably similar to those discussed for the previous experiment. This shows that the order of adsorption of the two adsorbates is not particularly important in this instance. Measurements performed upon the carbon sample with D_2O adsorbed, just prior to the addition of TMP, yielded a peak area ratio of almost exactly 90:10. Within two minutes of the addition of TMP this value had fallen to 36:64. The peak area ratio continued to decrease slowly throughout the experiment, eventually reaching a value of 30:70 after 20 hours. The area ratio of peak I to peak II for TMP increased from zero to 70:30 in the initial two minutes and continued to increase reasonably rapidly for the first few minutes, reaching a value of 80:20 within an hour. The peak area ratio continued to rise throughout the experiment reaching a value of 86:14 at the end of the experiment. The low-frequency chemical shift of the TMP shows a rapid initial increase from –8.25 ppm after 2 minutes to –8.60 ppm after 10 minutes followed by a slow increase to a final value of -8.70 ppm. The chemical shift of peak I for D_2O changes from -9.55 ppm to –8.10 ppm over the course of the experiment. Linewidth measurements for peak I for both species show a gradually slowing increase over the course of the experiment. The low-frequency peak of TMP increases in width from ~230 Hz to ~260 Hz over the course of the experiment whilst that of D_2O increases from 150 Hz to ~200 Hz.

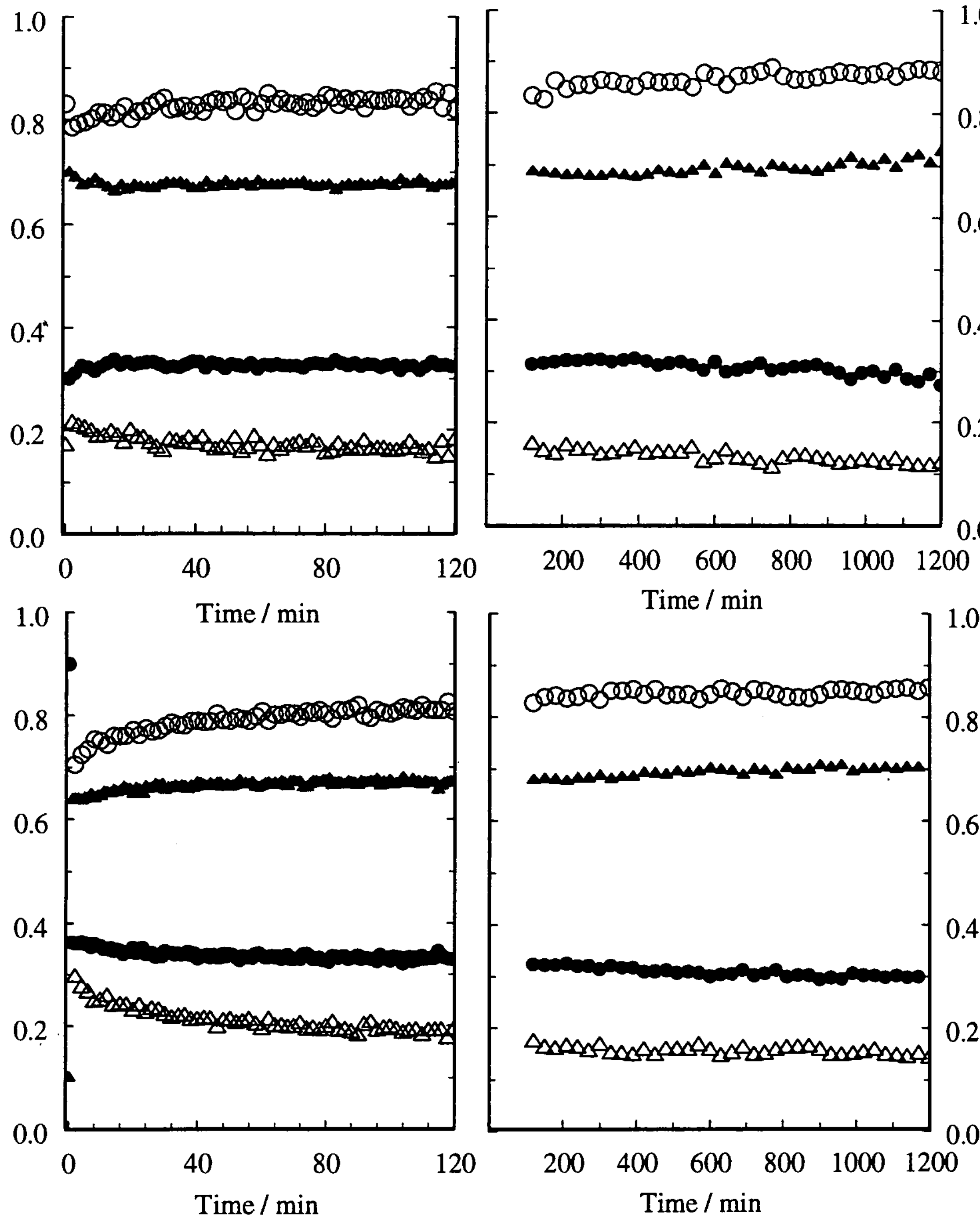

Figure 5.13. Variation in peak areas (total peak intensity for each species normalised to 1) The experiment in which water is added to SC2 with TMP pre-adsorbed is shown in the higher plots, the inverse experiment in the lower. TMP peak areas are denoted by hollow symbols, D_2O by solid. Circles describe peak I areas, triangles peak II

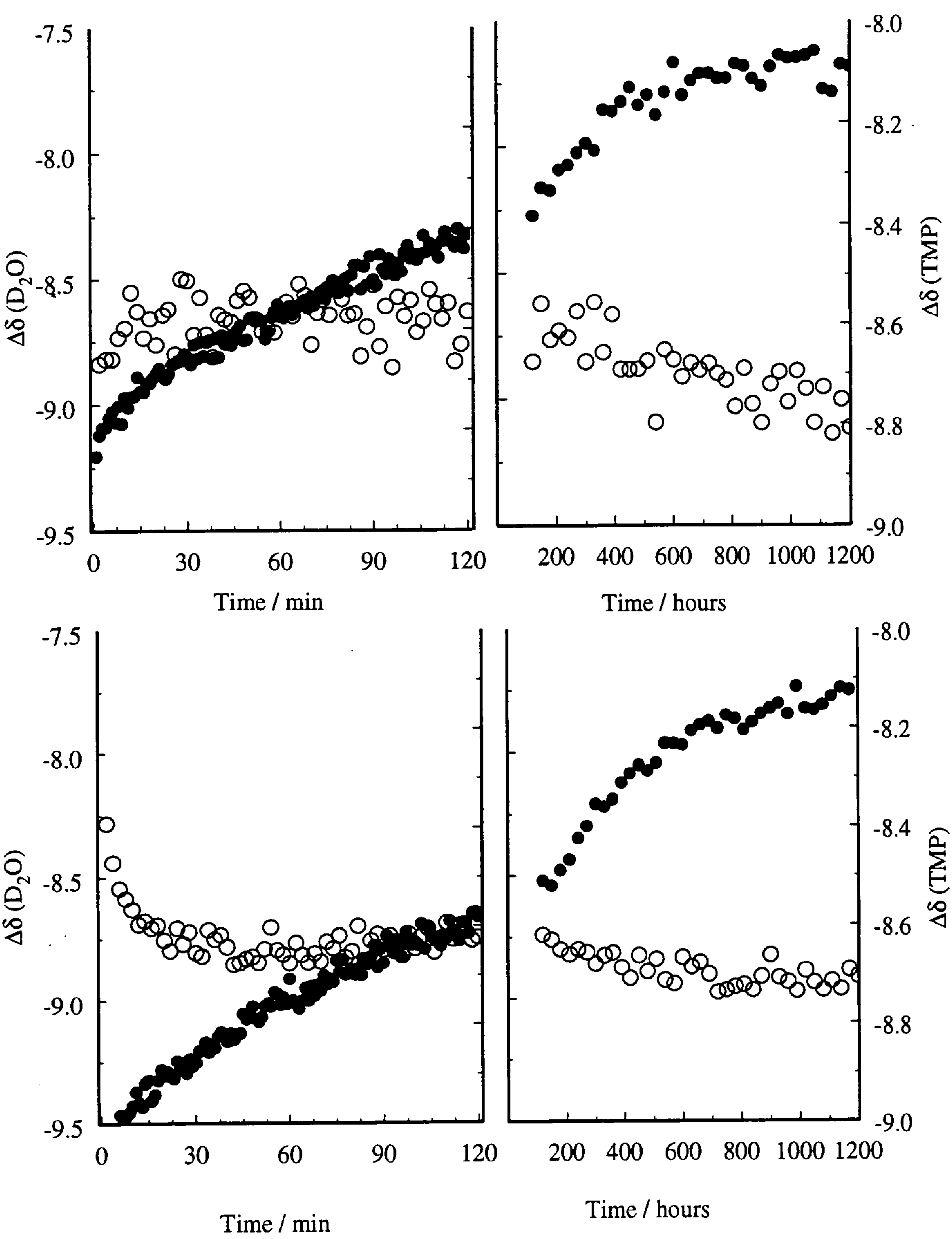

Figure 5.14. Variation in peak I chemical shift with time elapsed after addition of the second adsorbate. The top plots show the results from the experiment adding D_2O to SC2 with TMP pre-adsorbed. Hollow symbols represent TMP, solid symbols the chemical shift of D_2O.

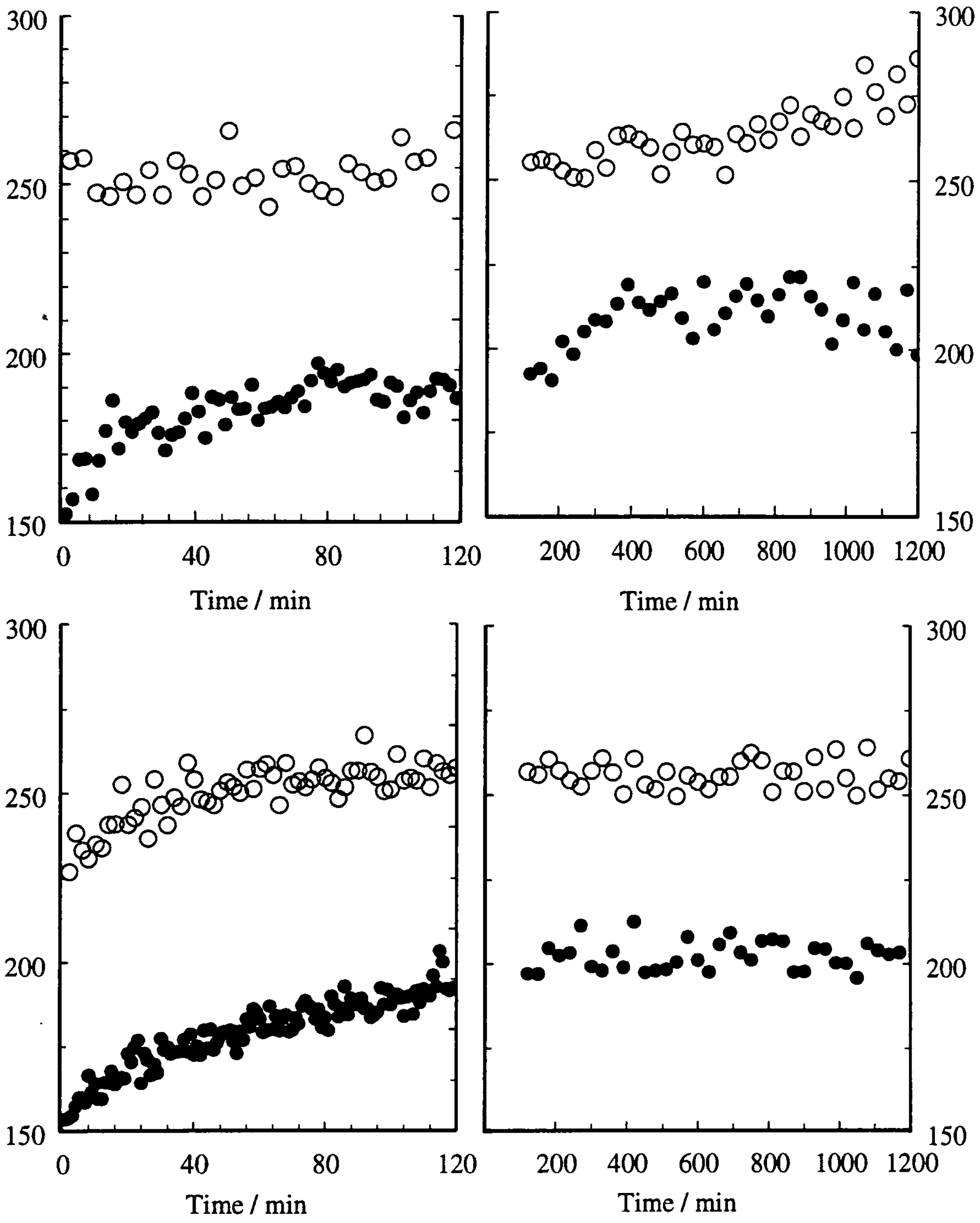

Figure 5.15. Variation in the width of the low-frequency peak with time elapsed after the addition of the second adsorbate. Top plots show the results obtained for the experiment in which water is added to SC2 with TMP pre-adsorbed, the lower plots show the inverse experiment. Hollow symbols represent TMP, solid D_2O

5.3.3. DISCUSSION

The measurements show that the adsorption of TMP is only affected slightly by the presence of water upon activated carbon. Comparison of the variation in peak areas with time for the adsorption of TMP on clean SC2, and upon SC2 with D_2O pre-adsorbed illustrates this point. The area ratio of peak I to peak II observed after two minutes in the experiment with pre-adsorbed water is ~70:30 compared to ~80:20 for addition to clean carbon, suggesting that the presence of water upon the carbon has slowed the entry of TMP into the porous volume by a small amount. This compares to the marked decrease observed in the rate of TMP pore entry observed upon a carbon sample with DMMP pre-adsorbed. The final peak area ratio in the experiment (87:13) is slightly lower than that observed for the addition of TMP to clean carbon (92:8) indicating that the amount of TMP adsorbed within the pores after 18 hours is decreased by ~5% by the presence of water. The TMP low-frequency chemical shift measured in the same experiment decreases from -8.25 ppm to –8.70 ppm over the course of the experiment, a result of continued adsorption within progressively smaller pores. The increase in the TMP low-frequency resonance linewidth may be explained via the greater range of chemical shifts explored by the adsorbed molecules. Comparison of these results with the values observed after the addition of TMP to clean SC2 carbon also show that the trends in chemical shift and linewidth are largely independent of the presence of D_2O.

Conversely, the addition of TMP affects the pre-adsorbed D_2O markedly. Within 2 minutes the amount of D_2O within the pores has been reduced to less than one half of its value prior to the addition of TMP. However, once this initial reduction has occurred there is very little further change in the peak area ratio. This suggests that there is a reasonably clear division between sites at which D_2O can be displaced easily by TMP and sites at which D_2O is preferentially adsorbed over TMP. The location of the sites at which preferential adsorption occurs is suggested by the large (over $1^1/_2$ ppm) decrease in the D_2O peak I low-frequency chemical shift during the experiment. As was mentioned previously, the magnetic susceptibility anisotropy about oxygenated heterogeneities will be smaller than that above a graphene plane. The importance of these sites in the adsorption of hydrophilic adsorbate molecules has also been noted. Thus it is suggested that the TMP molecules rapidly displace the water molecules adsorbed within accessible pores during the first moments after adsorption. The TMP molecules adsorb to the carbon surface far more strongly than the water molecules and therefore water molecules adsorbed upon the carbon surface are easily removed. The molecules adsorbed at oxygenated heterogeneities are strongly bound by hydrogen bonds and are not displaced by TMP molecules and therefore remain. This also provides an explanation for the reduced adsorption of TMP observed after 20 hours in the two competition experiments compared to that upon clean carbon. The presence of strongly bound water at some points within the pore volume means that TMP is not able to completely fill the pore volume. The increase in the D_2O low-frequency resonance linewidth results from the decreased average mobility of the remaining water molecules. As the displacement occurs the averaged chemical shift of the remaining water molecules (comprising those molecules at or near oxygenated sites and capillary condensate within pores that are less accessible to TMP) starts to shift towards higher frequency. As the adsorption of TMP continues, water is displaced from progressively less accessible pores and the proportion of capillary condensate giving rise to the D_2O low-frequency resonances decreases further. Thus the magnitude of the D_2O low-frequency peak chemical shift continues to decrease, with a simultaneous increase in resonance linewidth.

Comparison of the spectra obtained for pre-adsorbed water after the addition of a second adsorbate in both the previous and current set of experiments is also instructive. In the experiment analysing the displacement of deuterated water by a further addition of water approximately 70% of the pre-adsorbed material remained within the pores. In the current study only 30% of the initially adsorbed water remained after the addition of TMP. This further demonstrates the preferential adsorption of TMP over water upon activated carbon. The final chemical shift of the pre-adsorbed water in the current experiment is found to be at higher frequency than that observed in the D_2O / H_2O

experiment (-8.1 ppm compared to –8.25 ppm). This again shows that the sites at which water is preferentially adsorbed are those at which there is a smaller magnetic susceptibility anisotropy, namely oxygenated heterogeneities upon the walls of the pores.

The small effect that D_2O has upon the adsorption of TMP can also be seen in the peak area results from the experiment in which deuterated water is added to carbon with 50% w/w TMP pre-adsorbed. The addition of D_2O to the system causes a slight displacement of the pre-adsorbed TMP from within the pore volume (the TMP peak I to Peak II area ratio decreased from 83:17 to 79:21 after the addition of D_2O) but adsorption of TMP continues largely unaltered after this. After 20 hours the TMP peak area ratio observed was 89:11 compared to the value of 92:8 recorded for the adsorption of TMP to SC2 without the addition of D_2O to the system. The peak I chemical shift of TMP also continues to move towards low frequency as the adsorption continues, again in a similar manner to that observed for TMP without the addition of D_2O part of the way through the adsorption process. After 20 hours the TMP chemical shift observed in this experiment is ~-8.80 ppm compared to the value of –8.85 ppm observed for the adsorption of TMP on clean carbon. Despite the addition of D_2O having a limited effect upon TMP, it is clear that D_2O interacts significantly with the carbon. Within two minutes of addition approximately 30% of the D_2O has entered the pore volume (displacing only ~4% of the TMP). The chemical shift of the low-frequency resonance of D_2O also shows that the water molecules are deep within the pore volume. Once again the D_2O chemical shift gradually increases over time as there is rearrangement of molecules within the pore volume and the water molecules adsorb preferentially at the oxygenated heterogeneities within the pore volume.

The additional adsorption of material (the total volume of adsorbate within the pores increases from 0.35 cm^{-3} g^{-1} just prior to the addition of the secondary adsorbate to 0.48 cm^{-3} g^{-1} 20 hours later, an increase of ~37%) occurs almost completely within the first two minutes of the experiment. In the two previous series of experiments, studying the competitive adsorption of two similar adsorbates, the pore swelling occurred over several hours and was accompanied by a decrease in the low-frequency chemical shift of both adsorbates. The increase in the total volume of material within the pores for each of the competitive adsorption experiments (as a percentage of the total volume observed after 2 minutes) is shown in Figure 5.16.

The values in this graph were calculated from the sum of the peak I to peak II area ratios in each competition experiment, divided by the bulk liquid density of each adsorbate. In experiments where there were two sets of results, depending upon which adsorbate was added first, the order of addition was found not to alter the results significantly and the values obtained from each of the two runs were averaged. There is a clear similarity in the plots for the competition experiments performed in sections 5.1 and 5.2, in which the increased capacity of the pores was ascribed to pore expansion. It is obvious that the increase in the volume of material adsorbed within the pores in the current study arises from a different cause to that of the previous two sections. It is suggested that the increase in the volume of material adsorbed in this instance is due mainly to the fact that the two, very different, adsorbate molecules adsorb at different sites, rather than via a pore swelling mechanism. The TMP molecules adsorb directly upon the graphene planes whilst the hydrophilic water molecules nucleate about projecting activated sites.

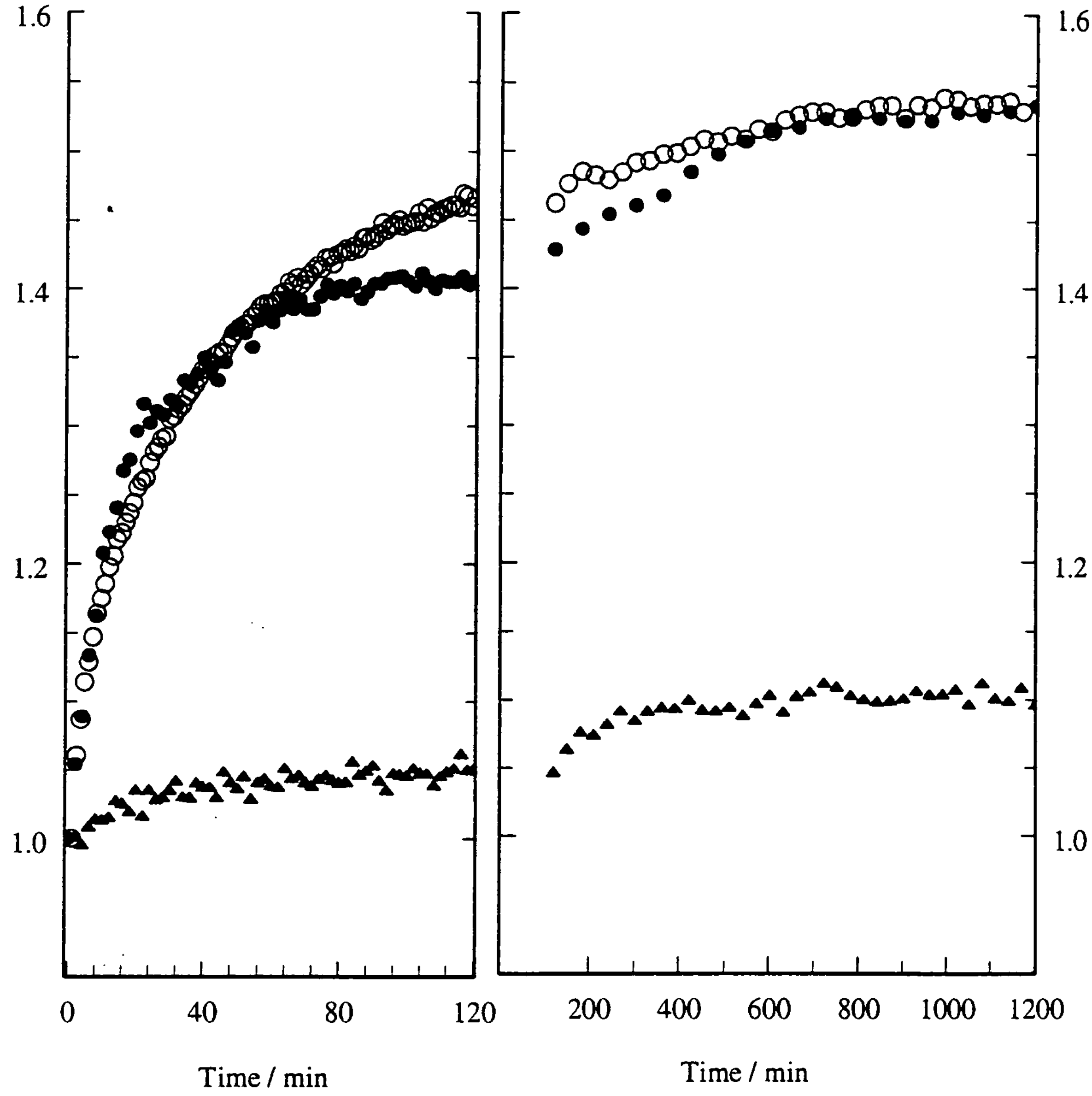

Figure 5.16. The variation in the total volume of adsorbate within the porous volume (expressed as a fraction of the volume adsorbed 2 minutes after the addition of the second adsorbate) with time elapsed after the addition of the second adsorbate. Solid circles show the results from section 5.1, the open circles illustrate the result obtained from section 5.2, whilst the solid triangles represent the results from the current experiment, section 5.3.

5.4 REFERENCES

1. D. H. Bangham, *Proc. Roy. Soc. A.*, **166**, 572 (1938)

2. P. J. M. Carrott, R. A. Roberts, K. S. W. Sing, *Carbon*, **25**, 59 (1987)

3. M. Hunger, T. Horvarth, *J. Chem. Soc. Chem. Commun.*, 1423 (1995)

4. J. Tabony, *Prog. NMR Spec.*, **14**, 1 (1980)

5. G. G. Malenkov, M. M. Dubinin, *Izv. Akad. Nauk SSSR, Ser. Khim.*, **6**, 1217 (1984)

6. S. J. Gregg, K. S. W. Sing, *"Adsorption, Surface Area and Porosity"*, Academic Press, London, 1976

7. M. M. Dubinin, *Carbon*, **19**, 402 (1981)

8. A. J. Juhola, E. O. Wiig, *J. Am. Chem. Soc.*, **71**, 2069 (1949)

9. A. V. Kiselev, *"The Structure and Properties of Porous Solids"*, Butterworth, London (1958)

10. J. Tabony, G. Bomchil, N. Harris, M. Leslie, J. W. White, P. Gamlen, R. K. Thomas, T. D. Trewern, *J. Chem. Soc. Faraday Trans. I,* **75**, 1570 (1979)

DYNAMIC NMR STUDIES OF THE MOTION OF ADSORBATES ON ACTIVATED CARBON

6.1. VARIABLE-TEMPERATURE 2D-EXSY EXPERIMENTS

6.1.1. THE 2D-EXSY EXPERIMENT

6.1.1.1. The 2D-EXSY Pulse Sequence

The use of 2D NMR to study chemical kinetics was first proposed by Jeener, Meier, Bachmann and Ernst[1]. The pulse sequence used is shown in Figure 6.1.

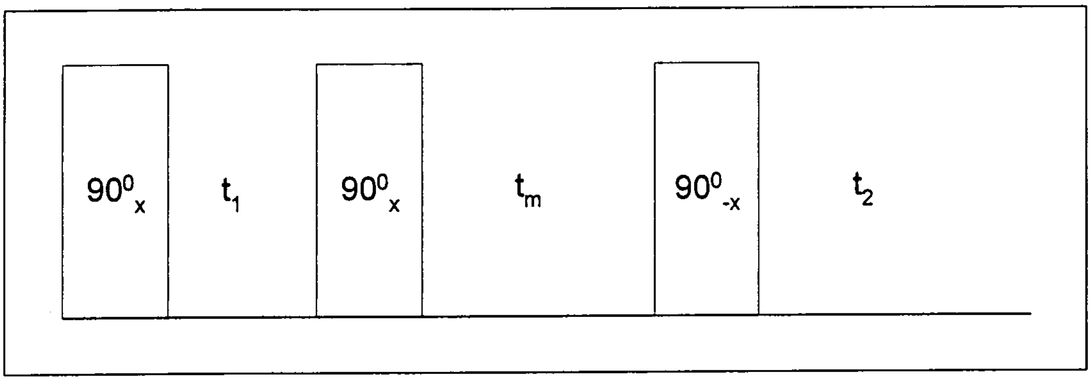

Figure 6.1. The 2D EXSY pulse sequence proposed by Jeener et al.

Transverse magnetisation is created by the initial 90° pulse, which rotates the magnetisation into the xy plane. The various spin isochromats are then allowed to evolve during t_1 according to the effective spin Hamiltonian in an identical way to a standard 1D experiment. It is assumed that chemical exchange does not occur during either of the short evolution periods, t_1 or t_2. The nature of the spin Hamiltonian can be controlled during this period in the same ways as were explored in Chapter 4. MAS was applied in the experiments performed upon these samples so the spin system evolves solely under the effect of the Zeeman and isotropic shielding Hamiltonians. The second 90° pulse rotates each of the isochromats into the xz plane, where they are left for a period, t_m. The x components of the magnetisation are allowed to decay away under the influence of the relaxation parameter, T_2, which may be decreased, if necessary, by the use of a homospoil pulse. This leaves only the z-component of each isochromat at the end of the mixing time. The remaining z-component magnetisation is simultaneously reduced via spin-lattice relaxation and this places a practical limit on the length of the mixing time that can be studied using this technique. Most importantly, during this mixing period the spins are free to move spatially within the sample. If there is a sufficiently rapid rate of exchange between chemically inequivalent sites then a significant proportion of molecules will have moved from one chemical environment to another during this time. The final 90° pulse rotates the remaining z-magnetisation into the transverse plane and a spectrum is acquired during t_2, once again with the spin system evolving under the effective spin Hamiltonian. The period t_2 is digitally sampled at the data acquisition rate in order to record a FID, and the period t_1 may be treated in an identical way. By regularly incrementing t_1 and recording an FID in t_2 for each discrete value of t_1, a 2-dimensional FID is generated which is a function of both t_1 and t_2. A Fourier transform is applied to the data set in the directly acquired t_2 dimension to generate a series of 1D spectra whose evolution was controlled by the spin Hamiltonian during t_2. The partially processed data set is a function of nuclear precession frequency during t_2 in the second dimension and time, t_1 in the first. The intensity of each spectral line within this series of spectra can be shown[2] to be directly proportional to the rotating frame magnetisation vector at t_1. Performing a second Fourier Transform in the t_1 dimension generates a spectrum in the first dimension that is a function of the nuclear frequency during the t_1 period. The final 2D-EXSY spectrum is thus a 2 dimensional plot, with chemical shift during the t_1 evolution period, ω_1, plotted against the chemical shift evolved during t_2, ω_2. If a spin isochromat has changed chemical environment during the intervening period, t_m, then the signal arising from the isochromat will appear at a position on the spectrum in which $\omega_1 \neq \omega_2$ and intensity will appear off the main $\omega_1 = \omega_2$ diagonal.

6.1.1.2. Theoretical treatment of the 2D-EXSY Experiment

The intensity of the peaks in the final 2D spectrum can be related to the rate constants of chemical exchange and the relaxation parameters of each peak. In order to do this, the effect of the three pulses and each evolution period on the magnetisation of the sample must be considered. The relation has been explored in several papers[3, 4, 5] and is discussed below in the case of a single -spin system exchanging between two sites.

The initial magnetisation arising from the nuclei within each of the two sites (labelled j = 1 and j = 2), is termed M_j^0, and is proportional to the signal observed in a simple one-dimensional spectrum. The initial density operator for this system may be treated as a sum of the separate magnetisations. After the first 90° pulse, the isochromats associated with each peak develop according to the effective spin Hamiltonian. In the MAS spinning experiment the effective Hamiltonian for an isolated spin, I, at site j may be written as

$$\hat{H}_{eff,j} = \hat{H}_{Z(I)} + \gamma_I I_z \overline{B}_0 \sigma_{iso,j} \qquad \textit{Equation 6.1}$$

The subscript j is necessary to describe the shielding tensor because the tensor associated with the environment giving rise to each resonance is different and has to be distinguished. The Hamiltonian may be evaluated within the rotating frame by pre- and post-multiplying the expression for the Hamiltonian by the evolution operator of the Zeeman Hamiltonian. The effective rotating frame Hamiltonian at each site within the rotating frame then becomes the familiar

$$\hat{H}_{eff,R,j} = \left(1 - \sigma_{iso,j}\right)\gamma_I \overline{B}_0 I_Z = \Delta\omega_j I_Z \qquad \textit{Equation 6.2}$$

The symbol $\Delta\omega_j$ denotes the frequency difference between the Larmor frequency of nucleus j and the transmitter frequency. To work out the state of the spin system at the end of the t_1 period, $\rho(t_1)$, the initial magnetisation is pre- and post-multiplied by the effective rotating frame evolution operator for that time period.

$$M_j(t_1) = \exp\left(i\hat{H}_{eff,R,j} t_1\right) \times M_j(0) \times \exp\left(-i\hat{H}_{eff,R,j} t_1\right) \qquad \textit{Equation 6.3}$$

The treatment makes no allowance for relaxation, so the expression for the magnetisation arising from the nuclei in each site at the end of the t_1 period also includes an additional exponential term describing the effect of T_2 whilst the nuclei are in the xy plane.

$$M_j(t_1) = M_j(0) \times \exp(i\Delta\omega_j t_1)\exp\left(\frac{-t_1}{T_{2,j}}\right) \qquad \textit{Equation 6.4}$$

The second 90° pulse rotates the various spin isochromats from the xy plane into the xz plane. T_2 relaxation during the mixing time then converts the xz magnetisation into pure z-magnetisation by acting upon the sine component of the spin isochromats. This means that only the cosine component of the magnetisation evolved during t_1 remains and this introduces difficulties in obtaining frequency-discriminated 2D spectra. The reasons for this are explored in the following section, but for now it is assumed that it is possible to collect both sine and cosine components. The resultant z-magnetisation at the start of the mixing time may then be written

$$M_{z,j} = -M_j(0)\exp(i\Delta\omega_j t_1)\exp\left(\frac{-t_1}{T_{2,j}}\right) \qquad \textit{Equation 6.5}$$

The effects of chemical exchange between the two peaks and T_1 relaxation upon the peak intensities are described by a pair of coupled differential equations describing the deviation of the magnetisation from equilibrium. The coupled differential equations developed may be written

$$\frac{d}{dt}\left[M_{z,j} - M_j(0)\right] = -\sum_i \overline{R}_{ji}\left[M_{z,i} - M_i(0)\right] \qquad \textit{Equation 6.6}$$

The matrix, **R**, is termed the exchange matrix and it completely describes the relaxation and chemical exchange occurring during the mixing period. The characterisation of the exchange matrix is the principal aim of the 2D EXSY experiment. Ignoring cross relaxation terms, in the present case **R** is a square 2x2 matrix with off-diagonal elements, R_{jl} = +k and diagonal elements, $R_{jj} = -(T_{1,j}^{-1} + k)$. The letter k is the pseudo-first order rate constant describing the rate of the exchange process between the two peaks.

The solution for the differential equations at time, t = t_m can be shown to be[6]

$$M_{z,j}(t_1,t_m) = M_j(0) + \exp\left(-\bar{R}t_m\right)\left[M_{z,j}(t_1,t_{m=0}) - M_j(0)\right]$$

$$= M_j(0) - \sum_{i=1}^{i=2} M_i(0)\left(\exp\left(-\bar{R}t_m\right)\right)_{ji}\left[1+\exp\left(i\Delta\omega_i t_1\right)\exp\left(\frac{-t_1}{T_{2,i}}\right)\right] \qquad \textit{Equation 6.7}$$

The third and final 90° pulse converts the z-magnetisation into transverse magnetisation suitable for detection. During the detection period the magnetisation precesses and decays. The subscripts indexing each peak, j and l, now refer to the total magnetisation arising from the peak during the t_1 period. As the magnetisation evolves during t_2 there are contributions to j from two peaks, where $\omega_j(t_1) = \omega_j(t_2)$ and that where $\omega_j(t_1) \neq \omega_j(t_2)$.

$$M_j(t_1,t_m,t_2) = -\exp\left(i\Delta\omega_j t_2\right)\exp\left(\frac{-t_2}{T_{2,j}}\right)M_{z,j}(t_1,t_m) \qquad \textit{Equation 6.8}$$

For example, calculating the magnetisation arising from nuclei that gave rise to the peak j = 1 during time t_1, a sum of terms is obtained, one of which refers to the peak appearing upon the main diagonal, and another referring to an off-diagonal peak. The first term and the 1 within each set of parentheses are oscillatory in t_2 only and arise from longitudinal magnetisation that recovered during t_m. These terms give rise to "axial" peaks, which appear as a peak, at $\omega_1 = 0$, along the ω_2 axis of the 2D spectrum. They do not convey information about exchange and can be removed by appropriate phase cycling.

$$\begin{aligned}M_1(t_1,t_m,t_2) &= M_1(0)\exp\left(-i\Delta\omega_1 t_2\right)\exp\left(\frac{-t_2}{T_{2,1}}\right)\\ &- M_1(0)\exp\left(-i\Delta\omega_1 t_2\right)\exp\left(\frac{-t_2}{T_{2,1}}\right)\left(\exp\left(-\bar{R}t_m\right)\right)_{11}\left[1+\exp\left(i\Delta\omega_1 t_1\right)\exp\left(\frac{-t_2}{T_{2,1}}\right)\right]\\ &- M_2(0)\exp\left(-i\Delta\omega_1 t_2\right)\exp\left(\frac{-t_2}{T_{2,1}}\right)\left(\exp\left(-\bar{R}t_m\right)\right)_{12}\left[1+\exp\left(i\Delta\omega_2 t_1\right)\exp\left(\frac{-t_2}{T_{2,2}}\right)\right]\end{aligned}$$

Equation 6.9

Ignoring the axial peaks, the total magnetisation detected is given by the double summation

$$M(t_1,t_m,t_2) = \sum_{i=1,j=1}^{i=2,j=2} \exp(i\Delta\omega_i t_2)\exp\left(\frac{-t_2}{T_{2,i}}\right)\left(M_i(0)\left\{\left(\exp(-\bar{R}t_m)\right)_{ji}\left[\exp(i\Delta\omega_j t_1)\exp\left(\frac{-t_1}{T_{2,j}}\right)\right]\right\}\right)$$

Equation 6.10

Double Fourier transformation of the signal yields a 2D spectrum, in which each term represents a complex 2D peak. Assuming the data set has been manipulated correctly, a pure absorption mode spectrum can be obtained in which the integrated intensity of each peak is given by[3]

$$I_{ij}(t_1,t_m,t_2) = M_j(0)\left(\partial_{ij} - t_m R_{ij} + \frac{1}{2!}t_m^{\,2}\sum_k R_{ik}R_{kj} - \frac{1}{3!}t_m^{\,3}\sum_{k,l} R_{ik}R_{kl}R_{lj} + \ldots\ldots\right)$$

Equation 6.11

The complicated series within the parentheses arises mathematically from the evaluation of the exponential of the matrix **R**. In practical terms the complication is introduced by the fact that an observed exchange of position from one chemical environment to another by a molecule may actually comprise several “there and back” exchanges. Many authors have approximated the summation to the first two terms by using the initial rate approximation[19], in which it is assumed that the mixing time is only sufficiently long for a single site exchange to occur. Techniques have been developed to solve the equations explicitly[24, 25]. The following expressions for the final magnetisation of each peak for a two-peak system were obtained by Jeener et al.[1].

$$a_{11}(t_1,t_m,t_2) = x_a\exp(-\alpha t_m)\left[\cosh(\gamma t_m) - \frac{\beta}{\gamma}\sinh(\gamma t_m)\right]$$

$$a_{22}(t_1,t_m,t_2) = x_b\exp(-\alpha t_m)\left[\cosh(\gamma t_m) + \frac{\beta}{\gamma}\sinh(\gamma t_m)\right]$$

$$a_{12}(t_1,t_m,t_2) = a_{21}(t_1,t_m,t_2) = x_a x_b\frac{k}{\gamma}\exp(-\alpha t_m)\sinh(\gamma t_m)$$

Equations 6.12

in which x is the proportion of molecules in each peak, such that $x_a = (1 - x_b)$, and the factors α, β and γ are given by the relations

$$\alpha = \frac{1}{2}\left\{\left(T_{1,1}{}^{-1} + x_b k\right) + \left(T_{1,2}{}^{-1} + x_a k\right)\right\}$$
$$\beta = \frac{1}{2}\left\{\left(T_{1,1}{}^{-1} + x_b k\right) - \left(T_{1,2}{}^{-1} + x_a k\right)\right\}$$
$$\gamma = \left(\beta^2 + x_a x_b k^2\right)^{1/2}$$

Using these equations it is possible to calculate the exchange rate between the two peaks. If the rate constant is thermodynamically determined then repetition of the experiment at various temperatures may be used to obtain the activation energy for the process.

6.1.1.3. Methods for obtaining frequency discriminated absorption lineshapes in two dimensions

One of the greatest practical problems in the development of two-dimensional NMR experiments has been the difficulty in obtaining pure absorption mode lineshapes in both dimensions. The way in which this is achieved is outlined below, first with reference to one-dimensional spectra and then extended to include two-dimensional spectra.

6.1.1.3.1. Quadrature Detection in 1D-NMR

NMR signals come from the probe at the Larmor frequency of the nucleus being studied, typically several hundred MHz at high field. The various signals present are all in a narrow band (chemical shifts are measured in parts per million) about the resonance frequency, which is of little interest. The signals have to be detected, and this is achieved by mixing them with a reference frequency, generally the transmitter frequency[7]. This brings the frequencies that have to be sampled by the analogue to digital converters (ADCs) down to the kHz range. This has several instrumental advantages, particularly in terms of the rate of data sampling required by the ADCs. The mixing process also shifts the resonances acquired into the rotating frame. The process of mixing down the signals means that each NMR resonance may be higher or lower in frequency than the reference transmitter frequency. In the rotating frame this corresponds to precession in opposite senses. A single detector is not able to discriminate between clockwise or anticlockwise precession, the result of this being that the spectrum obtained after Fourier transform is folded about the transmitter frequency, ω_0. If there are signals on both sides of the transmitter frequency this will cause unacceptable confusion. The original solution to this problem was to place the transmitter to one side of the entire frequency range of the sample and then disregard one half of the spectrum obtained. This has the disadvantages of using the available transmitter power inefficiently whilst the generation of two spectra from a single FID leads to a degradation in the S/N of √2. A further disadvantage, more specific to 2D spectra, is the need to store and handle much larger time-domain data sets than are actually required.

The use of quadrature detection[8, 9], which removes the ambiguity in the detected direction of precession, solves the problem. Quadrature detection, in principle, uses two receiver coils perpendicular to one another so that both the frequency and direction of nuclear precession may be determined. This means that the transmitter can be placed in the centre of the spectrum removing the problems outlined above. One receiver records the cosine component of the signal, the other records the sine component.

$$M_y(t) = \sum_i M_i(0)\left(\cos(\Delta\omega_i t) + \phi_i\right)\exp\left(\frac{-t}{T_2}\right)$$

$$M_x(t) = \sum_i M_i(0)\left(\sin(\Delta\omega_i t) + \phi_i\right)\exp\left(\frac{-t}{T_2}\right)$$

Equations 6.13

The two signals are combined to form a complex signal and a complex Fourier transform is then performed to yield real and imaginary spectra.

$$S(t) = \int_0^t \sum_i M_i(0)\exp(-i\Delta\omega t)\left(\exp\left(i\omega_i t + \phi_i\right)\exp\left(\frac{-t}{T_2}\right)\right)dt$$

$$= \sum_i M_i(0)\frac{T_{2,i}{}^{-1}}{\Delta\omega_i{}^2 + T_{2,i}{}^{-2}}\exp(i\phi_i) + \sum_i M_i(0)\frac{-i\Delta\omega_i}{\Delta\omega_i{}^2 - T_{2,i}{}^{-2}}\exp(i\phi_i)$$

Equation 6.14

The phase correction, ϕ_i, is set to zero manually during data processing, leaving the initial summation as a pure absorption mode spectrum, each peak centred at $\Delta\omega_i$ with width $(\pi T_{2,i})^{-1}$ Hz and intensity equal to $M_i(0)$. The second summation is a pure dispersion mode spectrum and is discarded. Once the phase correction angle is zero, the shorthand notation of Keeler and Neuhaus[11] may be introduced.

$$S(t) = \sum_i M_i(0)\left[A_{1,i} + iD_{1,i}\right] \qquad \textit{Equation 6.15}$$

$A_{n,j}$ and $D_{n,j}$ represent the absorption and dispersion peaks at frequency ω_j in the ω_n dimension. In the cases where peaks appear at $\pm\omega_j$ the corresponding lineshape functions are denoted $A_{n,j}^+$, $A_{n,j}^-$, $D_{n,j}^+$ and $D_{n,j}^-$.

6.1.1.3.2. Quadrature detection in 2D-NMR

The main obstacle in obtaining pure absorption mode lineshapes in 2 dimensions arises from the difficulty in applying quadrature in the indirectly detected direction. The basic pulse sequence for the 2D-EXSY experiment does not yield any information about the sign of $\Delta\omega_1$, and this may be demonstrated by considering the Fourier transform of a 2D-EXSY data set cosine-modulated in t_1.

From equation 6.10 the total magnetisation detected at the end of the acquisition period may be written

$$M(t_1,t_m,t_2) = \sum_{i=1,j=1}^{i=2,j=2} \exp(i\Delta\omega_i t_2)\exp\left(\frac{-t_2}{T_{2,i}}\right) M_i(0)\left(\exp(-\bar{R}t_m)\right)_{ij} \cos(i\Delta\omega_j t_1)\exp\left(\frac{-t_1}{T_{2,j}}\right)$$

Equation 6.16

Performing a Fourier transform on the directly acquired dimension and using the relation cos(x) = ½($e^{ix} + e^{-ix}$) leads to

$$S_c(t_1,t_m,\omega_2) = \frac{1}{2}\sum_{i=1,j=1}^{i=2,j=2} M_i(0)\left(\exp(i\Delta\omega_{1,i}t_1) + \exp(-i\Delta\omega_{1,i}t_1)\right)\exp\left(\frac{-t_1}{T_{2,j}}\right)\left(\exp(-\bar{R}t_m)\right)_{ij}\left[A_{2,j} + iD_{2,j}\right]$$

Equation 6.17

A second Fourier transform, applied in the t_1 dimension, yields

$$S_c(\omega_1,t_m,\omega_2)=\frac{1}{2}\sum_{i,j=1}^{2}M_i(0)\left[A_{1,i}{}^{+}+iD_{1,i}{}^{+}+A_{1,i}{}^{-}+iD_{1,i}{}^{-}\right]\left(\exp\left(-\bar{R}t_m\right)\right)_{ij}\left[A_{2,j}+iD_{2,j}\right]$$

Equation 6.18

Taking the real part of peak (i,j) leads to

$$\mathrm{Re}\left[S_c(\omega_1,t_m,\omega_2)_{ij}\right]=M_i(0)\left\lfloor A_{1,i}{}^{\pm}(e^{-\bar{R}t_m})_{ij}A_{2,i}-D_{1,i}{}^{\pm}(e^{-\bar{R}t_m})_{ij}D_{2,i}\right\rfloor$$

Equation 6.19

This corresponds to a pair of resonances at ($\pm\omega_{1,i}$, $\pm\omega_{2,j}$), each with a phase twist lineshape. The phase twist arises from the partial absorptive and dispersive components present within each signal. In an exactly analogous way to 1D NMR, the key to obtaining frequency discrimination in ω_1 is to acquire an imaginary data set that is sine modulated in t_1. This is done by phase shifting the coherence evolving during t_1 by 90°, which is achieved by altering the phase of all pulses prior to t_1 and the receiver phase by 90°. The complex signal acquired using this modification becomes

$$S(t_1,t_m,t_2)_{ij}=S_c(t_1,t_m,t_2)_{ij}+\exp\left(\frac{i\pi}{2}\right)S_s(t_1,t_m,t_2)_{ij}$$

$$=M_i(0)\left\{\left[\cos(\Delta\omega_{1,i}t)+i\sin(\Delta\omega_{1,i}t_1)\right]\exp\left(\frac{-t_1}{T_{2,i}}\right)\exp\left(-\bar{R}t_m\right)_{ij}\exp(i\Delta\omega_{2,j}t_2)\exp\left(\frac{-t_2}{T_{2,j}}\right)\right\}$$

Equation 6.20

Application of a complex Fourier transform in both dimensions leads to

$$\mathrm{Re}\left[S(\omega_1,t_m,\omega_2)_{ij}\right]=\left\lfloor A_{1,i}{}^{+}(e^{-\bar{R}t_m})_{ij}A_{2,i}-D_{1,i}{}^{+}(e^{-\bar{R}t_m})_{ij}D_{2,i}\right\rfloor$$

Equation 6.21

A single peak is attained but once again it still possesses an undesirable phase twist. This was regarded for several years as an inevitable consequence of a 2D FT. The broad dispersion tails meant that peak areas could not be measured quantitatively and the situation became even worse in more crowded spectra where the broad peak bases overlapped extensively. Efforts to limit the ill effects of the phase twist lineshape were largely confined to the application of strong apodisation functions during data processing. This led to a considerable reduction in S/N for the spectrum, introducing further problems to the technique.

The seemingly intractable problem was solved independently by two different groups in the early 1980s. Marion and Wuthrich[12] applied a time-proportional phase incrementation (TPPI) technique, based on Redfield's[13] technique used to obtain quadrature in 1D spectra on spectrometers with a single detector and ADC. The method that has been implemented in this study, however, is that due to States et al.[14] It was realised that to obtain frequency discrimination and pure 2D absorption lineshapes it was necessary to keep the two different t_1-modulated data sets separate. By applying similar processing procedures to the two data sets, two pure absorption mode spectra are obtained, with identical peaks at either side of ω_1. However, one of the two peaks in the sine-modulated data sets will be inverted by virtue of sine being an odd function. Simple addition of the two data sets will lead to one of the peaks cancelling, giving frequency discrimination whilst retaining a pure absorption lineshape in both dimensions for the remaining peak. This can be easily demonstrated using the mathematical relations

$$\sin x = -\frac{1}{2}i\left[\exp(ix) - \exp(-ix)\right]$$
$$\cos x = \frac{1}{2}\left[\exp(ix) + \exp(-ix)\right]$$

Equations 6.22

The partially processed sine and cosine t_1 modulated data sets may then be written

$$S_c\left(t_1, t_m, \omega_2\right)_{ij} = \frac{1}{2}\left[\left(\exp(i\Delta\omega_{1,i}t_1) + \exp(-i\Delta\omega_{1,i}t_1\right)\exp\left(\frac{-t_1}{T_{2,i}}\right)\right]\left(\exp(-\bar{R}t_m\right)_{ij}\left[A_{2j} + iD_{2j}\right]$$
$$S_s\left(t_1, t_m, \omega_2\right)_{ij} = -\frac{1}{2}i\left[\left(\exp(i\Delta\omega_{1,i}t_1) - \exp(-i\Delta\omega_{1,i}t_1\right)\exp\left(\frac{-t_1}{T_{2,i}}\right)\right]\left(\exp(-\bar{R}t_m\right)_{ij}\left[A_{2j} + iD_{2j}\right]$$

Equations 6.23

The imaginary part of both data sets is set to zero and the two data sets are added

$$S(t_1,t_m,\omega_2)_{ij} = \left[\cos(\Delta\omega_1 t)\exp\left(\frac{-t_1}{T_{2,i}}\right)\left(\exp(-\bar{R}t_m\right)_{ij} A_{2j}\right] + i\left[\sin(\Delta\omega_1 t)\exp\left(\frac{-t_1}{T_{2,i}}\right)\left(\exp(-\bar{R}t_m\right)_{ij} A_{2j}\right]$$

Equation 6.24

Fourier transform in the t_1 dimension finally yields a frequency discriminated pure adsorption lineshape.

$$\mathrm{Re}\left[S(\omega_1,t_m,\omega_2)\right]_{ij} = A_{1,i}{}^{+}\left(\exp(-\bar{R}t_m)\right)_{ij} A_{2,j}$$

Equation 6.25

6.1.1.3.3. Coherence Transfer Pathways and Phase Cycling

An alternative way to describe the evolution of the magnetisation is via coherence transfer and coherence transfer pathways[15]. The equilibrium coherence of the spin state is zero and coherence between states is introduced by radio-frequency pulses. The coherence transfer pathway required for the 2D EXSY experiment can be illustrated upon a coherence transfer map (Figure 6.2). It has been shown that it is necessary to maintain the p = ±1 pathways during the t_1 period in order to obtain pure absorption mode lineshapes[15].

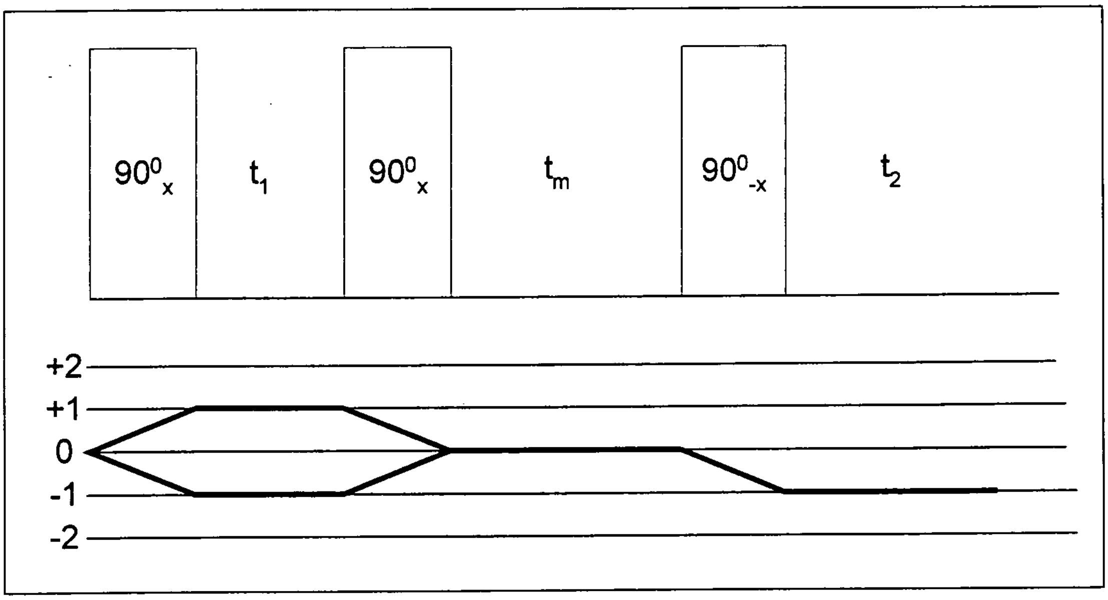

Figure 6.2. Coherence transfer pathway for the 2D-EXSY experiment

Coherence of 0 and ±1 can be described in terms of classical vectors, where a coherence of +1 corresponds to the magnetisation vector rotating at $+\omega_1$, a coherence of –1 corresponds to the magnetisation vector rotating at $-\omega_1$ and a coherence of 0 corresponds to the equilibrium situation in which there is no net magnetisation in the transverse plane. The phase cycling needed for any NMR experiment can be evaluated from the coherence transfer pathway of the experiment using several simple relations[15, 16]. The application of a pulse to a system can cause a change in the coherence order, p, of Δp. In order to select a unique value of Δp the number of phase cycles, N, must be at least equal to the number of possibilities in Δp. The initial 90° pulse can only generate single quantum coherence, with $\Delta p = -1, 0$ or 1 whilst we want to select the $\Delta p = \pm 1$ pathway. Thus a phase cycle of 2 is required for this pulse with an applied r.f. phase given by $\phi = k2\pi/N$ where $k = 0,1,2,\ldots,N-1$. Therefore selection of $\Delta p = \pm 1$ requires a r.f. phase of 0 and 180° to be applied to the first pulse.

The coherence order approach assumes that the receiver only detects coherence with $p = -1$. This presumes that the two receivers required for quadrature detection are exactly perpendicular and that the two receiver channels are perfectly gain-balanced[17]. This requirement is relaxed by the introduction of a cyclically ordered phase sequence[18] (CYCLOPS) to one of the pulses within the pulse sequence and the receiver phase. In the 2D-EXSY pulse sequence, the 4-stage CYCLOPS phase cycle is applied to the final detection pulse, detecting solely the $\Delta p = -1$ pathway. The application of CYCLOPS means that the only coherence transfer pathways detected by the receiver start at 0 and end at –1. This additional condition means that the phase cycling applied to the first and third pulses defines the desired coherence transfer pathway uniquely and the phase of the second pulse does not need to be cycled. The phase of the receiver, ϕ_{rec} is defined as minus the sum of $\Delta p\phi$ for each pulse. Thus the overall phase cycle for each of the two t_1-modulated data sets is given in Table 6.1.

Cosine modulation in t_1				**Sine modulation in t_1**			
P_1	**P_2**	**P_3**	**P_{rec}**	**P_1**	**P_2**	**P_3**	**P_{rec}**
0	0	0	0	0	90	0	90
180	0	0	180	180	90	0	270
0	0	90	90	0	90	90	180
180	0	90	270	180	90	90	0
0	0	180	180	0	90	180	270
180	0	180	0	180	90	180	90
0	0	270	270	0	90	270	0
180	0	270	90	180	90	270	180

Table 6.1. Phase cycling required for the 2D-EXSY experiment

6.1.2. EXPERIMENTAL CONDITIONS

The experiments were performed on SC2 carbon with ~70% w/w TMP added. The samples were sealed within glass ampoules under vacuum, and left to equilibrate for over 12 hours prior to the spectra being taken. The experiment was performed at three temperatures, 20°C, 80°C and 140°C. The B_1 power applied was equivalent to a 5 μs 90° pulse, set upon each sample. Each experiment was performed with a mixing time of 100 ms. 128 data points were recorded with a dwell time of 400 μs, giving a spectral width of 2.5 kHz in each dimension. 32 acquisitions were recorded for each t_1 value, with a recycle delay of 8 s. Cosine and sine components were recorded alternately, using the method of States et al., leading to a total experimental time of approximately 18 hours. 10 Hz Gaussian line broadening was applied and the data were zero-filled to 512 data points in each dimension prior to Fourier transformation. The 2D peak intensities were measured using a self-written analysis macro.

Re-arrangement of Equations 6.12, in order to obtain the exchange rate constant as a function of peak intensity, was not easily accomplished, so a one-parameter fitting process was performed using the Marquadt-Levenberg[27] algorithm within MATHCAD[28]. The two relaxation parameters, $T_{1,1}$ and $T_{1,2}$, were obtained from inversion recovery experiments (chapter 7), whilst the values x_a and x_b may be obtained directly from a typical one-dimensional spectrum or by summing the intensity over all the rows or columns in the two-dimensional spectrum. It was later deemed essential to ascribe the broad envelope intensity to contributions from both exchanging and non-exchanging peaks, necessitating a two-parameter fitting procedure. This is examined in more detail in the discussion section.

6.1.3. EXPERIMENTAL RESULTS

The spectrum obtained from the experiment performed at room temperature is shown in Figure 6.3. The higher of the two plots does not show much of significance besides the two peaks appearing upon the main diagonal. The contour plot of the data is rather more informative and shows evidence of two low intensity off-diagonal peaks, indicating that there is a limited amount of molecular exchange occurring between the two situations. The areas of each peak were calculated, and the results obtained from the spectrum recorded at each temperature are given in Table 6.2.

TEMPERATURE	Peak II	Peak I	OFF-DIAGONAL
20°C	16.9	78.0	5.0
80°C	16.5	78.4	5.1
140°C	17.6	77.3	5.1

Table 6.2. Peak areas expressed as a percentage of total spectral intensity obtained from 2D-EXSY experiments recorded at 3 temperatures

The unusual shape of the main diagonal low-frequency peak in each contour plot was also noted. The low-frequency end of the peak is broadened to a much greater extent in both dimensions than the end towards higher frequency. The possible causes for this behaviour are discussed in the following section. Closer examination of the spectrum also showed that the position of the two off-diagonal peaks did not correlate precisely with the centre of the low-frequency peak. The off-diagonal peaks appear at around –7.7 ppm in the 2D spectrum compared to the peak I chemical shift acquired in a standard 1D experiment of approximately -8.6 ppm. Given the inhomogenous nature of peak I, it was realised that the precise position of the off-diagonal peaks could provide information upon which of the constituent peaks within the overall broad peak envelope was exhibiting exchange behaviour with peak II. Comparison of the sum of all the rows comprising the 2D spectra with the sum of the rows subtracting the off-diagonal peaks identified clearly the position of the material giving rise to off-diagonal intensity. The spectrum obtained from a summation of all the rows in the spectrum was exactly the same as the 1D spectrum. In Figure 6.4 the two spectra obtained by this method are plotted on top of one another. The dotted line is the total intensity, whilst the solid line represents the intensity with the off-diagonal peaks subtracted. The off-diagonal peak intensity clearly arises from material towards the high-frequency end of peak I.

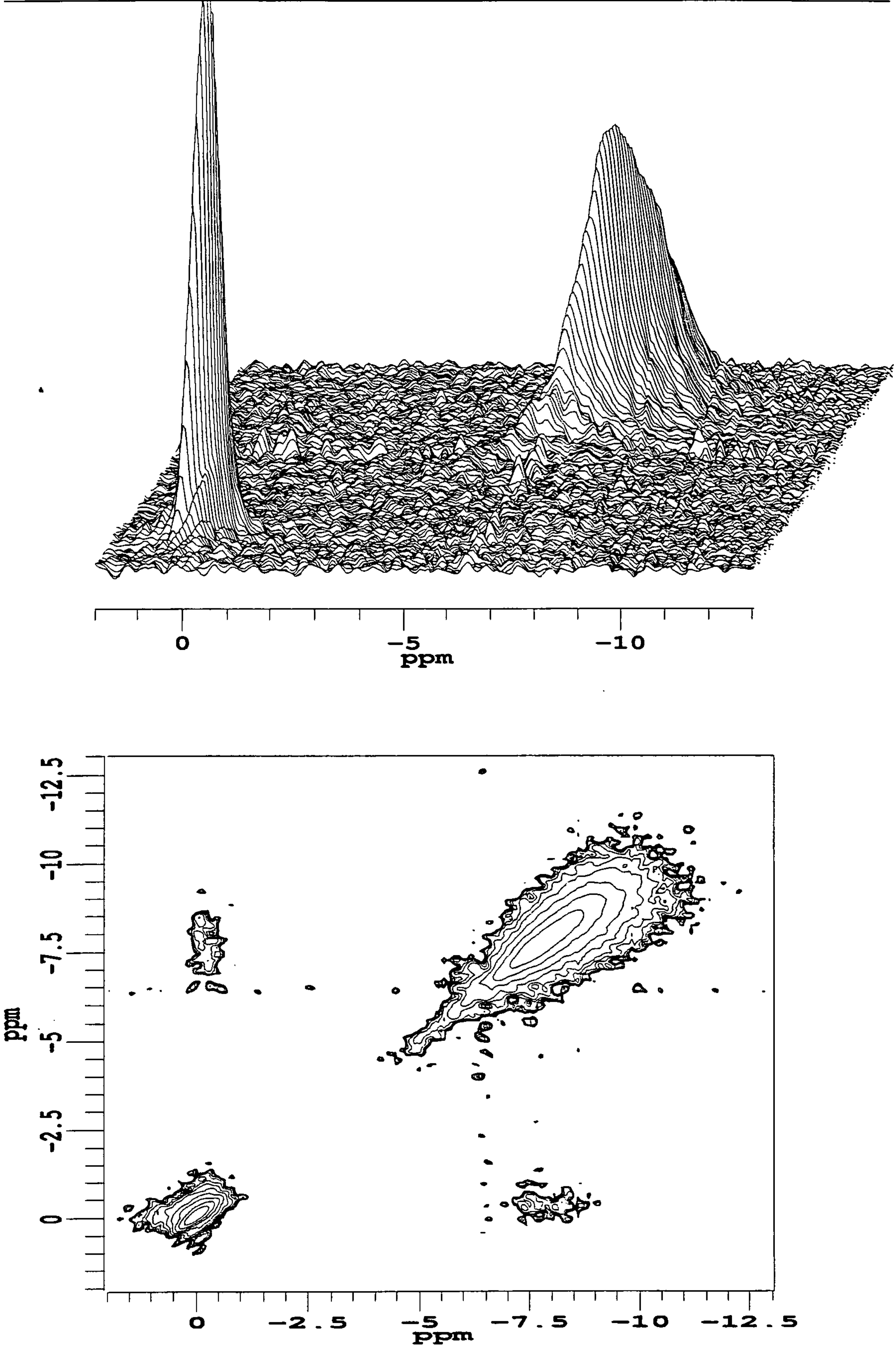

Figure 6.3. Results obtained from EXSY experiment performed at room temperature upon SC2 carbon with 70% w/w TMP pre-adsorbed.

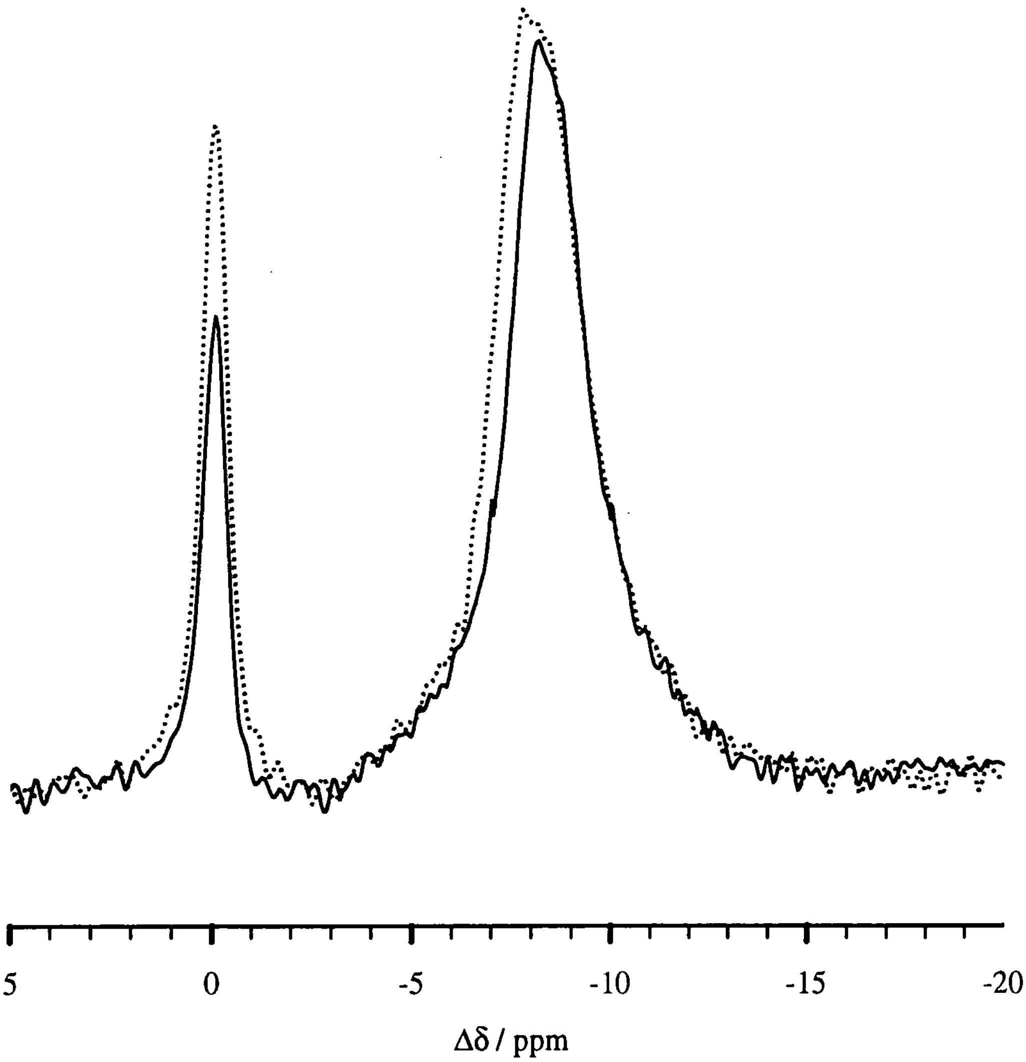

Figure 6.4. Comparison of spectra acquired by summation of rows from the 2D-EXSY spectrum. The dotted line represents the spectrum obtained from summation of the entire spectrum and is identical to the spectrum acquired in a 1D single-pulse experiment. The solid line represents the spectrum obtained from summing all the rows within the spectrum whilst setting the off-diagonal peak intensity to zero. The difference between the two plots is therefore caused by off-diagonal intensity.

6.1.4. Discussion

The peak area results obtained at a variety of temperatures are unusual in that they show no dependence in cross-peak intensity with temperature. This result, added to the fact that the cross peaks are each so small, only slightly above the background noise, meant that it became necessary to ascertain that the cross-peaks had not been generated in another manner. The possibility of magnetisation transfer via NOE can be discounted in the current situation (we are observing intermolecular effects) but it is still necessary to consider possible experimental artefacts. Instability in the experimental set-up over the course of the experiment (i.e. as t_1 is incremented) can introduce oscillations into the intensity of each spectral line, $f(t_1, \omega_2)$ which then cause complex fluctuations , termed "t_1 noise", in the 2D spectrum at the frequency, $\omega_{1,j}$ of each peak. Instability can be caused by small effects such as a fluctuation in temperature, or movement of objects about the spectrometer. Ripples in both dimensions at the transmitter frequency (evident in Figure 6.3) are the other common experimental artefacts observed in 2D NMR. Assuming the axial peaks have been phase-cycled away, the ripples are generally caused via Fourier transform of a d.c. offset in the relevant time dimension. D.c. offsets commonly arise from recording the first data point incorrectly or by setting the baseline of the FID at the incorrect level. Setting an incorrect FID baseline is frequently done unwittingly when processing the 2D time-domain data set, which is often truncated due to time limitations.

The most common way that cross-peak artefacts are generated is via symmetrisation of the data set, which multiplies the intensity of each point in the spectrum by the intensity of its counterpart generated by reflection in the main diagonal. This increases S/N by a factor of $\sqrt{2}$, but also introduces t_1 noise into the t_2 dimension. The two noise peaks then overlap at points equivalent to possible off-diagonal sites and may be mistaken for genuine intensity. However, the contour plots in this experiment were generated without symmetrisation being applied. Overlap of t_1 noise with the ω_2 d.c. offset peak was another possible cause of one off-diagonal peak, but could not account for both simultaneously. In any case identical results were obtained when the experiment was repeated with the transmitter set at a different point within the spectrum. Performing the experiment at two different MAS rates eliminated the possibility that the two peaks were spinning sidebands, though the fact that they were not centred at the same frequency as the low-frequency peak had made this unlikely. Having explored and discounted most common sources of artificial intensity it was concluded that the off-diagonal peaks were a genuine experimental result.

This then necessitates an explanation for the absence of any significant change in exchange rate with temperature. Standard thermodynamic theory predicts that the rate constant describing the exchange process will vary with temperature if the rate depends upon activation energy, E_a. The Arrhenius equation is an empirical relation that demonstrates the dependence of rate constants upon temperature.

$$k = A\exp\left(\frac{-E_a}{RT}\right) \qquad \textit{Equation 6.26}$$

The variation in exchange rate will be smallest when the activation energy is low, as would be expected for the physical diffusion of a relatively unhindered molecule from one environment to another. A low activation energy implies a rapid process, which in turn suggests that the off-diagonal peaks will be significant. However it is found that the off-diagonal peaks are extremely small. The intensity of the cross-peaks as a function of the exchange rate constant can be obtained from Equations 6.12. The calculations yielded a value for the exchange rate constant of $1.4 \pm 0.3\ \mathrm{s}^{-1}$. However, the two-peak calculation assumes that all molecules within the pore structure are able to exchange with the excess, surface adsorbate, whilst the results obtained from the SPI experiments, and the position of the off-diagonal peaks, suggest that this is not the case.

It is thought that the off-diagonal peaks are faint in the current study because only a small proportion of the adsorbed molecules within the porous volume are able to exchange situation with the excess adsorbate. Further information on the location of the adsorbed molecules that are able to exchange with the excess adsorbate is provided by the precise position of the off diagonal intensity in the 2D spectrum.

The off-diagonal peaks are centred at -7.7 ppm, with visible intensity extending from approximately –6.4 ppm to –8.8 ppm. The comparison of the two spectra obtained from row summation in Figure 6.4 yields similar results, though it is shown that the exchanging proportion extends further to higher frequency than was detected from the contour plot. These results suggest that the molecules that are exchanging with the excess adsorbate are those within larger pores, whilst molecules within smaller pores are not able to do so. The solutions given in equations 6.12 can easily be extended to include an additional term representing a non-exchanging peak (Equations 6.27).

$$a_{11}(t_1,t_m,t_2) = x_a \exp(-\alpha t_m)\left[\cosh(\gamma t_m) - \frac{\beta}{\gamma}\sinh(\gamma t_m)\right]$$

$$a_{22}(t_1,t_m,t_2) = x_c \exp\left(\frac{-t_m}{T_{1,2}}\right) + x_b \exp(-\alpha t_m)\left[\cosh(\gamma t_m) + \frac{\beta}{\gamma}\sinh(\gamma t_m)\right]$$

$$a_{12}(t_1,t_m,t_2) = a_{21}(t_1,t_m,t_2) = x_a x_b \frac{k}{\gamma}\exp(-\alpha t_m)\sinh(\gamma t_m)$$

Equations 6.27

The terms α, β and γ are defined as in Equations 6.12, whilst x_b now represents the mole fraction of the exchanging molecules within peak I and x_c represents the non-exchanging proportion of that peak. Evaluation of the modified solutions within MATHCAD and fitting the results to the experimental data shows that the product of the exchange rate, k, and the molar fraction of the exchanging molecules within peak I, x_b, is approximately 1.3 s^{-1}. However, it is not possible to separately evaluate the two parameters from measurement of a single mixing time. More information upon the values of x_b and k can be obtained from the Selective Polarisation Inversion (SPI) experiment.

The unusual "teardrop" shape of the low-frequency peak along the main diagonal could arise from one or both of two effects, each of which would broaden the peak inhomogeneously in both dimensions. The first of these possibilities is chemical exchange between different constituent peaks within the overall resonance. This would correspond to exchange between molecules within different sized pores. Assuming that this was the reason for the broadening, the teardrop shape would necessitate a greater exchange rate for the peaks at lower frequencies within the broad resonance envelope. The second possibility is that the shape arises from the variation in T_2 across the inhomogenous peak. A decrease in transverse relaxation rate as the peak I is traversed from high to low frequency would also cause the distinctive shape demonstrated in the contour plot. The two effects are indistinguishable in this experiment, as each effect would cause equal amounts of broadening along both the ω_1 and ω_2 axes. Relaxation experiments performed for these systems studying the variation in transverse relaxation time across the low-frequency peak are discussed in Chapter 7. The results from these experiments do indeed show a decreased relaxation time as the size of the low-frequency chemical shift increases. The trend in relaxation times is large enough to adequately explain the shape of the peak, suggesting that migration of molecules from one pore to another is not a particularly significant process.

6.2. SELECTIVE POLARISATION INVERSION

6.2.1. THE SPI EXPERIMENT

The 2D-EXSY experiments demonstrated that there is a certain amount of intermediate rate exchange occurring between peak II and the higher frequency portion of peak I. The study of the exchange is limited using the 2D-EXSY experiment due to the loss of magnetisation during the mixing period and the introduction of t_1 noise. The length of time required for each experiment also means that a limited range of mixing times can be explored. Much of the time requirement in 2D NMR is caused by the need to scan the range of t_1 values. Nearly all of the spectrum along the ω_1 axis is baseline, but it is not possible to omit the baseline regions by omitting some of the t_1 values because frequency and time domains are related by the Fourier transform so that each value of t_1 contributes to every frequency, ω_1. However, it is possible to choose values of t_1 such that most of the information obtained from the EXSY experiment is retained without the need to apply a FT in the t_1 dimension. The SPI experiment may be thought of as the 1D equivalent of the 2D-EXSY pulse sequence. The problems introduced into the study of exchange processes over longer mixing times are circumvented and a far greater range of mixing times may be explored. As a 1D experiment it is also considerably quicker to perform than the full 2D-EXSY experiment, meaning that results can be obtained from a greater number of mixing times in the same amount of time. The experiments require selective excitation of a single resonance (either by saturation or inversion) whilst leaving the others at equilibrium. The return to equilibrium of the excited resonance and deviations from equilibrium of the non-excited resonances can be fitted to theoretical models to provide evidence of exchange. Several techniques have been applied to achieve the initial selective excitation such as "soft pulses"[20] or the DANTE[21, 22] pulse sequence. Both these techniques involve long cycle times for the creation of the selective excitation, during which exchange can occur. It is also difficult to achieve a high degree of selectivity between two resonances that are relatively close. The simplest, and least technically demanding technique for inverting one of two peaks is that proposed by Robinson et al.[23]

6.2.1.1. The Selective Polarisation Inversion Pulse Sequence

The pulse sequence is very closely related to the pulse sequence for the 2D-EXSY experiment. The pulse sequence is shown in Figure 6.5.

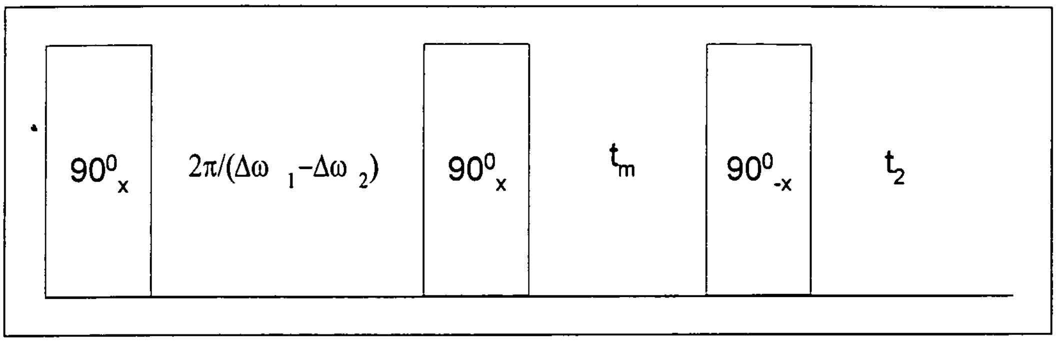

Figure 6.5. Pulse sequence for the Selective Polarisation Inversion experiment

The experiment is simpler to implement when the transmitter frequency is set to be equal to one of the two resonance frequencies[29, 30]. The initial 90° pulse creates transverse magnetisation, which is allowed to precess freely during the first evolution period, t_1. The evolution is governed by the effective spin Hamiltonian, which in the case of the MAS experiment corresponds to the sum of the Zeeman and isotropic shielding Hamiltonians. Because one of the signals is set on resonance, the magnetisation vector corresponding to that signal is static in the rotating frame. The t_1 period is set to be exactly the period required for the non-static resonance to precess through 180° to the -y-axis. A second 90° pulse then rotates each of the magnetisation vectors into the positive and negative z-axes. The second period, t_m, is the mixing period during which the two magnetisation vectors return to equilibrium via spin-lattice relaxation, and exchange can occur. The intensity of each magnetisation vector can be evaluated at any time by another 90° pulse that rotates the two vectors into the transverse plane, in which they may be observed. Thus the experiment is generally performed for a variety of mixing times, yielding a series of spectra that are a function of the t_m period. The integrals of each peak as a function of mixing time are then plotted and fitted to a theoretical function, from which a value for the rate constant may be obtained.

6.2.1.1. Theoretical treatment of the SPI Experiment

The similarity between the SPI and 2D-EXSY pulse sequences means that the evolution of magnetisation in each experiment is almost identical. However, the SPI experiment requires the transmitter to be set to the Larmor frequency of one of the resonances (in this example, $\Delta\omega_1 = 0$) and for the t_1 evolution duration to be set to the time required for one of the peaks' magnetisation vectors to precess 180°.

$$t_1 = \frac{1}{2|\nu_1 - \nu_2|} = \frac{\pi}{\Delta\omega_2} \qquad \textit{Equation 6.28}$$

Therefore at the end of the t_1 period the magnetisation evolved may be written

$$M(t_1) = \sum_j M_j(0) \times \exp(i\pi \frac{\Delta\omega_j}{\Delta\omega_2}) \exp\left(\frac{-t_1}{T_{2,j}}\right) \qquad \textit{Equation 6.29}$$

The second 90° pulse then rotates the magnetisation into the xz plane, though the resultant magnetisation is purely along the positive and negative z-axes.

$$M_z(t_1) = \sum_j (-1)^j M_j(0) \times \exp\left(\frac{-t_1}{T_{2,j}}\right) \qquad \textit{Equation 6.30}$$

The effect of the relaxation and exchange processes during the mixing time are described by an identical pair of differential equations to those used in the 2D-EXSY pulse sequence. From equation 6.8, the magnetisation at the end of the mixing time is

$$M_z(t_1, t_m) = \sum_j M_j(0) - \sum_{i=1}^{i=2} M_i(0) \left(\exp\left(-\bar{R}t_m\right)\right)_{ji} \left[1 + (-1)^i \exp\left(\frac{-t_1}{T_{2,i}}\right)\right] \qquad \textit{Equation 6.31}$$

A third 90° pulse rotates the magnetisation into the transverse plane where a FID is acquired. Phase cycling is used to remove magnetisation arising solely from the effect of the third pulse, leaving

$$M(t_1, t_m, t_2) = \sum_{i,j} (-1)^i M_i(0) \exp\left(\frac{-t_1}{T_{2,i}}\right) \left(\exp\left(-\bar{R}t_m\right)\right)_{ji} \exp\left(i\Delta\omega_j t_2\right) \exp\left(\frac{-t_2}{T_{2,j}}\right)$$

Equation 6.32

A complex Fourier transform is performed with respect to t_2 and, after phase correction, the absorption part of the final spectrum can be written

$$S(t_1,t_m,t_2)=\left\{-M_1(0)\exp\left(\frac{-t_1}{T_{2,1}}\right)\left(\exp\left(-\overline{R}t_m\right)\right)_{11}+M_2(0)\exp\left(\frac{-t_1}{T_{2,2}}\right)\left(\exp\left(-\overline{R}t_m\right)\right)_{12}\right\}\times T_{2,1}$$

$$+\left\{M_2(0)\exp\left(\frac{-t_1}{T_{2,2}}\right)\left(\exp\left(-\overline{R}t_m\right)\right)_{22}-M_1(0)\exp\left(\frac{-t_1}{T_{2,1}}\right)\left(\exp\left(-\overline{R}t_m\right)\right)_{21}+\right\}\times\frac{T_{2,2}{}^{-1}}{\Delta\omega_2{}^{2}+T_{2,2}{}^{-2}}$$

Equation 6.33

This corresponds to a peak at 0 ppm of width $\pi T_{2,1}$ Hz with intensity given by the terms in the first bracket and another peak of width $\pi T_{2,2}$ Hz occurring at $\Delta\omega_2$ with intensity denoted by the terms in the second bracket. The intensity of each peak can be fitted to a theoretical model, and information upon the exchange process can be obtained. Several parameters are required in order to do this, but they can be acquired from relaxation experiments and 1D spectra.

6.2.2. EXPERIMENTAL PROCEDURE

The experiments were performed upon samples of SC2 carbon with 100% w/w TMP adsorbed at ambient temperature only. A large amount of adsorbate was used in order to make sure that there was a reasonable amount of peak II intensity, ensuring that the exchange process was significant enough to be measured. Each sample was left to equilibrate for over 12 hours prior to the experiment. The B_1 power applied was equivalent to a 5 μs 90° pulse, set upon each sample. A simple 1D spectrum was recorded prior to the experiment and the frequency difference between the two peaks and linewidth measurements for each peak were obtained. The duration of t_1 was calculated from the frequency difference between the two and varied between 710 μs and 725 μs depending upon the exact chemical shift of peak I observed for each sample. The SPI experiment was conducted for 20 to 25 values of t_m, ranging from 0.002 s to 5 s. Each spectrum was acquired using 128 transients with a recycle delay of 12 seconds. The total experimental time for each experiment was thus approximately 11 hours. Two experiments were performed on each occasion, inverting each of the two peaks. The FIDs were processed as for a standard single-pulse experiment. The peak areas, obtained via the measurement of the integral between the outer limits of each peak, were obtained for each spectrum and plotted against the mixing time, t_1.

The results obtained were then fitted within MATHCAD to a theoretical model. In this instance the coupled differential equations were solved numerically using the fourth-order Runge-Kutta method[26] within MATHCAD. The exchange matrix, $\mathbf{R}_{ji}$, describing the exchange and T_1 relaxation is identical to that described in Equation 6.6.[*] The parameters were then fitted to the experimental data, first by eye and then using the Marquadt-Levenberg algorithm[27]. It was found that satisfactory convergence could not be achieved between the experimental data and the theoretical peak intensities using a two-peak model, so it was necessary to extend the model to a three-peak situation. The differential equations were extended to include a non-exchanging third peak, meaning that the exchange matrix, **R** then became

$$\bar{R} = \begin{pmatrix} -\left(\frac{1}{T_{1,1}} + k\right) & k & 0 \\ k & -\left(\frac{1}{T_{1,2}} + k\right) & 0 \\ 0 & 0 & -\left(\frac{1}{T_{1,2}}\right) \end{pmatrix} \qquad \textit{Equation 6.34}$$

6.2.3. EXPERIMENTAL RESULTS

Typical spectra obtained, inverting each of the two peaks, are shown in Figures 6.6 and 6.7. The graphs in the lower part of each figure plot the area of each peak as a function of t_1. Results for the first second, rather than for the whole experiment, are shown in order to accentuate the variation in peak intensity obtained in the first few ms.

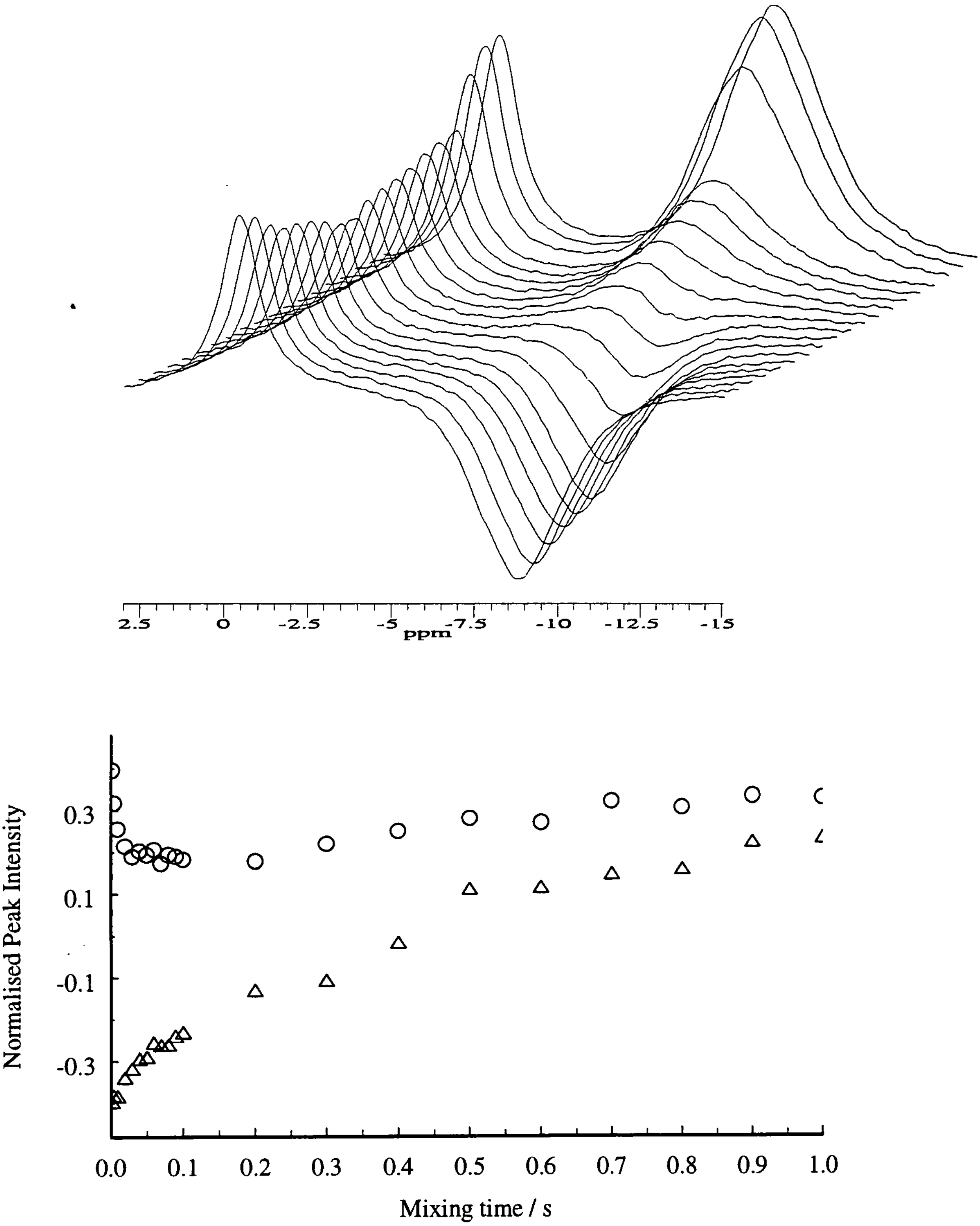

Figure 6.6. Integrals of peak I and II plotted against the duration of the mixing period in the SPI experiment for 100% w/w TMP upon SC2 carbon. The centre of the low-frequency peak was inverted in this experiment. The circles represent the area of peak I whilst the triangles represent the integral of peak II.

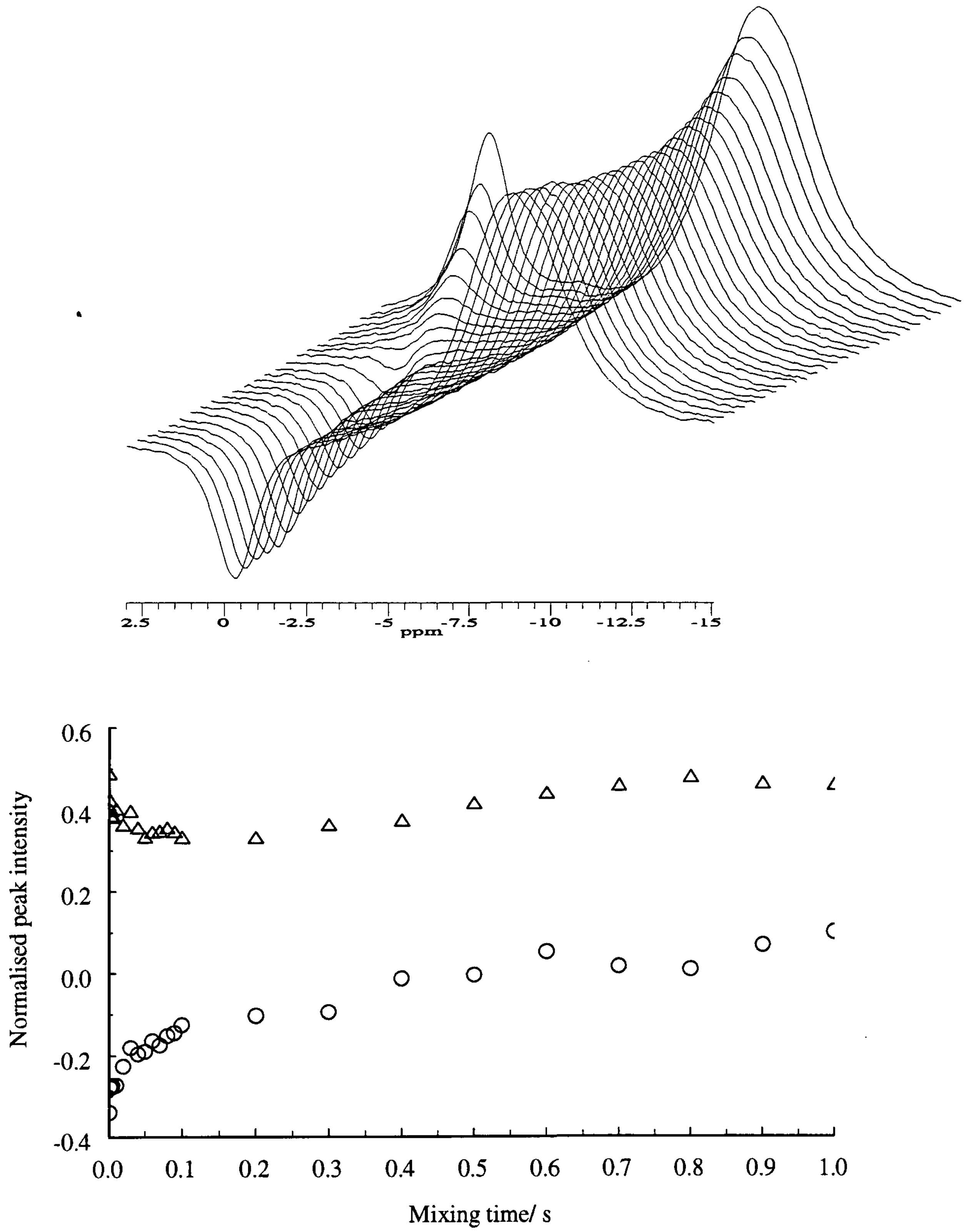

Figure 6.7. Integrals of peak I and II plotted against the duration of the mixing period in the SPI experiment for 100% w/w TMP upon SC2 carbon. The peak at 0 ppm was inverted in this experiment. The circles represent the area under peak I whilst the triangles represent the integral of peak II.

6.2.4. DISCUSSION

The plots shown in the lower portion of Figures 6.6 and 6.7 were initially fitted to a theoretical model that assumed that they resulted from two exchanging peaks. The values for x_a and x_b and the values of T_2 for each peak were obtained from the 1D spectrum of each sample, whilst the T_1 relaxation times were obtained from the inversion recovery experiments performed in Chapter 7. Molar fraction values used were $x_{peakI} = 0.55$ and $x_{peakII} = 0.45$. The relaxation values for the peak II resonance were $T_1 = 2.3$ s and $T_2 = 3.2$ ms whilst the corresponding values for peak I were $T_1 = 1.0$ s and $T_2 = 0.8$ ms. The relaxation times for the inhomogenous peak I are an average of the values obtained across the peak, but it was found that no significant problems were introduced into the fitting procedure by using this approximation.

The iterative fitting procedure for the two-peak model involved only a single parameter, k. The value obtained from the EXSY experiments ($k = 1.5\ s^{-1}$) was used as the starting point for the fitting process. It was found in each case that the iteration would not converge using the parameters that were obtained from the 1D spectra and relaxation experiments. Fitting the plots visually suggested that the best results occurred at approximately $k = 1\ s^{-1}$, but it was clear that the SPI results were not approximated at all well to the theoretical plot using the two-peak model. A simple consideration of the shape of each curve shows that this is what would be expected. In each experiment the magnetisation of the peak at resonance shows a rapid initial decrease. The non-inverted resonance is reduced in intensity by T_2 relaxation during t_1 and this magnetisation recovers via T_1 relaxation during the mixing time. The only way that a decrease in the magnetisation at that frequency would occur with an increase in t_m is via the transfer of magnetisation from the resonance at which the magnetisation is inverted. A corresponding small increase in the magnetisation of the inverted resonance within the first few hundredths of a second is also observed. Thus there is clearly rapid exchange occurring. However, the total size of the rapid change in magnetisation is small. This suggests that the proportion of molecules undergoing the rapid exchange is low, and shows why the experimental data cannot be approximated by a theoretical function that assumes every molecule within the sample is undergoing a slow exchange process.

2D-EXSY results suggested that only a proportion of the molecules comprising peak I underwent exchange and therefore a three-peak fit was considered more appropriate. In this model, the magnetisation of peak I was split into two contributions, one of which underwent exchange with peak II whilst the other returned to equilibrium solely under the influence of T_1 relaxation. Therefore the fitting procedure in this instance involved two parameters, the exchange rate, k, and the ratio of low-frequency peak molecules that underwent exchange. The fitted curves obtained using the two-parameter fit are shown in Figure 6.8. It can be seen that the calculated plots approximate the experimental curves reasonably well in this example. However, the fit was not always so good and there was significant variation between the values obtained when the experiment was repeated. This is shown by the large errors in the two parameters. The values of k and the fraction of peak I intensity involved in the exchange process, f_{ex}, calculated for the two experiments are shown in Table 6.3.

Peak inverted	**k / s^{-1}**	**f_{ex}**
Peak II	8 ± 3	0.24 ± 0.10
Peak I	6 ± 3	0.31 ± 0.15

Table 6.3. Results of the three-peak fitting procedure for 100% w/w TMP upon SC2

The errors are up to 50% in some instances and therefore it is not possible to view the results as any better than semi-quantitative. However, the table does show that exchange of molecules between the two sites occurs for a limited proportion (~30%) of the molecules comprising peak I, and that the exchange process is reasonably fast ($k \approx 7\ s^{-1}$).

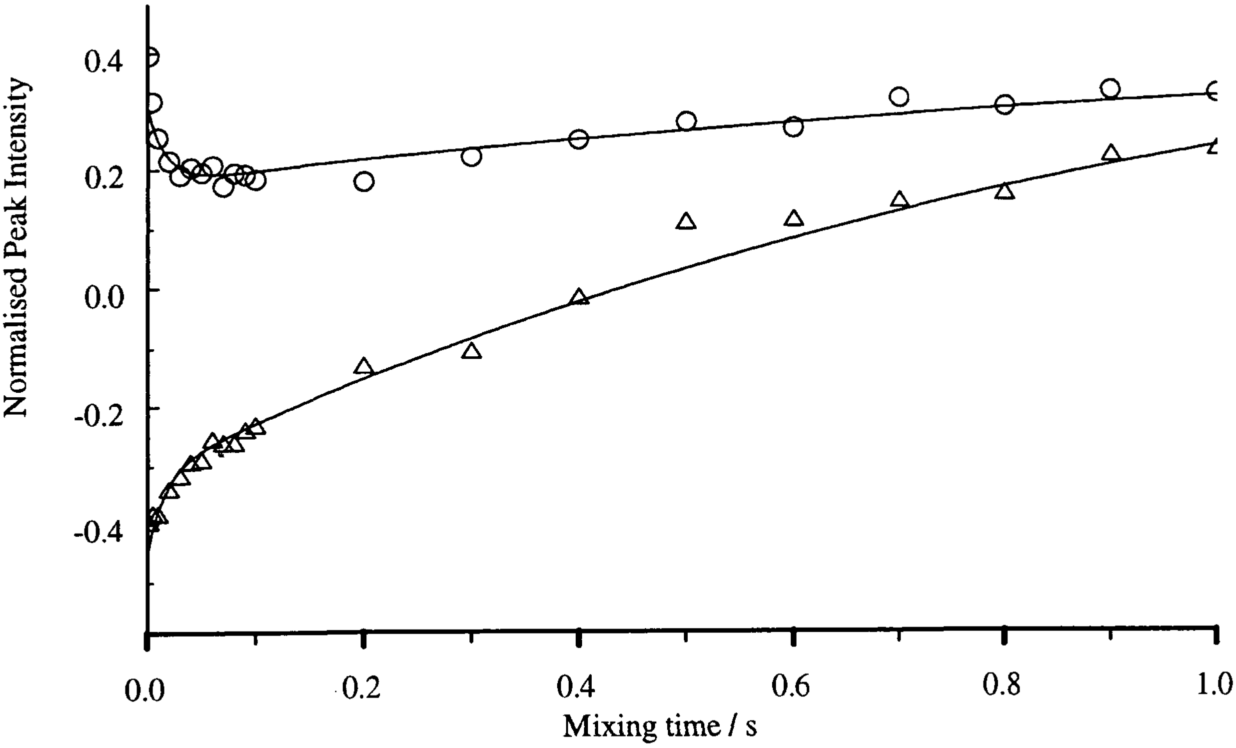

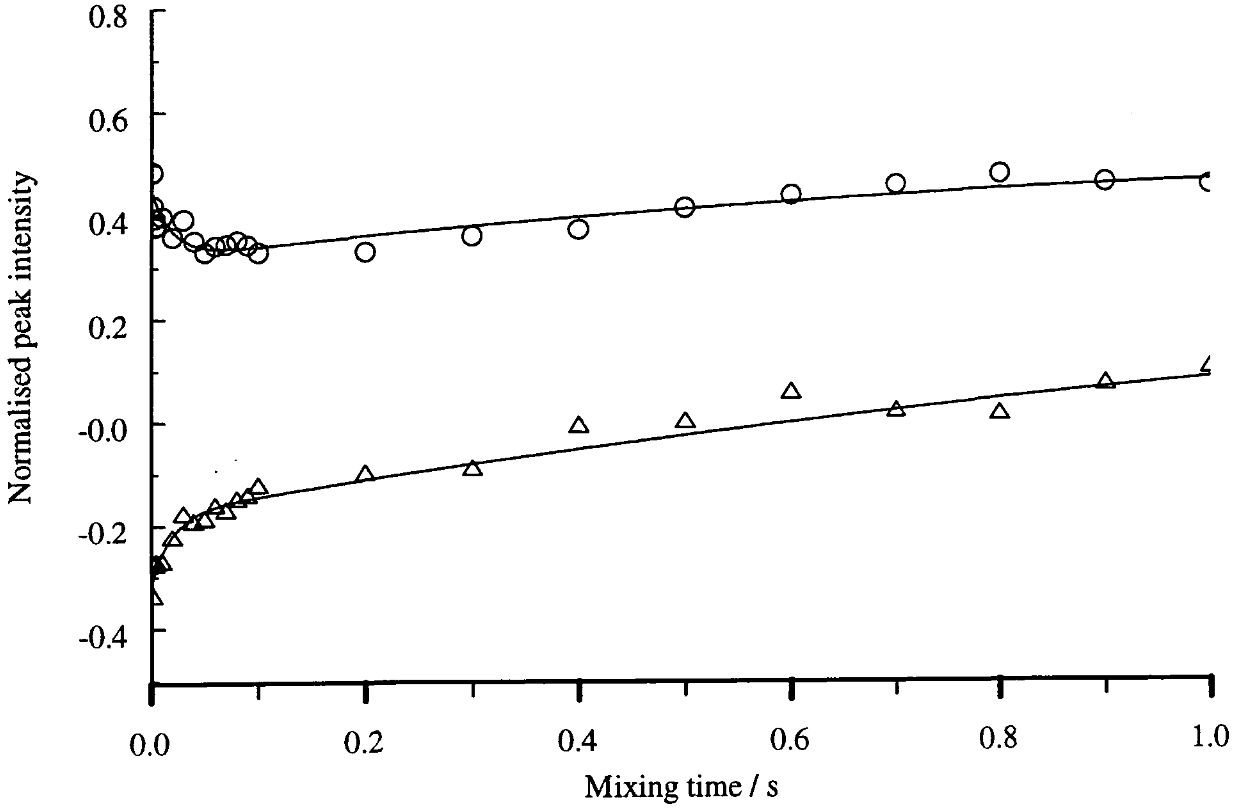

Figure 6.8. SPI experimental results for 100% w/w TMP added to SC2 carbon fitted to the three peak model. The top plot shows the results obtained after inverting the peak at 0 ppm whilst the lower plot results from the experiment inverting the low-frequency peak.

6.3. CONCLUSIONS REACHED BY DYNAMIC NMR

The results from the two previous chapters have shown that there is movement of molecules between the two peaks, and that this movement may occur in either direction. The two experimental techniques probing the movement of molecules between environments within the carbon adsorbent have provided complementary information upon the exchange process. The SPI experiments demonstrated that the exchange of magnetisation between the peaks could not be modelled assuming that all molecules within peak I were able to swap position with the molecules giving rise to peak II. Fitting the experimental results to a slightly more complex model in which only a proportion of the molecules within the porous volume could undergo exchange showed that approximately 30% of these molecules were able to swap environment with the excess adsorbate. The rate constant for the exchange process was found to be approximately 7 s^{-1}. The 2D-EXSY experiment provided more precise information upon the environment of the molecules that underwent exchange. It was found that the molecules that were able to migrate between environments were found towards the higher frequency end of peak I. No evidence of exchange between the low-frequency end of the peak I and peak II was detected. This demonstrates that molecules within larger pores and the excess adsorbate are able to swap environments whilst molecules within narrower pores are unable to do so. The excess adsorbate is thought to exist solely upon the exterior surface of the carbon particles and therefore the molecules within the porous volume that are able to exchange must be situated close to the particle surface. Thus we believe that it is demonstrated that larger pores are found toward the exterior of the pore system whilst the smaller pores are found deeper within the porous volume. Of course it is also true that molecules are held more firmly within the smaller pores.

Performing the 2D-EXSY experiment over a large variety of temperatures showed that the temperature did not affect the rate constant for the exchange. This shows that the rate of exchange is not thermodynamically controlled and therefore the limiting factor in the exchange of molecules between environments is simply the number of molecules in pores open to the carbon surface.

Finally, the results obtained from the three-peak SPI calculation performed on 50% w/w TMP upon SC2 were in excellent agreement with the peak intensities obtained in the 2D-EXSY experiment on a similar sample at the same temperature. A comparison of the 2D-EXSY experimental results and the expected 2D-EXSY peak intensities calculated using the parameters obtained from the SPI experiment is given in Table 6.4.

Method	**Peak II**	**Peak I**	**Off-Diagonal**
2D-EXSY results	16.9	78.0	5.0
Calculated from SPI results	16.8	78.0	5.2

Table 6.4. Comparison of peak intensities obtained from the 2D-EXSY experiment at ambient temperature and the theoretical values predicted from the results of the SPI experiment.

6.4. REFERENCES

1. J. Jeener, B. H. Meier, P. Bachmann, R. R. Ernst, *J. Chem. Phys.* **71**, 4546 (1979)
2. D. D. Traficante, *Concepts in Magnetic Resonance*, **1**, 7 (1989)
3. C. L. Perrin, T. J. Dwyer, *Chem. Rev.*, **90**, 935 (1990)
4. S. Macura, R. R. Ernst, *Mol. Phys.*, **41**, 95 (1980)
5. C. L. Perrin, R. K. Gipe, *J. Am. Chem. Soc.*, **106**, 4036 (1984)
6. G. E. H. Reuter, *"Elementary Differential Equations and Operators"*, Routledge and Kegan Paul Ltd. (1958)
7. D. D. Traficante, *Concepts in Magnetic Resonance*, **2**, 151 (1990)
8. D. D. Traficante, *Concepts in Magnetic Resonance*, **2**, 181 (1990)
9. J. D. Ellet Jr., M. G. Gibby, U. Haeberlen, L. M. Huber, M. Mehring, A. Pines, J.S. Waugh, *Adv. Magn. Resonance*, **5**, 117 (1971)
10. A. Bax, *"Two-dimensional NMR in Liquids"*, Delft University Press, Delft (1982)
11. J. Keeler, D. Neuhaus, *J. Magn. Reson.*, **63**, 454 (1985)
12. D. Marion and K. Wuthrich, *Biochem. Biophys. Res. Commun.*, **113**, 967 (1983)
13. A. G. Redfield, S. D. Kunz, *J. Magn. Reson.,* **19**, 250 (1975)
14. D. J. States, R. A. Haeberlen, D. J. Ruben, *J. Magn. Reson.*, **48**, 286 (1982)
15. R. R. Ernst, G. Bodenhausen, A. Wokaun, *Principles of NMR in One and Two Dimensions"*, Clarendon Press, Oxford (1987), Chapter 6
16. W. S. Veeman, Summer School at Durham (1997)

17. A. D. Bain, *J. Magn. Reson.*, **56**, 418 (1984)

18. D. I. Hoult, *Prog. NMR Spectrosc.*, **12**, 41 (1978)

19. A. Kumar, G. Wagner, R. R. Ernst, K. Wuthrich, *J. Am. Chem. Soc.*, **103**, 3654 (1981)

20. R. Freeman, *"A Handbook of NMR"*, Longman, 1991

21. G. Bodenhausen, R. Freeman, G. A. Morris, *J. Magn. Reson.*, **23**, 171 (1978)

22. G. A. Morris, R. Freeman, *J. Magn. Reson.*, **29**, 433 (1978)

23. G. Robinson, P. W. Kuchel, B. E. Chapman, D. M. Doddrell, M. G. Irving, *J. Magn. Reson.*, **63**, 314 (1985)

24. C. L. Perrin, R. K. Gipe, *J. Am. Chem. Soc.*, **106**, 4036 (1984)

25. J. W. Keepers, T. L. James, *J. Magn. Reson.*, **57**, 404 (1984)

26. W. H. Press, B. P. Flannery, S. A. Teukolsky, W. T. Vetterling, *"Numerical Recipes in C"*, 2nd edition, Cambridge University Press, 1992

27. D. W. Marquadt, *"Journal of the Society for Industrial and Applied Mathematics"*, **2**, 431 (1963)

28. MATHCAD v7.0, Mathsoft Inc.

29. H. H. Limbach, B. Wehrle, M. Schlabach, R. Kendrick, C. S. Yannoni, *J. Magn. Reson.,* 77, 84 (1988)

30. G. Robinson, P. W. Kuchel, B. E. Chapman, D. M. Doddrell, M. G. Irving, , *J. Magn. Reson.,* **63**, 314 (1985)

RELAXATION MEASUREMENTS PERFORMED ON ADSORBATES UPON ACTIVATED CARBON

The results within this thesis are presented and discussed on the basis that peak I is an inhomogenous entity. Much of the data obtained already suggests that this is the case. For example, the variable shape, shift and width of the low-frequency resonance in the 1D spectra reported in Chapters 4 and 5 and the exact position of the off-diagonal peaks in 2D-EXSY experiments both imply that peak I comprises more than one resonance. In order to analyse the inhomogeneity in this peak it is necessary to use a technique that discriminates between molecules in different positions. Relaxation measurements possess this attribute.

7.1 THEORY OF RELAXATION

The application of a radio-frequency pulse to a system of nuclear spins introduces a deviation from equilibrium. Bloch[1] studied the return of excited nuclei towards equilibrium, and in 1946 he proposed a set of phenomenological equations to describe the process. These described the observed decay of the magnetisation in terms of two distinct exponential time constants, T_1 and T_2.

$$\frac{dM_x}{dt} = -\frac{M_x}{T_2}$$
$$\frac{dM_y}{dt} = -\frac{M_y}{T_2}$$
$$\frac{dM_z}{dt} = -\frac{M_z - M_0}{T_1}$$

Equations 7.1

How these relaxation times arise is an extremely complex area of NMR. Almost every NMR textbook devotes one or more chapters to relaxation in ideal situations, whilst relaxation has been the sole subject of several extensive articles and books[2-5]. In the current study relaxation times are used qualitatively to try to discriminate between molecules giving signals at different positions within the broad peak envelope. However, relaxation times are intimately related to the mobility around the nucleus of study and therefore quantitative measurement of relaxation parameters may also provide information upon the extent of molecular motion. The basic quantum theory of relaxation was introduced by Bloembergen, Purcell and Pound[6], and BPP theory has been extended and developed extensively in subsequent publications, for example[7, 8]. The results of calculations performed for a simple spin system are outlined below to illustrate the way in which molecular motion affects relaxation times

Transitions between nuclear energy levels are induced by magnetic fields fluctuating at the correct frequency. In solutions the fluctuation in magnetic field is introduced by motion of molecules, which varies the local magnetic field at the nuclei. If a system of isolated spins, experiencing an isotropic, time-dependent variation in magnetic field, is considered then the relaxation times can be shown to be[9]

$$T_1^{-1} = \gamma_I^{\,2}\left[B^0{}_{xL}\right]^2 \frac{2\tau_C}{1+\omega_{0(I)}{}^2\tau_C{}^2}$$

$$T_2^{-1} = 2\left(\gamma_I^{\,2}\left[B^0{}_{xL}\right]^2 \frac{2\tau_C}{1+\omega_{0(I)}{}^2\tau_C{}^2}\right) + \frac{1}{2}\gamma_I^{\,2}\left[B^0{}_{zL}\right]^2 \times \int_{-\infty}^{\infty} \exp\frac{-\tau}{\tau_C}\,d\tau \qquad \textit{Equations 7.2}$$

The x and z components of the fluctuating isotropic field are represented by the terms within the square brackets, whilst τ_c is the correlation time for the motion of the molecule. For random molecular tumbling, τ_c is roughly the time required for the molecule to rotate through 1 radian. The variation of the relaxation times with the correlation times that may occur in solution is shown in Figure 7.1. Relaxation within the solid state is rather more complicated due to the presence of several distinct, possibly anisotropic, motions, each of which will have a separate correlation time. However, Figure 7.1 shows that an increase in the value of T_2 is caused by a decrease in the motional correlation time, representing an increase in molecular motion. The relation of T_1 with τ_c depends upon which side of the graph the motional correlation time is with respect to the T_1 minimum.

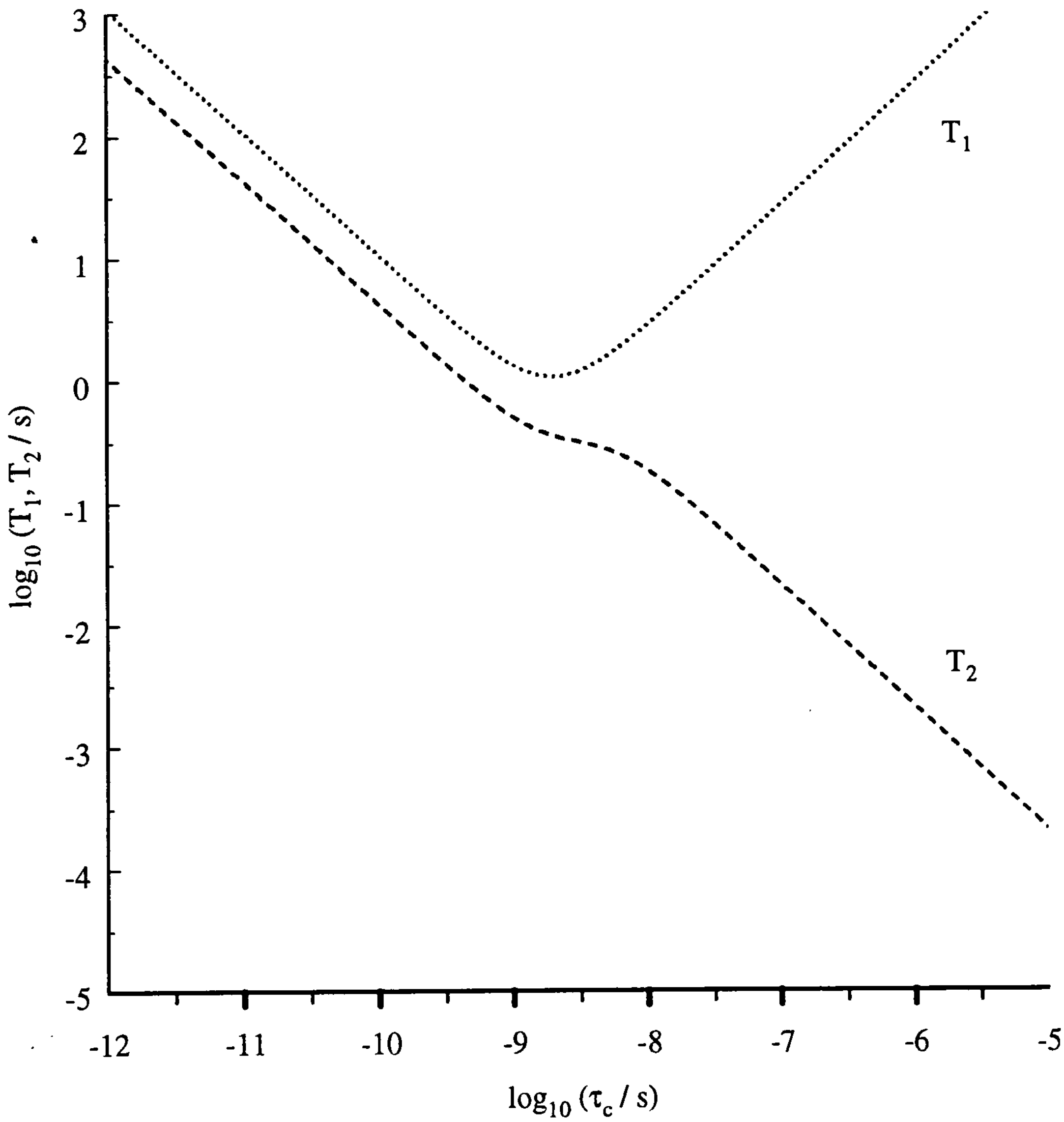

Figure 7.1. The dependence of relaxation times, T_1 and T_2, upon the correlation time, τ_c, for the relaxation of an isolated spin by random isotropic magnetic fields. The resonance frequency of the nucleus is at 81.01 MHz. A value of 0.2×10^{-3} T has been used to describe the r.m.s. average amplitude of the isotropic field.

7.2 SPIN-LATTICE RELAXATION

Spin-lattice relaxation is the process by which the magnetisation giving rise to each resonance returns along the z-axis back to its equilibrium value. The equilibrium-state of a spin-$^1/_2$ system was discussed in Chapter 1, and consists of a small net magnetisation in the positive z-direction. In simple cases the relaxation is exponential and the time constant for spin-lattice relaxation is termed T_1. T_1 is defined as the time required for the z-axis magnetisation to recover to $(1 - e^{-1})$ of its value prior to the perturbation from the equilibrium state. Pulse sequences require the spin system to be at equilibrium before each NMR experiment commences and thus it is important that T_1 is accurately measured in order to determine the optimal recycle delay between transients. Recycle delays of $5T_1$ are commonly used. After a delay of $5T_1$ 99.3% of the sample magnetisation has returned to equilibrium.

7.2.1 THE INVERSION-RECOVERY EXPERIMENT

Spin lattice relaxation times can be measured by a variety of NMR experiments[10, 11]. The most common technique for measuring T_1 in samples with reasonably short relaxation times is via the inversion-recovery experiment. The pulse sequence required for the inversion-recovery experiment is shown in Figure 7.2.

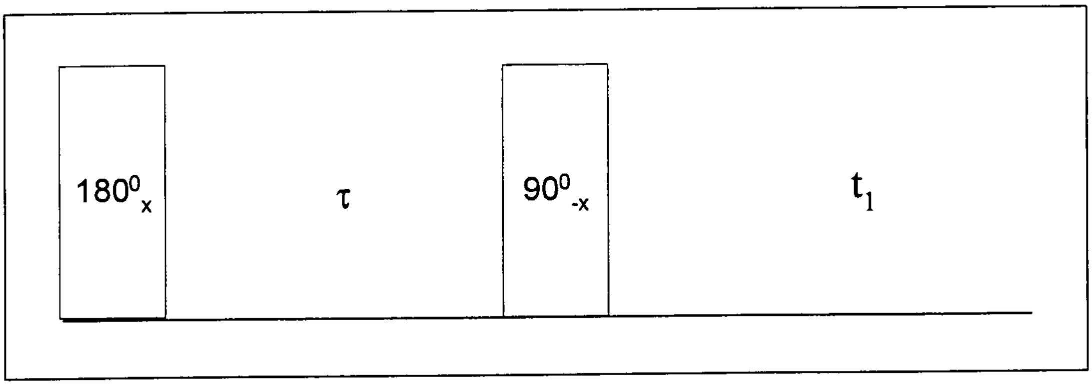

Figure 7.2. The inversion-recovery pulse sequence

The evolution of the magnetisation during the experiment is outlined below. The initial pulse rotates each of the magnetisation vectors from their equilibrium position along the positive z-axis through 180° to the negative z-axis. The magnetisation at the beginning of the τ period is simply minus the equilibrium magnetisation. The vectors are then allowed to relax back towards equilibrium via spin-lattice relaxation for a period, τ. The magnetisation at the end of this period is therefore

$$M(\tau) = \sum_j M_j(0) - 2M_j(0)\exp\left(\frac{-\tau}{T_{1,j}}\right) \qquad \textit{Equation 7.3}$$

After the variable time, τ, the magnetisation is rotated into the transverse plane by another 90° pulse where it evolves according to the effective spin Hamiltonian. The magnetisation is detected during this period.

$$M(\tau) = \sum_j M_j(0)\left\{1 - 2\exp\left(\frac{-\tau}{T_{1,j}}\right)\right\} \times \exp(i\Delta\omega_j t_1)\exp\left(\frac{-t_1}{T_{2,j}}\right) \qquad \textit{Equation 7.4}$$

A complex Fourier Transform is applied to the FID with respect to t_1, resulting in a standard 1D spectrum with the intensity of each resonance within the spectrum determined by the duration of τ and the value of the relevant T_1. The real part of the spectrum may be written

$$S(\tau, t_1) = \sum_j M_j(0)\left\{1 - 2\exp\left(\frac{-\tau}{T_{1,j}}\right)\right\} \times \frac{T_{2,j}^{-1}}{\Delta\omega_j^{2} - T_{2,j}^{-2}} \qquad \textit{Equation 7.5}$$

The experiment is repeated for a number of tau periods and the intensity of each resonance is then plotted as a function of τ. The decay of each resonance in the spectrum determines the value of T_1 for the nuclei within molecules at that site.

7.2.2 VARIABLE-TEMPERATURE INVERSION-RECOVERY EXPERIMENT

As was shown in Figure 7.1 the variation of T_1 with molecular motion depends upon which side of the T_1 minimum the motional regime that is being studied falls. In the present study the nuclei possess an intermediate amount of motion. The nuclei are not as restricted as in solid materials but conversely they are not as mobile as in solutions and it is not known which side of the T_1 minimum their motion falls. Thus an isolated inversion-recovery experiment conducted at a single temperature, whilst it may demonstrate the inhomogeneity of the low-frequency peak, does not provide any information upon the variation in motion with position in the broad peak envelope. Variable-temperature experiments allow the correlation times of the various motions to be altered manually. From a comparison of results at several temperatures it is possible to ascertain which side of the T_1 minimum the motional regime occurs.

7.2.2.1 Experimental Procedure

The experiments were conducted upon SC2 carbon with 100% w/w TMP pre-adsorbed. The samples were sealed within glass ampoules and left to equilibrate for 48 hours prior to acquisition. A 10 μs 180° pulse was calibrated upon the actual sample that was used in each experiment. Experiments were performed at nine separate temperatures, ranging from –30°C to 60°C. 64 transients were recorded for each value of τ with a recycle delay of 10 s. Approximately 20 values of τ, ranging from 0.01 ms to 5 s, were used in each experiment leading to a total experimental time of just under four hours. Given the additional complications in determining pulse durations within these samples, a compensated[12] 180° pulse was utilised. The compensated pulse allows for off-resonance effects and inaccurate B_1 power setting, thus ensuring that the initial population inversion is as accurate as possible.

The FIDs obtained after the 90° pulse for each value of tau were each processed in an identical manner. The spectra obtained were then plotted against τ and the intensity of selected frequencies within the spectrum recorded as a function of τ. The relaxation of peak I was recorded every 0.05 ppm. The graphs plotting intensity against τ at each frequency were then fitted to an exponential function (Equation 7.6) using the Levenberg-Marquardt algorithm[13] within SPSS[14], leading to a series of values for T_1 at different frequencies.

$$S_{\Delta\delta}(\tau) = A_{\Delta\delta}(0) \times \left\{1 - 2\exp\left(\frac{-\tau}{T_{1,\Delta\delta}}\right)\right\} \qquad \text{Equation 7.6}$$

The results were then compared between experiments performed at a variety of temperatures.

7.2.2.2 Experimental Results

A typical spectrum obtained from an inversion-recovery experiment recorded for 100% w/w TMP upon SC2 is shown in Figure 7.3. The results obtained from analysis of peak I for the experiment performed at –30°C are shown in Figure 7.4, whilst the results obtained from the same experiment at 60°C are presented in Figure 7.5. In each case the error in the value of T_1 calculated increases at the less intense portions of the peak envelope. This arises because random fluctuations in spectral intensity due to noise represent a larger proportion of the signal at these points. The regression calculation performed using these data then yields fitted parameters with a greater uncertainty. The T_1 results obtained for peak II are shown in Table 7.1. The values given within the table are those obtained from analysis of the resonance at 0.0 ppm, whilst the errors represent the variation in T_1 obtained about that point.

The T_1 value obtained for the low-frequency peak varied between 0.8 and 1.5 s depending upon temperature and the frequency at which the relaxation was analysed.

The results of each of the experiments can be combined to form a 3D plot (Figure 7.6). Slices of this plot can then be taken along either the temperature or frequency axes. If slices are taken along the frequency axis plots such as those in Figure 7.7 are obtained. These slices all showed a T_1 relaxation minimum occurring at approximately +10°C, irrespective of the frequency at which the slice was taken, though the actual value of T_1 at the minimum point varies with frequency.

Temperature / °C	**Measured T_1 for the peak at 0 ppm / s**
-30	1.3 ± 0.1
-20	1.4 ± 0.1
-10	1.8 ± 0.2
0	1.8 ± 0.2
10	2.1 ± 0.2
20	2.3 ± 0.3
30	2.2 ± 0.3
40	2.5 ± 0.4
50	2.6 ± 0.2

Table 7.1. The variation in T_1 of the resonance at 0 ppm with temperature

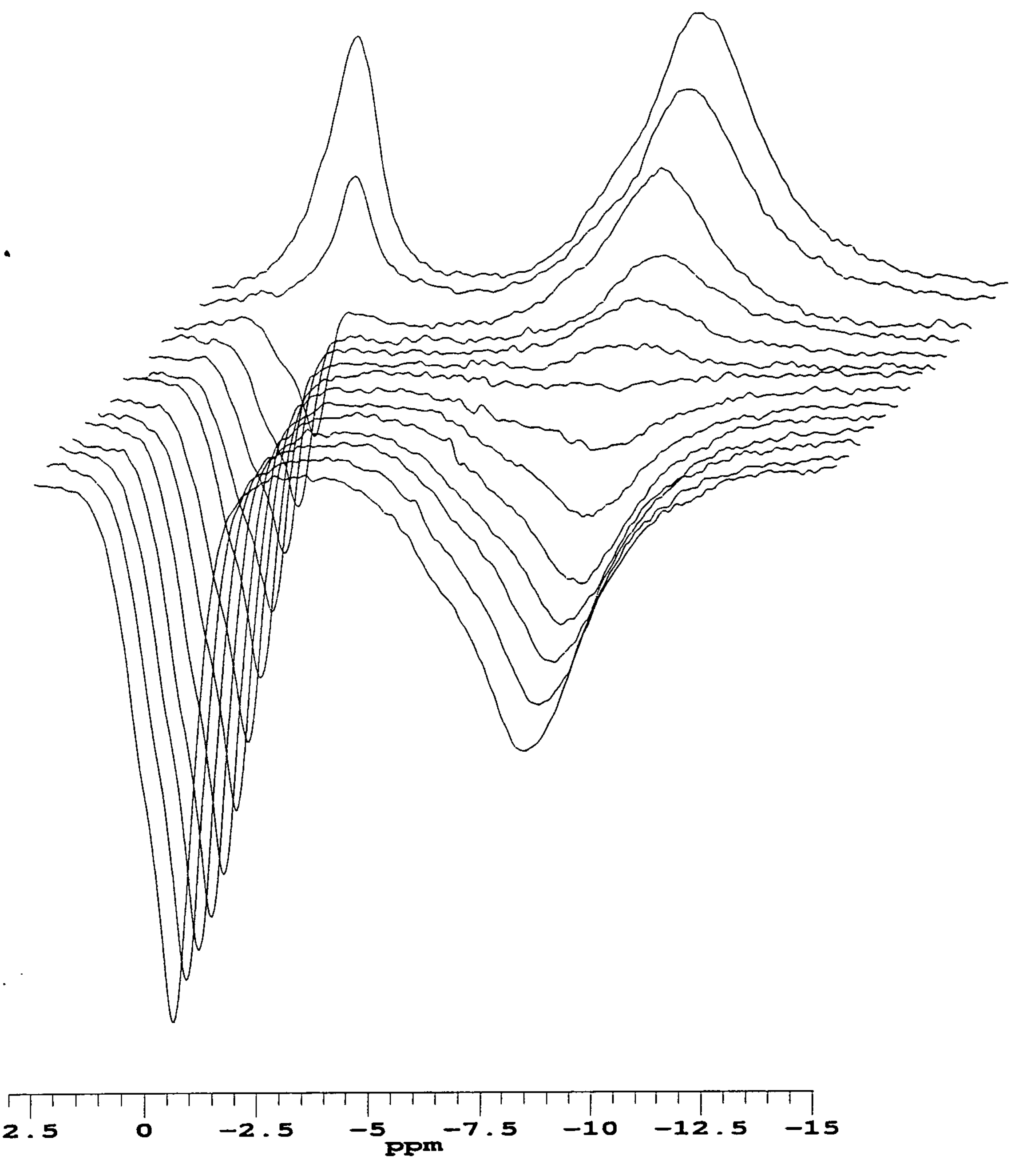

Figure 7.3. Spectra obtained from an inversion -recovery experiment performed at room temperature upon a sample of 100% w/w TMP adsorbed upon SC2 carbon. Tau increases along the y-axis, [tau/s = 0.01, 0.05, 0.1, 0.2, 0.3, 0.4, 0.5, 0.75, 1.0, 1.25, 1.5, 1.75, 2.0, 2.5, 3.0, 3.5, 5.0]

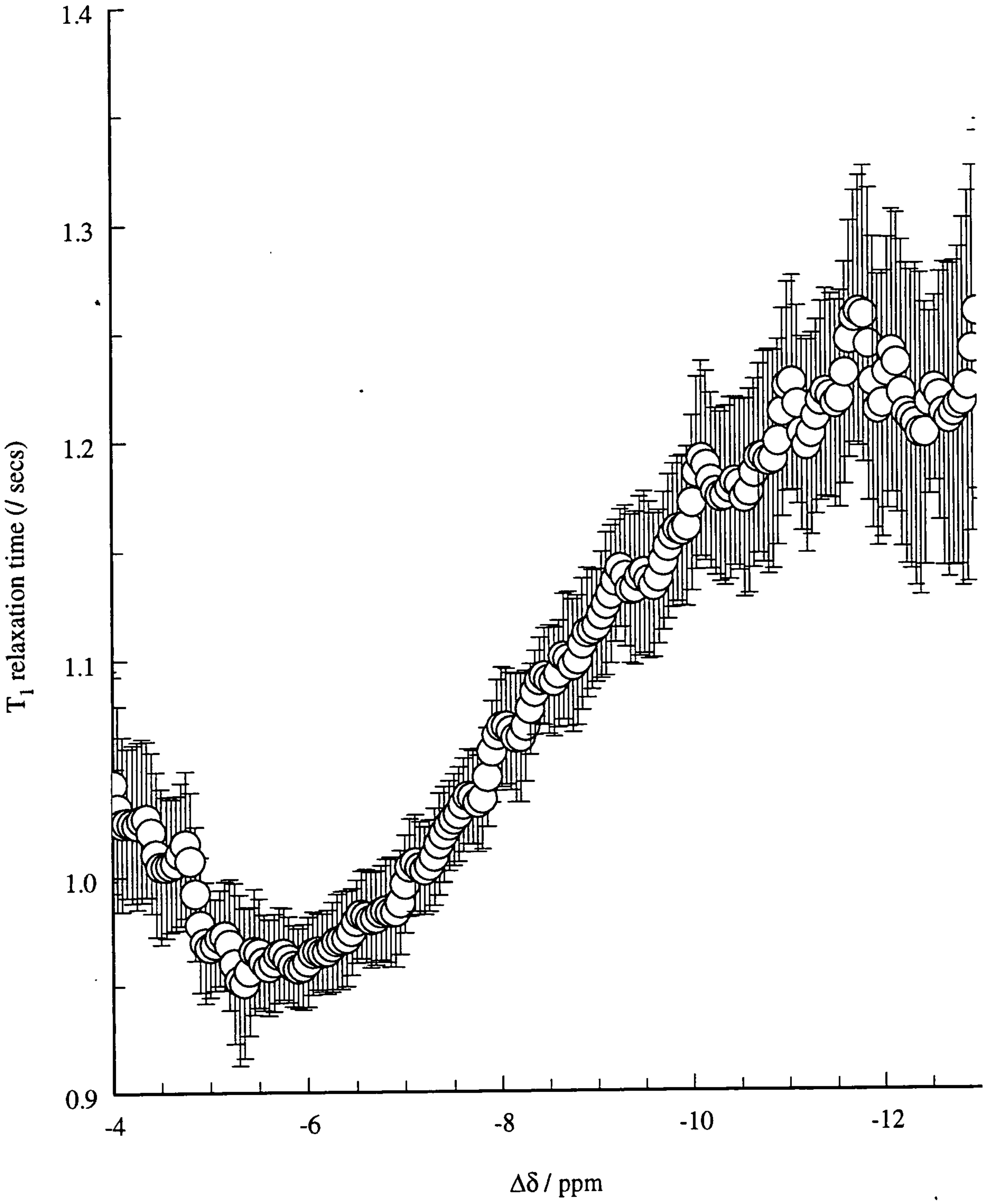

Figure 7.4. T_1 relaxation times plotted against resonance frequency for 100% w/w TMP upon SC2 activated carbon at minus 30°C. The relaxation times at each point were derived using the method explained in the text.

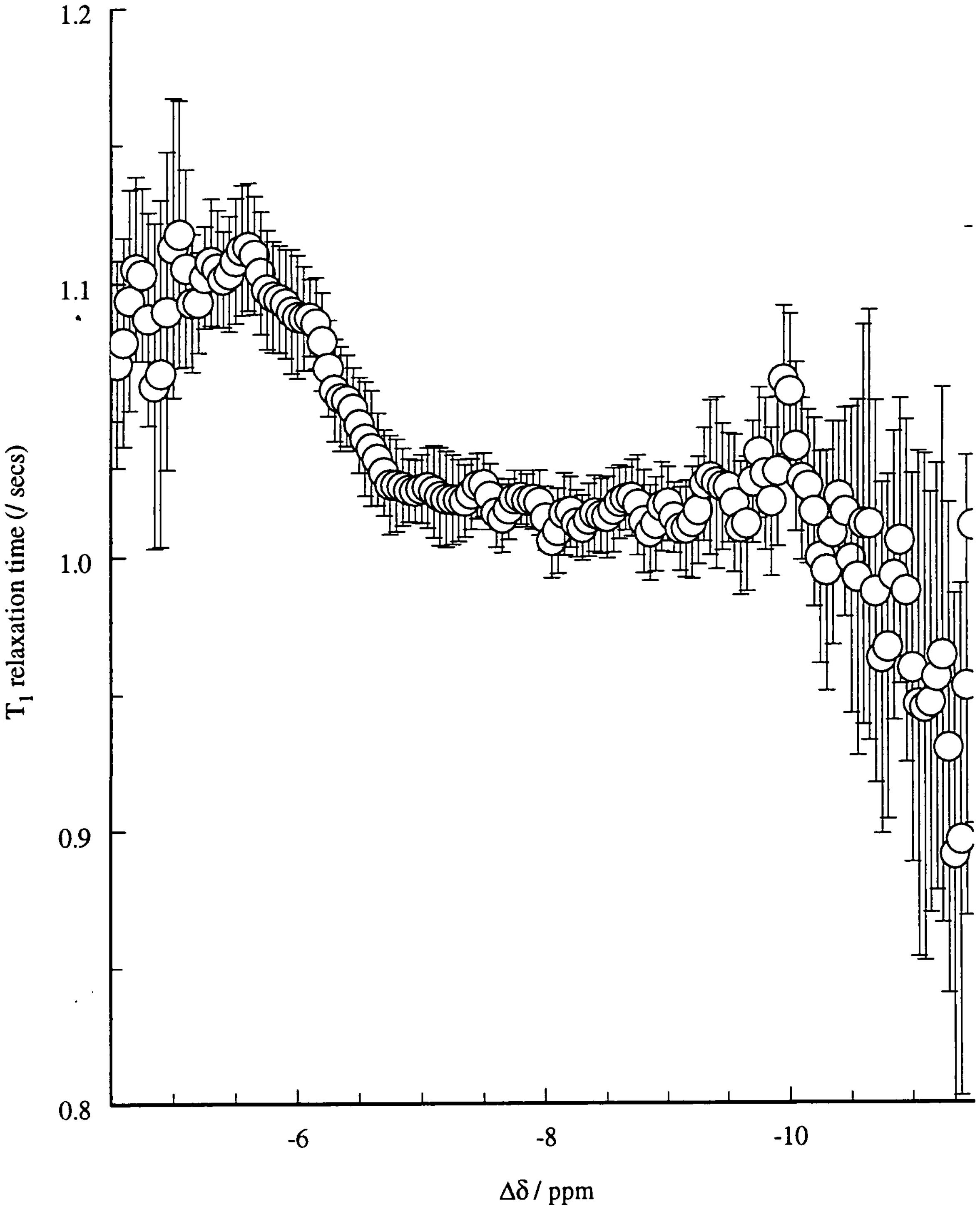

Figure 7.5. T_1 relaxation times plotted against resonance frequency for 100% w/w TMP upon SC2 activated carbon at 60^0C. The relaxation times were derived using the method explained in the text.

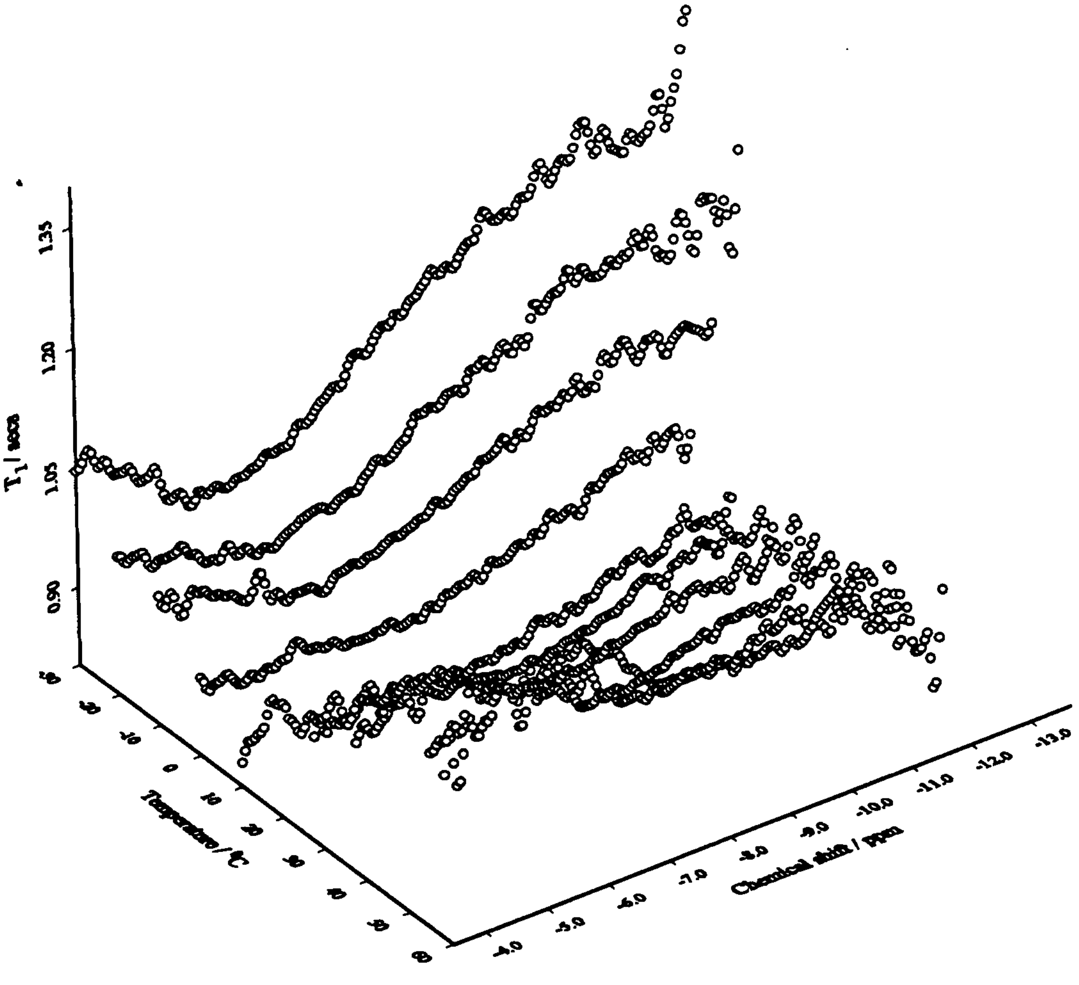

Figure 7.6. Variation in measured T_1 with sample temperature and resonance frequency. Note the T_1 minimum observed at approximately 10^0C.

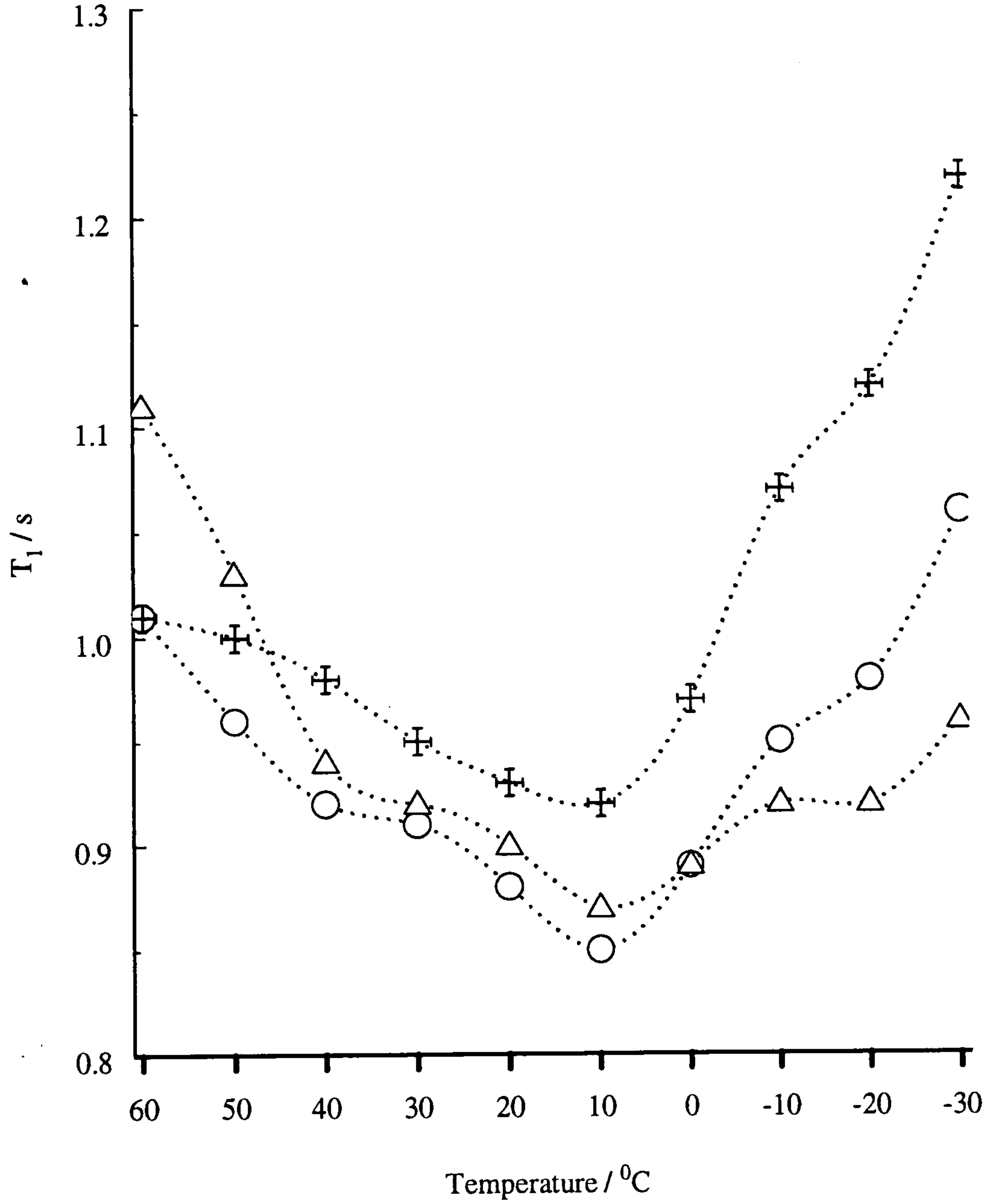

Figure 7.7. Variation in T_1 relaxation time with temperature for a variety of resonance frequencies (crosses represent data acquired at -11 ppm, circles data at -8.5 ppm and triangles data at -5 ppm).

7.2.2.3 Discussion

Relaxation measurements have shown that there is a significant difference in the mobility of molecules giving rise to the resonance at each point upon the low-frequency peak envelope. This clearly means that peak I is inhomogenous, and explains why the results within the preceding chapters have been rationalised in the way that they have. Whilst there are large differences in T_1 with frequency as peak I is traversed (up to 40% at some temperatures) it should be realised that the actual variation in relaxation times between molecules giving rise to each resonance is likely to be significantly greater. This is because the T_1 value obtained at each point on the broad peak envelope is effectively an average of the T_1 values of all the peaks contributing intensity to that point, therefore minimising the apparent variation. In comparison, the variation in T_1 values across peak II, which is believed to be homogenous in character, was much less.

Variable-temperature experiments have allowed the differences in T_1 to be discussed in terms of molecular mobility. The 3D plot and Figure 7.7 show that there is a T_1 minimum at approximately +10°C, irrespective of the frequency along peak I at which the measurement is taken. From the basic relaxation theory described earlier, an increase in T_1 at temperatures below this value (towards the right hand side of Figure 7.1) should indicate a decrease in molecular motion. The results of the relaxation experiments performed at lower temperatures (for example, those shown in Figure 7.4) show a marked increase in T_1 values with increasing low-frequency chemical shift. This suggests that the low-frequency portion of peak I arises from signals generated by more hindered molecules. The experiments performed within Chapter 4 demonstrated that the lower frequency signals in the spectra of TMP arose from molecules adsorbed within smaller pores. The increased chemical shift arose because there was a higher ratio of molecules adsorbed at the pore surface to those within the pore body. It is not surprising that molecules in these situations show lesser amounts of motional freedom than those adsorbed in larger pores, where there is a greater proportion of non-adsorbed molecules. The results of experiments performed at temperatures above the T_1 minimum, for example Figure 7.5, show the opposite trend in the variation of T_1 with temperature. At this temperature an increase in T_1 is the result of an increase in molecular motion. The shorter values for T_1 obtained in the lower temperature experiments at the low frequency end of the broad peak envelope again demonstrate that the mobility of the adsorbed molecules is lowest at that point. The results obtained for the peak at 0 ppm also show that the molecules giving rise to this resonance are in the motional regime above the T_1 minimum. The T_1 values obtained were considerably larger than those recorded for the low-frequency peak and increased markedly as the temperature of the sample was raised. This shows that the molecules giving rise to peak II intensity are less hindered in their motion than any within the broad peak I envelope.

One result that is not easily rationalised is that obtained at the extreme high-frequency end of peak I. In the experiments performed at temperatures both above and below the T_1 minimum the molecules giving rise to intensity at frequencies higher than -6 ppm show decreased mobility with respect to the molecules at slightly lower frequency. This is unexpected, given the conclusions above and from Chapter 4. One tentative suggestion for this effect is that it is the result of magnetisation transfer from peak II to peak I during the τ period. It was demonstrated in Chapter 6 that there was a significant amount of rapid chemical exchange occurring between the molecules giving rise to intensity in peak II and this portion of the low-frequency peak. The τ period in these experiments, extending up to 5 seconds, is clearly sufficient for exchange to occur. In general the T_1 values obtained for peak II are greater than those for the high-frequency portion of peak I. Thus it would be expected that exchange of magnetisation between the two peaks would increase the observed value of T_1 at the sites giving rise to the high-frequency portion of peak I. Whilst this explanation could account for the increase in the observed T_1 at the high-frequency positions across peak I at low temperature, it does not seem to explain the decrease in T_1 observed at temperatures above 10°C.

7.3 SPIN-SPIN RELAXATION

Spectra are acquired by rotating the equilibrium magnetisation into the transverse plane and observing the resulting magnetisation over the acquisition period. At equilibrium there is no net magnetisation in the transverse plane and therefore the intensity of the signal acquired decays exponentially to zero. The way in which this decay occurs can be neatly divided into two effects, that of true spin-spin relaxation, described by the relaxation parameter, T_2, and the effect of magnetic field inhomogeneity, described by another parameter, T_2'. The reciprocals of the two relaxation times are summed to provide a rate constant describing the apparent transverse relaxation observed for each resonance of $1/T_{2*}$. Previously within this thesis the distinction between the relaxation mechanisms has not been important and the total transverse relaxation time, T_{2*} has simply (and incorrectly) been termed T_2.

True T_2 relaxation arises from the random exchange of energy between the nuclei in the α and β states. Immediately after the 90° pulse has been applied, all the spin isochromats are aligned along the same axis within the transverse plane. The phase coherence introduced by the pulse is gradually lost, mainly via exchange of energy between neighbouring spins. The exchange of energy between nuclei is a random process, and any information regarding the phase of the spin is lost. A nucleus that changes spin-state from the excited β state down to the α state and back up to the β state will possess a completely random phase irrespective of its phase initially. As a random phase is introduced to more nuclei, the phase coherence of the spin system is lost. The process is frequently exponential in nature (at least for relatively mobile systems) as the chances of the exchange of energy involving a nucleus contributing to phase coherence decrease with the number of phase-coherent nuclei remaining.

The two effects can be demonstrated by considering the MAS evolution of a single-spin system after a 90° pulse. The rotating frame spin Hamiltonian for the spin system under these conditions has already been calculated (Equation 6.2). The magnetisation arising from each resonance, j, comprises molecules in a variety of spatial positions, k, with different effective B_0 fields. B_0 inhomogeneity can be explored by introducing a further term, ΔB_k, into the Hamiltonian yielding

$$\hat{H}_{eff,R} = \sum_j \left(1 - \sigma_{iso,j}\right)\gamma_I I_z \times \left(B_0 + \sum_k \Delta B_k\right)$$

Equation 7.7

Applying the evolution operator derived from this Hamiltonian to the spin system (cf. Equation 6.4), and allowing for genuine T_2 relaxation, yields an expression for the development of magnetisation over the detection period, t.

$$M(t) = \sum_j M_j(0)\exp\left(i\left(\Delta\omega_j + \sum_k \Delta\omega_k\right)t\right)\exp\left(\frac{-t}{T_{2,j}}\right)$$

Equation 7.8

Re-arranging the expression yields an expression analogous to the standard equation for the evolution of the spin system with MAS applied

$$M(t) = \sum_j M_j(0)\exp\left(i\Delta\omega_j t\right)\exp\left(\frac{-t}{T_{2,j}}\right)\exp\left(\sum_k i\Delta\omega_k t\right)$$

Equation 7.8

For large enough values of k the final term is approximated accurately by an exponential decay and the standard sample spinning evolution operator is obtained

$$M(t) = \sum_j M_j(0)\exp\left(i\Delta\omega_j t\right)\exp\left(\frac{-t}{T_{2,j}} + \frac{-t}{T_2'}\right) = \sum_j M_j(0)\exp\left(i\Delta\omega_j t\right)\exp\left(\frac{-t}{T_{2,j}^*}\right)$$

Equation 7.9

Thus T_{2*} determines the decay of the FID. The decay of the FID controls the width of each resonance within the spectrum. Fourier transformation of the above expression yields

$$S(t) = \sum_j M_j(0) \frac{T_{2,j}^{-1}}{\Delta\omega_j^2 + T_{2,j}^{-2}} \qquad \textit{Equation 7.10}$$

This corresponds to intensity centred at $\Delta\omega_j$, with integral $M_j(0)$ and width $(\pi T_2)^{-1}$. Thus the width of each resonance is determined by T_{2*}. The T_1 experiments showed that peak I was inhomogenous and that molecular mobility increased towards the higher frequency end of this peak. T_2 experiments are able to provide corroboration to the conclusions about molecular mobility obtained from the VT T_1 experiments and also enable analysis of the actual inherent linewidth of the peaks comprising the broad peak I envelope.

7.3.1 THE HAHN ECHO EXPERIMENT

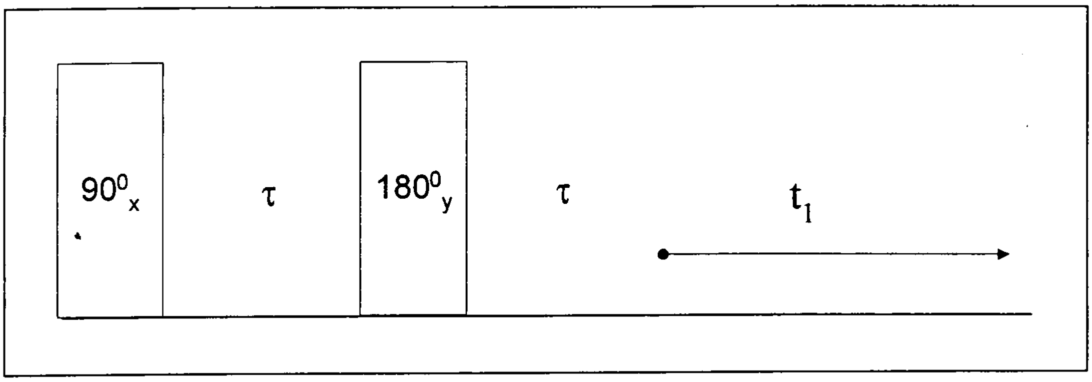

Figure 7.8. Pulse sequence used for the Hahn echo experiment

The pulse sequence used for the Hahn echo experiment is shown in Figure 7.8. The expected form of the spectra obtained from this experiment is calculated below using the expression for the effective spin Hamiltonian derived in the previous section (Equation 7.8). At the end of the first τ period, the magnetisation of the sample is

$$M(\tau)=\sum_j M_j(0)\exp\left(i\left(\Delta\omega_j+\sum_k \Delta\omega_k\right)\tau\right)\exp\left(\frac{-\tau}{T_{2,j}}\right) \qquad \textit{Equation 7.11}$$

The application of the 180°$_y$ pulse causes the sine component of each of the spin isochromats to be reflected about the y-axis. The evolution of the spin system then continues until the echo is generated at 2τ, where acquisition commences. The magnetisation evolution during t_1 may be written

$$M(2\tau,t_1)=\sum_j M_j(0)\left(\cos\left(\Delta\omega_j+\sum_k \Delta\omega_k\right)\tau-i\sin\left(\Delta\omega_j+\sum_k \Delta\omega_k\right)\right)\exp\left(\frac{-\tau}{T_{2,j}}\right)\times$$

$$\exp\left(i\left(\Delta\omega_j+\sum_k \Delta\omega_k\right)\tau+t_1\right)\exp\left(\frac{-\tau+t_1}{T_{2,j}}\right) \qquad \textit{Equation 7.12}$$

The relation $(\cos x - i\sin x)(\cos x + i\sin x) = 1$ removes all precession frequency dependence from the expression for the magnetisation. Fourier transformation with respect to t_1 yields the spectrum

$$S(2\tau,t_1) = \sum_j M_j(0)\exp\left(\frac{-2\tau}{T_{2,j}}\right) \times \frac{T_{2,j}{}^{*-1}}{\Delta\omega_j{}^2 - T_{2,j}{}^{*-2}} \qquad \text{Equation 7.13}$$

Therefore the intensity of each resonance, j, depends upon the period 2τ and the transverse relaxation time for molecules giving rise to that resonance. Repetition of the experiment for a variety of τ periods allows the parameter, T_2 to be evaluated at each site, j.

7.3.1.1 Experimental Procedure

At this stage in the project CBDE altered the type of carbon that was supplied for these experiments. The new carbon, termed PICA, is extremely similar in structure and adsorption behaviour to SC2 and it is expected that the conclusions obtained for the experiments performed upon PICA can be applied equally to SC2. Additionally, CBDE were able to supply a form of PICA (PICA.Cl) that had been treated with chlorine to remove a large proportion of the oxygenated surface heterogeneities. T_2 experiments were conducted upon both samples with ~60% w/w TMP pre-adsorbed. The samples were sealed within glass ampoules and left to equilibrate for over 48 hours prior to acquisition. Pulse calibration was performed upon the actual sample used in each experiment. 256 transients were recorded for each value of τ with a recycle delay of 10 s. Approximately 20 values of τ, ranging from 0.01 ms to 2 s, were used in each experiment, leading to a total experimental time of about 14 hours. The spectra obtained for each value of τ were then plotted and analysed in an analogous way to that for the inversion-recovery experiment. The echo intensity of each position across peak I was fitted to Equation 7.15.

$$S_{\Delta\delta}(2\tau) = A_{\Delta\delta}(0) \times \exp\left(\frac{-2\tau}{T_{2,\Delta\delta}}\right) \qquad \text{Equation 7.14}$$

7.3.1.2. Experimental Results

The results obtained from this pair of experiments are shown in Figure 7.10. In addition to the Hahn echo experiment, a single-pulse experiment was also performed on each of the samples. A comparison of the spectra acquired for the two samples is shown in Figure 7.9. The parameters used in previous chapters to describe the differences between spectra quantitatively are shown in Table 7.2.

Figure 7.10 shows the results of a T_2 analysis performed upon the low-frequency peak for each sample. For comparison, the T_2 values of peak II in each experiment were also studied and the results are shown in Table 7.3. Again the errors describe the variation in the relaxation time obtained when measuring at different points upon the unshifted peak.

	PICA	**PICA-Cl**
Peak Area Ratio	86:14	93:7
$\Delta\delta_{(peakI)}$ **/ ppm**	-8.1	-7.0
$\Delta\nu_{1/2(peakI)}$ **/ Hz**	215	220

Table 7 2. Differences in spectral parameters obtained from 1D spectra of 60% w/w TMP adsorbed upon PICA and PICA-Cl.

	PICA	**PICA-Cl**
T_2 **/ s**	0.014 ± 0.001	0.013 ± 0.001
$\Delta\nu_{1/2}$ **/ Hz**	24 ± 2	25 ± 2

Table 7.3. T_2 measurements obtained for peak II from Hahn echo experiments performed upon 60% w/w TMP added to PICA and PICA-Cl

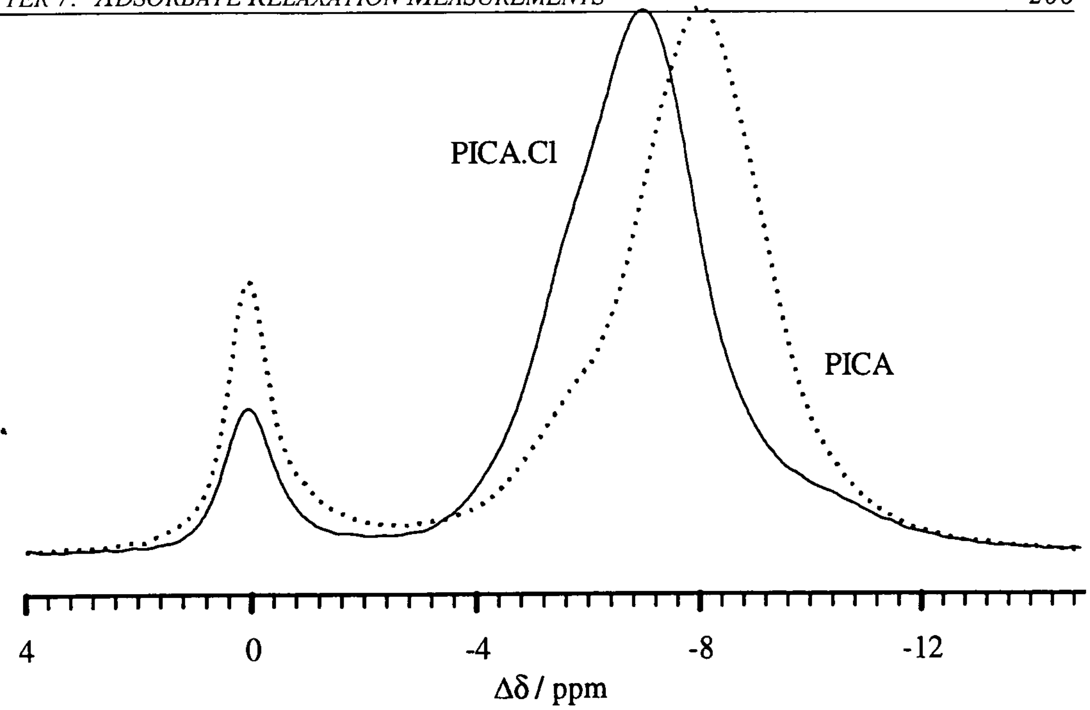

Figure 7.9. Spectra recorded for 60% w/w addition of TMP upon PICA and chlorine-treated PICA. The dashed line repesents spectrum recorded upon PICA.

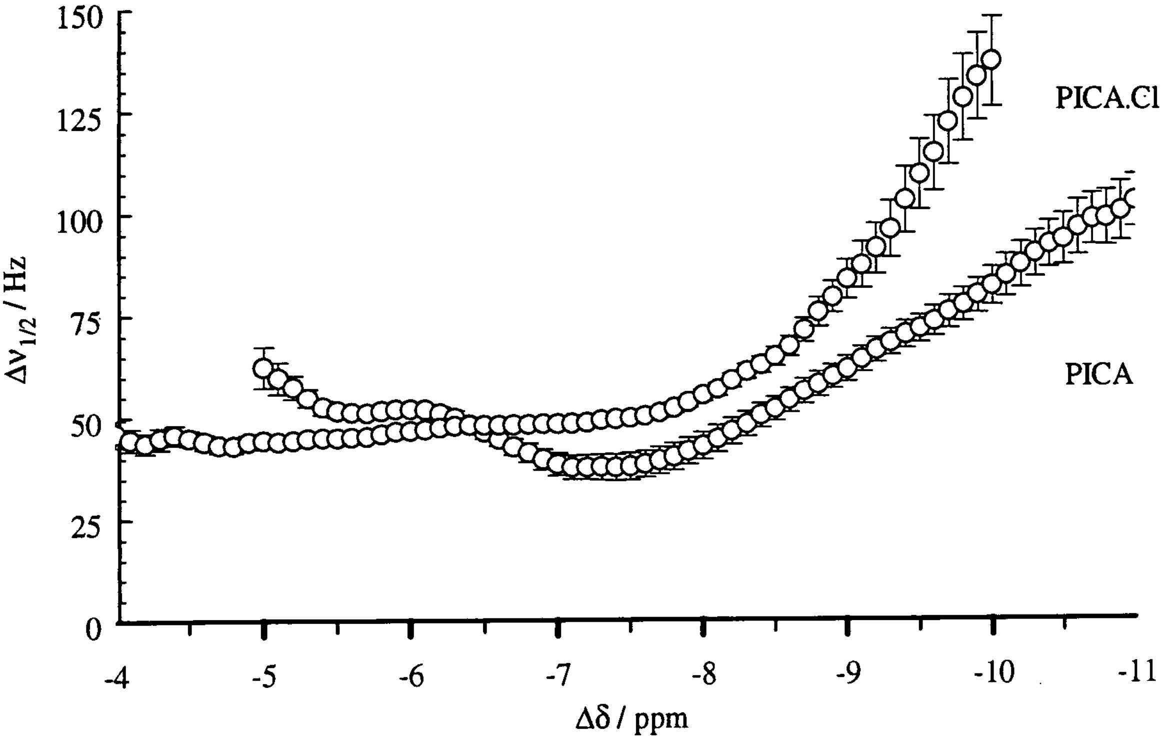

Figure 7.10. Calculated $\Delta\nu_{1/2}$ values obtained from T_2 measurements at various positions across the envelope of peak I. The two plots show the results obtained from 60% w/w TMP adsorbed upon PICA and chlorine-treated PICA.

7.3.1.3. Discussion

The discussion of these results is best approached in two sections, the first relating to the results obtained for PICA alone whilst the second part tries to explain the differences in the spectra and T_2 measurements observed between the two samples.

As expected there was a reasonably marked variation in the value of T_2 obtained for the TMP nuclei adsorbed upon PICA with resonance position within the broad peak I envelope. The values of T_2 obtained ranged from 3 to 9 ms, corresponding to values for the true linewidths of various portions of the peak of 40 to 100 Hz. Simply from the magnitude of these values it is clear that a major contribution to the width of the low-frequency peak is the overlap of peaks occurring at slightly different resonance frequencies. To generate an observed "linewidth" of 300 to 400 Hz there must be a very large number of such narrow constituent peaks underneath the peak envelope. The rationale that peak I is made up of peaks arising from every different sized pore, each at a slightly different resonance frequency, accounts for the large number and variety of peaks required. The variation in T_2 across peak I again shows that the mobility of the molecules is reduced in smaller pores, in agreement with the results obtained from the VT T_1 experiments. However, the narrow natural linewidths observed suggest that there is still a great deal of residual motion present within the sample, even in the smallest pores. It is also noted that the results obtained for PICA show a decrease in T_2 at high frequency. This again suggests that the mobility of molecules giving rise to intensity at the extreme high frequency end of the broad peak envelope is rather smaller than would be expected using solely pore size arguments.

Standard gravimetric measurements performed at CBDE have suggested that chlorine treatment of the activated carbon leaves the pore structure of the adsorbent completely untouched[15]. The treatment is thought to selectively remove the oxidised sites within the pores, leaving a carbon surface that is much more homogeneous. Comparison of the spectra and the T_2 experiments obtained from 60% w/w TMP upon each of the two adsorbates would therefore be expected to provide information upon the role of oxygenated sites in the adsorption of organophosphates upon activated carbon. The greatest difference between the two spectra is the increased low-frequency shift shown by the adsorbate upon the untreated carbon. Figure 7.9 shows that there is a great deal of intensity at high frequency in the spectrum obtained from TMP upon PICA.Cl that is not present in the spectrum acquired for TMP upon PICA. This intensity arises from molecules that encounter a smaller magnetic susceptibility anisotropy than those adsorbed upon PICA. In addition there are no longer as many molecules at positions experiencing large magnetic susceptibility anisotropies on PICA.Cl compared to PICA, shown by the decreased intensity at the low-frequency end of peak I.

The reduction in magnetic susceptibility anisotropy experienced by the adsorbed molecules would conventionally be thought to indicate that the chlorine treatment had caused the pore sizes within the carbon to increase or had altered the adsorbate accessibility to pores of differing size. In discussions it has often been suggested that such a reactive molecule as chlorine might well be expected to react with the carbon surface and would be unlikely to leave the graphene pore surface untouched. However, as mentioned previously, gravimetric techniques appear to demonstrate that this is the case. Another possibility is that the chlorine, in the process of removing the oxygenated surface groups, causes the aromaticity of the graphene planes to be reduced. This would explain why the peak shape and width observed are not altered greatly despite the notable variation in chemical shift. However, if it is assumed that the chlorine treatment does not alter the carbon adsorbent beyond the removal of oxygenated heterogeneities then the differences must arise from their absence within the PICA.Cl sample. The way in which this causes the observed differences between the spectra is not clear, though it has been suggested that the absence of oxygenated sites might allow more efficient pore-filling. This would then result in a decreased ratio of surface adsorbed to non-adsorbed molecules within pores filled via capillary condensation and consequently a slight decrease in the magnitude of the adsorbate low-frequency chemical shift arising from these molecules would be observed.

The Hahn echo experiments demonstrate the difference in the adsorption behaviour of TMP upon the two adsorbents. The TMP molecules upon PICA.Cl generally appear to be held more firmly than those upon PICA, illustrated by the reduced T_2 (increased linewidth) observed in the experiment upon PICA.Cl. This may arise because there are no longer any oxygenated sites to disrupt the adsorption of TMP molecules on the graphene planes. Molecules giving rise to signals at the high frequency end of the peak I upon PICA.Cl show increased mobility with respect to molecules at that frequency upon PICA. A large proportion of the signals arising at that frequency upon normal activated carbon are thought to arise from molecules adsorbed at oxygenated sites. The removal of the oxygenated sites then means that the remaining molecules giving rise to signals at that frequency (now corresponding solely to capillary condensate within larger pores) are no longer as hindered. The presence of oxygenated sites in untreated activated carbons would also explain the anomalous motional results obtained for molecules at the high-frequency end of the resonance in the inversion-recovery experiment. However, as noted before, the intensity of the high-frequency end of peak I is increased in PICA.Cl with respect to PICA –the opposite of what would conventionally be expected if the chlorine treatment simply removed the oxygenated sites.

Comparison of the results obtained shows that there are many differences between the adsorption behaviour of TMP upon the two adsorbents. However, it is extremely difficult to ascertain the reasons for the differences, and whilst tentative suggestions may be proposed to explain one or other aspect of the adsorbates' behaviour upon the carbon, no firm conclusions can be made. Further experiments, either using organophosphates, or perhaps D_2O, are clearly required to understand the role of oxygenated sites in the adsorption processes upon these carbons.

7.4. REFERENCES

1. F. Bloch, *Phys. Rev.*, **70**, 460 (1946)
2. E. L. Hahn, *Concepts Magn. Reson.*, **6**, 1994
3. J. M^{c}Connell, *"The Theory of NMR Relaxation in Liquids"*, Cambridge University Press, Cambridge (1987)100 NMR Experiments book
4. N. Bloembergen, *Concepts Magn. Reson.*, **6**, 1994
5. D. D. Traficante, "Relaxation: An Introduction", Encyclopedia of NMR (Editors D. M. Grant and R. K. Harris), Wiley, London, 1996
6. N. Bloembergen, E. M. Purcell, R. V. Pound, *Phys. Rev.*, **73**, 679 (1948)
7. I. Solomon, *Phys. Rev.*, **99**, 559 (1955)
8. A. G. Redfield, *"Advances in Magnetic Resonance"*, ed. J. S. Waugh, Academic Press, New York, **9**, 189 (1979)
9. R. K. Harris, *"Nuclear Magnetic Resonance Spectroscopy –a physicochemical approach"*, Longman Scientific and Technical (1987)
10. J. S. Frye, *Concepts Magn. Reson.*, **1**, 27 (1989)
11. S. Braun, H.-O. Kalinowski, *"100 and More Basic NMR Experiments"*, VCH, Germany (1996)
12. R. Freeman, S. P. Kempsall, M. H. Levitt, *J. Magn. Reson.*, **38**, 453 (1980)
13. D. W. Marquardt, *Journal of the Society for Industrial and Applied Mathematics*, **2**, 431 (1963)
14. SPSS v7.5 for Solaris, SPSS Inc.
15. *"Carbon Surface Modification"*, P. R. Norman, S. E. Meech, L. Pears, presented at British Carbon Group Conference on Current U.K. Research in Carbon, University of Loughborough, Sept. 1997

FUTURE WORK

Solid-state NMR is the only technique that is able to obtain quantitative data upon the variation in the position of molecules within the carbon pore system over time. This enables differences in the mechanism of adsorption for different molecules to be established, and it is possible to infer the positions within the carbon at which adsorption occurs. The work presented within this thesis has resulted in several insights to the adsorption process that could not be reached by any other technique. However, after three years the most definite conclusion that has been established is that there remain innumerable further avenues to explore in the study of adsorbates upon activated carbon by NMR.

An example of the information that can be obtained by NMR involved results obtained from a series of Spin Echo Double Resonance experiments performed upon a sample of TMP on SC2 carbon. SEDOR experiments enable the residual heteronuclear dipolar coupling present within a sample to be calculated. By fitting the value for the dipolar coupling obtained to theoretical models it is then possible to obtain information upon the motion of the adsorbate molecules upon the carbon surface. Preliminary results upon adsorbed TMP suggest that there is free rotation about the methoxy arms and about the main carbonyl axis. Variable temperature SEDOR experiments should enable activation energies for each process to occur, and again provide information upon the interaction between the molecules and the carbon surface.

Because the data obtained from NMR is unique, one of the major problems encountered in the study of these systems is the absence of corroborating data from other sources. The recent development of techniques to tailor both the P.S.D. and surface polarity of activated carbons at Porton Down should provide a way of circumventing this problem. Comparison of spectra (and more complex measurements) obtained from a number of carbons that differ from one another in a well-characterised manner will undoubtedly yield useful information upon the features arising from the characteristics of each of the carbons. This approach was demonstrated in Chapter 7, where comparison of spectra obtained from TMP adsorbed upon PICA and PICA.Cl allowed inferences to be drawn on the role of oxygenated sites in the adsorption of organophosphates upon activated carbon. More explicit differences would be expected if similar experiments were performed using D_2O as the probe molecule, due to the importance of oxygenated sites in the adsorption of polar molecules onto a largely hydrophobic carbon surface.

An entire area that warrants study is the spectra obtained from adsorbates upon carbon samples that have undergone vapour-phase adsorption. Porton Down have a variety of techniques for following the vapour-phase adsorption process gravimetrically and if it proved possible to combine and compare data from both sources a clearer picture of the possible role of NMR in adsorption studies could be established. For example, the shape of isotherms obtained from vapour-phase adsorption is routinely interpreted by separating the adsorption process into several regimes in which the role of different features of the activated carbon becomes important. Study of the NMR spectra obtained from samples taken at a variety of positions along the adsorption isotherm would allow the theoretical treatment to be tested. Of course, the amounts of adsorbate within the sample will be much reduced in the vapour-phase adsorption with respect to the experiments presented in the current study and would require correspondingly longer NMR experiments to be conducted upon them. The use of labelled adsorbates (D_2O provides far superior S/N to the organophosphates and phosphonates) may become necessary.

APPENDIX

Research Conferences Attended

NMR of solids and solid-like materials, NMR discussion group meeting, University College, London 19th December 1995

Summer School on NMR of Solids, University of Durham, 16-20th September 1996

Royal Society of Chemistry Annual Congress and Young Researchers Meeting, University of Durham, 6-9th April 1998

Oral Presentations

NMR Studies of Adsorption Processes upon Activated Carbon, Final year Graduate symposium, University of Durham, 1st June 1998

Advances in the Study of Adsorption Process by NMR, CBDE, Porton Down, 8th September 1998

Poster Presentations

COPS IV (reference pending)[†]

MAS NMR Study of Adsorption Processes upon Activated Carbon, I.C.I. Poster Competition, University of Durham, 22nd December 1997

Variable-temperature ^{31}P MAS NMR Studies of Organophosphates adsorbed on Activated Carbon, R.S.C. Young Researchers Meeting, 6th April 1998.[*]

[†] Presented by Dr. P. R. Norman

[*] Winner of Best Poster, RSC Young Researchers Congress, Physical Chemistry section

Publications

"*Magic-angle spinning NMR studies of adsorption onto activated carbons*", R. K. Harris, T. V. Thompson, J. A. Shaw and P. R. Norman in "Characterisation of Porous Solids IV" (eds. B. McEnaney, T. J. Mays, J. Roquerol, F. Rodriguez-Reinoso, K. S. W. Sing and K. K. Unger), RSC Publications

"*Magic-angle NMR Study of the Competitive Adsorption of an Organo-phosphate and Organo-phosphonate Adsorbate on Activated Carbon*", J. A. Shaw, R. K. Harris, P. R. Norman, accepted for publication, Langmuir, July 1998

Research conducted outside the Department

Worked with employees of DERA on instrument calibration, gas chromatography and vapour phase adsorption techniques. CBDE, Porton Down, Wilts. 2-6th February 1996

Research colloquia, seminars and lectures given by invited speakers

1995

October 11	Prof. P. Lugar, Frei University of Berlin, FRG Low Temperature Crystallography
October 25	Dr. D. Martin Davies, University of Northumbria Chemical reactions in organised systems
November 22	Prof. I Soutar, Lancaster University A Water of Glass? Luminescence Studies of Water-Soluble Polymers

1996

January 10	Dr Bill Henderson, Waikato University, NZ Electrospray Mass Spectrometry - a new sporting technique
January 17	Prof. J. W. Emsley, Southampton University Liquid Crystals: More than Meets the Eye

January 31	Dr J. Penfold, Rutherford Appleton Laboratory, Soft Soap and Surfaces
February 28	Prof. E. W. Randall, Queen Mary & Westfield College New Perspectives in NMR Imaging
March 12	RSC Endowed Lecture - Prof. V. Balzani, University of Bologna Supramolecular Photochemistry
March 13	Prof. Dave Garner, Manchester University Mushrooming in Chemistry
October 9	Professor G. Bowmaker, University of Auckland, NZ Coordination and Materials Chemistry of the Group 11 and Group 12 Metals: Some Recent Vibrational and Solid State NMR Studies
October 22	Professor B. J. Tighe, Department of Molecular Sciences and Chemistry, University of Aston Making Polymers for Biomedical Application - Can we meet Nature's Challenge? Joint lecture with the Institute of Materials
October 23	Professor H. Ringsdorf (Perkin Centenary Lecture), Johannes Gutenberg-Universitat, Mainz, Germany Function Based on Organisation
October 29	Professor D. M. Knight, Department of Philosophy, University of Durham. The Purpose of Experiment - A Look at Davy and Faraday
November 6	Dr Melinda Duer, Chemistry Department, University of Cambridge Solid-state NMR Studies of Organic Solid to Liquid-crystalline Phase Transitions
November 12	Professor R. J. Young, Manchester Materials Centre, UMIST New Materials - Fact or Fantasy? Joint Lecture with Zeneca & RSC
November 20	Professor J. Earnshaw, Department of Physics, Belfast University Surface Light Scattering: Ripples and Relaxation

November 27	Dr Richard Templer, Imperial College, London Molecular Tubes and Sponges

1997

January 21	Mr D. Rudge, Zeneca Pharmaceuticals High Speed Automation of Chemical Reactions
January 29	Dr Julian Clarke, UMIST What can we learn about polymers and biopolymers from computer-generated nanosecond movie-clips?
February 4	Dr A. J. Banister, University of Durham From Runways to Non-metallic Metals - A New Chemistry Based on Sulfur
February 19	Professor Brian Hayden, University of Southampton The Dynamics of Dissociation at Surfaces and Fuel Cell Catalysts
March 11	Dr A. D. Taylor, ISIS Facility, Rutherford Appleton Laboratory Expanding the Frontiers of Neutron Scattering
March 19	Dr Katharine Reid, University of Nottingham Probing Dynamical Processes with Photoelectrons
October 15	Dr. R. Mark Ormerod, Department of Chemistry, Keele University Studying catalysts in action
October 23	Prof. M.R. Bryce, University of Durham, Inaugural Lecture New Tetrathiafulvalene Derivatives in Molecular, Supramolecular and Macromolecular Chemistry: controlling the electronic properties of organic solids
October 29	Prof. Bob Peacock, University of Glasgow Probing chirality with circular dichroism
October 28	Prof. A P de Silva, The Queen's University, Belfast Luminescent signalling systems

November 19	Dr. Gareth Morris, Department of Chemistry, Manchester University Pulsed field gradient NMR techniques: Good news for the Lazy and DOSY
November 26	Prof. R.W. Richards, University of Durham, Inaugural Lecture A random walk in polymer science
December 2	Dr. C. J. Ludman, University of Durham Explosions
December 10	Sir Gordon Higginson, former Professor of Engineering in Durham and retired Vice-Chancellor of Southampton University. 1981 and all that

1998

January 20	Prof. J. Brooke, University of Lancaster What's in a formula? Some chemical controversies of the 19th century
February 3	Dr J. Beacham, ICI Technology The chemical industry in the 21st century
February 17	Dr. S. Topham, ICI Chemicals and Polymers Perception of environmental risk: The River Tees, two different rivers
February 18	Prof. Gus Hancock, Oxford University Surprises in the photochemistry of tropospheric ozone
March 18	Dr John Evans, Oxford University Materials which contract on heating (from shrinking ceramics to bulletproof vests)